

# **A computational model for the description of electrostatic precipitator performance**

**S Arif**

 **orcid.org 0000-0002-9234-4964**

MS Process Engineering, Pakistan Institute of  
Engineering & Applied Sciences, Islamabad, Pakistan  
BSc Chemical Engineering, UET, Lahore,  
Pakistan

Thesis submitted in fulfilment of the requirements for the degree  
*Doctor of Philosophy in Chemical Engineering* at the North-  
West University

Supervisor: Dr. DJ Branken  
Co-supervisors Prof. RC Everson  
Prof. HWJP Neomagus

Graduation: May 2019  
Student number: 25283448

---

---

*“Life is difficult. This is a great truth, one of the greatest truths. It is a great truth because once we truly see this truth, we transcend it. Once we truly know that life is difficult-once we truly understand and accept it-then life is no longer difficult. Because once it is accepted, the fact that life is difficult no longer matters.”*

***From “The Road Less Traveled”, book authored by M Scott Peck***

*“And after you have suffered a little while, the God of all grace, Who has called you to His eternal glory in Christ Jesus, will Himself complete and make you what you ought to be, establish and ground you securely, and strengthen, and settle you.”*

***1 Peter 5:10***

*“All men dream but not equally. Those who dream by night in the dusty recesses of their minds wake in the day to find that it was vanity; but the dreamers of the day are dangerous men, for they may act their dream with open eyes to make it possible.”*

***T.E. Lawrence***

*“Every great dream begins with a dreamer. Always remember, you have within you the strength, the patience, and the passion to reach for the stars to change the world.”*

***Harriet Tubman***

*“Reach high, for stars lie hidden in your soul. Dream deep, for every dream precedes the goal.”*

***Pamela Vaull Starr***

*“Our truest life is when we are in dreams awake”*

***Henry David Thoreau***

*“So often times it happens that we live our lives in chains*

*And we never even know we have the key.”*

***From “Already Gone”, performed by the Eagles for their 1974 On the Border album.***

---

## DECLARATION

I, S Arif, hereby declare that the thesis entitled: “*A computational model for the description of electrostatic precipitator performance*”, submitted in fulfillment of the requirements for the degree *Philosophiae Doctorate* in Chemical Engineering is my own work, except where acknowledged in the text, and has not been submitted to any other tertiary institution in whole or in part.

Signed at North-West University (Potchefstroom Campus)



S. Arif

25283448

November 2018

## ACKNOWLEDGEMENTS

All the praise and glory is to Allah (The God), for without Him the completion of this work would never have been possible. After that I would like to acknowledge role of several individuals that proved to be very instrumental for my PhD research work and compilation of this thesis successfully.

First of all I would like to express my sincere gratitude to my supervisor Dr. Dawie Branken for encouraging me to pursue the project and providing guidance throughout the course of this research project. He provided me with a stress free research environment which stimulates original thinking and initiative and I really enjoyed working in his supervision. He encouraged and supported me for any novel addition to my research work which can add valuable contribution to the study field apart from following specific objectives.

I am also sincerely thankful to my co-supervisor Prof. R.C. Everson for helping and guiding me throughout the course of study period and providing valuable inputs to my research work. I would also like to thank him for being concerned about each and every need of me and my family during my research work apart from providing necessary guidance and support related to studies.

My deepest and sincere appreciation goes to my co-supervisor Prof HWJP Neomagus for providing invaluable assistance and recommendations throughout the research project. Without his guidance and help it would not been possible to speed up and complete my studies during the last phase of the study schedule. I am really thankful to him for extracting time from his busy schedule to go through my articles and thesis draft and providing recommendations and suggestions in less than a week's time. He always guided me well in terms of thesis drafting, arranging text etc. whenever I asked him even without making an appointment.

I would like to convey my thanks to Louis le Grange for helping and guiding me during the computational modelling code development phase of my research work. He guided me well relating to software debugging issues and also whenever I had some issues developing CFD model.

CD-Adapco officials Christiaan de Wet and Paco Ezquerro are highly acknowledged for providing guidance and resolving software related issues. Their help throughout the research work is highly appreciated.

I would like to thank Dr Maciej Noras, University of North Carolina at Charlotte, USA and his team for helping us getting permittivity data for South African fly ash samples and carrying out necessary experiments at their facilities.

Geecom Air pollution control systems South Africa is also highly appreciated for providing technical information regarding their innovative G Spike discharge electrode design and data for CFD simulation purposes. I would also like to thank especially Dan Picolo from Geecom for his extreme efforts regarding measurements of V-I curves experimentally.

My special thanks also go to our North-West University workshop staff, particularly Adrian and Jan for providing help during necessary modifications of the experimental ESP rig at very short notices. I would also like to thank Warren for helping me throughout the experimental work.

I also acknowledge the support of the Eskom Power Plant Engineering Institute (EPPEI), particularly for the financial support provided to me as an EPPEI student at the Emissions Control Specialisation Centre at the North-West University.

Lastly, my deepest appreciation belongs to my family, particularly my father, my mother and my boys (Ayyan and Rayan) for supporting and encouraging me during the final stages of my work when it was much needed. I am also thankful to my husband Arif for supporting and encouraging me during hardships encountered during the study period.

## ABSTRACT

A comprehensive computational model of an electrostatic precipitator was developed by incorporating the interacting phenomenon of fluid dynamics, particle dynamics and electrostatics using the commercial software STAR-CCM+® and the open source software package OpenFOAM®. The electrostatic equations were solved using OpenFOAM while particle charging and particle dynamics were solved using STAR-CCM+. The Euler-Lagrange approach was used to model the respective gas and particle flow, and turbulence were taken into account using the k- $\epsilon$  turbulence model. The developed computational model was intermittently validated with experimental results available in literature in terms of the electrostatics properties as well as particle collection efficiency. The results of a sensitivity analysis with respect to varying geometric and operating parameters are also reported. In this regard, the computational modelling results showed, in accordance with the literature, that the particle collection efficiency increases with increasing particle diameter, decreasing air velocity, decreasing wire-to-plate spacing and with an increasing number of discharge wires. It was further found that variation of relative permittivity also has significant influence on the particle collection efficiency which increases with increasing relative permittivity.

The model was subsequently further refined and validated with experimental and computational results taken from the literature to study the shielding effect that can arise in the case of multi-electrode ESP systems. Shielding was shown to significantly influence the space charge and current density distributions that are obtained during corona discharge. More specifically, the computational modelling results showed that the current density and space charge density developed around the inner wire-electrodes were suppressed relative to the outermost wires. The intensity of shielding was quantified in terms of the peak current density and space charge density resulting from corona discharge from the outer wires relative to that of the inner wires. Consequently, the modeling results showed that the intensity of shielding was dependent on the wire-to-wire spacing, the plate-to-plate spacing, and the number of wire-electrodes, although the plate-to-plate spacing was found to be the most influential parameter.

The developed computational model was finally validated with experimental results obtained using an in-house laboratory-scale ESP. The use of both wire-electrodes and spiked electrodes were studied, and the modeled and experimentally measured V-I relationships and particle collection efficiencies were compared under shielding and non-shielding conditions. Good agreement was achieved between the measured and modeled V-I relationships of the wire-electrodes, both under shielding and non-shielding conditions. Consequently, the shielding effects predicted with the computational model was confirmed in terms of the V-I characteristics and particle collection efficiencies that were achieved under varying geometric parameters. Additionally, the experimental results obtained with a spiked electrode also confirmed the validity of the computational model with respect to modeling ESP operation with irregularly shaped electrodes.

**Keywords:** *Computational modelling, electrostatic precipitator, Euler-Lagrange, electrostatics, particle dynamics, fluid dynamics, shielding effect, spiked electrode*

## PREFACE

### Format of thesis

The format of this thesis is in accordance with the academic rules of the North-West University (approved on November 22<sup>nd</sup>, 2013), where rule **A.5.4.2.7** states: “Where a candidate is permitted to submit a thesis in the form of a published research article or articles, or as an unpublished manuscript or manuscripts in article format and more than one such article or manuscript is used, the thesis must still be presented as a unit, supplemented with an inclusive problem statement, a focused literature analysis and integration and with a synoptic conclusion, and the guidelines of the journal concerned must also be included.”

Rule **A.5.4.2.8** states: “Where any research article or manuscript and/or internationally examined patent is used for the purpose of a thesis in article format to which other authors and/or inventors than the candidate contributed, the candidate must obtain a written statement from each co-author and/or co-inventor in which it is stated that such co-author and/or co-inventor grants permission that the research article or manuscript and/or patent may be used for the stated purpose and in which it is further indicated what each co-author’s and/or co-inventor’s share in the relevant research article or manuscript and/or patent was.”

Rule **A.5.4.2.9** states: “Where co-authors or co-inventors as referred to in A.5.4.2.8 above were involved, the candidate must mention that fact in the preface and must include the statement of each co-author or co-inventor in the thesis immediately following the preface.”

### Format of numbering and referencing

It should be noted that the formatting, referencing style, numbering of tables and figures, and general outline of the manuscripts were adapted to ensure uniformity throughout the thesis. The format of manuscripts which have been submitted and/or published adhere to the author guidelines as stipulated by the editor of each journal, and may appear in a different format to what is presented in this thesis. The headings and original technical content of the manuscripts were not modified from the submitted and/or published versions, and only minor spelling and typographical errors were corrected.

## STATEMENT FROM CO-AUTHORS

To whom it may concern,

The listed co-authors hereby give consent that Samrana Arif may submit the following manuscript(s) as part of her thesis entitled: A computational model for the description of electrostatic precipitator performance, for the degree Philosophiae Doctor in Chemical Engineering, at the North-West University:

- S. Arif, D.J. Branken, R.C. Everson, H.W.J.P. Neomagus, L.A. le Grange, A. Arif. CFD modeling of particle charging and collection in electrostatic precipitators. Journal of Electrostatics 2016, 84, 10-22.
- S. Arif, D.J. Branken, R.C. Everson, H.W.J.P. Neomagus, A. Arif. The influence of design parameters on the occurrence of shielding in multi-electrode ESPs and its effect on performance. Journal of Electrostatics 2018, 93, 17-30.

(This letter of consent complies with rules A 5.4.2.8 and A 5.4.2.9 of the academic rules as stipulated by the North-West University)

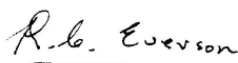
Signed at Potchefstroom



28/05/2018

.....  
D.J. Branken

.....  
Date



28/05/2018

.....  
R.C. Everson

.....  
Date



28/05/2018

.....  
H.W.J.P. Neomagus

.....  
Date



28/05/2018

.....  
L.A. le Grange

.....  
Date



28/05/2018

.....  
A. Arif

.....  
Date



## LIST OF JOURNAL PUBLICATIONS AND CONFERENCE CONTRIBUTIONS RELATED TO THIS STUDY

The content of this thesis is largely based on the following journal publications:

**S. Arif**, D.J. Branken, R.C. Everson, H.W.J.P. Neomagus, L.A. le Grange, A. Arif. *CFD modeling of particle charging and collection in electrostatic precipitators*. **Journal of Electrostatics** 2016; 84: 10-22.

**S. Arif**, D.J. Branken, R.C. Everson, H.W.J.P. Neomagus, A. Arif. *The influence of design parameters on the occurrence of shielding in multi-electrode ESPs and its effect on performance*. **Journal of Electrostatics** 2018; 93: 17-30.

**S. Arif**, D.J. Branken, R.C. Everson, H.W.J.P. Neomagus, A. Arif. *Experimental validation of a computational model of a laboratory-scale electrostatic precipitator*. (to be submitted)

In addition to the abovementioned journal publications, the following conference contributions were made based on the work presented in this thesis:

**S. Arif**, D.J. Branken, R.C. Everson, H.W.J.P. Neomagus. *Using CFD modeling to establish optimized discharge electrode spacings for electrostatic precipitators*. **4<sup>th</sup> Eskom Power Plant Engineering Institute Student Workshop.**, May 29-30 (2017), Eskom Academy of Learning, Midrand, South Africa.

Samrana Arif, **David Branken**, Ray Everson, Hein Neomagus, Louis le Grange. *The influence of discharge electrode geometry and the associated discharge characteristics on electrostatic precipitator performance*. The **8<sup>th</sup> International Conference on Clean Coal Technologies (CCT 2017)**., May 08-12 (2017), Cagliari, Sardinia, Italy.

**S. Arif**, R.C. Everson, D.J. Branken, H.W.J.P. Neomagus. *An advanced CFD model for electrostatic precipitators*. **3<sup>rd</sup> Eskom Power Plant Engineering Institute Student Workshop.**, July 11-12 (2016), Eskom Academy of Learning, Midrand, South Africa.

S. Arif, **D.J. Branken**, R.C. Everson, H.W.J.P. Neomagus, A. Arif, L.A. le Grange. *Particle charging and transport dependence on permittivity and fluid dynamics*. The **7<sup>th</sup> International Conference on Clean Coal Technologies (CCT 2015)**., May 17-21 (2015), Krakow, Poland.

**S. Arif**, H.W.J.P. Neomagus, R.C. Everson, D.J. Branken, A. Arif, L.A. le Grange. *An advanced CFD model for electrostatic precipitators*. The **20<sup>th</sup> South African Conference on Research in Coal Science and Technology.**, November 24-25 (2015), North West University, Potchefstroom Campus, South Africa.

---

---

## TABLE OF CONTENTS

<b>DECLARATION</b>	<b>ii</b>
<b>ACKNOWLEDGEMENTS</b>	<b>iii</b>
<b>ABSTRACT</b>	<b>v</b>
<b>PREFACE</b>	<b>vi</b>
<b>STATEMENT FROM CO - AUTHORS</b>	<b>vii</b>
<b>LIST OF JOURNAL PUBLICATIONS AND CONFERENCE CONTRIBUTIONS RELATED TO THIS STUDY</b>	<b>viii</b>
<b>LIST OF TABLES</b>	<b>xiv</b>
<b>LIST OF FIGURES</b>	<b>xvi</b>
<b>LIST OF SYMBOLS</b>	<b>xxii</b>
<b>LIST OF ABBREVIATIONS</b>	<b>xxiii</b>
 <b>Chapter 1. INTRODUCTION</b>	 <b>1</b>
1.1 Background and motivation	1
1.2 Problem statement	7
1.3 Aim and objectives	7
1.3.1 Aim	7
1.3.2 Objectives	7
1.3.3 Scope	7
1.4 Outline of thesis	8
1.5 References	9
 <b>Chapter 2. LITERATURE SURVEY</b>	 <b>12</b>
2.1 Emissions at coal fired power stations and regulations	12
2.2 Processes for particulate matter removal	13
2.2.1 Industrial scale processes	13
2.2.2 Comparison and effectiveness of different PM removal processes	14

2.2.3	Principles and fundamentals of electrostatic precipitators	15
2.3	Electrostatic precipitation: Industrial application	17
2.3.1	Different industrial electrostatic precipitators	17
2.4	Electrostatic precipitation: Overview of recent research	18
2.4.1	Laboratory and pilot plant experimentation	18
2.4.2	Empirical modelling and validation	20
2.4.3	Computational modelling and validation	21
2.5	Summary	24
2.6	References	25
<b>Chapter 3.</b>	<b>CFD MODELING OF PARTICLE CHARGING AND COLLECTION IN ELECTROSTATIC PRECIPITATORS</b>	<b>29</b>
3.1	Introduction	30
3.2	Numerical modeling and solution methods	32
3.2.1	Electrostatic field	32
3.2.2	Fluid and particle dynamics	35
3.2.2.1	Continuous phase fluid dynamics	35
3.2.2.2	Particle dynamics	35
3.2.2.3	Particle charging	36
3.2.3	Simulated ESP geometries	38
3.3	Results and discussion	40
3.3.1	Electrostatics	40
3.3.2	Fluid and particle dynamics	43
3.3.3	CFD model validation against previously reported experimental and simulated results	45
3.3.4	The effect of varying ESP geometry and operating parameters on collection efficiency	46
3.3.5	Effect of discharge electrode geometry	49

3.4	Conclusions	50
3.5	Supplementary data	51
3.6	References	51
<b>Chapter 4.</b>	<b>THE INFLUENCE OF DESIGN PARAMETERS ON THE OCCURRENCE OF SHIELDING IN MULTI-ELECTRODE ESPs AND ITS EFFECT ON PERFORMANCE</b>	<b>54</b>
4.1	Introduction	55
4.2	Numerical modeling and solution methods	57
4.2.1	Simulated ESP geometries	57
4.2.1.1	Validation of numerical model using literature data	57
4.2.1.2	Computational model used for evaluation of shielding	58
4.3	Results and discussion	60
4.3.1	CFD model validation	60
4.3.2	Analysis of shielding	63
4.3.2.1	The influence of the plate-to-plate spacing on the degree of shielding	63
4.3.2.2	The influence of the wire-to-wire spacing on the degree of shielding	66
4.3.2.3	The influence of the number of discharge wires on the degree of shielding	67
4.3.2.4	The influence of the discharge electrode voltage on the degree of shielding	71
4.3.3	The influence of shielding on the particle collection efficiency	71
4.4	Conclusions	73
4.5	References	74

<b>Chapter 5.</b>	<b>EXPERIMENTAL VALIDATION OF A COMPUTATIONAL MODEL OF A LABORATORY-SCALE ELECTROSTATIC PRECIPITATOR</b>	<b>77</b>
5.1	Introduction	78
5.2	Computational modelling	81
5.2.1	Modelling parameters	81
5.3	Experimental method	83
5.3.1	Laboratory scale ESP	83
5.3.2	Fly Ash concentration and air flow velocity measurements	85
5.3.3	Fly ash preparation and characterization	85
5.3.4	Experiment program	86
5.4	Results and discussion	87
5.4.1	Validation of the shielding effects predicted by the computational model	88
5.4.2	ESP performance with wire-electrodes	89
5.4.3	ESP performance with a commercial spiked electrode	93
5.4.3.1	Electrostatic properties of the spiked electrode	93
5.4.3.2	Particle collection efficiency	96
5.5	Conclusions	99
5.6	References	99
<b>Chapter 6.</b>	<b>CONCLUSIONS AND RECOMMENDATIONS</b>	<b>103</b>
6.1	Summary and conclusions	103
6.2	Contribution to the current knowledge	105
6.3	Recommendations	105
<b>Appendix A:</b>	<b>SUPPLEMENTARY INFORMATION FOR CHAPTER 3</b>	<b>107</b>
<b>Appendix B:</b>	<b>COMPUTATIONAL MODELLING SUMMARY</b>	<b>111</b>

---

---

<b>Appendix C: SUPPLEMENTARY INFORMATION ON THE COMPUTATIONAL MODELLING PROCEDURE</b>	<b>117</b>
<b>Appendix D: ADDITIONAL COMPUTATIONAL MODELLING RESULTS FOR SPIKE DISCHARGE ELECTRODE</b>	<b>123</b>
<b>Appendix E: EXPERIMENTAL METHOD - SUPPLEMENTARY INFORMATION</b>	<b>127</b>
<b>Appendix F: NORTH WEST UNIVERSITY EXPERIMENTAL SET UP DRAWINGS AND GEECOM SPIKED DISCHARGE ELECTRODE DATA</b>	<b>139</b>

---



---

## LIST OF TABLES

Table 1.1:	Atmospheric emissions (%) in South Africa	2
Table 1.2:	Minimum emission standards applicable to solid fuel combustion installations according to NEM: AQA	3
Table 1.3:	Emission limits implemented at various South African CFFPs in 2015 under normal conditions of 273 K and 101.3 kPa relative to 10% O <sub>2</sub>	4
Table 2.1:	Characteristics of PM control/removal processes	14
Table 2.2:	Summary of the experimental studies related to laboratory scale ESPs	20
Table 2.3:	Summary of the empirical/theoretical modelling studies related to laboratory scale ESPs	21
Table 2.4:	Summary of the CFD modelling studies related to pilot plant/laboratory scale ESPs	24
Table 3.1:	Summary of boundary conditions	34
Table 3.2:	Specifications of the experimental ESP used by Penney and Matick	38
Table 3.3:	Geometric and operational parameters of the experimental ESP setup used in the study of Kihm	39
Table 3.4:	Summary of the experimental ESP's simulated	40
Table 4.1:	Specifications of the single-channel wire-electrode ESPs used for validation	58
Table 4.2:	Geometric and operational parameters of the ESP setup used in this study	59
Table 4.3:	The degree of shielding at the wire-plane and the collecting plate-plane with varying plate-to-plate spacing	64
Table 4.4:	The degree of shielding at the wire-plane and the collecting plate-plane with varying wire-to-wire spacing	67
Table 4.5:	The degree of shielding at the wire-plane and the collecting plate-plane with a varying number of discharge wires	69
Table 5.1:	Geometric and operational parameters of the ESP system used in the present computational modelling study	82
Table 5.2:	Summary of experiments performed with the wire discharge electrode assembly	87
Table 5.3:	Summary of experiments performed with the spiked discharge electrode assembly	87
Table B-1:	Description of governing equations for CFD modelling	111
Table B-2:	Summary of boundary conditions	112

---

---

Table C-1:	The basic characteristics of the computational model	118
Table E-1:	Measured relative permittivity of South African CFPP fly ash at varying temperature and humidity	130
Table E-2:	ESP parameters that have been used in previous experimental studies	131
Table F-1:	V-I data for different discharge electrodes including the G-Spike electrode	146



---



---

## LIST OF FIGURES

Fig 1.1:	Energy related PM <sub>2.5</sub> emissions by region and sector for 2015	2
Fig 1.2:	South African power station PM emissions in 2015	5
Fig 1.3:	Field interaction in electrostatic precipitators	6
Fig 2.1:	Contribution of energy sector for selected primary air pollutants, 2015	12
Fig 2.2:	Particle size range covered by different PM removal processes along with important atmospheric impurities range	15
Fig 2.3:	ESP basic operating principle	16
Fig 2.4:	A conventional electrostatic precipitator	17
Fig 3.1:	A 3-D computational model of a single-channel ESP	39
Fig 3.2:	Distribution of (a) the electric potential (kV), (b) the space charge density, and (c) the electrostatic field magnitude through the ESP channel corresponding to the experimental system of Penny and Matick at $V = 25.5$ kV	41
Fig 3.3:	Comparison of CFD results with the experimental measurements of Penney & Matick at (a) $x = 228.6$ mm (b) $x = 266.7$ mm and (c) $x = 304.8$ mm	42
Fig 3.4:	Simulated trajectories of dust particles through the ESP channel corresponding to Kihm [13] for particles with uniform diameters of respectively (a) $2\text{ }\mu\text{m}$ , (b) $6\text{ }\mu\text{m}$ , and (c) $10\text{ }\mu\text{m}$ at $V = 9$ kV	44
Fig 3.5:	Air flow streamlines indicating the effects of electro hydrodynamic flow on gas (ion) flow at an inlet velocity of (a) $0.1$ m/s, (b) $1$ m/s	45
Fig 3.6:	Comparison between the particle collection efficiency predicted by the current CFD model and (a) experimental results (Kihm, 1987), and the simulation results of Long and Yao (2010) using (b) the PMHW charging model, and (c) the Lawless charging model	46
Fig 3.7:	The effect of (a) varying particle diameter and (b) varying inlet velocity on particle collection efficiency for various discharge electrode potentials	47
Fig 3.8:	The effect of (a) variable collection plate to discharge electrode spacing, and (b) the number of discharge wires on particle collection efficiency at different discharge electrode potentials	48
Fig 3.9:	The effect of relative permittivity of dust particles on ESP collection efficiency at different applied voltages	48
Fig 3.10:	Simulated distribution of the space charge density for (a) a spike discharge electrode, and (b) a wire discharge electrode in an ESP channel corresponding to the experimental system of Podlinski [26]. The discharge potential in both cases was $19.2$ kV	49
Fig 3.11:	Comparison between (a) the particle collection efficiency predicted by the current CFD model and the corresponding experimental results of Podlinski	

	obtained with a spike discharge electrode. Figure (b) represents a comparison between the collection efficiency predicted for spike and wire discharge electrodes using the current CFD model	50
Fig 4.1:	3-D computational model of a single-channel ESP	59
Fig 4.2:	Comparison of current density at the collecting plate surface computed with present CFD model and experimental results by Lawless	60
Fig 4.3:	The corona current per unit wire length computed using the present numerical model, compared to the numerical modeling results of Long and Yao	61
Fig 4.4:	Comparison of V-I curves generated from numerical simulations (this study) with the experimental results of Kasdi with varying discharge electrode voltage and wire-to-wire spacing (w)	61
Fig 4.5:	Comparison between the experimentally measured current density distributions at the collecting plate surface of the ESP system used by Kasdi and that predicted by the current numerical model	62
Fig 4.6:	Space charge density distributions for plate-to-plate spacings of (a) 100 mm (b) 160 mm (c) 220 mm at an applied discharge electrode voltage of 45 kV using four discharge wire-electrodes	63
Fig 4.7:	Current density distribution along the horizontal axis of symmetry (a) and the collecting plate surface (c), and the corresponding space charge density distribution along the horizontal axis of symmetry (b) and the collecting plate surface (d) at plate-to-plate spacings (p) of 100, 160 and 220 mm respectively, with a constant discharge electrode voltage of 45 kV. The effect of the plate-to-plate spacing, and therefore the degree of shielding (Table 3) on the corona current (I) as a function of the applied discharge electrode voltage (V) is also shown (e). In all cases the wire-to-wire spacing was 116 mm and four discharge wire-electrodes were modeled	65
Fig 4.8:	Current density distribution along the horizontal axis of symmetry (a) and the collecting plate surface (c), and the corresponding space charge density distribution along the horizontal axis of symmetry (b) and the collecting plate surface (d) at wire-to-wire spacings (w) of 50, 80, and 116 mm respectively, with a constant discharge electrode voltage of 45 kV. The effect of the wire-to-wire spacing, and therefore the degree of shielding (Table 4) on the corona current (I) as a function of the applied discharge electrode voltage (V) is also shown (e). In all cases the plate-to-plate spacing was 100 mm and four discharge wire-electrodes were modeled	66
Fig 4.9:	Current density distribution along the horizontal axis of symmetry (a) and the collecting plate surface (c), and the corresponding space charge density distribution along the horizontal axis of symmetry (b) and the collecting plate surface (d) at a constant plate-to-plate spacing (p) of 100 mm, and a constant discharge electrode voltage of 45 kV. The effect of the number of discharge wires, and therefore the degree of shielding (Table 5) on the corona	

	current (I) as a function of the applied discharge electrode voltage (V) is also shown (e)	68
Fig 4.10:	Current density distribution along the horizontal axis of symmetry at a constant discharge electrode voltage of 45 kV (a), and the resulting corona current (I) as a function of the applied discharge electrode voltage (V) (b) for 4, 5 and 6 discharge wires and a plate-to-plate spacing of 160 mm	69
Fig 4.11:	Current density vector plots of the corona discharge for a plate-to-plate spacing of 100 mm and an applied discharge electrode voltage of 35 kV for 4 wires (a) 6 wires (b), and 8 wires (c)	70
Fig 4.12:	Current density distribution along the collecting plate surface under varying applied discharge electrode voltage with a constant number of five discharge wires and a constant plate-to-plate spacing of 100 mm	71
Fig 4.13:	Particle trajectories for particle collection in a single-channel ESP with a plate-to-plate spacing of 220 mm and an applied discharge electrode voltage of 55 kV with four (a), and eight discharge wires (b) respectively	72
Fig 4.14:	Particle collection efficiency comparison for 1 $\mu\text{m}$ particles at a plate-to-plate spacing of 100 mm and the applied discharge electrode voltages as shown in the graph (a). Also shown is a comparison between the particle collection efficiency for two different particle diameters using a plate-to-plate spacing of 100 mm and an applied discharge electrode voltage of 30 kV (b)	73
Fig 5.1:	A discretized 3-D computational model of (a) a single spike in a single-channel ESP system with a spiked discharge electrode (b) close up view of one of the tines of the spiked electrode	81
Fig 5.2:	A schematic diagram of ESP system	83
Fig 5.3:	(a) Wire discharge electrode assembly, and (b) spiked discharge electrode	84
Fig 5.4:	Comparison of the experimentally measured V-I relationship and that calculated from the computational modelling results for three discharge wire electrodes spaced 175 mm apart and with a plate-to-plate spacing of 100 mm and 160 mm	88
Fig 5.5:	Comparison of the experimentally measured and modelled V-I curves for a single-channel wire-plate ESP equipped with four wire-electrodes. The effect of varying (a) plate-to-plate spacing while the wires were spaced 116 mm apart, and the effect of (b) the wire-to-wire spacing while the plate-to-plate spacing was kept fixed at 100 mm are shown	89
Fig 5.6:	: Comparison of the computational modelling results with the experimental measurements obtained under varying (a) plate-to-plate spacing (P), (b) wire-to-wire spacing (w), (c) number of wires, and (d) air flow velocity. The solid curves represent the computational modelling predictions (thick lines for $d_p > 75 \mu\text{m}$ , and thin lines for $d_p < 75 \mu\text{m}$ ). CE means collection efficiency and CC means corona current.	90

Fig 5.7:	Comparison of the computational modelling results with the experimental measurements obtained under varying number of wires for both particle size ranges of fly ash and plate to plate spacing of 220 mm. The solid curves represent the computational modelling predictions (thick lines for $dp > 75 \mu\text{m}$ , and thin lines for $dp < 75 \mu\text{m}$ )	92
Fig 5.8:	Comparison of the experimentally measured V-I relationship of the commercial spiked electrode to that of respectively one and three discharge wire-electrodes. The wire-to-wire spacing for the three wire electrodes was 175 mm, and a plate-to-plate spacing of 220 mm was used in all cases. The broken lines are drawn to serve as a visual aid	93
Fig 5.9:	Experimentally measured V-I relationships of a single spiked electrode at plate-to-plate spacings of 160 and 400 mm respectively. The broken lines are drawn to serve as a visual aid	94
Fig 5.10:	Two-dimensional space charge density distributions for (a) the commercial spiked discharge electrode, and (b) a wire-electrode. In both cases the plate-to-plate spacing was 400 mm and the model calculations were done at a discharge electrode voltage of 40 kV	95
Fig 5.11:	Comparison of experimental and computational modelling results of ESP collection efficiency obtained when using one and three wire-electrodes and a single spiked electrode respectively. The parameters that were kept constant in each case are summarized on the figure as well.	96
Fig 5.12:	Particle collection efficiency obtained from computational modelling calculations and experimental measurements for plate-to-plate spacings of 160 and 400 mm respectively while using a spiked electrode and fly ash particles with diameters smaller than $75 \mu\text{m}$	97
Fig 5.13:	Particle collection efficiency obtained from computational modelling calculations and experimental measurements for two different air flow velocities while using a single spiked electrode and fly ash particles with diameters larger than $75 \mu\text{m}$	97
Fig 5.14:	Particle collection efficiency obtained from computational modelling calculations and experimental measurements for two different fly ash particle size ranges while using a single spiked electrode and a plate-to-plate spacing of 220 mm	98
Fig A-1:	Space Charge Density distributions for different flow velocities ranging from 0 m/s to 200 m/s	109
Fig A-2:	Variation of space charge density with gas flow velocity between two successive wire discharge electrodes	110
Fig. B-1:	Main steps in the OpenFOAM modeling of the electrostatic field	115
Fig. B-2:	Main steps in the STAR CCM+ modeling of the fluid and particle dynamic fields	116

Fig C-1:	Close-up view of a cylindrical wire-electrode and surrounding computational zone that was discretized using (a) a coarse mesh with 70 120 cells, and (b) a fine mesh with 121 780 cells	121
Fig C-2:	The results of mesh independence studies to characterise the influence of the number of discretised cells on (a) the corona current, and (b) the collection efficiency for the ESP geometry as described above	121
Fig. D-1:	(a) 3-D geometry of a single-electrode ESP channel, and (b) dimensions of the spiked discharge electrode	123
Fig. D-2:	Comparison of the computational modelling results of discharge current produced by a spike and wire discharge electrode respectively for the same ESP geometry.	123
Fig. D-3:	Computational modelling results for the effect of the air flow velocity on collection efficiency for the single-channel ESP.	124
Fig. D-4:	Computational modelling results for the effect of particle diameter on collection efficiency for a single-channel ESP equipped with a spiked discharge electrode.	124
Fig. D-5:	The effect of air flow velocity on the space charge density distribution of a simple spiked discharge electrode	125
Fig. D-6:	Graphical representation of the effect of air flow velocity on the space charge density distributions for a spike discharge electrode. The planes along which data was extracted for the plot (b) is shown in the figure on the left (a)	126
Fig E-1:	Particle size distribution of the power plant fly ash used in this study for (a) the sample fraction that passed through the 75 $\mu\text{m}$ sieve, and (b) the sample fraction that passed through the 150 $\mu\text{m}$ sieve while being retained by the 75 $\mu\text{m}$ sieve	128
Fig. E-2:	3-D Representation of the laboratory-scale ESP system used for fly ash collection experiments in the present study	132
Fig. E-3:	3-D representation of the inlet duct to the ESP with the baffles and honeycomb structure that was used to homogenize the air flow.	132
Fig. E-4:	Close-up view of the inlet duct and ESP section.	133
Fig. E-5:	Collecting plate assembly with (1) collecting plate guide bars, and (2) collecting plates.	133
Fig. E-6:	(a) Discharge electrode assembly with (1) top guide tube that was also connected to the electrical supply, (2) wire-electrodes, (3) bottom guide tube, and (b) the spiked RDE (G Spike electrode) as used in this study.	134
Fig E-7:	(a) Experimentally measured air flow velocity distributions at the ESP inlet-plane, and (b) air flow distribution through the ESP section along the vertical and the horizontal centre-line plane as predicted by the CFD model. The arrow indicates the direction of flow.	137

---

---

Fig. F-1:	Top, front and side view of the laboratory-scale ESP unit.	139
Fig. F-2:	Different sections of the laboratory-scale ESP unit.	140
Fig. F-3:	Close-up view of the ESP section.	141
Fig. F-4:	Collecting plates assembly.	142
Fig. F-5:	Discharge electrode assembly with wire electrodes.	143
Fig. F-6:	Dimensions of the Geecom G Spike electrode.	144
Fig. F-7:	Geecon G-Spike electrode assembly.	145
Fig. F-8:	V-I curves for different discharge electrodes including the G-Spike electrode.	146

## LIST OF SYMBOLS

$V$	Electric Potential (V)		
$\vec{E}$	Electrostatic field (V/m)	$b_1, b_2, b_3, b_4$	Model parameters
$\vec{J}$	Current density ( $A/m^2$ )	<b>Greek symbols</b>	
$b$	Mobility of ions ( $m^2/V.s$ )	$\alpha$	Model constant
$D_i$	Ion diffusion coefficient ( $m^2/s$ )	$\rho_w$	Ionic space charge density ( $C/m^3$ )
$\vec{E}_p$	Average Electrostatic field (V/m)	$\epsilon_o$	Permittivity of air (F/m)
$r_c$	Corona wire radius (cm)	$\epsilon_r$	Relative permittivity of particles
$\vec{u}_{gas}$	Gas velocity vector (m/s)	$\rho_f$	Gas density ( $kg/m^3$ )
$F_d$	Drag force (N)	$\rho_p$	Particle density ( $kg/m^3$ )
$F_g$	Gravitational force (N)	$\mu$	Viscosity (kg/m.s)
$F_u$	Coulomb's force (N)	$\mu_{eff}$	Effective viscosity (kg/m.s)
$d_p$	Particle diameter (m)	$\mu_{turb}$	Turbulence viscosity (kg/m.s)
$P$	Actual Pressure (Pa)	$\mu_{visc}$	Air viscosity (kg/m.s)
$Q_{sat}$	Saturation charge (C)	$w$	Model constant
$Q_p$	Particle charge (C)	$\tau_c$	Charging time constant (s)
$C_d$	Drag coefficient	$\tau_l$	Model constant (s)
Re	Relative Reynolds number	$\chi$	Shape factor
$A_p$	Projected area of the particle ( $m^2$ )	<b>Subscripts and superscripts</b>	
$v_s$	Particle Slip velocity (m/s)	i	Ion
$m_p$	Mass of the particles (kg)	d	drag
$v_p$	Velocity of the particles (m/s)	g	gravitational
$e$	Electron charge (C)	p	particle
$T$	Actual temperature (K)	sat	saturation
$k_B$	Boltzmann's coefficient (J/K)	w	wire
$g$	Gravitational acceleration ( $m/s^2$ )	c	corona/charging
t	Time (s)	f	fluid (gas) phase
s	Surface area of sphere ( $m^2$ )	p	Peek's formula
S	Actual surface area of particle ( $m^2$ )		
$\tilde{u}$	Thermal velocity of the ions (m/s)		

**LIST OF ABBREVIATIONS**

CFPPs	Coal fired power plants
EIA	Energy information administration
PM	Particulate matter
NAAQS	National ambient air quality standards
IEA	International energy agency
IIASA	International institute for applied systems analysis
NEM: AQA	National environmental management air quality act
ESPs	Electrostatic precipitators
FFPs	Fabric filter plants
GDP	Gross domestic product
RDE	Rigid discharge electrode
EHD	Electro hydrodynamic
CFD	Computational fluid dynamics
EPA	Environmental protection agency
FEM	Finite element method
FVM	Finite volume method
FDM	Finite difference method
FCT	Flux corrected transport
MoC	Method of characteristics
BEM	Boundary element method
CSM	Charge simulation method
DCM	Donor cell method



## Chapter 1. INTRODUCTION

### 1.1 Background and motivation

South Africa contributes to about 3.5% of the world's coal resources [1] and is ranked 5<sup>th</sup> in the list of hard-coal exporting countries and 6<sup>th</sup> in the list of hard-coal producing countries [2]. South African coal reserves are sufficient to meet the needs for more than a century at the present rates of production [1], and the country depends heavily on coal as a source of economic value, employment and energy [3]. According to the department of energy, coal fulfilled 77% of South Africa's total energy requirements. 95% of the electricity used in South Africa is produced by Eskom SOC Ltd., 90% of which are derived from coal in coal-fired power stations (CFPPs) [2]. According to the Energy Information Administration (EIA) International Energy Outlook 2017 report [4], coal consumption in Africa is projected to increase steadily at an average rate of 1.2% until 2050. Such an increase in coal consumption is not environmentally sustainable unless the capacity for the mitigation of pollution arising from the use of coal in coal-fired power generation facilities is expanded in parallel with the increased coal consumption.

Particulate matter (PM) emissions from CFPPs and other industrial and domestic sources that arises from the mineral matter contained in coal during combustion processes are a major concern in South Africa [5,6,7]. PM is broadly classified according to the size of the particles, namely having diameter equal to or less than 2.5  $\mu\text{m}$  (PM<sub>2.5</sub>), and that having a diameter equal to or less than 10  $\mu\text{m}$  (PM<sub>10</sub>). The potential adverse environmental effects of PM include the formation of smog, which causes limited visibility, respiratory problems, and reduced growth of vegetation [5]. In terms of the potential impacts of particulates on human health, PM<sub>2.5</sub> are especially concerning as they can be easily inhaled and can be deposited in the lower airways of the lungs [6], which can lead to various diseases such as asthma, decreased lungs function, irritation of the airways, difficulty breathing, and even heart failure [7].

In developing countries, and particularly in Africa as a whole, PM emissions from buildings, e.g. households in informal settlements, where coal is used as fuel for cooking and heating, contributes to 78% of the continent's PM<sub>2.5</sub> emissions as shown in Fig. 1.1 [5]. The second highest contributor to particulate matter (PM) emission in Africa is the industrial sector. In South Africa, however, the contribution of the energy sector to the country's total PM emissions are more profound compared to the emissions from households, as it accounts for 36% [8] of the total PM emissions (Table 1.1). Nonetheless, the geographic distribution of CFPPs in South Africa, and the fact that informal settlements where coal is frequently used as primary energy source is also located near the CFPPs, results in specific regions being characterized by poor air quality that does not meet the national ambient air quality standards (NAAQS) [9]. Consequently, it has been estimated that air pollution contributed to more than 2200 annual premature deaths in South Africa, in addition to being a documented cause of respiratory diseases [10,11].

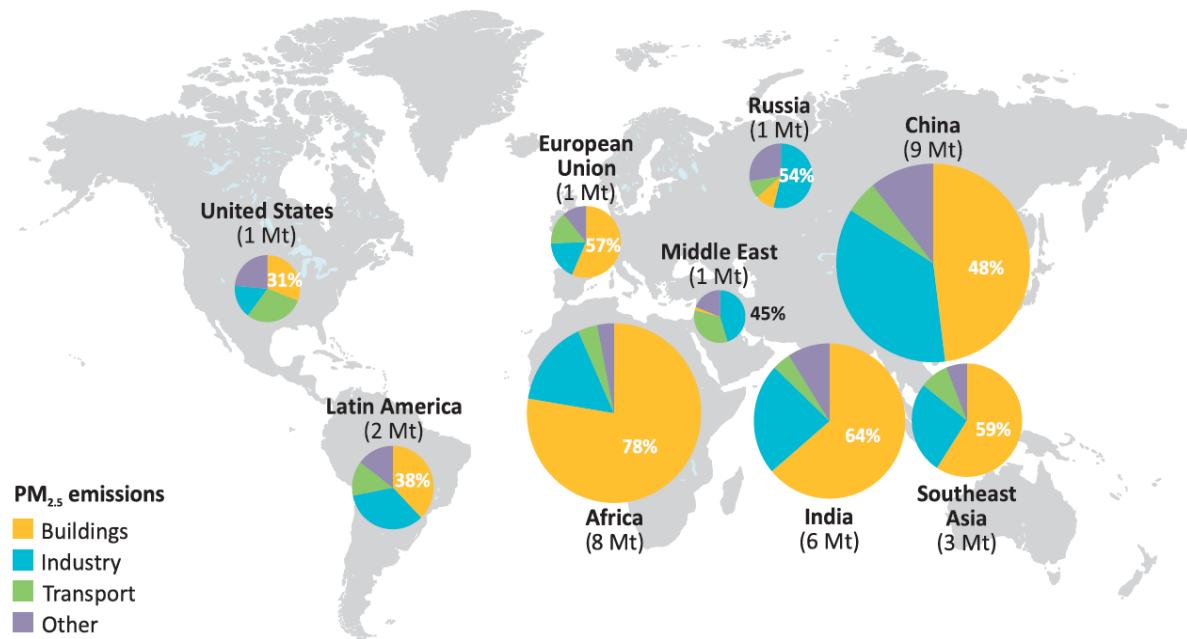


**Fig 1.1:** Energy related PM<sub>2.5</sub> emissions by region and sector for 2015. Taken from IEA analysis based on IIASA data [5].

Therefore, to aid in addressing the negative impact of PM emissions on the environment and human health, the minimum emissions standards with respect to criteria emissions pollutant emissions from solid fuel combustion installations have been redefined according to the National Environmental Management: Air Quality Act, or NEM: AQA (Act no 39 of 2004) [12], as summarized in Table 1.2.

**Table 1.1:** Atmospheric emissions (%) in South Africa [8]

Parameter	PM	SO <sub>2</sub>	NO <sub>x</sub>
Energy sector	36	70	55
Commercial/Industrial/Institutional burning	44	27	23
Domestic burning	9	0.8	0.2
Biomass burning	6	0	0.3
Vehicle emissions	5	2	21

**Table 1.2:** Minimum emission standards applicable to solid fuel combustion installations according to the NEM: AQA [12].

Pollutant	Chemical symbol	Plant status	Emissions limit in mg/Nm <sup>3</sup>
			Under normal conditions of 273 K and 101.3 kPa, relative to 10% O <sub>2</sub>
Particulate matter	N/A	New <sup>1</sup>	50
		Existing	100
Sulphur dioxide	SO <sub>2</sub>	New	500
		Existing	3500
Oxides of nitrogen	NO <sub>x</sub> expressed as NO <sub>2</sub>	New	750
		Existing	1100

South African coals generally have a relatively high minerals content when compared to that of the United States, Germany and China [8], which contributes to the generation of a relatively high volume of fly ash (PM) that puts increased pressure on particulate removal equipment to meet the minimum emissions standards as enforced by the NEM:AQA [12]. For example, the minerals contents of typical South African coals are in the order of 30 wt.%, whereas that of China, US and Germany is 23 wt.%, 9 wt.% and 9 wt.% [8] respectively.

Several techniques are available to control PM emissions, of which electrostatic precipitators (ESPs), fabric filter plants (FFPs), or a combination of ESP and FFP technology are most popular for CFPPs and are also implemented in South Africa [8]. The minerals content and coal consumption rate, coupled with the efficiency of PM control devices that remove the fly ash from the boiler flue gas stream before leaving through the stack determines the level of PM emitted to the atmosphere. During the energy crisis that was experienced in South Africa between 2007 and 2010, the minimal opportunities for maintenance of PM removal units at the power stations gradually led to increased levels of PM emissions due to the declining PM removal efficiencies of the ESP and FFP units [8].

Due to this event, it is expected, from projections made by Pretorius et al. [8], that PM emissions can increase by 40% in 2030, relative to 2015, if a “worst case” scenario applies. The 2030 PM emissions based on the “business as usual” scenario, which in the same paper was defined as when the PM removal units are maintained well, but no improvements are implemented, is projected to be stable compared to the 2015 baseline. Significant reductions in the PM emissions by 2030 are projected in the case of well-maintained PM removal equipment that are characterized by a high availability and high PM removal efficiencies respectively, i.e. the “intermediate” (c.a. 30% PM emissions reductions) and the “best case” (c.a. 40% PM emissions reductions) scenarios as defined by Pretorius et al. [8]

<sup>1</sup>Any power station built after 2015 will be considered as new whereas the power stations that was already operational in 2015 are classified as existing power stations. All power stations, irrespective of whether being new or existing must conform to the new standards by 2020.

The emission limits that were implemented at various South African CFPPs in 2015 are summarized in Table 1.3. From the data presented in Table 1.3 it is clear that most power stations did not conform to the minimum PM emission standards (Table 1.2) that is to be implemented in 2020 to all CFPPs, and that the minimum PM emissions standard for existing CFPPs were already being exceeded at some power stations at that time. It is therefore clear that regular upgrading of PM emission control equipment, i.e. ESPs and FFPs, are required to enable the reduction of particulate matter emissions from South African power stations to facilitate compliance with the increasingly stringent environmental regulations.

**Table 1.3:** Emission limits implemented at various South African CFPPs in 2015 under normal conditions of 273 K and 101.3 kPa, relative to 10% O<sub>2</sub> [8].

Power Station	PM (mg/Nm <sup>3</sup> )	NO <sub>x</sub> (mg/Nm <sup>3</sup> )	SO <sub>2</sub> (mg/Nm <sup>3</sup> )
A	50	760	1400
B	75	1100	2100
C	50	1100	2700
D	100	860	2100
E	125	1100	2100
F	100	900	2100
G	50	1100	1900
H	100	760	3300
I	175	1100	2400
J	250	1100	2100
K	50	990	2400
L	300	1500	3000
M	100	1200	1600
N	50	750	750
O	50	750	750

Historically, ESPs have been the most widely used PM abatement technology at South African power stations, and offers some advantages over FFPs, such as being able to accommodate a large range of gas volumes with a wide range of inlet temperatures, pressures, dust volumes, and acid gas conditions [2, 11]. Properly designed and maintained ESP units can deliver particulate collection efficiencies as high as 99.9%, although the major disadvantage of ESPs compared to FFPs are that submicron particles are not effectively collected using ESPs [13]. Although FFPs are also routinely capable of delivering higher

particle collection efficiencies, and thus typically ensures lower emissions as shown in Fig. 1.2, the operation of these units is more sensitive to varying process conditions. It has been estimated that the costs of upgrading all remaining ESP units at South African CFPPs to FFP units would roughly amount to almost 1% of the nominal South African GDP [14]. However, as is also clear from Fig. 1.2, the ESP units at some South African power stations have matched the performance of FFP units in the past with respect to meeting the  $50 \text{ mg/Nm}^3$  minimum emissions standard that should be adhered to at all power stations from 2020 [15]. The operation and design of these ESP units were therefore optimized relative to the plant conditions, whereas this is not typically the case at the majority of the other power stations at which ESPs are operated. Improving ESP performance through design alterations and the manipulation of process variables is therefore a more economically viable option for the reduction of PM emissions from South African CFPPs, instead of replacing ESP units with FFPs. Accurate computational models can greatly aid in identifying suitable design modifications and efficient operating parameters to meet the prescribed minimum emissions standards.

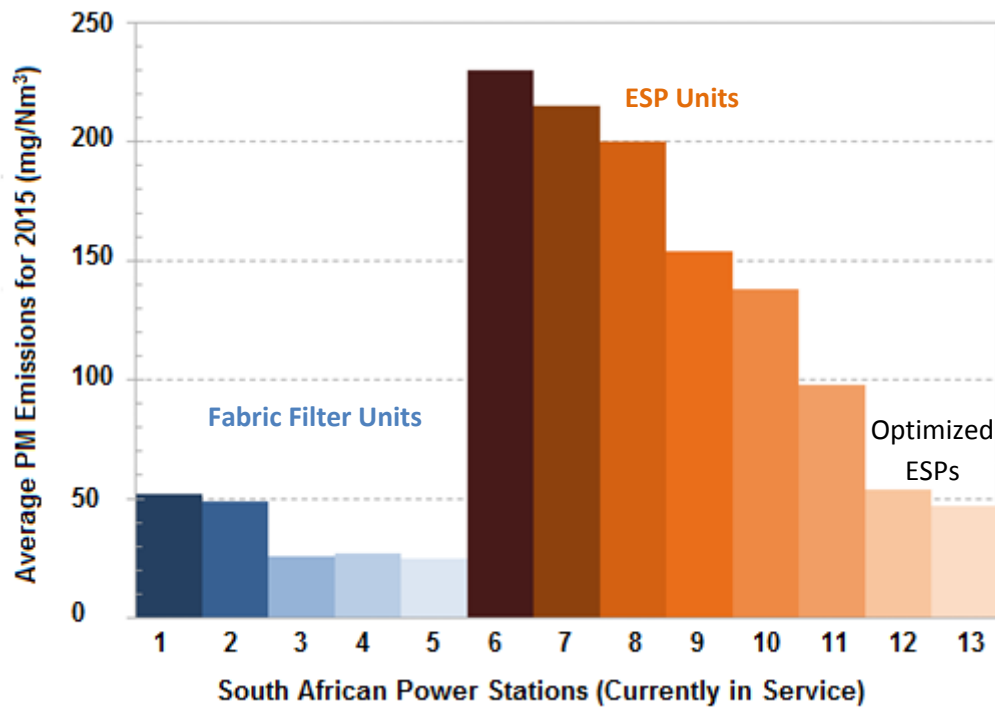


**Fig 1.2:** South African power station PM emissions in 2015 [15].

Particulate matter collection using ESPs is achieved by imparting a negative electrical charge to the particles as they move through the ESP channels, which then cause the particles to be attracted to the positive, grounded collecting plates due to Coulomb forces acting on the particles. The particles are charged by the gas ions that are generated through the corona discharge at the high-voltage discharge electrodes, and in addition to the resulting Coulomb force, the particles also experience drag forces [16]. The particle trajectories are therefore dependent on the interaction between the electrostatic field, the fluid dynamic field, and the particle dynamic field as illustrated in Fig. 1.3. The interaction between these fields take place through the mechanisms as summarized in Fig. 1.3 that are also in turn influenced by

the ESP design. Empirical models developed by Deutsch [17], Cooperman [18], Zhibin & Guoquan [19] and Leonard et al. [20] are only applicable to a narrow range of operating parameters. These empirical models also do not take all ESP design and operating parameters into account, are based on many simplifications, and therefore do not take the complex interactions between the various fields as depicted in Fig. 1.3 into account. On the other hand, such simplified models might implicitly incorporate these complex interactions, although the range of applicability is normally limited [21].

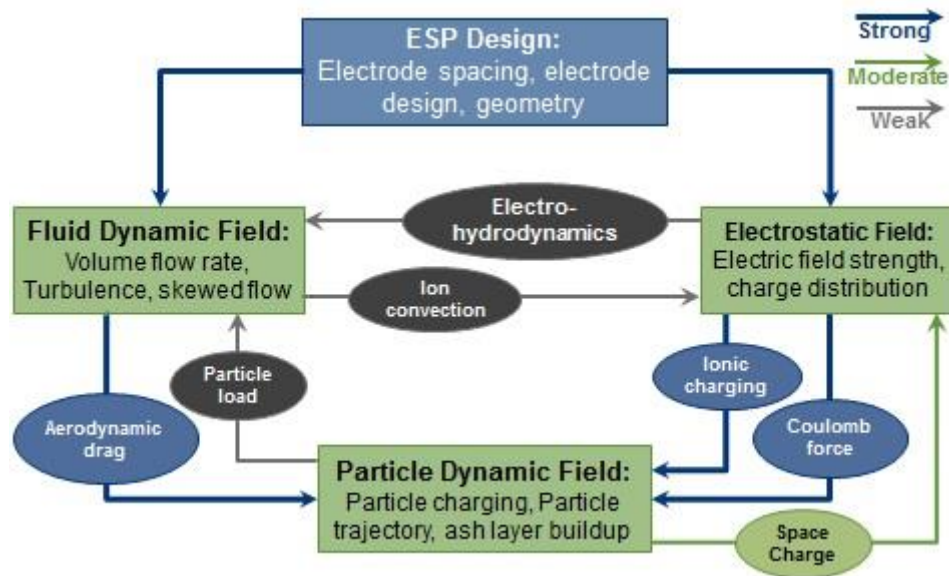


**Fig 1.3:** Field interaction in electrostatic precipitators, Adapted from Farnoosh et al. [16].

Computational fluid dynamics (CFD) is a modelling technique that provides an invaluable platform to model processes in which many interrelated variables affect the overall process performance [13,22,23]. Previous CFD studies related to electrostatic precipitators have been mainly limited to the analysis of the gas [24,25] and particle flow [16,26] and how these can be manipulated to enhance particle collection. The modelling of the corona discharge and subsequent charging of dust particles as they travel through the ESP while being subjected to the interacting electrostatic, fluid dynamic and particle dynamic fields has been reported by several researchers. Nonetheless, the relationship between coal ash properties, i.e. the relative permittivity, and the charging rate and collection efficiency has not received much attention in the literature. Additionally, the potential effect of varying degrees of shielding that can occur in multi-electrode ESP systems have also been neglected in most studies, while computational descriptions of corona discharge have been mostly confined to simple wire electrodes. These and other shortcomings first need to be addressed before such modelling techniques can be extended to model plant-scale ESP operation with inclusion of each of the three interacting fields as presented in Fig. 1.5, instead of only confining the computational modelling description to the fluid dynamics field [24,25,27].

## **1.2 Problem statement**

Although computational modelling techniques, which includes CFD, can be used to gain deeper insight into the potential operating and design parameters that may be manipulated to improve ESP performance, the development of accurate and predictive computational models with enhanced complexity requires rigorous experimental validation [26].

Modelling of plant scale ESPs are limited by computational resources and industrial ESPs are also not freely accessible to conduct measurements to validate computational models. Alternatively, improved models can be developed for laboratory-scale systems with which measurements can also be made to validated newly developed models. The smaller scale of laboratory systems also facilitates the development of computational models from first principles such as to provide an accurate representation of the underlying physics. Following validation of such a detailed computational model with laboratory data, the model may be used to derive simplified models that can be more conveniently applied to full-scale systems the validated model can be readily used for predicting performance of industrial scale ESPs.

## **1.3 Aim and objectives**

### **1.3.1 Aim**

The aim of this thesis is to contribute to the development of a comprehensive and accurate, experimentally validated, computational model of a single-channel multi-electrode ESP system that incorporates the effects of shielding and discharge electrode design on particle collection efficiency.

### **1.3.2 Objectives**

To assist in reaching the aim of this thesis, the following objectives were identified, namely to:

1. Develop, and intermittently validate, a computational modelling method based on a fundamental description of the interacting fields of electrostatics, fluid dynamics, and particle dynamics.
2. Adapt the modelling method to incorporate the simulation of the corona discharge produced by commercially available discharge electrodes of varying geometry.
3. Apply the developed model to quantify the degree of shielding between adjacent discharge electrodes as a function of ESP process parameters.
4. Validate the developed model using experimental data obtained with a single-channel, multi-electrode ESP unit.

### **1.3.3 Scope**

In the present work, a comprehensive 3-D computational model of a laboratory-scale ESP unit is developed within the framework of computational fluid dynamics (CFD) using the Euler-Lagrange approach. The shortcomings listed in the preceding section, namely (i) the effect of permittivity on particle charging and collection, (ii) analysis of the shielding effect

that can occur in multi-electrode ESPs, (iii) the influence of various ESP parameters on the degree of shielding, and in turn, on the particle collection efficiency, and finally, (iv) modelling of the corona discharge from commercially available spiked discharge electrodes are addressed in this thesis. A specific rigid discharge electrode (RDE), i.e. the G-Spike electrode [28,29], that is patented and manufactured locally by Geecom (Pty) Ltd. was used as a representative design in this study. The open source software OpenFOAM®, and the commercial CFD software package Star-CCM+® were used for all simulations in this work. More specifically, OpenFOAM was used to model the corona discharge and the resulting electrostatic field, which was used as input in the STAR-CCM+ model in which fluid flow and particle charging and dynamics were simulated. The composite modelling results were first compared with the available experimental data in the literature to validate the basic model, and subsequently with the performance data obtained with an in-house laboratory-scale ESP unit. The performance of the laboratory-scale ESP, equipped with the spiked RDEs (G-spike electrodes), was investigated both experimentally and computationally, and compared to the performance obtained when equipped with multiple wire-electrodes under shielding and non-shielding conditions. The fly ash was sampled from the ESP hopper of a South African coal-fired power station, from which homogenized samples split into two size fractions were prepared and used for the collection efficiency experiments.

## 1.4 Outline of thesis

This thesis is divided into six chapters in which the detail of the various aspects of the work done is presented. Following this introductory chapter, the remainder of the five chapters are namely:

**Chapter 2** in which an extensive literature review is presented that covers an overview of the various types of commercial ESPs and modelling strategies that have been used to date to model ESP operation. Details regarding the shortcomings that are addressed in the present study are also discussed.

**Chapter 3** in which the development of the composite computational model is described. It is shown that the model produces results that correlate well with experimental data obtained using different ESP systems as detailed in the literature. It is furthermore shown that negligible coupling exists between the electrostatic field and the gas flow, and because of this, the composite modelling approach can be used to separately model the electrostatic field and the particle and fluid dynamic fields.

**Chapter 4** in which it is shown how the developed model may be adapted to allow quantification of the shielding effect that can arise between adjacent discharge electrodes in multi-electrode ESPs under certain conditions. The shielding effect is subsequently quantified as a function of ESP parameters such as electrode-to-electrode spacing, plate-to-plate spacing, and the number of discharge electrodes for simple cylindrical wire-electrodes.

**Chapter 5** in which the shielding effect predicted with the computational model simulations in Chapter 4 are experimentally validated using the laboratory-scale ESP. Additionally, the



findings of the ash collection experiments are presented for ESP operation with cylindrical wire-electrodes and the spiked RDEs respectively, while other ESP parameters were also varied. The results are further compared to the corresponding computational modelling results, which correlated well with one another in terms of the electrostatic properties (V-I curves) and the particle collection efficiencies.

**Chapter 6** in which a summary of the main findings of this thesis is presented, and the implication of these findings are discussed in addition to a list of recommendations that might be considered for further study.

**Appendices** in which various supporting information is presented such as the technical details of the CFD modelling methods that were adopted. The results of the mesh independence studies and aspects related to solution times, convergence and accuracy of the modelling results are presented. Furthermore, the design of the laboratory scale ESP that was built and commissioned with the help of Geecom (Pty) Ltd. is described, and the results of various quality checks with respect to the measurements and measurement instruments are described.

## 1.5 References

- [1] Chamber of mines of South Africa-Coal, <http://www.chamberofmines.org.za/sa-mining/coal>.
- [2] A. Eberhard, The future of South African coal: Market, investment, and policy challenges, *Progr. Energy Sustain. Dev.* (2011) 20,21,30. doi:10.1017/CBO9781316136058.005.
- [3] Statistics South Africa-The importance of coal, <http://www.statssa.gov.za/?p=4820>.
- [4] EIA-International Energy Outlook 2017, [https://www.eia.gov/outlooks/ieo/pdf/ieotab\\_7.pdf](https://www.eia.gov/outlooks/ieo/pdf/ieotab_7.pdf).
- [5] International Energy Agency, Energy and Air Pollution, World Energy Outlook - Spec. Rep. (2016) 266. doi:10.1021/ac00256a010.
- [6] Air quality standards and objectives, pp. 17–29. [https://www.environment.gov.za/sites/default/files/docs/stateofair\\_executive\\_iaiquality\\_standardsonjectives.pdf](https://www.environment.gov.za/sites/default/files/docs/stateofair_executive_iaiquality_standardsonjectives.pdf).
- [7] U.S.E.P. Agency, Health and environmental effects of particulate matter, <https://www.epa.gov/pm-pollution/health-and-environmental-effects-particulate-matter-pm>.
- [8] I. Pretorius, S. Piketh, R. Burger, H. Neomagus, A perspective on South African coal fired power station emissions, *J. Energy South. Africa.* 26 (2015) 27–40. [http://www.scielo.org.za/scielo.php?script=sci\\_arttext&pid=S1021-447X2015000300004&nrm=iso](http://www.scielo.org.za/scielo.php?script=sci_arttext&pid=S1021-447X2015000300004&nrm=iso).

- 
- [9] RSA, National ambient air quality standards, Gov. Gaz. GN32816 (2009) 6–9. <http://www.epa.gov/air/criteria.html>.
- [10] Healthy energy initiative, <http://www.healthyenergyinitiative.org/south-africa-report-coal-plants-cause-2200-premature-deaths-and-cost-2-billion-annually/> (accessed March 11, 2018).
- [11] M. Holland, Health impacts of coal-fired power generation in South Africa, (2016). <https://www.phasa.org.za/wp-content/uploads/2016/08/M-Holland-groundWork-September-2017.pdf> (accessed March 11, 2018).
- [12] Department of Environmental Affairs, National Environmental Management: Air Quality Act, Gov. Gaz. (2010) 3–36. [https://www.environment.gov.za/sites/default/files/gazetted\\_notices/nemaqa\\_listofactivities\\_g33064gon248.pdf](https://www.environment.gov.za/sites/default/files/gazetted_notices/nemaqa_listofactivities_g33064gon248.pdf).
- [13] N. Farnoosh, K. Adamiak, G.S.P. Castle, 3-D numerical simulation of particle concentration effect on a single-wire ESP performance for collecting poly-dispersed particles, *IEEE Trans. Dielectr. Electr. Insul.* 18 (2011) 211–220. doi:10.1109/TDEI.2011.5704512.
- [14] S. Arif, D.J. Branken, R.C. Everson, H.W.J.P. Neomagus, L.A. le Grange, The influence of discharge electrode geometry and the associated discharge characteristics on electrostatic precipitator performance, in: Eighth Int. Conf. Clean Coal Technol. (CCT2017), 8 – 12 May 2017, Cagliari, Sardinia, 2017.
- [15] Van Wyk, Marabwa, ESKOM Holdings SOC Ltd, (2015).
- [16] N. Farnoosh, K. Adamiak, G.S.P. Castle, 3-D numerical analysis of EHD turbulent flow and mono-disperse charged particle transport and collection in a wire-plate ESP, *J. Electrostat.* 68 (2010) 513–522. doi:10.1016/j.elstat.2010.07.002.
- [17] W. Deutsch, Bewegung und Ladung der Elektrizitätssträger im Zylinderkondensator, *Ann. Phys.* 373 (1922) 335–344. doi:10.1002/andp.19223731203.
- [18] P. Cooperman, A new theory of precipitator efficiency, *Atmos. Environ.* 5 (1971) 541–551. doi:10.1016/0004-6981(71)90064-3.
- [19] Z. Zhibin, Z. Guoquan, New model of electrostatic precipitation efficiency accounting for turbulent mixing, *J. Aerosol Sci.* 23 (1992) 115–121. doi:10.1016/0021-8502(92)90048-Z.
- [20] G.L. Leonard, M. Mitchner, S.A. Self, Experimental study of the effect of turbulent diffusion on precipitator efficiency, *J. Aerosol Sci.* 13 (1982) 271–284. doi:10.1016/0021-8502(82)90030-1.
- [21] S. Kim, K. Lee, Experimental study of electrostatic precipitator performance and comparison with existing theoretical prediction models, *J. Electrostat.* 48 (1999) 3–25. doi:10.1016/S0304-3886(99)00044-3.
- [22] S. Arif, D.J. Branken, R.C. Everson, H.W.J.P. Neomagus, L.A. le Grange, A. Arif, CFD modeling of particle charging and collection in electrostatic precipitators, *J.*

- 
- Electrostat. 84 (2016) 10–22. doi:10.1016/j.elstat.2016.08.008.
- [23] A. Arif, The simulation of an industrial wet flue gas desulfurization absorber, North West University Potchefstroom Campus South Africa, 2017.
- [24] S.M.E. Haque, M.G. Rasul, M.M.K. Khan, A. V. Deev, N. Subaschandar, Influence of the inlet velocity profiles on the prediction of velocity distribution inside an electrostatic precipitator, *Exp. Therm. Fluid Sci.* 33 (2009) 322–328. doi:10.1016/j.expthermflusci.2008.09.010.
- [25] S.M.E. Haque, M.G. Rasul, A.V. Deev, M.M.K. Khan, N. Subaschandar, Flow simulation in an electrostatic precipitator of a thermal power plant, *Appl. Therm. Eng.* 29 (2009) 2037–2042. doi:10.1016/j.applthermaleng.2008.10.019.
- [26] T. Iváncsy, J.M. Suda, Behavior of polydisperse dust in electrostatic precipitators, *J. Electrostat.* 63 (2005) 923–927. doi:10.1016/j.elstat.2005.03.062.
- [27] X. Ye, Y. Su, B. Guo, A. Yu, Multi-scale simulation of the gas flow through electrostatic precipitators, *Appl. Math. Model.* 40 (2016) 9514–9526. doi:10.1016/j.apm.2016.06.023.
- [28] F. August Mischkulnig, Discharge electrode, US Patent. 7, 160, 364B2 (2007).
- [29] G. Mischkulnig, P. Bento, Enhanced corona discharge using innovative rigid discharge electrodes (RDE), in: 9th Int. Conf. Electrostat. Precip.: pp. 1–12.

## Chapter 2. LITERATURE SURVEY

This chapter comprises a brief description of electrostatic precipitators, their operation, charging mechanism and collection as well as a thorough literature survey related to experimental, modelling and validation of electrostatic precipitator fundamentals with special emphasis on computational modelling that serves to supplement the material presented in Chapter 3, 4 and 5.

### 2.1 Emissions at coal fired power stations and regulations

The implementation of strict emissions regulations and standards for the air pollutants have forced industries to install more efficient control equipment in new plants and retrofitting of control technologies in present power plants to meet the necessary emission standards [1] which are listed in Table 1.2 of the previous chapter defining emissions standards according to the National Environmental Management Air Quality Act [2]. The initial focus in the regulations in most of the countries is on PM control which is further followed by SO<sub>2</sub> and NO<sub>x</sub>. In Fig 2.1, the contribution of the energy sector towards selected primary air pollutants is illustrated, where it can be seen that the energy sector is responsible for 85% of PM<sub>2.5</sub> emissions to the atmosphere.

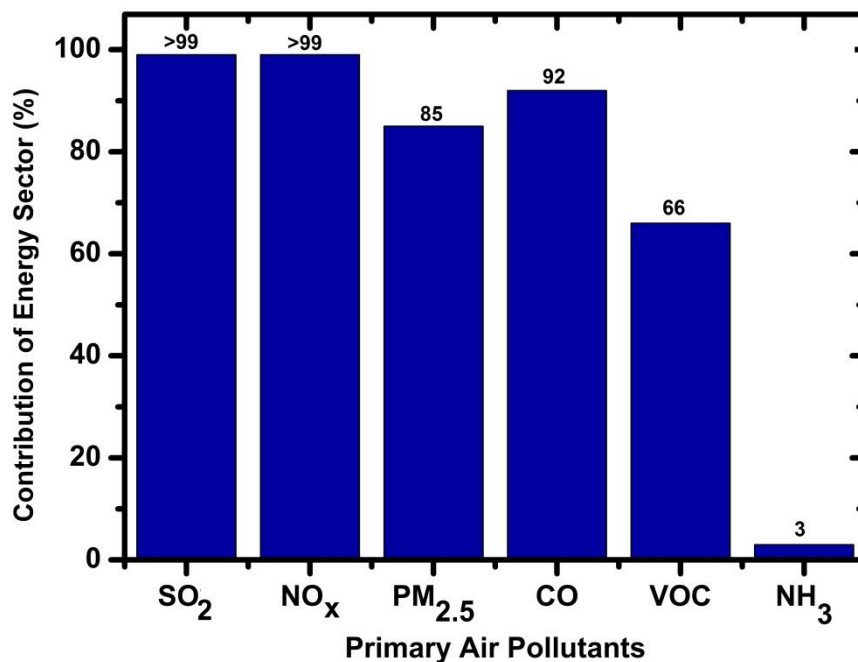


**Fig 2.1:** Contribution of energy sector for selected primary air pollutants, 2015 [1].

In Table 1.3, it was indicated that most of the South African coal fired power plants do not comply with the emissions standards defined in Table 1.2, and to meet the defined standards, emission control technologies require significant attention in order to improve removal efficiencies. The control technologies for air pollutants in the power generation can be

divided into two types as primary combustion technologies and end of the pipe technologies. Primary combustion technologies include measures that prevent production of emissions while end of pipe technologies include measures that control the pollutants from being released into the atmosphere [1] downstream the boiler. A typical emission control system that falls in end of pipe technologies to reduce pollutants emissions to atmosphere include electrostatic precipitators and fabric filters for PM control, flue gas desulphurization to absorb SO<sub>2</sub> in solid matter and selective catalytic and non-catalytic reduction systems for decreasing NO<sub>x</sub> [1].

## **2.2 Processes for particulate matter removal**

There are various processes of particle removal from process streams using different principles e.g. cyclones uses gravity or inertial separation, fabric filters are based on impaction and diffusion differences, electrostatic precipitators uses electrical means, while wet scrubbers are dependent on contacting, impingement and impaction [3]. Because of the different basic principles used by each form of separator, they each have different properties regarding collection efficiency, process and application suitability [3].

### **2.2.1 Industrial scale processes**

The different types of industrial scale control/removal processes are briefly described as follows:

#### ***Electrostatic precipitators***

The particles from the gas stream are charged while passing through electrostatic precipitators and are attracted towards collection plates due to Coulomb's forces and are collected. Particles with a larger diameter attain charge more quickly as compared to smaller diameter particles and are collected more easily and rapidly [2].

#### ***Fabric filters***

The particles from particle laden gas streams are filtered while passing through a woven porous filter allowing the clean gas to pass through. The separation is therefore largely particle size dependent, although electrical charge effects also may play a role [2]. A plain woven cloth formed into a bag or sock comprised the filter media which is surface treated to reduce particle penetration. As the dust layer on the filter media builds, up the efficiency of the device is typically > 99% [2].

#### ***Inertial separators***

In Inertial separators like cyclones or centrifugal collectors, the particles contained in the incoming gas/air stream rotate or spin in a cylindrical container. As the mass of the particles is much larger as compared to the gas molecules the centrifugal force on the particles being larger and causes the particles to move towards wall of the container and finally to fall downwards [2]. For high collection efficiency, the diameter of the particles should be > 10 μm [2].

### *Wet collectors*

Wet collectors operate on the principle of contacting the particles with excess of liquid in the turbulent region of the device. The size and mass of the particles increases after impaction or impingement on the water droplets [2]. As the particles are large and wetted they can be removed from the gas stream in a simple impingement or cyclonic form of separator. Wet collectors have excellent mass transfer characteristics, so they are widely used to control gaseous emissions [2].

### **2.2.2 Comparison and effectiveness of different PM removal processes**

The comparison of advantages and disadvantages of various particulate matter control/removal processes are presented in Table 2.1. It can be concluded that all PM control devices have their own advantages and disadvantages.

**Table 2.1:** Characteristics of PM control/removal processes [3]

Device	Advantages	Disadvantages
<b>Electrostatic Precipitator</b>	<ul style="list-style-type: none"> <li>• Flexible size and efficiency</li> <li>• Wide particle size range</li> <li>• Low pressure drop</li> <li>• Less maintenance required</li> <li>• Long life</li> <li>• Wet and dry collection</li> </ul>	<ul style="list-style-type: none"> <li>• High capital cost</li> <li>• Efficiency sensitive to dust resistivity</li> <li>• Large foot print</li> </ul>
<b>Fabric Filter</b>	<ul style="list-style-type: none"> <li>• High efficiency</li> <li>• Reasonable foot print</li> </ul>	<ul style="list-style-type: none"> <li>• High pressure drop</li> <li>• Media temperature limitation</li> <li>• Fire/melting risk</li> <li>• Media of limited life span</li> <li>• Unsuitable for sticky/adhesive dust</li> </ul>
<b>Inertial Separator</b>	<ul style="list-style-type: none"> <li>• Simple construction</li> <li>• Low construction cost</li> <li>• Low maintenance</li> <li>• No temperature Limitation</li> <li>• Wet and dry applications</li> </ul>	<ul style="list-style-type: none"> <li>• Limited effective particle size range</li> <li>• High pressure drop</li> <li>• Possible erosion</li> </ul>
<b>Wet Collector</b>	<ul style="list-style-type: none"> <li>• Simple construction</li> <li>• Low capital cost</li> <li>• Small footprint</li> <li>• Sticky particulates</li> <li>• Effective on wet gas and dusts</li> </ul>	<ul style="list-style-type: none"> <li>• High pressure drop</li> <li>• Large water usage</li> <li>• Wet effluent</li> <li>• Low plume buoyancy</li> <li>• Possible plume odor</li> </ul>

The effectiveness of different particulate matter control processes can also be judged from Fig 2.2 in which the particle size range in microns covered by different PM control devices for which reasonable collection efficiencies can be achieved is given. From Fig 2.2 it can be concluded the most promising of all the control devices are the fabric filters and electrostatic precipitators. Electrostatic precipitators generally preferred over fabric filter units for large

coal-fired units [4], and in particularly with coal that have high sulfur contents. The choice between the two control technologies is highly dependent on the emission limitations, the ash and calorific value of the coal used, ash properties and need to replace bag in case of fabric filters [5]. Fig 1.2 of the previous chapter also supports the fact that optimized ESPs are comparable in efficiency to fabric filters.

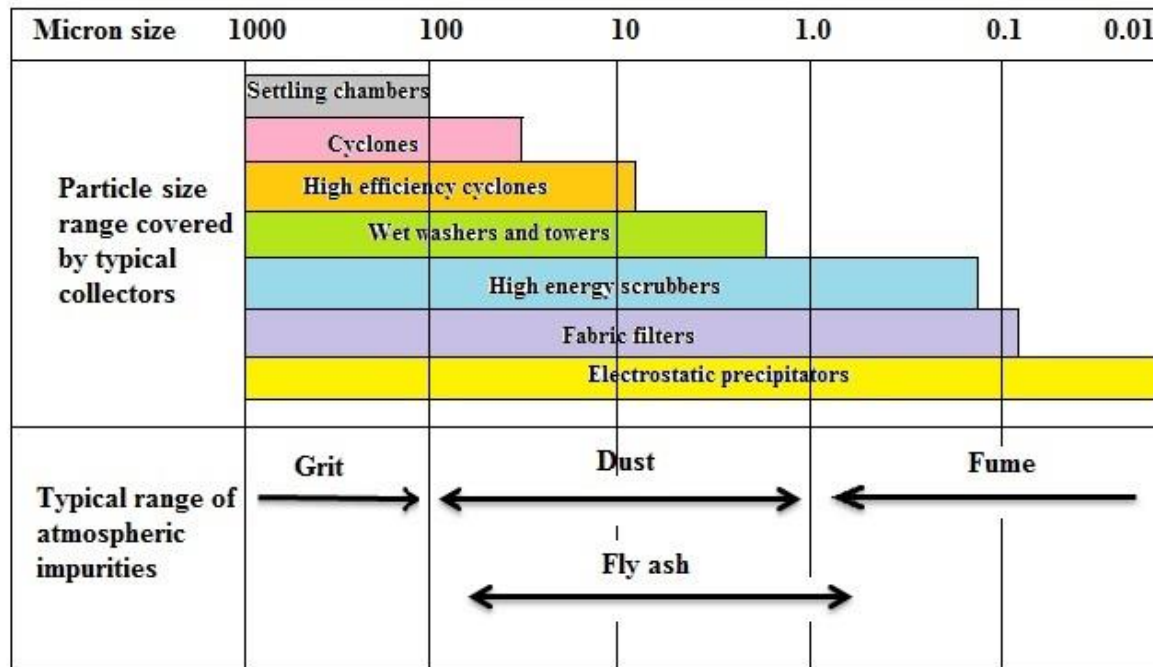


**Fig 2.2:** Particle size range covered by different PM removal processes along with important atmospheric impurities range. Taken from Parker [3].

### 2.2.3 Principles and fundamentals of electrostatic precipitators

The detailed description of steps/principles involved in the removal process of dust particles, components, and operation of electrostatic precipitators are detailed as follows.

#### *Principles of electrostatic precipitation*

In electrostatic precipitation, the removal of particles from flue gas is based on electrical means. The removal process can be classified into five different steps as follows [3]:

- 1) Charge carriers' production near the corona wire.
- 2) Particles' charging in the ionization zone.
- 3) Particles' deflection and separation.
- 4) Dust deposition on collection plates.
- 5) Dust removal induced by a dislodge device and collection in hoppers.

These different processes cannot be isolated from each other during ESP operation, of which a simplified representation is shown in Fig 2.3.

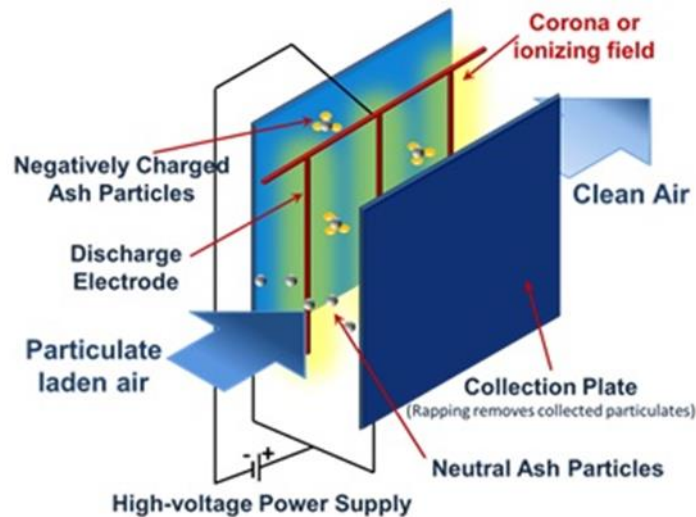


**Fig 2.3 :** ESP basic operating principle [6].

### *Components of electrostatic precipitator*

The following essential components [7] are present in electrostatic precipitators and are also shown in Fig 2.4:

- 1) Discharge electrodes: they are small diameter metal wires and hang vertically in ESP. A number of wires are attached together in rigid frames. A strong electrostatic field is created around discharge electrodes when voltage is applied to the wires and ionizes flue gas and successively the ionization charges particles in the gas.
- 2) Collection electrodes: particles that are charged are collected there. They can be flat plates or tubes and have charge opposite that of the discharge electrodes.
- 3) High voltage electrical systems: provides the high voltage to the discharge electrodes which results in strong electrostatic field between the discharge and collection electrodes and is used to charge particles in the ESP.
- 4) Rappers: used to remove the collected dust on the collection electrodes by providing an impact or a vibration action.
- 5) Hoppers: present at the bottom of the precipitator. The dust removed during rapping action is temporarily collected and stored in hoppers.
- 6) Shell: provides the base to support and enclose the ESP components and the unit.



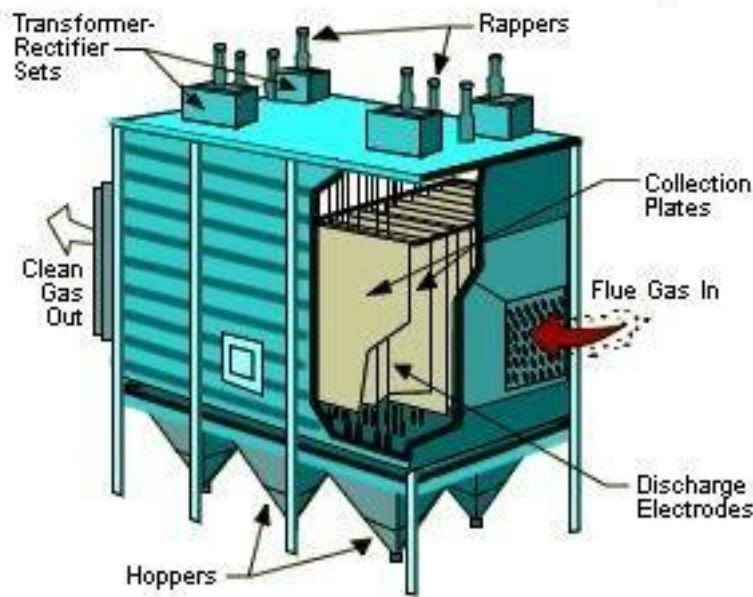


**Fig 2.4 :** A conventional electrostatic precipitator [8].

### 2.3 Electrostatic precipitation: Industrial application

Different types of electrostatic precipitators can be used in industrial applications which are explained briefly in the following subsequent section.

#### 2.3.1 Different industrial electrostatic precipitators

Industrial electrostatic precipitators can be divided into different types depending upon differentiating features in their design [9, 10]. These features are:

- 1) The geometric design and operation of discharge electrodes and collection electrodes.
- 2) The process of charging.
- 3) The operating temperature.
- 4) The particle removal procedure from collection plates.

ESP's can be grouped as:

- 1) Tubular and Plate ESPs.
- 2) Single stage and two stage ESPs.
- 3) Cold side and hot side ESPs.
- 4) Wet and dry ESPs.

#### ***Tubular and plate ESPs***

Tubular ESPs consists of tubes in the form of cylinder as collection electrodes and wires as discharge electrodes mounted in the center of the tubes. The dust particles collected at tubes are removed by washing the tubes with water sprays available above the tubes. Tubular precipitators are used mostly for collection of mist or fogs and when the particles that are

being collected are wet or sticky [10]. Plate type ESPs are used for collection of dry particles such as fly ash from industrial and utility boilers and are most common in use as compared to tubular ESPs. Plate type ESPs consists of two plates as collection electrodes and discharge electrodes are wires hanged in the middle of the plates. Discharge electrodes can be plates, spike electrodes, or any other shape mounted in the middle of two collection plates [10].

### ***Single stage and two stage ESPs***

This classification of ESPs is based on the number of stages used for the charging and collection of particles from gas stream. In case of single stage ESPs particles are charged and collected in the same chamber and a high voltage of 50 to 70 kV is used for the purpose of charging the particles. The ESPs used for reducing particulate emissions from boilers and other industrial processes are usually single stage ESPs [9,10].

The two stage ESPs have separate particle charging and collection chambers and are different from single stage ESPs in both design and amount of applied voltage. The amount of applied voltage is usually lower as compared to single stage precipitators. They are used mostly for collecting liquid aerosols and have limited use for particulate emission control [9,10].

### ***Cold side and hot side ESPs***

Electrostatic precipitators are also classified based on the temperature of the flue gas entering the ESP. The cold side ESPs are used for flue gas with temperatures of  $< 204^{\circ}\text{C}$  while hot side ESPs are utilized for flue gas temperatures  $> 300^{\circ}\text{C}$ . As the cold side ESPs work at lower temperature as compared to the hot side ESPs the volume of the flue gas passed through it is smaller so the size of the unit is smaller and less costly as compared to hot side ESPs [9,10].

### ***Wet and dry ESPs***

Wet ESPs are favorable when dust particles collected are sticky and corrosive. The water sprays can be used continuously or periodically to remove the dust collected at collection plates into the hopper or sump. The problems associated with rapping entrainment and with back corona can be removed by using wet ESPs. Dry ESPs on the other hand uses rappers to remove the collected dust at the collection plates as compared to water washing applied in wet ESPs [9, 10].

## **2.4 Electrostatic precipitation: Overview of recent research**

The ESP performance improvement experimental research conducted by researchers so far is discussed in this section.

### **2.4.1 Laboratory and pilot plant experimentation**

Experimental studies related to particle collection as well as electrostatic properties have been a topic of interest in the field of particle collection & separation by electrostatic precipitators. A lot of researchers focused on finding the optimum dimensions (wire to plate spacing, wire

to wire spacing, size of discharge wires) and operating parameters (gas velocity, applied voltage, particle diameter) for maximizing particle collection efficiency in electrostatic precipitators. Few researchers also reported experimental findings for different designs of discharge electrodes and their effects on collection efficiency. Some experimental studies conducted recently are discussed supplementing the information related to literature studies as given in Section 5.1.

Kim & Lee [11] conducted experiments for an eight wire single channel laboratory scale ESP operated in a wind tunnel for finding optimum operating and geometric conditions for increasing particle collection efficiency. They proposed a set of operating and geometric parameters based upon the experimental results for increasing efficiency as well as designed some rapping systems to maintain higher collection efficiency which are also explained in detail in Section 5.1.

Jedrusik et al. [12] reported the effect of particle diameter and different discharge electrode geometry (barbed plate, wire, barbed tube and spike band) on the particle migration velocity. It was concluded that barbed plate and wire discharge electrodes provide higher particle migration velocities. In another publication [13] Jedrusik et al. discussed findings on an experimental study for three different designs of discharge electrodes having different spike designs and varying distances between spikes. They reported the V-I curves for different discharge electrodes as well as particle collection efficiencies for two different ashes from which the discharge electrode that yielded the optimum collection efficiency was identified. In another paper [14] two more type of discharge electrode designs were analyzed by Jedrusik et al. and results for V-I curves as well as collection efficiencies are reported. All of these studies are also explained in detail in chapter 5 of the thesis.

Podlinski et al. [15] reported results of electro hydrodynamic secondary flow and particle collection efficiencies for spike and plate electrostatic precipitator. It was concluded that very complicated flow patterns were present along with the strong dependence of Electro Hydro Dynamic (EHD) secondary flow on applied voltage and particle collection efficiencies for submicron particles significantly reduces in the range of 0.25 to 0.5  $\mu\text{m}$  particle diameter. Al Hamouz et al. [16] reported the experimental results for the electrostatic properties in the form of corona power loss and ground plate current density and found a good agreement between experimental and simulated results. The effect of varying discharging wire to plate spacing, wire radii and applied voltage polarity on corona power loss was also reported. They also pointed out that shielding effect is present between the adjacent discharge electrodes in case of multi wire ESP systems.

In a recent publication by Xu et al. [17], the effect of electrode geometry (saw, spiked and rod) on particle collection in a temperature ranging from low to high value in an electrostatic precipitator was reported. It was concluded that saw or spiked electrode provided better collection efficiencies and discharge current at lower temperatures for fine particles but for increased temperatures rod type discharge electrodes exhibit good particle collection efficiencies results. In a recent publication, He et al. [18] reported on an experimental study for the design of electrostatic precipitator for removing suspended particles from gas turbine

inlet air flow, and optimized operating parameters for combination of wires and applied voltage to achieve maximum collection efficiency were proposed.

Kasdi [19] also recently reported on an experimental study on the electrostatic properties in the form of corona current, current density, space charge density and electric potential which has also been used in this study for validation of CFD simulation results which are presented in Chapter 4. He reported the effect of varying number of discharge wires, discharge wires radii, distances between discharge wires on the corona current and other electrostatic properties with variation of applied voltage at the discharge wire. He concluded that all the above variables have significant influence on the V-I curve and also have an effect on the degree of shielding. In Table 2.2, the experimental studies are summarized.

**Table 2.2:** Summary of the experimental studies related to laboratory scale ESPs.

References	Scale	Findings
<b>Kim &amp; Lee [11]</b>	Laboratory scale (eight wires)	V-I curves, effect of wire to plate and wire to wire spacing, air velocity, turbulence intensity, wire diameter and particle diameter on collection efficiency [11].
<b>Jedrusik [12,13,14]</b>	Laboratory scale (different discharge electrodes design)	V-I curves for different discharge electrodes, collection efficiency as a function of voltage for different design of discharge electrodes, particle migration velocity as a function of particle diameter and discharge electrode design [12,13,14].
<b>Podlinski [15]</b>	Laboratory scale spike plate type electrostatic precipitator	V-I curves, analysis of electro hydrodynamic flow, particle collection efficiency as a function of particle diameter and applied discharge voltage [15].
<b>Al Hamouz[16]</b>	Laboratory scale wire plate discharge electrodes	Effect of different geometric and operating parameters on corona power loss and ground plate current density. Shielding effect was also pointed out [16].
<b>Xu et al. [17]</b>	Laboratory scale (different design of discharge electrodes)	Effect of discharge electrode designs on collection efficiency as a function of varying temperature from low to high [17].
<b>He et al. [18]</b>	Laboratory scale electrostatic precipitator for use with gas turbine	Operating parameters for maximum collection efficiency [18].
<b>Kasdi [19]</b>	Laboratory scale wire plate electrostatic precipitator	Different electrostatic parameters and their effect of variation on V-I curves, current density, space charge density. Shielding effect is also reported [19].

## 2.4.2 Empirical modelling and validation

Empirical modelling also provides deep insight in the understanding of various phenomena involved in field of electrostatic precipitators. Kim et al. [11,20] in a series of two publications provide predictions of collection efficiencies as a function of particle diameter, air velocity, and wire to plate spacing with the help of theoretical models along with experimental validations. Lawless and Sparks [21] studied the electrical conditions in wire duct electrostatic precipitators and reported V-I curves generation as a function of the applied

voltage, and an empirical model was derived from the results. These results, as reported by Lawless and Sparks are also used for validation of the computational model developed in this study. McDonald and Smith [22] also reported about the variation of electrical conditions with different operating parameters like wire size, wire to wire spacing and plate to plate spacing in wire duct electrostatic precipitators. In Table 2.3, the empirical modelling studies reported in literature and explained in this section are summarized.

**Table 2.3:** Summary of the empirical/theoretical modelling studies related to laboratory scale ESPs.

References	Scale	Findings
<b>Kim et al. [11,20]</b>	Laboratory scale wire plate electrostatic precipitator	Collection efficiency using different theoretical models is evaluated as a function of particle diameter, air velocity, and wire to plate spacing [11, 20].
<b>Lawless and Sparks [21]</b>	Laboratory scale wire plate electrostatic precipitator	A model for the electrical conditions is developed and V-I curves and other electrostatic parameters are evaluated and compared with literature experimental findings [21].
<b>McDonald and Smith [22]</b>	Laboratory scale wire plate electrostatic precipitator	Effect of wire size, wire to wire and wire to plate spacing on electrostatic properties is reported [22].
<b>Jedrusik et al. [13]</b>	Laboratory scale different discharge electrode design ESP	Collection efficiency for two different ashes was evaluated by Deutsch equation as a function of applied voltage and compared with experimental findings [13].

### 2.4.3 Computational modelling and validation

Apart from experimental studies, computational modelling also received significant attention during the last decade because of saving capital investments required for setting experimental laboratory scale or pilot plant ESP set ups.

The CFD studies were mostly confined to the studies of flow through an ESP for predicting and improving uniform flow distributions, prediction of electrostatic properties and V-I curves and also the prediction and calculation of particle charging and collection as well as particle separation by applying high voltage to the discharge wires [23]. Recently Ye et al. [24] reported gas flow simulations through electrostatic precipitators to determine parameters for perforated plates as well as an ESP itself. It was concluded that optimization of the flow distribution in the ESP section can be effectively performed with the use of CFD by adopting several adjusting measures like changing position of perforated plates as well porosity etc. Previously Haque et al. [25] also worked on the behavior of flow through an electrostatic

precipitator and reported the gas flow simulations through a large scale industrial ESP of a thermal power plant. The comparison between simulation findings and on site velocity measurements data showed good agreement and are further discussed in the introductory section of Chapter 3. In another publication, Haque et al. [26] reported that for computational modelling the inlet velocity profile is quite important for predicting the velocity profiles through the ESP section and that the real velocity profile at the inlet predicts velocity distributions through the ESP section more accurately as compared to an ideal velocity profiles at the inlet. These studies supported the fact that CFD studies can be a cost effective, efficient, and reliable tool for predicting flow through an electrostatic precipitator after modifications in perforated plate designs and baffle arrangements.

In addition to the flow studies to improve velocity distributions in ESPs, a lot of researchers also focused on the simulations of the electrical conditions such as voltage distributions, corona current, current density distributions, electrostatic field distributions, and current density at collection plate using only a 2-D approach. The computational modelling methods, mostly applied for such electric conditions predictions were based on specialized techniques which are mentioned in Chapter 3 of the thesis [27–32]. Neimarlija et al. [33] presented a computational modelling method based on the finite volume discretization of the solution domain by arbitrary polyhedral control volumes and resulting set of algebraic equations were solved iteratively for the calculation of electric and space charge density fields in ESP.

During the last few years a large amount of researchers focused on the computational modelling studies for prediction and calculation of particle charging, collection and separation during flow through ESPs along with electrical conditions predictions [34,35]. Recently Lu et al. [36] developed an integrated computational model that describes the particle charging and transport behavior in a wire plate electrostatic precipitator. The authors investigated the particle charging process for different sizes of particles and found that the field charging mechanism is dominant for larger particles while for smaller particles (1  $\mu\text{m}$  range) diffusion charging is the dominant mechanism. Al-Hamouz conducted a study [37] in which the finite element method and a modified method of characteristics were used to solve the governing equations inside ESP. He reported the influence of different geometrical and operating parameters of a single stage wire duct ESP on the fly ash collection efficiency.

Farnoosh et al. [38,39] presented a CFD model for a single channel single electrode ESP system using wire discharge electrodes which are explained in details in Chapter 3 of the thesis. Farnoosh et al. [40,41] also reported CFD modelling results of a spiked discharge electrode describing EHD flow and particle collection efficiencies and compared this to literature findings, which are further detailed in Chapter 3. In a study by Long and Yao [42] a computational model of an ESP was developed in which different particle charging models were evaluated and are explained in Chapter 3. Few of the experimental and computational modelling results used in this paper are also used for validation of the CFD model given in Chapter 3 and 4.

Al Hamouz [16] and Kasdi [19], validated their computational modelling results with experimental results and both reported the presence of shielding effect present on the middle

wires in case of multi electrode ESP systems. The presence and variation of the degree of shielding due to a change of geometric and operating parameters in case of multi electrode ESPs was also studied as part of this thesis.

Ming Dong et al.[43] recently reported on a computational modelling study on the charging and transport of fine particles in wire plate ESPs. The influence of different parameters (applied discharge electrode voltage, inlet height and wire spacing on particle charging and transport and effect of ESP structure on particle trapping) was investigated. They found that influence of injection position of particles on particle trapping was important as the particles which were injected nearer to the collection plates and in the center of ESP channel were more easily collected and attained higher charge. Similarly, changing the discharge electrode arrangement in the ESP also showed to have a significant influence on the particle charging and collection and different arrangements were tested to find the best arrangement. However, the study was not confined to different designs of discharge electrodes and the effect of shielding was also not reported and quantified.

Sander et al.[44] recently reported computational modelling findings using wire and spiked wire discharge electrode design to investigate the particle behavior and collection efficiency. Based upon the electrostatic properties and collection efficiency results they concluded that use of spiked discharge electrodes was more advantageous as compared to wire discharge electrodes particularly in case of micron sized particles. The presence of shielding effect and rigorous validation with onsite experimental measurements were ignored during the reported study.

Skodras et al. [45] and Ivancsy et al. [46] developed 2-D models that also takes into account the three interacting fields of fluid dynamics, particle dynamics and electrostatics and are explained in detail in Chapter 3. Gutierrez Ortiz et al. [47,48] presented a dimensional analysis together with a similarity analysis to obtain a functional dependence between a certain target value which is collection efficiency and dimensionless variables where by the results could be used to develop working models based on regression analysis that were validated using a pilot scale ESP. Thereby a frame work was established through which particle collection efficiency could be easily predicted.

Zhongjie et al. [49,50] in their recent publications reported on the development and validation of a 3-D computational model using commercial software COMSOL and also used that validated model for studying the effects of different parameters in ESPs using FEM simulations for predicting effects of multiple variables. A brief description of the above described literature is given in Table 2.4 below.

**Table 2.4:** Summary of the CFD modelling studies related to pilot plant/laboratory scale ESPs.

References	Scale	Findings
<b>Ye et al. [24]</b>	Pilot plant electrostatic precipitator	Flow simulations by varying porosity and changing position of perforated plates as well as velocity profiles are reported [24].
<b>Haque et al. [25,26]</b>	Industrial scale electrostatic precipitator	Flow behavior and velocity distributions were predicted and compared with measured data [25, 26].
<b>Farnoosh et al. [38-41]</b>	Single channel single wire/spike ESP system	A CFD model was developed and compared with literature results for varying geometric and operating parameters. Analysis of EHD flow was also carried out in case of wire and spike discharge electrodes [38-41].
<b>Zhongjie et al. [49,50]</b>	Laboratory scale wire plate electrostatic precipitator	A CFD model was developed and validated with literature data for varying geometric and operating parameters. A factorial design variation of different parameters was evaluated and optimized operating parameters were proposed [49, 50].
<b>Skodras et al. [45], Ivancsy et al. [46]</b>	Laboratory scale electrostatic precipitator	2-D CFD model for predicting electrical properties, flow and particle dynamics was developed [45, 46].

## 2.5 Summary

A brief description of the different PM removal processes was given together with a comparison of the advantages and disadvantages of the different processes. The basic principles involved in electrostatic precipitation and the major components and different types of electrostatic precipitators were also discussed. Subsequently, experimental, empirical, and computational modelling studies were reviewed and a lack of 3-D computational modelling that includes an extensive description of the electrostatics, fluid and particle dynamics was noted. Furthermore, computational modelling of different types of discharge electrodes have received only relatively little attention in the literature. Finally, any developments in terms of computational modelling of ESP processes require rigorous experimental validation, which together with the abovementioned aspects are addressed in this thesis.



---

## 2.6 References

- [1] International Energy Agency, Energy and Air Pollution, World Energy Outlook - Spec. Rep. (2016) 266. doi:10.1021/ac00256a010.
- [2] Department of Environmental Affairs, National Environmental Management: Air Quality Act, Gov. Gaz. (2010) 3–36. [https://www.environment.gov.za/sites/default/files/gazetted\\_notices/nemaqa\\_listofactivities\\_g33064gon248.pdf](https://www.environment.gov.za/sites/default/files/gazetted_notices/nemaqa_listofactivities_g33064gon248.pdf).
- [3] K.R. Parker, Applied Electrostatic Precipitation, 1<sup>st</sup> edition, 1997. doi:10.1007/s13398-014-0173-7.2.
- [4] Norton Engineering LLC, Environmental Balance: Baghouses vs Precipitators, <http://www.environmentalengineering.net/environmental/baghouses.php>. (accessed on 11<sup>th</sup> March 2018)
- [5] E.W. Stenby, R.W. Scheck, S.D. Severson, F.A. Horney, D.P. Teixeira, Fabric Filters versus Electrostatic Precipitators, *Environ. Int.* 6 (1981) 103–114.
- [6] Principles of electrostatic precipitator, <http://www.hitachi-infra.com.sg/services/energy/dustcollection/principle/dustcollection.html>.
- [7] Electrostatic Precipitator Components, <http://www.neundorfer.com/wp-content/uploads/2016/05/ESP-KnowledgeBase-02-Components.pdf>.
- [8] J.R. Richards, Control of Particulate Emissions Student Manual (APTI Course 413), U S Environ. Prot. Agency. (1995).
- [9] Electrostatic Precipitator Operation, <http://www.neundorfer.com/wp-content/uploads/2016/05/ESP-KnowledgeBase-01-Operation.pdf>.
- [10] S Madhava Reddy, G Dayanand, Review on development of an automated system for gas distribution test of ESP, *Int. J. Mech. Eng. Robot. Res.* 2
- [11] S. Kim, K. Lee, Experimental study of electrostatic precipitator performance and comparison with existing theoretical prediction models, *J. Electrostat.* 48 (1999) 3–25. doi:10.1016/S0304-3886(99)00044-3.
- [12] M. Jdrusik, J.B. Gajewski, A.J. Wierczok, Effect of the particle diameter and corona electrode geometry on the particle migration velocity in electrostatic precipitators, *J. Electrostat.* 51-52 (2001) 245–251. doi:10.1016/S0304-3886(01)00047-X.
- [13] M. Jedrusik, A. Swierczok, R. Teisseyre, Experimental study of fly ash precipitation in a model electrostatic precipitator with discharge electrodes of different design, *Powder Technol.* 135-136 (2003) 295–301. doi:10.1016/j.powtec.2003.08.021.
- [14] M. Jedrusik, A. Świerczok, The correlation between corona current distribution and collection of fine particles in a laboratory-scale electrostatic precipitator, *J. Electrostat.* 71 (2013) 199–203. doi:10.1016/j.elstat.2013.01.002.
- [15] J. Podlinski, A. Niewulis, J. Mizeraczyk, Electrohydrodynamic flow and particle

- collection efficiency of a spike-plate type electrostatic precipitator, *J. Electrostat.* 67 (2009) 99–104. doi:10.1016/j.elstat.2009.02.009.
- [16] Z. Al-Hamouz, A. El-Hamouz, N. Abuzaid, Simulation and experimental studies of corona power loss in a dust loaded wire-duct electrostatic precipitator, *Adv. Powder Technol.* 22 (2011) 706–714. doi:10.1016/j.apr.2010.10.005.
- [17] X. Xu, C. Zheng, P. Yan, W. Zhu, Y. Wang, X. Gao, et al., Effect of electrode configuration on particle collection in a high-temperature electrostatic precipitator, *Sep. Purif. Technol.* 166 (2016) 157–163. doi:10.1016/j.seppur.2016.04.039.
- [18] Z. He, E.T.M. Dass, G. Karthik, Design of electrostatic precipitator to remove suspended micro particulate matter from gas turbine inlet airflow: Part I. Experimental study, *J. Aerosol Sci.* 108 (2017) 14–28. doi:https://doi.org/10.1016/j.jaerosci.2017.03.003.
- [19] A. Kasdi, Computation and measurement of corona current density and V-I characteristics in wires-to-plates electrostatic precipitator, *J. Electrostat.* 81 (2016) 1–8. doi:10.1016/j.elstat.2016.02.005.
- [20] S.H. Kim, H.S. Park, K.W. Lee, Theoretical model of electrostatic precipitator performance for collecting polydisperse particles, *J. Electrostat.* 50 (2001) 177–190. doi:10.1016/S0304-3886(00)00035-8.
- [21] P.A. Lawless, L.E. Sparks, A mathematical model for calculating effects of back corona in wire-duct electrostatic precipitators, *J. Appl. Phys.* 51 (1980) 242–256. doi:10.1063/1.327416.
- [22] J.R. McDonald, W.B. Smith, H.W. Spencer, L.E. Sparks, A mathematical model for calculating electrical conditions in wire-duct electrostatic precipitation devices, *J. Appl. Phys.* 48 (1977) 2231–2243. doi:10.1063/1.324034.
- [23] K. Adamiak, Numerical models in simulating wire-plate electrostatic precipitators: A review, *J. Electrostat.* 71 (2013) 673–680. doi:10.1016/j.elstat.2013.03.001.
- [24] X. Ye, Y. Su, B. Guo, A. Yu, Multi-scale simulation of the gas flow through electrostatic precipitators, *Appl. Math. Model.* 40 (2016) 9514–9526. doi:10.1016/j.apm.2016.06.023.
- [25] S.M.E. Haque, M.G. Rasul, A.V. Deev, M.M.K. Khan, N. Subaschandar, Flow simulation in an electrostatic precipitator of a thermal power plant, *Appl. Therm. Eng.* 29 (2009) 2037–2042. doi:10.1016/j.applthermaleng.2008.10.019.
- [26] S.M.E. Haque, M.G. Rasul, M.M.K. Khan, A. V. Deev, N. Subaschandar, Influence of the inlet velocity profiles on the prediction of velocity distribution inside an electrostatic precipitator, *Exp. Therm. Fluid Sci.* 33 (2009) 322–328. doi:10.1016/j.expthermflusci.2008.09.010.
- [27] J. Anagnostopoulos, G. Bergeles, Corona discharge simulation in wire-duct electrostatic precipitator, *J. Electrostat.* 54 (2002) 129–147. doi:10.1016/S0304-3886(01)00172-3.

- 
- [28] J.L. Davis, J.F. Hoburg, Wire-duct precipitator field and charge computation using finite element and characteristics methods, *J. Electrostat.* 14 (1983) 187–199. doi:10.1016/0304-3886(83)90006-2.
- [29] P.L. Levin, J.F. Hoburg, Donor cell-finite element descriptions of wire-duct precipitator fields, charges, and efficiencies, *Ind. Appl. IEEE Trans.* 26 (1990) 662–670. doi:10.1109/28.55991.
- [30] A.A. Elmoursi, G.S. Peter Castle, Modeling of corona characteristics in a wire-duct precipitator using the charge simulation technique, *IEEE Trans. Ind. Appl.* IA-23 (1987) 95–102. doi:10.1109/TIA.1987.4504872.
- [31] Z.M. Al-Hamouz, A combined algorithm based on finite elements and a modified method of characteristics for the analysis of the corona in wire-duct electrostatic precipitators, *Ind. Appl. IEEE Trans.* 38 (2002) 43–49. <http://ieeexplore.ieee.org/ielx5/28/21119/00980343.pdf?tp=&arnumber=980343&isnumber=21119>.
- [32] Z. Lin, K. Adamiak, Numerical Simulation of the Electrohydrodynamic Flow in a Single Wire-Plate Electrostatic Precipitator, *Ind. Appl. IEEE Trans.* 44 (2008) 683–691. doi:10.1109/TIA.2008.921453.
- [33] N. Neimarlija, I. Demirdžić, S. Muzaferija, Finite volume method for calculation of electrostatic fields in electrostatic precipitators, *J. Electrostat.* 67 (2009) 37–47. doi:10.1016/j.elstat.2008.10.007.
- [34] Q. Liu, S. song Zhang, J. pei Chen, Numerical analysis of charged particle collection in wire-plate ESP, *J. Electrostat.* 74 (2015) 56–65. doi:10.1016/j.elstat.2014.11.007.
- [35] M. Feldkamp, M. Dickamp, C. Moser, Electrostatic Precipitation: 11th International Conference on Electrostatic Precipitation, Hangzhou, 2008, in: K. Yan (Ed.), Springer Berlin Heidelberg, Berlin, Heidelberg, 2009: pp. 141–150. doi:10.1007/978-3-540-89251-9\_30.
- [36] Q. Lu, Z. Yang, C. Zheng, X. Li, C. Zhao, X. Xu, et al., Numerical simulation on the fine particle charging and transport behaviors in a wire-plate electrostatic precipitator, *Adv. Powder Technol.* 27 (2016) 1905–1911. doi:10.1016/j.appt.2016.06.021.
- [37] Z. Al-Hamouz, Numerical and experimental evaluation of fly ash collection efficiency in electrostatic precipitators, *Energy Convers. Manag.* 79 (2014) 487–497. doi:10.1016/j.enconman.2013.11.047.
- [38] N. Farnoosh, K. Adamiak, G.S.P. Castle, 3-D numerical analysis of EHD turbulent flow and mono-disperse charged particle transport and collection in a wire-plate ESP, *J. Electrostat.* 68 (2010) 513–522. doi:10.1016/j.elstat.2010.07.002.
- [39] N. Farnoosh, K. Adamiak, G.S.P. Castle, 3-D numerical simulation of particle concentration effect on a single-wire ESP performance for collecting poly-dispersed particles, *IEEE Trans. Dielectr. Electr. Insul.* 18 (2011) 211–220. doi:10.1109/TDEI.2011.5704512.
- [40] N. Farnoosh, K. Adamiak, G.S.P. Castle, Numerical calculations of submicron particle
-

- 
- removal in a spike-plate electrostatic precipitator, in: IEEE Trans. Dielectr. Electr. Insul., 2011: pp. 1439–1452. doi:10.1109/TDEI.2011.6032814.
- [41] N. Farnoosh, K. Adamiak, G.S.P. Castle, Three-dimensional analysis of electrohydrodynamic flow in a spiked electrode-plate electrostatic precipitator, *J. Electrostat.* 69 (2011) 419–428. doi:10.1016/j.elstat.2011.06.002.
- [42] Z. Long, Q. Yao, Evaluation of various particle charging models for simulating particle dynamics in electrostatic precipitators, *J. Aerosol Sci.* 41 (2010) 702–718. doi:10.1016/j.jaerosci.2010.04.005.
- [43] M. Dong, F. Zhou, Y. Zhang, Y. Shang, S. Li, Numerical study on fine-particle charging and transport behaviour in electrostatic precipitators, *Powder Technol.* (2018). doi:<https://doi.org/10.1016/j.powtec.2018.02.038>.
- [44] S. Sander, S. Gawor, U. Fritsching, Separating polydisperse particles using electrostatic precipitators with wire and spiked-wire discharge electrode design, *Particuology*. (2017). doi:10.1016/j.partic.2017.05.014.
- [45] G. Skodras, S.P. Kaldis, D. Sofialidis, O. Faltsi, P. Grammelis, G.P. Sakellariopoulos, Particulate removal via electrostatic precipitators - CFD simulation, *Fuel Process. Technol.* 87 (2006) 623–631. doi:10.1016/j.fuproc.2006.01.012.
- [46] T. Iváncsy, J.M. Suda, Behavior of polydisperse dust in electrostatic precipitators, *J. Electrostat.* 63 (2005) 923–927. doi:10.1016/j.elstat.2005.03.062.
- [47] F.J. Gutiérrez Ortiz, B. Navarrete, L. Cañadas, Assessment of plate-wire electrostatic precipitators based on dimensional and similarity analyses, *Fuel*. 90 (2011) 2827–2835. doi:10.1016/j.fuel.2011.04.006.
- [48] F.J. Gutiérrez Ortiz, B. Navarrete, L. Cañadas, Dimensional analysis for assessing the performance of electrostatic precipitators, *Fuel Process. Technol.* 91 (2010) 1783–1793. doi:10.1016/j.fuproc.2010.07.013.
- [49] Z. He, E.T.M. Dass, Correlation of design parameters with performance for electrostatic precipitator. Part II. Design of experiment based on 3D FEM simulation, *Appl. Math. Model.* (2017). doi:<https://doi.org/10.1016/j.apm.2017.06.031>.
- [50] Z. He, E.T.M. Dass, Correlation of design parameters with performance for electrostatic Precipitator. Part I. 3D model development and validation, *Appl. Math. Model.* (2017). doi:<https://doi.org/10.1016/j.apm.2017.05.042>.

### **Chapter 3. CFD MODELING OF PARTICLE CHARGING AND COLLECTION IN ELECTROSTATIC PRECIPITATORS**

This chapter is based on the following publication: S. Arif, D.J. Branken, R.C. Everson, H.W.J.P. Neomagus, L.A. le Grange, A. Arif, CFD modeling of particle charging and collection in electrostatic precipitators, J. Electrostat. 84 (2016). p. 10 – 22. doi: 10.1016/j.elstat.2016.08.008.

#### **Abstract**

A CFD model was developed to describe the particle laden gas flow through an ESP, particle charging and collection. The corona discharge was modeled using the open source software OpenFOAM to solve the Poisson and charge conservation equations, and results were entered using user-defined field functions in the commercial CFD software STAR-CCM+. The gas flow, EHD flow, particle charging and dynamics were modeled using STAR-CCM+. The developed CFD model allows for direct solution of the drift and diffusional flux of gas ions. The influence of the various ESP dimensions, operating parameters and ash properties on the collection efficiency are reported.

**Key words:** *CFD model, Electrostatic precipitation (ESP), Electro-hydrodynamic (EHD) flow, Permittivity, Particle charging, ESP collection efficiency.*

### 3.1 Introduction

Electrostatic precipitation is one of industrial scale particulate collection technologies that are frequently used to meet particulate emissions standards as determined by the various international legislators. Large gas volumes with a wide range of inlet temperatures, pressures, dust volumes and acid gas conditions can be accommodated using ESP technology, and collection efficiencies of more than 99% can be achieved, although submicron particles are collected with much lower efficiencies and further research is required to improve this aspect [1].

The basic working principle of ESP devices entail charge transfer from the corona discharge to the ash particles, where the corona is created by the high electric potential difference between the discharge electrode and collection electrodes. The corona discharge causes ionized gas molecules to collide with the particles, which are subsequently negatively charged and attracted towards the positive, grounded collection plates by Coulomb forces. The particles trajectories are therefore influenced by the interacting electrostatic, fluid dynamic and particle dynamic fields within the individual ESP channels. The electro hydrodynamic (EHD) flow phenomenon further complicates the flow of gas ions (aerodynamics) between the discharge and collection electrodes, although previous studies have shown that this effect is only significant at low linear flow velocities [2]. The migration velocity of charged particles towards the collecting plates is therefore greatly affected by the magnitude of the Coulomb forces acting on the individual particles, which is determined by the total particle charge at any given point in time that is in turn determined by the rate at which particles are charged. The rate of particle charging is a function of the ease of electrical charge acceptance, which is described by the classical Deutsch model using resistivity as the characteristic material property [3,4]. However, the Deutsch model, its derivatives and other theoretical correlations fail to give an accurate description under a wide range of operating variables [4]. Recently, the focus has shifted towards using CFD, in favor of theoretical correlations, to model ESP processes in an effort to determine the optimized fluid flow and ESP dimensions that allow for increased ash collection efficiencies [5–11]. This is because the complex behavior of flow within ESPs can efficiently be modeled using computational fluid dynamics (CFD) modeling, and by incorporating the electrostatic and particle dynamic fields in the numerical models one is able to predict particle trajectories and collection efficiencies [5–7,12]. Currently, CFD models still require rigorous validation against experimental data, and thus a considerable amount of experimental, numerical and theoretical research has been dedicated to the optimization of ESP operation during the last decades [2,13–16].

In addition, the majority of CFD studies have focused only on the complex flow distributions within an ESP that are mainly due to the intricate geometry. Haque et al [17] modeled the gas flow through an industrial-scale ESP of a thermal power plant using the FLUENT CFD code and compared the results with onsite measured data. They predicted the gas velocity profile

throughout the ESP by also considering the baffles and perforated plates to describe their influence on the flow pattern throughout the ESP. It was found that the model provides a very useful tool for predicting the behavior of flow through an ESP in response to any modification in the geometry.

Farnoosh [6] presented a three-dimensional modeling approach to study the relevant interacting phenomena in a single channel, single electrode ESP model. For this purpose, a hybrid finite element (FEM), flux corrected transport (FCT) method for modeling corona discharge was developed and implemented in the commercial FLUENT code for modeling gas flow and particle motion under the influence of electrostatic forces. They assumed that the particle space charge is negligible due to the relatively low particle concentration but later extended the model to also take into account the influence of the particles and the particle concentration on the space charge density distribution to accurately study the behavior of poly-dispersed ash particles [18]. It was concluded that an increasing particle concentration influences the air flow pattern and induces more turbulence which results in an increased collection efficiency of smaller particles. In another study, a spiked discharge electrode was used instead of the traditional circular wire electrode [10] and it was found that the discharge electrode structure plays a significant role in determining the characteristics of EHD flow as well as turbulence, which both play a role in collection efficiency.

In a study by Long and Yao [7] a numerical model of an ESP was developed in which nine different particle charging models based on the field charging theory, the diffusion charging theory and the combined field diffusion theory were evaluated. It was concluded that the charging model based on the combined field diffusion theory developed by Lawless [15] is preferred due to its acceptable level of accuracy and little computation time. Skodras et al. [5] developed a model that focused mainly on coupling the three coexisting and interacting fields of gas flow, particle dynamics and electrostatics. The model was applied to a two-dimensional geometry using the FLUENT CFD package. The particle space charge density effects were also included, and particle charging was based on the model of Pauthenier & Moreau-Hanot [7] that only takes field charging into account. The general observations that the collection efficiency was decreased as the particle size decreased and that the collection efficiency could be increased by increasing the voltage of the discharge electrode or by reducing the inlet velocity could be confirmed. Ivancsy et al. [16] developed a model that also takes into account the three interacting fields of fluid dynamics, particle dynamics and electrostatics and considered poly-dispersed ash particles in their work. Particle charging was described by both field and diffusion charging and it was confirmed that the collection efficiency increases as particle size increases.

In comparison with the fluid dynamics, the electrostatic field and its coupling with the particle dynamic field and its influence on particle trajectories and collection efficiencies has only received little attention in CFD modeling studies. On the other hand, Skodras et al. [5] and Iváncsy and Suda [16] reported a 2-D analysis of the influence of the electrostatic

conditions on the particle trajectories, while neglecting the effect of fluid flow. In more detailed CFD studies numerical methods such as the Finite Element (FEM)-Method of Characteristics (MoC) [14,19], the FEM-Boundary Element (BEM)-MoC [20], the FEM-Charge simulation (CSM) [21], the FEM-Donor Cell (DCM) [22] and the Finite Difference (FDM)-MoC [23] methods. These specialized numeric techniques are not accessible to many researchers due to not being included in most commercial CFD packages. Consequently, computational studies into the underlying relationships between ESP design, electrostatic field properties, ash properties and collection efficiency (ESP performance) is restricted.

This paper is aimed at addressing this shortcoming, and therefore a detailed CFD model in which the interacting fields that affect the efficiency of particle collection is described and evaluated. For this purpose, a relatively simple computational procedure was developed to describe the drift of gas ions that are caused by corona discharge. Simultaneously, the fluid dynamic and particle dynamic fields were also modeled to allow the systematic study of the effect of the various ESP parameters, including the particle properties, on the ESP collection efficiency.

### **3.2 Numerical modeling and solution methods**

The commercial CFD software package STAR-CCM+ is used in tandem with the open source code OpenFOAM to solve the transport equations for the continuous phase, the electrostatic field, particle motion and particle charging. The mathematical equations that govern the flow of particle-laden gas through an ESP while influenced by the electrostatic and aerodynamic fields are described in Section 3.2.1 and Section 3.2.2. A detailed description of the 3-D model of the single-channel ESP and its variations is given in Section 3.2.3

#### **3.2.1 Electrostatic field**

In the single-channel ESPs (Section 3.2.3) modeled in this study, a high voltage was (virtually) applied to the discharge electrodes, which take on the form of cylindrical wires with small radii that were mounted in the middle of an ESP channel consisting of two parallel collection plates. As a result of the high electrical potential difference applied across the positively and negatively charged electrodes, a corona discharge developed as a result of ionization of the surrounding gas molecules. This corona discharge resulted in a space charge being developed in the drift region, with the gas ions imparting their charge to the dust particles. The Poisson equation given in Eq. (3.1) [6] was used to describe the electrostatic field

inside the ESP:

$$\nabla^2 V = -\frac{\rho_w}{\epsilon_0} \quad (3.1)$$



where

$$\vec{E} = -\nabla V \quad (3.2)$$

$V$  in Eq. (3.1) and (3.2) represent the electric potential (V),  $\rho_w$  is the ionic space charge density (C/m<sup>3</sup>),  $\epsilon_0$  is the permittivity of gas (F/m) and  $\vec{E}$  is the electrostatic field intensity (V/m). The resulting gas ions are attracted to the collection electrodes under the influence of Coulomb body forces, that results in an electric current with a density [6] defined by Eq. (3.3):

$$\vec{J} = \rho_w \left( b\vec{E} + \vec{u}_{gas} \right) - D_i \nabla \rho_w \quad (3.3)$$

where  $\vec{J}$  is the current density (A/m<sup>2</sup>),  $b$  is the mobility of ions (m<sup>2</sup>/V.s),  $D_i$  is the ion diffusion coefficient (m<sup>2</sup>/s) and  $\vec{u}_{gas}$  is the gas velocity (m/s). The terms on the right-hand side of Eq. (3.3) respectively represent the drift ( $b\rho_w\vec{E}$ ), convection ( $\rho_w\vec{u}_{gas}$ ) and diffusion currents ( $D_i \nabla \rho_w$ ). Under normal ESP operating conditions, the drift velocity (due to the Coulomb forces) of ions is much larger than the gas velocity. In other words, the current density,  $\vec{J}$ , is not significantly affected by the convective flow of the gas, as shown in the supporting info (SI). Furthermore, gas diffusion is negligible compared to the convective and drift effects, and for these reasons Eq. (3.3) can be simplified to give Eq. (3.4):

$$\vec{J} = b\rho_w \vec{E} \quad (3.4)$$

Under steady state conditions, charge conservation is satisfied [6], and therefore:

$$\begin{aligned} \nabla \cdot \vec{J} &= 0 \\ \nabla \cdot (b\rho_w \vec{E}) &= 0 \end{aligned} \quad (3.5)$$

The coupled equations, Eq. (3.1) to Eq. (3.5) were solved simultaneously using OpenFOAM [31] to obtain the electric potential distribution, electrostatic field distribution and space charge density distribution. The OpenFOAM framework allows for versatile solution of these equations due to the generic nature of its basic code. Consequently, only a few simplistic lines of code are used to solve the electric potential and space charge density equations to obtain the space charge density distribution throughout the computational domain. This result is currently not easily achievable using commercial CFD codes, which showcases the broad field of application of the open source software.

The method was executed by compiling the model within OpenFOAM, while preserving the geometry and mesh that was generated using STAR-CCM+ (Section 3.2.3). Once the electrostatic equations were solved using OpenFOAM, the results of the space charge density,

electric potential and electrostatic field distribution were extracted in the form of a data table that gave the value of the various quantities for each individual discretized cell, which was then used as input to STAR-CCM+ through user defined field functions. This allowed for calculation of particle dynamics and particle charging as a function of position relative to the discharge electrodes and collecting plates respectively, through which particle collection was also simulated. The boundary condition for discharge potential was varied between 6 and 13 kV, while a constant collection electrode potential of 0 V was used in all simulations. An indirect boundary condition value was used for the space charge density by applying an initial estimated value as input for the space charge density at the discharge electrode surface, and then solved iteratively until the average electrostatic field magnitude on the wire surface converged to the value given by Peek's formula [6,24]:

$$\vec{E}_p = 3.1 \times 10^6 \left( 1 + \frac{0.308}{\sqrt{r_c}} \right) \quad (3.6)$$

where  $\vec{E}_p$  is the average electrostatic field magnitude on the wire surface (V/m) and  $r_c$  is the radius of the corona wire (cm). This approach was applicable only to the cylindrical (symmetric) discharge electrodes [6, 24], but is not applicable to discharge electrodes with irregular geometries due to the non-uniform distribution of charge along the electrode surface. In the case of a spike discharge electrode, which was also modeled, the total corona discharge current obtained from numerical simulation was instead compared with, and fitted to experimental measurements that are available in the literature for the specific system that was simulated [25]. This was achieved by adjusting the initial space charge density value on the discharge electrode surface until close agreement was achieved with the experimental data [26], i.e. such that the deviation was smaller than 2%. These boundary conditions are summarized in Table 3.1.

**Table 3.1:** Summary of boundary conditions

Geometric surface	Gas flow	Electric potential	Space charge density	Particle
Inlet	Velocity inlet	$\frac{\partial V}{\partial n} = 0$	$\frac{\partial \rho_w}{\partial n} = 0$	Enter
Outlet	Pressure outlet	$\frac{\partial V}{\partial n} = 0$	$\frac{\partial \rho_w}{\partial n} = 0$	Escape
Collection plates	Stationary walls	$V=0$	$\frac{\partial \rho_w}{\partial n} = 0$	Trap
Side walls	Stationary walls	$\frac{\partial V}{\partial n} = 0$	$\frac{\partial \rho_w}{\partial n} = 0$	Reflect
Wires	Stationary walls	$V = 6 - 13 \text{ kV}$	Peek's law	Reflect
Spikes	Stationary walls	$V = 19 - 30 \text{ kV}$	Exp. V- I Curves [26]	Reflect

### 3.2.2 Fluid and particle dynamics

#### 3.2.2.1 Continuous phase fluid dynamics

The air flow through the ESP channel was modeled as steady and turbulent while assuming constant density and viscosity. This was done by solving the continuity and the Navier-Stokes equations using the commercial CFD software STAR-CCM+. The effects of EHD flow were also taken into account by accounting for the body force, i.e. the Coulomb force, exerted on the gas molecules ( $\rho_w \vec{E}$ ) and was introduced into the momentum equation (shown in Eq. (3.7) in its simplified form) via a user-defined function [6].

$$\rho_f \left[ \frac{\partial \vec{u}_{gas}}{\partial t} + \vec{u}_{gas} \cdot \nabla \vec{u}_{gas} \right] = -\nabla P + \mu_{eff} \nabla^2 \vec{u}_{gas} + \rho_w \vec{E} \quad (3.7)$$

where

$$\mu_{eff} = \mu_{visc} + \mu_{turb}$$

In Eq. (3.7),  $\rho_f$  represents the gas density ( $\text{kg/m}^3$ ),  $P$  is the absolute pressure (Pa),  $\mu_{visc}$  is the air viscosity ( $\text{kg/m.s}$ ) and  $\mu_{turb}$  is the turbulence viscosity. The momentum equation, Eq. (3.7), was coupled with the continuity equation (Eq. (3.8)) for steady state flow.

$$\nabla \cdot \vec{u}_{gas} = 0 \quad (3.8)$$

Turbulence effects were introduced using the standard k- $\epsilon$  turbulence model [27].

#### 3.2.2.2 Particle dynamics

Due to the relatively low concentration of the particles, the particle space charge was assumed to be negligible, therefore only one-way coupling in which the dispersed phase had no influence on the fluid flow or the electrostatics, was assumed [6]. The generic form of the equation for conservation of momentum [27] of a particle is given by Eq. (3.9):

$$m_p \frac{dv_p}{dt} = F_d + F_g + F_u \quad (3.9)$$

where  $m_p$  is the mass of the particle (kg),  $v_p$  is the velocity of the particle (m/s),  $F_d$  is the drag force (N),  $F_g$  is the gravitational force (N) and  $F_u$  is the Coulomb force (N). The particles were therefore subjected to the electrostatic body forces (Coulomb forces), gravitational forces and aerodynamic drag forces while passing through the ESP channel. The particle inertia was calculated by performing a force balance on the particles as shown in Eq. (3.10) [27]:

$$m_p \frac{dv_p}{dt} = \frac{1}{2} C_d \rho_f A_p |v_s| v_s + m_p g \left( \frac{\rho_p - \rho_f}{\rho_f} \right) + Q_p \vec{E} \quad (3.10)$$

where  $A_p$  is the projected area of the particle ( $\text{m}^2$ ),  $v_s$  is the particle slip velocity ( $\text{m/s}$ ),  $g$  is the gravitational acceleration ( $\text{m/s}^2$ ),  $\rho_p$  is the particle density ( $\text{kg/m}^3$ ) and  $Q_p$  is the particle charge (C).

The drag coefficient  $C_d$  was calculated from correlations given by Haider and Levenspiel [28]:

$$C_d = \frac{24}{\text{Re}} \left( 1 + b_1 \text{Re}^{b_2} \right) + \frac{b_3 \text{Re}}{b_4 + \text{Re}}$$

$$b_1 = \exp(2.3288 - 6.4551\chi + 2.4486\chi^2)$$

$$b_2 = 0.0964 + 0.5565\chi$$

$$b_3 = \exp(4.905 - 13.8944\chi + 18.4222\chi^2 - 10.2599\chi^3)$$

$$b_4 = \exp(1.4681 + 12.2584\chi - 20.7322\chi^2 + 15.8855\chi^3) \quad (3.11)$$

where  $b_1, b_2, b_3, b_4$  are the model parameters. The shape factor ( $\chi$ ) is defined as (Eq. (3.12)):

$$\chi = \frac{s}{S} \quad (3.12)$$

where  $s$  is the surface area of the sphere having the same volume as the particle and  $S$  is the actual surface area of the particle. The corresponding Reynolds number  $\text{Re}$  is found with the diameter of a sphere having the same volume.

### 3.2.2.3 Particle charging

The particles entering the ESP channel were assumed to be spherical and neutral in charge. Dust particles attained a charge through collisions with the ionized gas molecules and were accelerated towards the collection electrodes due to the Coulomb force acting on each particle. The magnitude of the force experiences was dependent on the extent to which the individual particles were charged.

More specifically, charging occurs through field charging and diffusion charging mechanisms [7]. Field charging is dominant when the particle charge is smaller than the saturation charge and diffusion charging is dominant when the particle charge is above the saturation level, although its contribution is minimal [6]. The saturation charge was calculated using Eq. (3.13) [6]:

$$Q_{sat} = \frac{3\varepsilon_r}{\varepsilon_r + 2} \pi \varepsilon_0 d_p^2 \left| \vec{E} \right| \quad (3.13)$$

where  $Q_{sat}$  is the saturation charge (C),  $\epsilon_r$  is the relative permittivity of the particles,  $d_p$  is the particle diameter (m) and  $|\vec{E}|$  is the electrostatic field magnitude (V/m).

Two particles charging models were used, namely that of Pauthenier & Moreau-Hanot (1932) and White and Lawless (1996). Both these charging models describe particle charge as a function of time by summing the field charging theory and diffusion charging theory models, which results in Eq. (3.14) [7]:

$$Q_p(t) = Q_{sat} \left( \frac{t}{t + \tau_c} \right) + \frac{2\pi\epsilon_o d_p K_B T}{e} \ln \left( 1 + \frac{t}{\tau_l} \right) \quad (3.14)$$

where

$$\tau_c = \frac{4\epsilon_o}{b\rho_w} \quad (3.15)$$

and

$$\tau_l = \frac{8\epsilon_o K_B T}{d_p e \tilde{u} \rho_w} \quad (3.16)$$

$\tau_c$  represents the charging time constant (s),  $t$  is the time (s),  $K_B$  is Boltzmann's coefficient (J/K),  $T$  is the actual temperature (K),  $e$  is the electron charge (C),  $\tau_l$  is the model constant and  $\tilde{u}$  is the terminal velocity of ions (m/s).

The charging model of Lawless (1996) [15] is based on the rate of particle charge being a combination of the field charging rate and the diffusion charging rate, as described by Eq. (3.17) [6]:

$$\frac{dQ_p}{dt} = \begin{cases} \frac{Q_{sat}}{\tau_c} \left( 1 - \frac{Q_p}{Q_{sat}} \right)^2 + \frac{2\pi\alpha\rho_w b K_B T d_p}{e}, & Q_p < Q_{sat} \\ \frac{\alpha}{4\tau_c} (Q_p - Q_{sat}) \exp \left( \frac{e(Q_{sat} - Q_p)}{2\pi\epsilon_o K_B T d_p} \right), & Q_p > Q_{sat} \end{cases} \quad (3.17)$$

where

$$\alpha = \begin{cases} 1 & w < 0.525 \\ \frac{1}{(w+0.457)^{0.575}} & w \geq 0.525 \end{cases} \quad (3.18)$$

$$w = \frac{e d_p}{2 K_B T} |\vec{E}| \quad (3.19)$$

with  $\alpha$  and  $w$  being the model constants. The abovementioned charging equations from Eq. (3.13) to Eq. (3.19) and force-balance equations Eq. (3.10) and Eq. (3.11) were introduced into the STAR-CCM+ computational algorithm through the user defined functions.

### 3.2.3 Simulated ESP geometries

The electrostatic simulation method using OpenFOAM was first validated against the experimental results of Penney and Matick [29], who used a simple wire-plate system that contained four discharge wires. The variation of electric potential distribution between the discharge electrodes and collecting plate was measured and reported while no gas flow was considered [8], which was compared with the numerical modeling results. The specific characteristics of ESP system of Penney and Matick are summarized in Table 3.2.

**Table 3.2:** Specifications of the experimental ESP used by Penney and Matick [29]

Parameter	Value
Wire radius (mm)	0.1524
Wire to plate spacing (mm)	114.3
Wire to wire spacing (mm)	152.4
Applied voltage (kV)	25.5 & 43.5
Number of wires	4

Another ESP system, used in the experimental study of Kihm [13] that also consisted of a simple wire-plate system with eight discharge wires, was also simulated and is illustrated in Fig. 3.1. This particular single-channel ESP system was used as a base-case for further validation of the numerical model, i.e. the combined OpenFOAM and STAR-CCM+ method. Additional simulations were also done with the base geometry while varying the discharge electrode spacing, the collecting electrode to discharge electrode spacing, particle size, gas flow velocity and particle permittivity to investigate the influence of these parameters on collection efficiency. The discharge electrodes were located in the middle of the channel along the positive  $z$ -direction, with the flow of the particle laden gas in the positive  $x$ -direction (Fig. 3.1). The total length of the rectangular ESP channel was 0.75 m with a side length of 0.05 m. The discharge electrodes that were modeled had a diameter of 0.1 mm [7].

The computational domain was discretized into 254900 tetrahedral cells and a prism layer mesher, surface remesher and extruder mesher was used as meshing models in STAR-CCM+ to reduce the number of computational cells as far as possible to speed up simulations. The mesh conditions for discharge electrodes were set separately due to its small diameter. Consequently, the mesh was much finer near the discharge electrodes to maximize the accuracy of the calculated gradients within the higher current density regions.

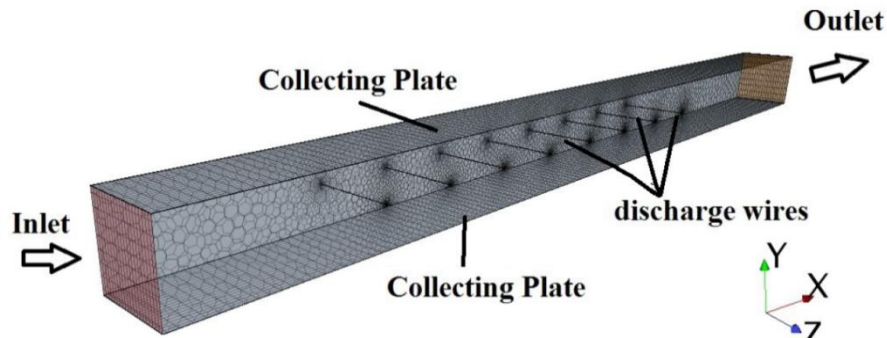


**Fig 3.1:** A 3-D computational model of a single-channel ESP

The boundary conditions for gas flow, electric potential, space charge density and particles coincide with the summary given in Table 3.1. The gas flow was considered to be that of air with a turbulence intensity of 1% at the inlet, which was replicated in the present CFD simulations in which the gas density and viscosity was set equal to  $1.225 \text{ kg/m}^3$  and  $1.8 \times 10^{-5} \text{ kg/m.s}$  respectively. The dust particles were introduced into the computational domain at the inlet to the ESP channel and had a mass density of  $893.5 \text{ kg/m}^3$ , a relative permittivity of 2.5, in accordance with the experiments of Kihm [13]. The particles were further modeled as having a uniform diameter that was varied between 2 and  $10 \text{ }\mu\text{m}$ , and an inlet velocity equal to the operating gas velocity at the inlet, which was assumed to be uniform at  $2 \text{ m/s}$ . These parameters were chosen to replicate the actual experiments of Kihm [13], as was also done by Long and Yao [7]. Further information regarding the experimental parameters used by Kihm [13] is listed in Table 3.3.

**Table 3.3:** Geometric and operational parameters of the experimental ESP setup used in the study of Kihm [13]

Parameter	Value
Length of collection plate	40 cm
Length of upstream extension	10 cm
Length of downstream extension	25 cm
Height of collection plate	5 cm
Spacing between collection & discharge electrode	2.5 cm
Spacing between discharge electrodes	5 cm
Number of wires	8
Diameter of wire	0.1 mm
Gas flow velocity	2 m/s
Supply voltage	6 – 13 kV
Pressure	101.3 kPa
Temperature of gas	293 K
Ion mobility	$2.4 \times 10^{-4} \text{ m}^2/(\text{V s})$
Particles flow rate	$7.49 \times 10^{-10} \text{ kg/s}$
Relative permittivity of particles	2.5
Diameter of particles	$4 \text{ }\mu\text{m}$

Simulations were also done for a single-channel ESP system with a single spike discharge electrode to investigate the effect of discharge electrode geometry on particle collection efficiency. Consequently, ESP operation was simulated with a wire and a spike discharge electrode respectively, while keeping the rest of the single-channel ESP parameters unchanged. The single channel ESP dimensions used for these simulations were as reported in the literature by Podlinski [26], with which experimental data was also obtained. This particular single-channel ESP consisted of two parallel collecting plates and a spike discharge electrode in the middle of channel. The length, width and height of the ESP channel were 600 mm, 200 mm and 100 mm respectively.

The discharge electrode had a series of spikes upstream and downstream to the air flow, and oriented parallel to the air flow. This electrode was 200 mm in length, 1 mm thick, and the tip-to-tip width was 30 mm. Applying a high voltage to the spike electrode resulted in corona discharge at the spike tips. Therefore, the value of the space charge density in between the spike tips was assumed to be zero for the purpose of the simulations. The rest of the boundary conditions used for the simulation of the spike discharge electrode are the same as reported in Table 3.1. The gas flow was considered to be that of air with a velocity of 0.6 m/s at the channel inlet, with a density of  $1.205 \text{ kg/m}^3$  and a viscosity of  $1.57 \times 10^{-5} \text{ kg/m.s}$  [26]. The dust particles injected at the ESP channel inlet had a relative permittivity of 4.0, and a density of  $998.9 \text{ kg/m}^3$  [25]. The three main ESP geometries that were simulated are summarized in Table 3.4 for convenient comparison.

**Table 3.4:** Summary of the experimental ESP's simulated

ESP Geometry	ESP Configuration	Purpose of simulations
Penney & Matick	Single-channel, four discharge wires.	Validate the CFD model w.r.t. the electrostatic field properties.
Kihm	Single-channel, eight discharge wires.	Validate the CFD model w.r.t. the fluid dynamic field, i.e. particle charging & collection efficiencies.
Podlinski	Single-channel, single spike discharge electrode.	Investigate the influence of discharge electrode geometry on EP collection efficiency.

### 3.3 Results and discussion

#### 3.3.1 Electrostatics

The simulated electric potential distribution, space charge density distribution and electrostatic field distribution results corresponding to the experimental system reported by Penney and Matick [29] are shown in Fig. 3.2 (a – c) respectively. It is clear from the figures that the electric potential, electrostatic field and space charge density values are at their respective maxima at the respective points of discharge, i.e. the discharge electrodes, and



decreases towards the collection plates which are at 0 V. As a result, particles that are located within close proximity of the discharge electrodes are more easily (rapidly) charged due to the strong electrostatic field and space charge density near the corona wire.

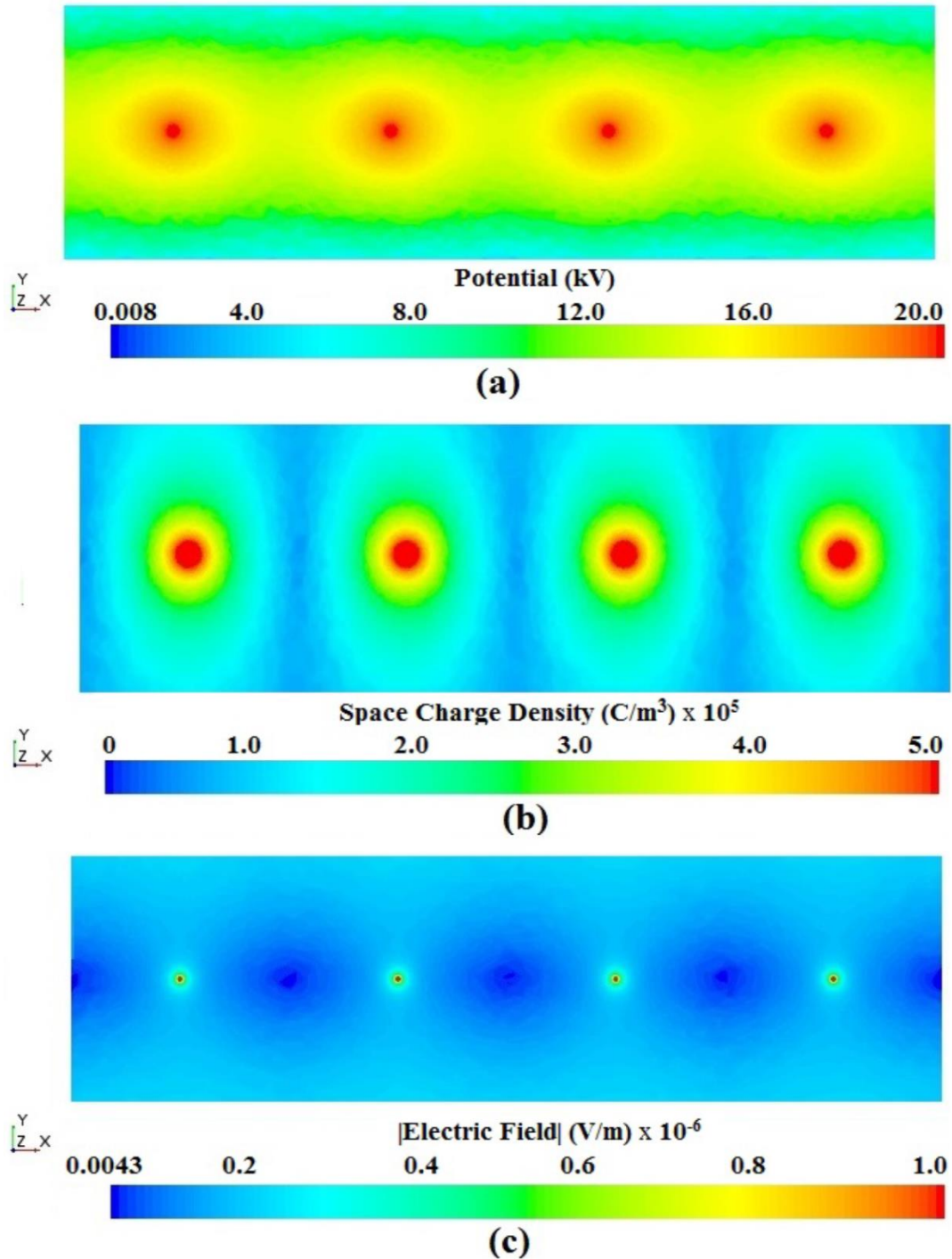


**Fig 3.2:** Distribution of (a) the electric potential (kV), (b) the space charge density, and (c) the electrostatic field magnitude through the ESP channel corresponding to the experimental system of Penny and Matick [29] at  $V = 25.5$  kV.

For quantitative comparison of the OpenFOAM results with the measured results of Penney and Matick [29], the electric potential distribution was measured along the y-direction at a distance of 228.6 mm, 266.7 mm and 304.8 mm in the x-direction for Fig 3.3 (a – c) respectively. The selection of the distance points in the x-direction was done to correspond with the experimental measurements of Penney and Matick, so that the simulation results could be directly compared with the experimental measurements. The results along with comparison with the experimental results reported by Penney and Matick are shown in Fig. 3.3 (a – c). It is clear that the OpenFOAM simulation results agree well with the experimental results [29].

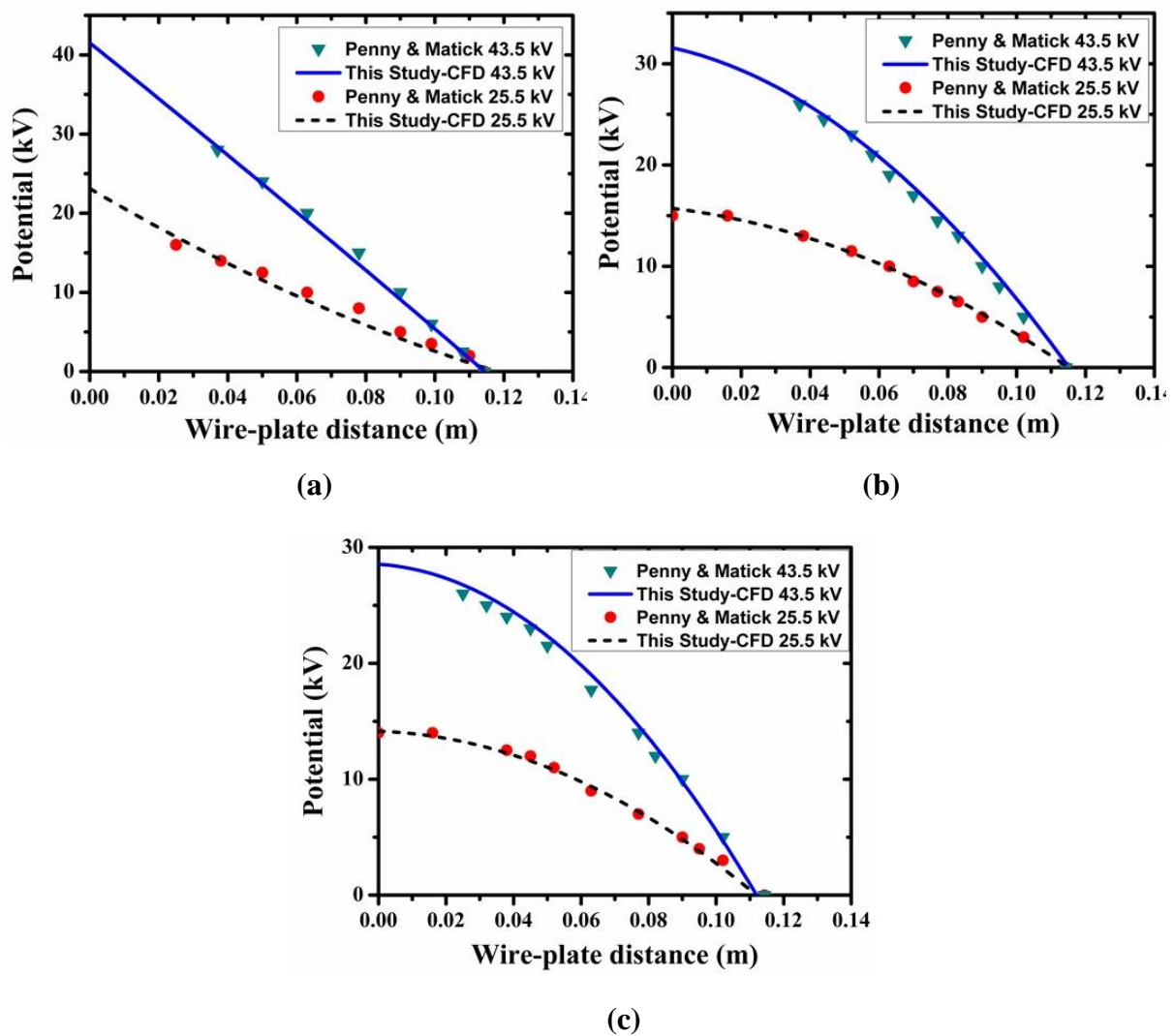


**Fig 3.3:** Comparison of CFD results with the experimental measurements of Penney & Matick at (a)  $x = 228.6$  mm (b)  $x = 266.7$  mm and (c)  $x = 304.8$  mm.

### 3.3.2 Fluid and particle dynamics

Since the OpenFOAM numerical method proved to be effective in yielding an accurate representation of the electrostatic field in an ESP in which no gas flow was present, the next step was to validate the results obtained when coupling the electrostatic field with the fluid and particle dynamics. Therefore, particle trajectories and collection efficiencies were calculated from simulations involving the use of two different particle charging models, namely Pauthenier & Moreau-Hanot (1932) and White and Lawless (1996) [7]. Accordingly, the particle collection efficiencies obtained as a result of STAR-CCM+ simulations, in which the corresponding OpenFOAM electrostatic field results were incorporated, were compared with the experimental results reported by Kihm [13]. The experimental results of Kihm were used to validate the particle charging and collection efficiency predicted with the present CFD model, since the experimental results of Penney and Matick [29] did not include particle collection efficiencies.

By introducing a known number of particles into the computational domain, the collection efficiencies and particles trajectories could be determined. The particles are charged at varying rates as they travel along the ESP channel of the computational domain, depending on their position and are accelerated with varying migration velocities to the collecting plates where they are trapped (escape from the computational domain), while some escape through the outlet. The simulations were done with particles that had diameters of 2, 4, 6, 8 and 10  $\mu\text{m}$  respectively, and in each individual case a total of 361 particles were introduced at the ESP's inlet. The particles were instantaneously injected from a part injector at the inlet to the computational domain, at initial velocities equal to the inlet gas velocity. The collection efficiency was taken as the value obtained when the solution reached convergence, i.e. when the particle collection efficiency for successive particle injections were equal, and the particle trajectories also converged. In all cases, a continuous gas flow was applied [5, 6].

The modeled particle trajectories of the 2, 6, and 10  $\mu\text{m}$  particle simulations with an applied voltage of 9 kV are shown in Fig. 3.4 (a - c) respectively. It is apparent from the results of Fig. 3.4 that the particle collection efficiency increased with increasing particle diameter and therefore larger particles are easier collected when compared to smaller particles. These results therefore qualitatively confirm that the CFD model is capable of reproducing the basic underlying phenomena with respect to ESP operation. The particles are attracted towards the collection plates due to the Coulomb forces acting on them, which in turn is proportional to the charge attained by the particles. The fact that some individual particles followed a steeper trajectory (Fig. 3.4) is due to these particles having attained a higher electrostatic charge when moving past the corona discharge of the first two discharge electrodes. This is because these particles were closer to the first two discharge electrodes when they were charged, and so were in a region of higher charge density compared to the particles above and below them.

As a result, these particles experienced a higher migration velocity, and therefore a steeper trajectory.

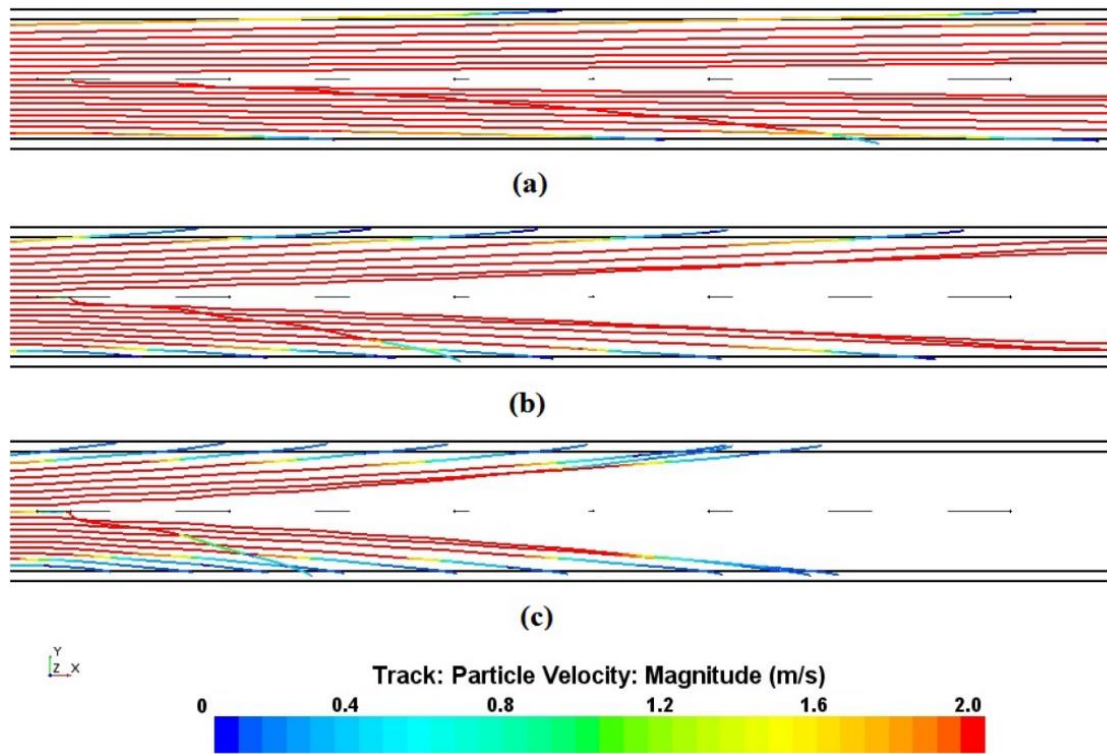


**Fig 3.4:** Simulated trajectories of dust particles through the ESP channel corresponding to Kihm [13] for particles with uniform diameters of respectively (a) 2  $\mu\text{m}$ , (b) 6  $\mu\text{m}$ , and (c) 10  $\mu\text{m}$  at  $V = 9$  kV.

Airflow streamlines for the electrostatic precipitator case of Kihm are presented in Fig. 3.5, where by the effect of electro hydrodynamic (EHD) flow on the air flow was evaluated for linear flow velocity of 0.1 m/s as shown in Fig. 3.5(a). It is clear from the figure that electro hydrodynamic flow is dominant at low flow velocity of 0.1 m/s as indicated by the vortices formed around each wire, although its effects on fluid flow gradually diminishes as the flow velocity is increased from 0.1 to 1 m/s gradually. The close up view in Fig. 3.5(a) shows EHD flow effect between two wires which are at the edges. The two big vortices are formed at the top and bottom of each wire and between the wires swirling motion as well as two small vortices is present. As the velocity of main gas flow is increased from 0.1 m/s to 1 m/s, the vortices at the top and bottom of each wire as well as swirling motion and vortices between wires becomes smaller until they virtually disappear at a gas velocity of 1 m/s as shown in Fig. 3.5(b). Under normal operating conditions the continuous phase velocity inside an ESP typically range between 1 to 2 m/s [1]. Based on the simulation results presented in Fig. 3.5 (b) the effect of electro hydrodynamic flow is therefore minimal [6] under such conditions, and will further diminish as the collecting plate spacing is increased.

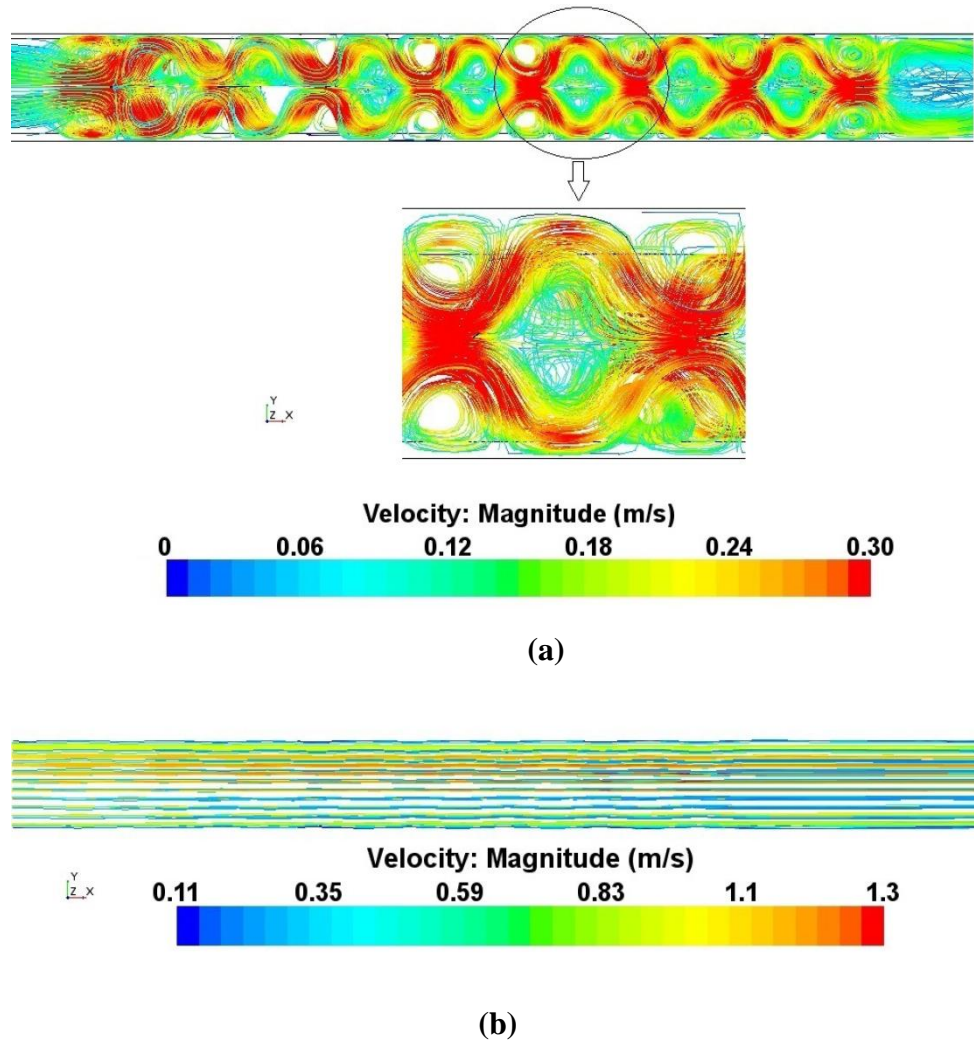


**Fig 3.5:** Air flow streamlines indicating the effects of electro hydrodynamic flow on gas (ion) flow at an inlet velocity of (a) 0.1 m/s, (b) 1 m/s.

### 3.3.3 CFD model validation against previously reported experimental and simulated results

As noted in Section 3.3.2, the collection efficiency was calculated from the number of particles entering and exiting the ESP channel respectively. In addition to the simulations described in Section 3.3.1 and Section 3.3.2, simulations were also performed by varying the electric potential applied at the discharge electrodes, and the results are compared with that of Long and Yao (2010), who also simulated the experimental system described by Kihm. The comparison of the experimental [13] and calculated collection efficiencies using two different charging models are presented in Fig. 3.6 (a) from which it is concluded that the charging model of Pauthenier, Moreau-Hanot & White (PMHW) predicted collection efficiencies that more closely corresponded with the experimental results compared to the charging model of Lawless. A comparison of the simulated collection efficiency results obtained in this study



through the use of the two charging models with the simulation results of Long and Yao [7] using the similar two charging models are presented in Fig. 3.6 (b) & Fig 3.6 (c). From the figures it is clear that the CFD results agreed well with the simulation results of Long and Yao, in addition to the high correlation obtained with the original experimental results. Furthermore, the linear dependence of the collection efficiency on the electric potential is also confirmed. This is a consequence of the increase in the space charge density as the discharge potential is increased. This leads to increased particle charging rate, resulting the particles being accelerated with a higher migration velocity to the collection plates.

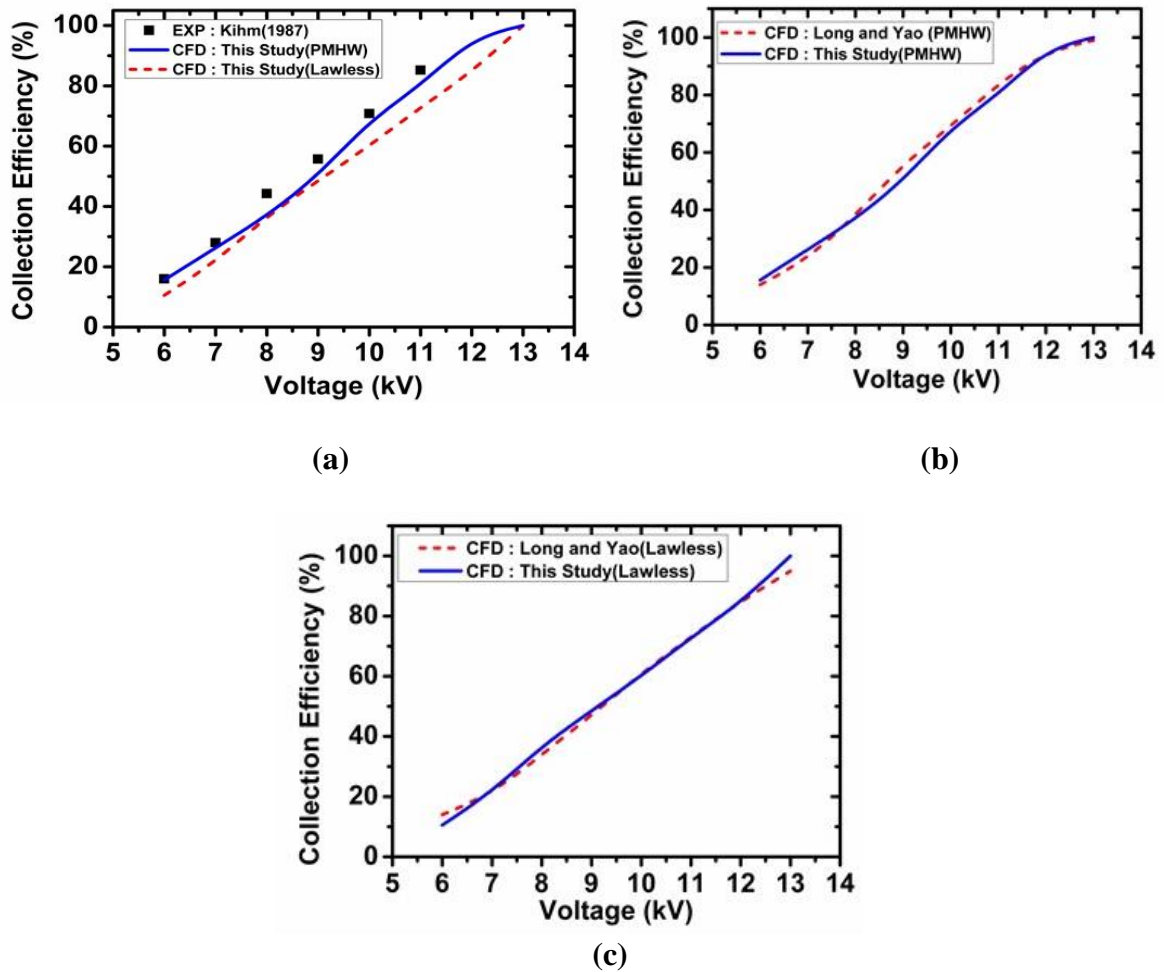


**Fig 3.6:** Comparison between the particle collection efficiency predicted by the current CFD model and (a) experimental results (Kihm, 1987), and the simulation results of Long and Yao (2010) using (b) the PMHW charging model, and (c) the Lawless charging model.

### 3.3.4 The effect of varying ESP geometry and operating parameters on collection efficiency

Since favorable correlations were obtained between the collection efficiencies calculated from the simulation results and the previously reported experimental results (Kihm, 1987), the model was applied as a first step in quantifying the effects of various geometric and

operating parameters on ESP collection. The effect of varying particle diameter and inlet velocity on the collection efficiency of dust particles is shown in Fig. 3.7 (a) and Fig. 3.7 (b). It is clear from Fig. 3.7 (a) that collection efficiency increases in accordance with the results of Fig. 3.4 as the diameter of the particles increases. On the other hand, the results of Fig 3.7 (b) indicate that the collection efficiency decreases with increasing inlet velocity and is due to the fact that an increase of fluid velocity results in a decrease in the residence time of the particles in the ESP channel. A reduced residence time in turn results in a smaller charging rate of the particles, which also leads to a reduction in their individual migration velocities. It is also depicted from Fig. 3.7 (b) that as the applied voltage on discharge electrode is increased from 8 kV to 10 kV the velocity above which the collection efficiency starts dropping significantly below 90% is also increased. Also, by increasing the velocity from 0.5 m/s to 1 m/s the decrease in collection efficiency is more significant if the applied voltage is 8 kV as compared to other plots where applied voltages are higher.

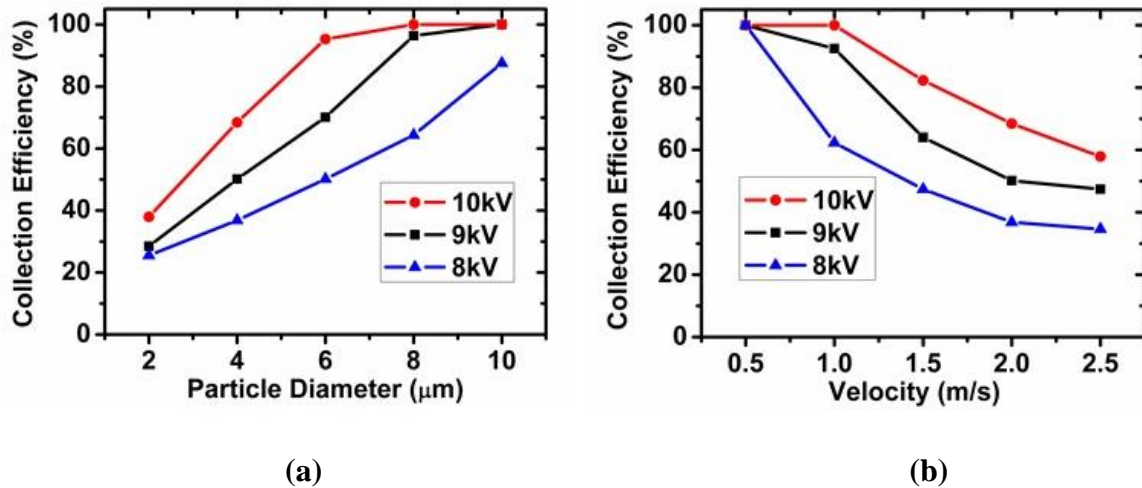


**Fig 3.7:** The effect of (a) varying particle diameter and (b) varying inlet velocity on particle collection efficiency for various discharge electrode potentials.

Using the basic ESP design as described in Section 3.3.2, the relative influence of various geometric and operating variables was further investigated. The results of collection efficiency vs. varying wire-to-plate spacing, and a varying number of discharge electrodes are shown respectively in Fig. 3.8 (a) and Fig. 3.8 (b). As is clear from Fig. 3.8 (a), the collection efficiency was predicted to decrease with an increase in the wire-to-plate spacing, which can be explained in terms of the reduced space charge density close to the collecting plates that in turn results in reduced force of attraction being experienced by particles that are further away from the discharge electrode. Further, as the number of discharge wires increased, the collection efficiency was predicted to increase as shown in Fig 3.8 (b). This is due to an increase in the number of discharge electrodes leading to the creation of a more uniform space charge density distribution, which enhances the charging rate of the dust particles.

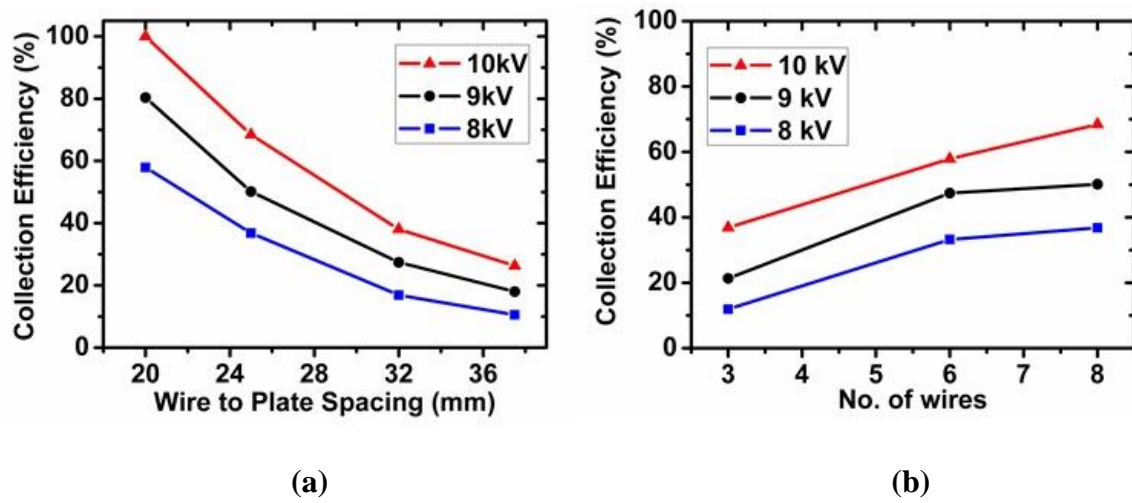


**Fig 3.8:** The effect of (a) variable collection plate to discharge electrode spacing, and (b) the number of discharge wires on particle collection efficiency at different discharge electrode potentials.

While the ESP operating variables and dimensions clearly have a significant influence on collection efficiency, the properties of the ash particles also play a significant role with regards to the efficiency with which the particles accept an electrical charge [30], and therefore also directly influences the collection efficiency. Particles with a larger relative permittivity are easily charged as they travel through the channel and are more readily collected, while those with lower relative permittivity values are more resistant to electrostatic charging thus not collected as efficiently as shown in Fig. 3.9.

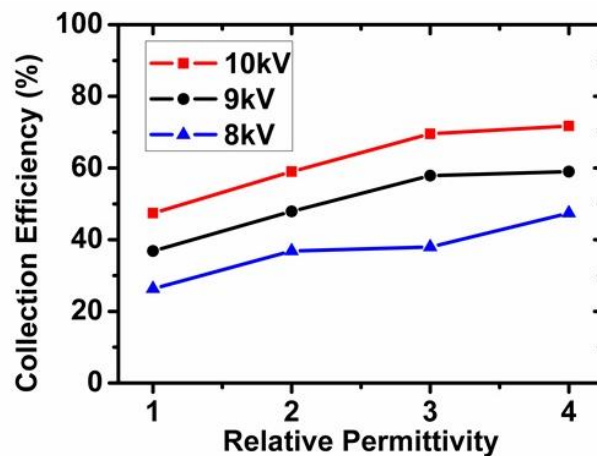


**Fig 3.9:** The effect of relative permittivity of dust particles on ESP collection efficiency at different applied voltages.



### 3.3.5 Effect of discharge electrode geometry

The numerical results of space charge density distribution with the spike discharge electrode ESP of Podlinski [26] are shown in Fig. 3.10(a) for an applied voltage of 19.2 kV. It is apparent from Figure 3.10 that the spike tips yield a high localized space charge density. In comparison, the space charge density distribution for a wire discharge electrode (Fig. 3.10(b)) is uniform along the length of the discharge wire. However, it is also clear that a maximum space charge density that is roughly one order of magnitude larger is attained with the spike discharge electrode compared to the wire discharge electrode. As a result, the space charge density is also larger near the collecting electrodes for the spike electrode relative to that attained with the wire electrode.

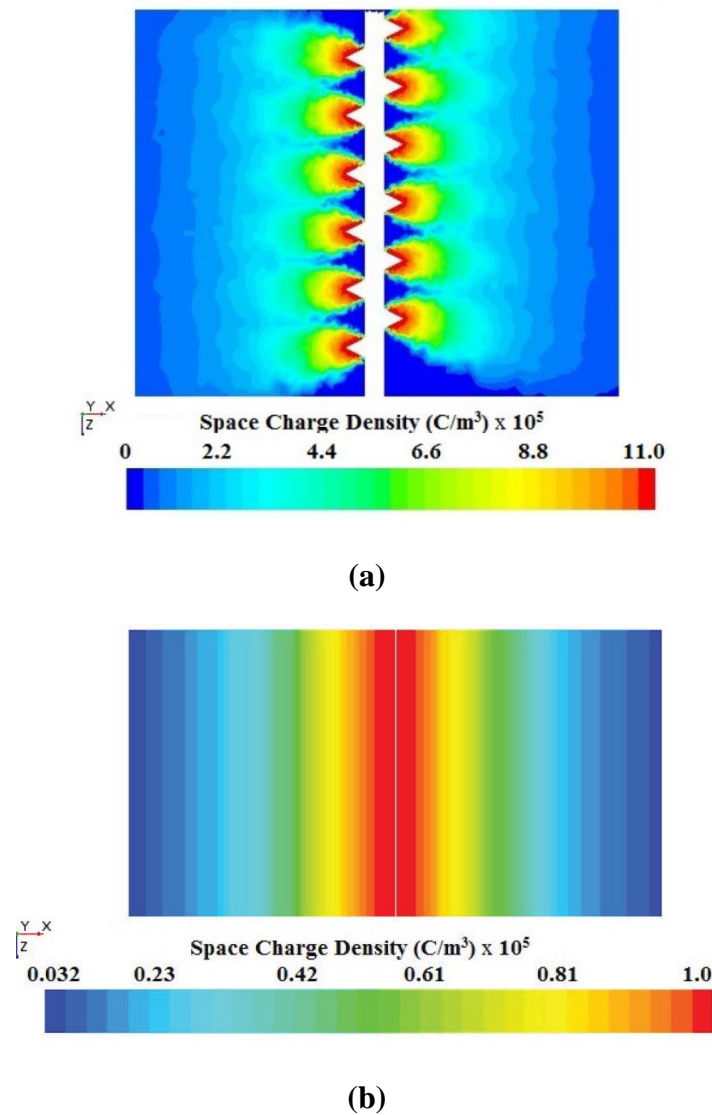


**Fig 3.10:** Simulated distribution of the space charge density for (a) a spike discharge electrode, and (b) a wire discharge electrode in an ESP channel corresponding to the experimental system of Podlinski [26]. The discharge potential in both cases was 19.2 kV.

A known number of particles of 1  $\mu\text{m}$  diameter were released at the channel inlet into the computational domain to determine the particle collection efficiencies. The simulations were carried out with discharge electrode potentials of 19.2 kV, 23.5 kV, 27.5 kV and 30 kV. The computational results that were obtained are compared with the experimental results as reported by Podlinski [26] in Fig. 3.11(a). It is clear that the current CFD model underestimated the collection efficiencies compared to the experimental measurements, which was also noted by Farnoosh et al. [25] when their CFD results for a spike discharge electrode were compared to experimental results.

The performance of the ESP operation with a wire discharge electrode (1 mm diameter) was also simulated while keeping all other parameters unchanged, and the collection efficiency results are compared to those obtained with the spike discharge electrode as shown in Fig. 3.11(b). It is clear that significantly higher collection efficiencies were predicted for the spike discharge electrode, in accordance with the higher space charge densities that are produced by the spike electrode (Fig. 3.10).

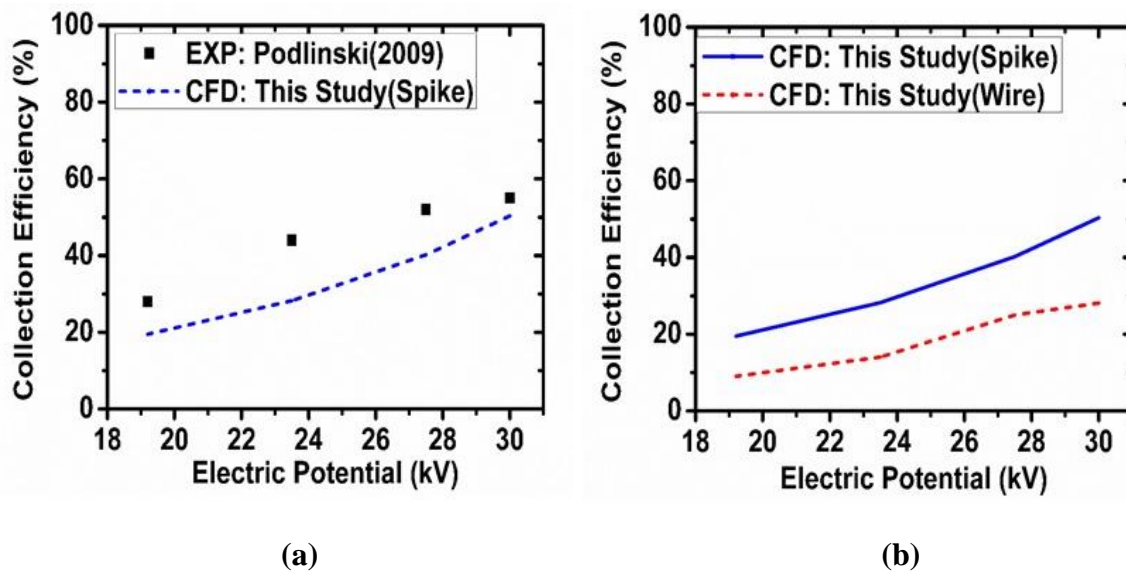


**Fig 3.11:** Comparison between (a) the particle collection efficiency predicted by the current CFD model and the corresponding experimental results of Podlinski [26] obtained with a spike discharge electrode. Figure (b) represents a comparison between the collection efficiency predicted for spike and wire discharge electrodes using the current CFD model.

### 3.4 Conclusions

A simple numerical method was presented in which direct solution of the drift and diffusional ion flux that governs the charge distribution throughout the ESP channel was achieved with the use of OpenFOAM. By coupling the OpenFOAM results with the commercial STAR-CCM+ CFD code, the modeling results were found to correlate well with previously published experimental results, yielding an accurate and effective framework for modeling electrostatic precipitation. No additional numerical techniques are required with the present

method, and by combining the strengths of both the open source and the commercial software it is possible to accurately describe the interaction between the complex electrostatic, particle dynamic, and fluid dynamic fields from first principles. This yields a convenient CFD modeling method that can be used to gain further insight into ESP operation.

Accordingly, it was shown that the model allows convenient quantification of the influence of geometric variables such as collector plate spacing, discharge electrode spacing, discharge electrode design and the influence of electrostatic properties such as the particle permittivity on collection efficiency. The simulation results predicted that a spike discharge electrode would yield significantly higher particle collection efficiencies than a normal wire-type discharge electrode. Therefore, quantifying the influence of particle permittivity, in addition to geometric variables such as discharge electrode design, and operational variables on ESP efficiency for the purpose of maximizing particulate removal from industrial flue gases is currently being further investigated.

### **3.5      Supplementary data**

Supplementary data related to this chapter explaining effect of air flow velocity on electrostatic properties can be found in appendix A while additional computational results regarding sensitivity analysis of spike discharge electrode can be found in appendix D of the thesis.

### **3.6      References**

- [1] H.J. White, Electrostatic Precipitation Of Fly Ash, J. Air Pollut. Control Assoc. 27 (1977) 15–22. doi:10.1080/00022470.1977.10470386.
- [2] A. Soldati, On the effects of electrohydrodynamic flows and turbulence on aerosol transport and collection in wire-plate electrostatic precipitators, J. Aerosol Sci. 31 (2000) 293–305. doi:10.1016/S0021-8502(99)00055-5.
- [3] S.H. Kim, H.S. Park, K.W. Lee, Theoretical model of electrostatic precipitator performance for collecting polydisperse particles, J. Electrostat. 50 (2001) 177–190. doi:10.1016/S0304-3886(00)00035-8.
- [4] S. Kim, K. Lee, Experimental study of electrostatic precipitator performance and comparison with existing theoretical prediction models, J. Electrostat. 48 (1999) 3–25. doi:10.1016/S0304-3886(99)00044-3.
- [5] G. Skodras, S.P. Kaldis, D. Sofialidis, O. Faltsi, P. Grammelis, G.P. Sakellaropoulos, Particulate removal via electrostatic precipitators - CFD simulation, Fuel Process. Technol. 87 (2006) 623–631. doi:10.1016/j.fuproc.2006.01.012.
- [6] N. Farnoosh, K. Adamiak, G.S.P. Castle, 3-D numerical analysis of EHD turbulent flow and mono-disperse charged particle transport and collection in a wire-plate ESP, J. Electrostat. 68 (2010) 513–522. doi:10.1016/j.elstat.2010.07.002.

- [7] Z. Long, Q. Yao, Evaluation of various particle charging models for simulating particle dynamics in electrostatic precipitators, *J. Aerosol Sci.* 41 (2010) 702–718. doi:10.1016/j.jaerosci.2010.04.005.
- [8] M. Feldkamp, M. Dickamp, C. Moser, Electrostatic Precipitation: 11th International Conference on Electrostatic Precipitation, Hangzhou, 2008, in: K. Yan (Ed.), Springer Berlin Heidelberg, Berlin, Heidelberg, 2009: pp. 141–150. doi:10.1007/978-3-540-89251-9\_30.
- [9] N. Neimarlija, I. Demirdžić, S. Muzaferija, Finite volume method for calculation of electrostatic fields in electrostatic precipitators, *J. Electrostat.* 67 (2009) 37–47. doi:10.1016/j.elstat.2008.10.007.
- [10] N. Farnoosh, K. Adamiak, G.S.P. Castle, Three-dimensional analysis of electrohydrodynamic flow in a spiked electrode-plate electrostatic precipitator, *J. Electrostat.* 69 (2011) 419–428. doi:10.1016/j.elstat.2011.06.002.
- [11] F.J. Gutiérrez Ortiz, B. Navarrete, L. Cañadas, Assessment of plate-wire electrostatic precipitators based on dimensional and similarity analyses, *Fuel*. 90 (2011) 2827–2835. doi:10.1016/j.fuel.2011.04.006.
- [12] Q. Liu, S. song Zhang, J. pei Chen, Numerical analysis of charged particle collection in wire-plate ESP, *J. Electrostat.* 74 (2015) 56–65. doi:10.1016/j.elstat.2014.11.007.
- [13] K.D. Kihm, Effects of nonuniformities on particle transport in electrostatic, 1987.
- [14] J.L. Davis, J.F. Hoburg, Wire-duct precipitator field and charge computation using finite element and characteristics methods, *J. Electrostat.* 14 (1983) 187–199. doi:10.1016/0304-3886(83)90006-2.
- [15] P.A. Lawless, Particle charging bounds, symmetry relations, and an analytic charging rate model for the continuum regime, *J. Aerosol Sci.* 27 (1996) 191–215. doi:10.1016/0021-8502(95)00541-2.
- [16] T. Iváncsy, J.M. Suda, Behavior of polydisperse dust in electrostatic precipitators, *J. Electrostat.* 63 (2005) 923–927. doi:10.1016/j.elstat.2005.03.062.
- [17] S.M.E. Haque, M.G. Rasul, A.V. Deev, M.M.K. Khan, N. Subaschandar, Flow simulation in an electrostatic precipitator of a thermal power plant, *Appl. Therm. Eng.* 29 (2009) 2037–2042. doi:10.1016/j.applthermaleng.2008.10.019.
- [18] N. Farnoosh, K. Adamiak, G.S.P. Castle, 3-D numerical simulation of particle concentration effect on a single-wire ESP performance for collecting poly-dispersed particles, *IEEE Trans. Dielectr. Electr. Insul.* 18 (2011) 211–220. doi:10.1109/TDEI.2011.5704512.
- [19] Z.M. Al-Hamouz, A combined algorithm based on finite elements and a modified method of characteristics for the analysis of the corona in wire-duct electrostatic precipitators, *Ind. Appl. IEEE Trans.* 38 (2002) 43–49. <http://ieeexplore.ieee.org/ielx5/28/21119/00980343.pdf?tp=&arnumber=980343&isnumber=21119>.

- [20] Z. Lin, K. Adamiak, Numerical Simulation of the Electrohydrodynamic Flow in a Single Wire-Plate Electrostatic Precipitator, *Ind. Appl. IEEE Trans.* 44 (2008) 683–691. doi:10.1109/TIA.2008.921453.
- [21] A.A. Elmoursi, G.S. Peter Castle, Modeling of corona characteristics in a wire-duct precipitator using the charge simulation technique, *IEEE Trans. Ind. Appl.* IA-23 (1987) 95–102. doi:10.1109/TIA.1987.4504872.
- [22] P.L. Levin, J.F. Hoburg, Donor cell-finite element descriptions of wire-duct precipitator fields, charges, and efficiencies, *Ind. Appl. IEEE Trans.* 26 (1990) 662–670. doi:10.1109/28.55991.
- [23] J. Anagnostopoulos, G. Bergeles, Corona discharge simulation in wire-duct electrostatic precipitator, *J. Electrostat.* 54 (2002) 129–147. doi:10.1016/S0304-3886(01)00172-3.
- [24] K. Luo, Y. Li, C. Zheng, X. Gao, J. Fan, Numerical simulation of temperature effect on particles behavior via electrostatic precipitators, *Appl. Therm. Eng.* 88 (2014) 127–139. doi:10.1016/j.applthermaleng.2014.11.078.
- [25] N. Farnoosh, K. Adamiak, G.S.P. Castle, Numerical calculations of submicron particle removal in a spike-plate electrostatic precipitator, in: *IEEE Trans. Dielectr. Electr. Insul.*, 2011: pp. 1439–1452. doi:10.1109/TDEI.2011.6032814.
- [26] J. Podlinski, A. Niewulis, J. Mizeraczyk, Electrohydrodynamic flow and particle collection efficiency of a spike-plate type electrostatic precipitator, *J. Electrostat.* 67 (2009) 99–104. doi:10.1016/j.elstat.2009.02.009.
- [27] CD-ADAPCO, User Guide STAR CCM+ V. 9.02, (2014) 4482–4484.
- [28] A. Haider, O. Levenspiel, Drag coefficient and terminal velocity of spherical and nonspherical particles, *Powder Technol.* 58 (1989) 63–70. doi:10.1016/0032-5910(89)80008-7.
- [29] G.W. Penney, R.E. Matick, Potentials in D-C corona fields, *Trans. Am. Inst. Electr. Eng. Part I Commun. Electron.* 79 (1960) 91–99. doi:10.1109/TCE.1960.6368550.
- [30] R.A. Fjeld, D. Wu, A.R. McFarland, The dielectric constant and particle charging calculations, in: *Ind. Appl. Soc. Annu. Meet. 1990.*, Conf. Rec. 1990 IEEE, 1990: pp. 761–765 vol.1. doi:10.1109/IAS.1990.152271.
- [31] OpenFOAM. (2014). User Guide (2nd ed.). OpenCFD Ltd.

## **Chapter 4. THE INFLUENCE OF DESIGN PARAMETERS ON THE OCCURRENCE OF SHIELDING IN MULTI-ELECTRODE ESPs AND ITS EFFECT ON PERFORMANCE**

This chapter is based on the following publication: S. Arif, D.J. Branken, R.C. Everson, H.W.J.P. Neomagus, A. Arif, The influence of design parameters on the occurrence of shielding in multi-electrode ESPs and its effect on performance, J. Electrostat. 93 (2018). p. 17 – 30. doi: 10.1016/j.elstat.2018.03.001.

### **Abstract**

A numerical model in which OpenFOAM® is used to model the electrostatic field resulting from corona discharge in single-channel wire-plate electrostatic precipitators (ESPs) was applied to systematically study the shielding effect that can arise between adjacent discharge electrodes. It is shown that the OpenFOAM model is capable of accurately quantifying the extent of shielding, and that the degree of shielding is predicted to increase as the spacing between the cylindrical discharge electrodes are decreased. This increase in the degree of shielding consequently resulted in a reduction of the discharge current. The numerical model was also used to quantify the effect of various other ESP parameters on the degree of shielding by studying the space charge density and current density distributions, and the plate-to-plate spacing was found to be the most influential parameter. By incorporating the electrostatic field obtained from the OpenFOAM model in a CFD model based in Star-CCM+®, it is further shown that a decrease in particle collection efficiency is predicted to occur when the shielding intensity increases. Such a systematic study to quantify the extent of shielding and its effect on ESP performance in terms of particle collection efficiency has not received much attention in the literature to date. Predicting the incidence and extent of shielding as a function of geometric ESP parameters are also invaluable to avoid laboratory or pilot scale results that are biased because of the occurrence of shielding.

**Key words:** *Numerical ESP model, Electrostatic precipitator (ESP), Shielding effect, Space charge density, Current density, Particle collection efficiency.*

## 4.1 Introduction

Electrostatic precipitators (ESPs) are still widely used for the removal of particulate matter (PM) from industrial gas streams since these units offers advantages such as long service life, low maintenance requirements, excellent reliability, and relatively flexible operation compared to fabric filter units [1]. Increasingly stringent environmental legislation that governs point-source gaseous and PM emissions from industrial stacks necessitates regular upgrading and improvement of the design and operation of emissions abatement units, and particularly that of ESPs. This is specifically significant in developing countries such as India and South Africa, where the costly retrofit of existing ESPs to fabric filter units is undesirable [1]. Since optimally designed and operated ESPs can deliver PM collection efficiencies that are comparable to that which is routinely obtained using fabric filter units, improving existing ESP performance by the implementation of design and process control modifications are more financially attractive. Detailed three-dimensional numerical modeling combined with CFD modeling can be an invaluable tool in this regard, i.e. to study ESP processes and to formulate scalable process models and improvement strategies. Although such numerical models need to be extensively validated against measurements, it can also be applied to gain deeper insight into the underlying principles that govern ESP performance, which is not easily feasible with an empirical approach. Consequently, numerical modeling of ESP processes have gained significant attention during the last few years [2].

To date, numerical modeling studies of ESP processes have mainly focused on the solution of the governing equations involving the complex corona discharge for small laboratory-scale ESPs using methods such as the finite element (FEM)-method of characteristics (MoC) [3,4], the FEM-boundary element method (BEM)-MoC [5], the FEM-charge simulation method (CSM) [6], the FEM-donor cell method (DCM) [7], and the finite difference method (FDM)-MoC [8]. Other CFD studies have focused on modeling the gas flow through multi-plate industrial-scale ESPs to analyze and improve the gas flow distributions through the ESP while neglecting the electrostatic field and particle dynamics [9,10]. Modeling of the electrostatic field along with fluid and particle dynamics has also been performed, but due to the complexity of describing the three interacting fields, such models are typically applied only to single-channel, single discharge electrode ESP systems [11,12], or single-channel multi-electrode ESP systems [13]. Additionally, simple cylindrical discharge electrodes (wires) were modeled in the majority of studies, while only a few studies have reported on modeling of the corona discharge produced by more sophisticated discharge electrodes such as simple spike-electrodes [14–16]. Modeling of the particle collection efficiency in single-channel wire-plate ESP systems as a function of parameters such as the discharge electrode voltage, the number of discharge electrodes, and the collection plate spacing have subsequently also been reported along with comparisons between the model predictions [16,17] and the experimental results [17–21].

One way of increasing the particle charging rate and therefore the particle collection efficiency is by increasing the discharge (corona) current ( $I$ ) achieved under a specific applied discharge electrode voltage ( $V$ ). This may be accomplished by changing the discharge electrode design [16], or by increasing the number of discharge electrodes per ESP channel. However, when studying the effect of the number of discharge electrodes on particle collection efficiency, Kasdi [21], who reported on the V-I characteristics of single channel, multi-wire electrode ESP systems both experimentally and numerically, found that the discharge current from adjacent discharge wires are suppressed by each another under certain conditions. More specifically, it was found that the current density at the collecting plate surface opposite to the inner discharge wire-electrodes were lower compared to the current density on the collecting plate surface opposite to the outer discharge electrodes [21–23]. The cumulative effect of this phenomenon was a reduction in the total corona current when decreasing the electrode-to-electrode spacing beyond a certain threshold. Al Hamouz et al. [24], and Abdel-Salam and Eid [25] also reported such a loss in the corona current when studying the performance of small-scale wire-plate ESPs as a function of the discharge electrode-to-electrode spacing for wire-electrodes, the wire-electrode radii, and electrode-to-plate spacing using experimental measurements and numerical modeling techniques. Similar to the results of Kasdi [21], the reduction in the current density at the collecting plate surface corresponding to the position of the inner wire-electrode relative to that of the two outer wire-electrodes in the various three-electrode, single channel ESPs studied by Al Hamouz et al. [24], and Abdel-Salam and Eid [25] was also noted. This phenomenon of reduction of the corona discharge current of the inner electrodes in a multi-electrode ESP is colloquially referred to as shielding, and its influence has usually been neglected in most numerical modeling studies. Also, the potential effect that shielding can have on the particle collection efficiency has not yet been described to date.

This paper is aimed at addressing this shortcoming, and therefore a previously validated 3-D numerical model [16] was used to further study the shielding effect that can arise between adjacent electrodes in multi-electrode ESP systems. The ability of the previously published numerical model [16] to accurately describe the current loss under shielding conditions was verified by comparison with the experimental results of Kasdi [21], Long and Yao [13], and Lawless [26]. Consequently, the shielding of adjacent cylindrical wire-electrodes is systematically studied by analyzing the space charge density profiles, the current density profiles, and the V-I characteristics under a varying number of discharge electrodes, varying electrode-electrode spacing, varying plate-to-plate spacing, and varying discharge electrode voltage in a single-channel multi-electrode ESP system. By coupling the results of the electrostatic OpenFOAM® model with a CFD model based in Star-CCM+®, the effect of shielding on the particle trajectories and particle collection efficiency is also analyzed. Although all simulations were performed using 3-D models, only the two-dimensional analyses (at  $z = 0$ ) of the space charge density and current density profiles are presented in this paper, as the profiles did not vary considerably along the length of the wire-electrodes.



## 4.2 Numerical modeling and solution methods

The open source code, OpenFOAM® [27], was used to solve the governing equations for the electrostatic field arising due to corona discharge, and the output was imported in the form of user-defined field functions into the commercial CFD software package STAR-CCM+® [28] that was used to solve the transport equations for the continuous phase, and dispersed phase. Particle charging was also modeled using user-defined functions in Star-CCM+.

The governing equations used for modeling the electrostatic field, the continuous phase fluid dynamics, the particle dynamics, and particle charging as well as boundary conditions are summarized in Table G-1 and Table G-2 of the appendix G. A detailed description of the composite model may be found in a previously published paper [16]. To simulate the independent corona discharge of each individual discharge electrode, and thus to describe the shielding effect, the boundary conditions for the electrostatic field and the space charge density were defined for each individual electrode independently. Each discharge electrode was thus defined as an individual boundary. The differentiation between the discharge characteristics of each individual wire-electrode was further achieved by adopting Kaptzov's hypothesis and iteratively adjusting the surface space charge density of each wire-electrode, followed by calculation of the electrostatic field magnitude at each electrode's surface until the values converged (tolerance was set at 0.5%) with the value calculated using Peek's formula (Table A-1). The surface space charge density of each wire-electrode was further assumed to be constant over the wire-electrode surface, which was further subject to the charge conservation criteria.

### 4.2.1 Simulated ESP geometries

#### 4.2.1.1 Validation of numerical model using literature data

The corona current and current density distributions at the collector plate were validated against the published experimental measurement results of Kasdi [21], in which a simple wire-plate ESP system with three cylindrical discharge wire-electrodes was used. In the work of Kasdi [21], the current density distributions at the collecting plate was measured and reported while no gas flow was present, and was used in this paper for comparison with the numerical modeling results. The model results for current density at the collecting plates were further validated against the experimental measurement results of Lawless [26], which also consisted of a wire-plate ESP system without gas flow. Additionally, the numerical modeling results for corona current per unit wire length were also compared with modeling results reported by Long and Yao [13]. In the experimental results reported by Kasdi [21], shielding was shown to be present and was also accounted for in the subsequent numerical modeling, while no mention was made of shielding in the experimental results of Lawless [26], nor in the numerical modeling results presented by Long and Yao [13]. In modeling of the latter two cases in this paper for comparative purposes, shielding was also not taken into consideration. Based on the results reported in this paper regarding the relationship between the degree of

shielding and the electrode-to-electrode and plate-to-plate spacing, it is likely that shielding would have been negligible in these two cases. Therefore, for validation of the current model's ability to describe the shielding effect, the results of Kasdi [21] was used, while the results of Lawless [26] and Long and Yao [13] was used to first validate the current model w.r.t. describing the V-I characteristics of multi-electrode ESPs. The characteristics of the ESP systems used for these validations and comparisons are summarized in Table 4.1.

**Table 4.1:** Specifications of the single-channel wire-electrode ESPs used for validation

Parameter	Lawless [26]	Long and Yao [13]	Kasdi [21]
Wire radius	1.59 mm	0.05 mm	0.2 mm
Wire to plate spacing	114 mm	25 mm	50 mm
Wire to wire spacing	228 mm	50 mm	60 mm
Discharge electrode voltage	42.5-60 kV	6-13 kV	16-26 kV
Number of wire electrodes	5	8	3
Ion mobility	$1.82 \times 10^{-4} \text{ m}^2/(\text{V s})$	$1.6 \times 10^{-4} \text{ m}^2/(\text{V s})$	$1.8 \times 10^{-4} \text{ m}^2/(\text{V s})$

#### 4.2.1.2 Computational model used for evaluation of shielding

Following the validation of the numerical model using the case studies from literature (Table 4.1), the effect of various dimensional parameters on the degree of shielding, the current density profiles, and the space charge density profiles were studied using a single-channel multi-electrode ESP system with a fixed plate height and length that differed from the geometries used for validation (Table 4.1). A representative illustration of this single-channel multi-electrode ESP is shown in Fig. 4.1, and it was subsequently also applied to study the effects of shielding on the particle collection efficiency as a function of the ESP dimensions and other operating parameters. In this particular ESP geometry (Fig. 4.1), the discharge wire-electrodes are located in the middle of the channel along the positive  $z$ -direction, with the flow of the particle laden gas in the positive  $x$ -direction. The length of the collecting plates was fixed at 753 mm, while their height was fixed at 376 mm. The simulated discharge electrodes had a radius of 1.2 mm. The computational domain was discretized into tetrahedral cells and a prism layer mesher, surface remesher and extruder mesher was used as meshing models in STAR-CCM+ to reduce the number of computational cells as far as possible. The appropriate meshing conditions that yielded mesh-independent solutions were determined by carrying out simulations with different meshing conditions and monitoring the resulting effect on parameters such as the particle collection efficiencies. The number of cells varied between 158700 and 264343 depending on the number of wires used and the distance between collection plates, both of which were varied. The mesh conditions for the discharge electrodes were set separately due to its small diameter. Consequently, the mesh was much finer near the discharge electrodes to maximize the accuracy of the calculated gradients within the higher current density regions.

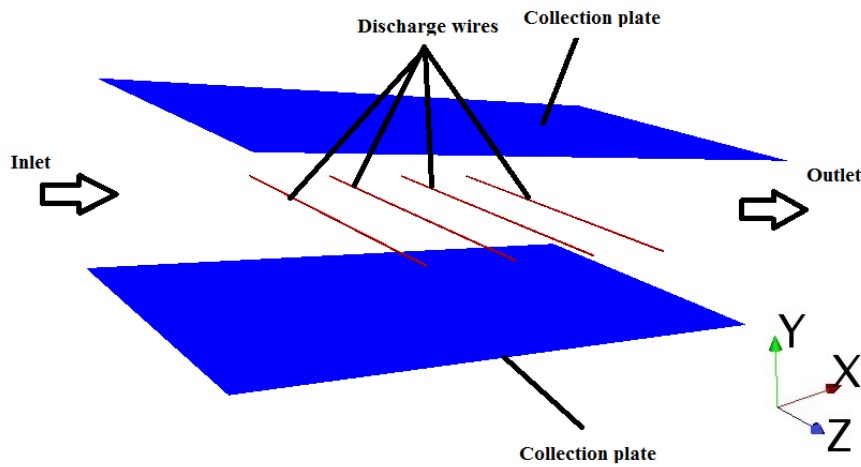


**Fig 4.1:** 3-D computational model of a single-channel ESP

The boundary conditions for gas flow, electric potential, space charge density and particles are summarized in Table G-2 of the appendix G. The gas flow was simulated using air as the continuous phase (the gas density and viscosity was set to  $1.225 \text{ kg/m}^3$  and  $1.8 \times 10^{-5} \text{ kg/m.s}$  respectively) with a turbulence intensity of 1% at the ESP inlet. The dust particles were introduced into the computational domain at the inlet to the ESP channel and had a density of  $893.5 \text{ kg/m}^3$ , and a relative permittivity of 2.5. The particles were further modeled as having a uniform diameter of  $1\text{-}5 \text{ }\mu\text{m}$ , and an inlet velocity equal to the operating gas velocity at the inlet, which was assumed to be uniform at  $1 \text{ m/s}$ . Further details regarding the geometric and operational parameters used in this study with the single-channel ESP (Fig. 4.1) are listed in Table 4.2.

**Table 4.2:** Geometric and operational parameters of the ESP setup used in this study

Parameter	Value
Length of collection plate	75.3 cm
Height of collection plate	37.6 cm
Spacing between collection and discharge electrode	5,8 and 11 cm
Spacing between discharge electrodes	5 cm - 17.5 cm
Number of wires	3 - 8
Wire radius	1.2 mm
Gas flow velocity	1 m/s
Discharge electrode voltage	30 – 55 kV
Pressure	101.3 kPa
Temperature of gas	293 K
Ion mobility	$2.4 \times 10^{-4} \text{ m}^2/(\text{V s})$
Particles flow rate	$7.49 \times 10^{-10} \text{ kg/s}$
Relative permittivity of particles	2.5
Diameter of particles	$1\text{-}5 \text{ }\mu\text{m}$

### 4.3 Results and discussion

Apart from model validation results using three sets of literature data, the effect of varying wire-to-wire spacing, plate-to-plate spacing, number of discharge wires and applied discharge electrode voltage on the intensity of shielding is reported. Subsequently, the relative influence of the shielding effect, as a function of the abovementioned parameters, on the particle collection efficiency is also reported using the previously validated CFD model [16].

Although the results of all parameter variations, as summarized in Table 4.2, are not shown in this paper, a few representative cases were identified of which representative results are discussed in the subsequent sections.

#### 4.3.1 CFD model validation

The simulation results for current density at the collecting plate surface (calculated as the average value across the collecting plate surface corresponding to a particular discharge electrode voltage) as compared with the experimental results of Lawless [26] are shown in Fig. 4.2, and the corona current per unit wire length computed using the present numerical model compared to the modeling results of Long and Yao [13] are shown in Fig. 4.3. In both cases, good agreement with the literature data was obtained.

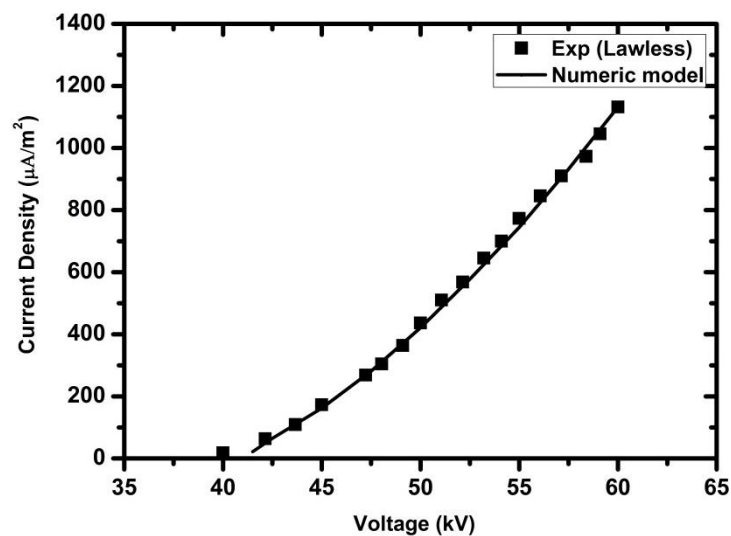


**Fig 4.2:** Comparison of current density at the collecting plate surface computed with present CFD model and experimental results by Lawless [26]

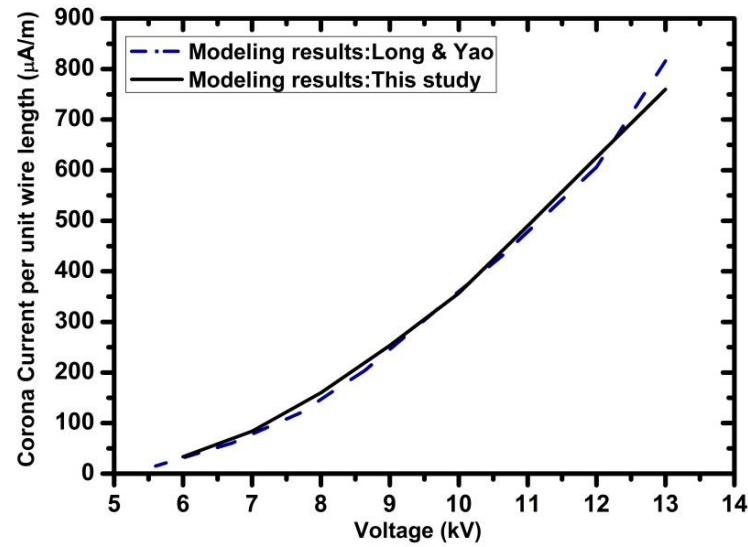


**Fig 4.3:** The corona current per unit wire length computed using the present numerical model, compared to the numerical modeling results of Long and Yao [13].

The electrostatic (OpenFOAM) model was further validated against the experimental results obtained by Kasdi [21] by comparing the corona current ( $I$ ) at the collection plate, computed using the present numerical model as a function of the discharge electrode voltage ( $V$ ), with the corresponding experimental measurements. The results, as shown in Fig. 4.4, indicated a good agreement between the calculated corona current at the collecting plate and the experimental measurements of Kasdi [21].

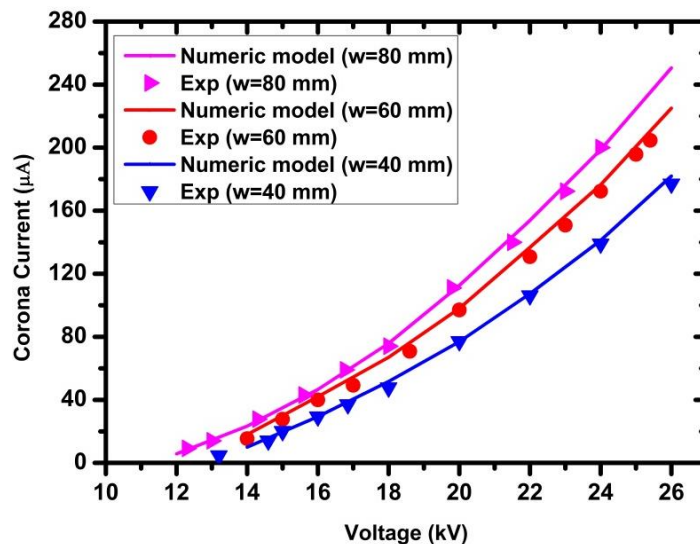


**Fig 4.4:** Comparison of V-I curves generated from numerical simulations (this study) with the experimental results of Kasdi [21] with varying discharge electrode voltage and wire-to-wire spacing ( $w$ ).

It is also clear from Fig. 4.4 that the present numerical model accurately predicted the corona current produced by three discharge wires of which the wire-to-wire spacing ( $w$ ) was varied. Accordingly, the corona current decreased with a reduction in the wire-to-wire spacing ( $w$ ). In other words, the corona current increased with an increase in the wire-to-wire spacing ( $w$ ), although it is expected that such an increase in the current would not be possible beyond a certain limiting value of  $w$ .

The reduction in the corona current as shown in Fig. 4.4 is due to shielding, as is illustrated in Fig. 4.5 where the current density distributions predicted by the numerical model used in this study at the collecting plate surface is compared to the measurements of Kasdi [21]. It is clear from the figure that the current density reached a maximum at the points located directly across the discharge wires, and gradually decreased to a minimum at the points that are directly across the midway point between the adjacent wires. Furthermore, the current density that corresponds with the central discharge wire was visibly suppressed, and this effect was also accurately predicted by the numerical simulation results. The suppression of the corona current due to the interaction between the electrostatic field generated by adjacent discharge wires, i.e. shielding, has also been noted by other researchers [24,25]. This differentiation between the discharge characteristics of each individual wire-electrode was achieved by applying the space charge density boundary condition, in accordance with Peek's law (Table B-2), independently to each electrode.

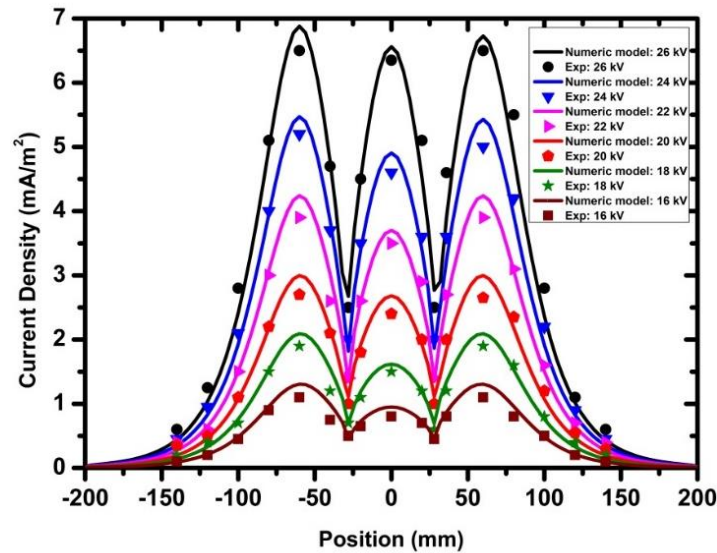


**Fig 4.5:** Comparison between the experimentally measured current density distributions at the collecting plate surface of the ESP system used by Kasdi [21] and that predicted by the current numerical model.

From the preceding results, it is clear that the current numerical model yielded accurate results that were in good agreement with previously published experimental measurements and numerical modeling results. The numerical model used in this study was therefore

subsequently applied to systematically study the influence of various ESP parameters on the degree of shielding and its effect on ESP performance. This was done using the single-channel ESP parameters as summarized in Table 4.2, and the results are discussed in the subsequent sections.

### 4.3.2 Analysis of shielding

#### 4.3.2.1 The influence of the plate-to-plate spacing on the degree of shielding

To study the incidence of shielding as a function of the ESP plate-to-plate spacing, simulations were performed for three plate-to-plate spacings ( $p$ ) of 220, 160 and 100 mm respectively. A fixed number of four discharge wire-electrodes were used with a constant discharge electrode voltage of 45 kV. In all cases, a fixed wire-to-wire spacing ( $w$ ) of 116 mm was simulated.

The current density distribution resulting from the corona discharge is a combination of the ion mobility, electrostatic field magnitude, and the space charge density. In addition to the current density distribution, the space-charge density distribution was therefore also investigated of which representative results are shown in Fig. 4.6. It is evident from Fig. 4.6 that the space charge density due to corona discharge from the central wire was significantly suppressed as the plate-to-plate spacing was increased from 100 to 160 mm and subsequently to 220 mm. In other words, the space charge density required at the central wires' surface to achieve the electrostatic field magnitude calculated from Peek's formula was significantly reduced compared to that of the outer discharge wires, and this effect becomes more pronounced as the plate-to-plate spacing was increased. It is also evident from Fig. 4.6 (c) that the corona discharge was not symmetric due to the shielding effect, since a non-symmetric space charge density distribution was obtained around the outer discharge wires.

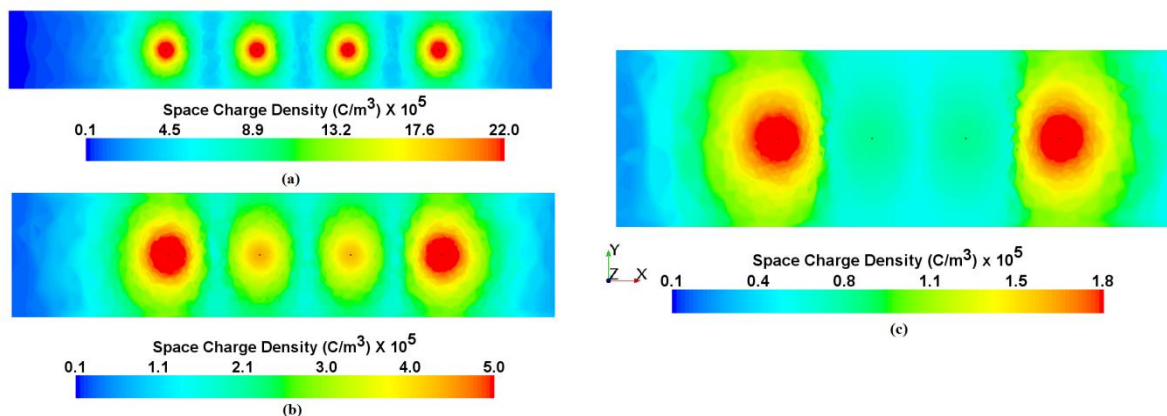


**Fig 4.6:** Space charge density distributions for plate-to-plate spacings of (a) 100 mm (b) 160 mm (c) 220 mm at an applied discharge electrode voltage of 45 kV using four discharge wire-electrodes.

The associated one-dimensional space charge density and current density distribution along the length of the ESP channel (longitudinal, or  $x$ -direction) and along the horizontal axis of symmetry at the discharge wires' surfaces ( $y = 0$ , the axis passing through the wires) are shown in Fig. 4.7 (a) and (b), while the corresponding distribution at the collecting plate surface is shown in Fig. 4.7 (c) and (d). It is clear from Fig. 4.7 that the space charge density and current density, both along the axis passing through the wires and along the collecting plate surface, generally decreased when the plate-to-plate spacing was increased. The effect of this decrease in the space charge density and current density is a significant decrease in the total corona discharge current with varying discharge electrode voltage, as shown in the V-I curves of Fig. 4.7 (e).

It is also clear from Fig. 4.7 (a) – (d) that the degree of shielding contributes to the decrease in the total corona current, which is quantified in Table 4.3 in terms of the ratios of the peak space charge density and current density values obtained at the  $x$ -positions that coincide with the outer discharge wires' positions, relative to the peak values obtained at the  $x$ -positions coinciding with the position of the two inner discharge wires. A higher value of these ratios therefore indicates a larger degree of shielding.

**Table 4.3:** The degree of shielding at the wire-plane and the collecting plate-plane with varying plate-to-plate spacing

Plate to plate spacing (mm)	Current density ratio		Space charge density ratio	
	Wire-plane	Collecting plate-plane	Wire-plane	Collecting plate-plane
100	1.10	1.02	1.04	1.02
160	1.48	1.21	1.44	1.20
220	2.57	1.81	2.50	1.79

A higher discharge electrode voltage is generally required (even in the absence of shielding) to achieve a constant discharge current with increasing plate-to-plate spacing, as also attested by the corona onset voltage, which increases as the plate-to-plate spacing is increased. Since the above analysis was performed at a constant discharge electrode voltage, the increase in the degree of shielding with increasing plate-to-plate spacing (Table 4.3) suggests that a discharge electrode system is especially sensitive towards shielding at low discharge currents.



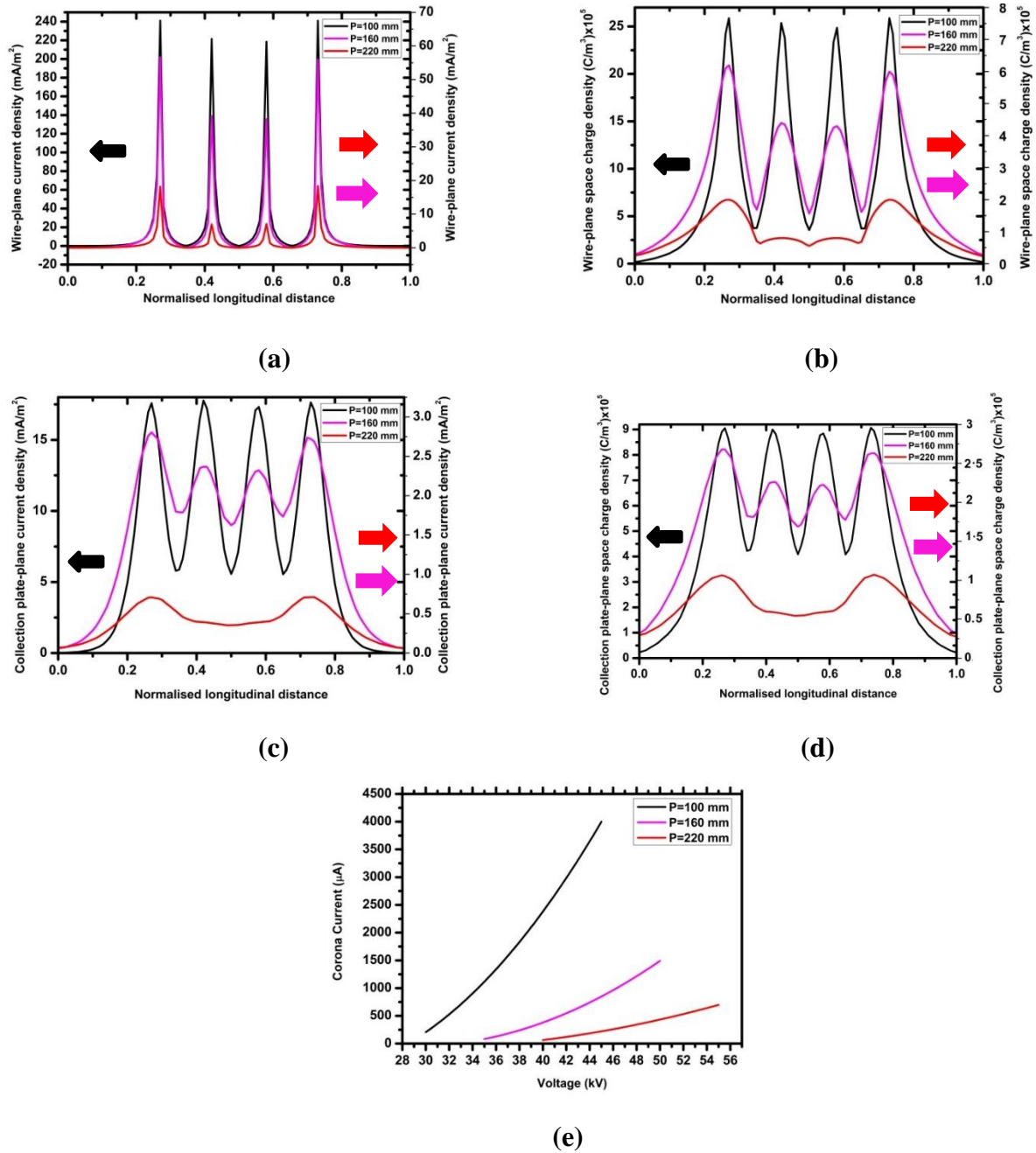


**Fig 4.7:** Current density distribution along the horizontal axis of symmetry (a) and the collecting plate surface (c), and the corresponding space charge density distribution along the horizontal axis of symmetry (b) and the collecting plate surface (d) at plate-to-plate spacings (p) of 100, 160 and 220 mm respectively, with a constant discharge electrode voltage of 45 kV. The effect of the plate-to-plate spacing, and therefore the degree of shielding (Table 4.3) on the corona current (I) as a function of the applied discharge electrode voltage (V) is also shown (e). In all cases the wire-to-wire spacing was 116 mm and four discharge wire-electrodes were modeled.

#### 4.3.2.2 The influence of the wire-to-wire spacing on the degree of shielding

The influence of the wire-to-wire spacing on the degree of shielding was studied using a constant plate-to-plate spacing ( $p$ ) of 100 mm, an applied discharge electrode voltage of 45 kV and four discharge wires. Wire-to-wire spacings ( $w$ ) of 50, 80 and 116 mm were simulated, and the resulting space charge density, current density, and corona current vs. discharge electrode voltage is shown in Fig. 4.8 (a) – (e).

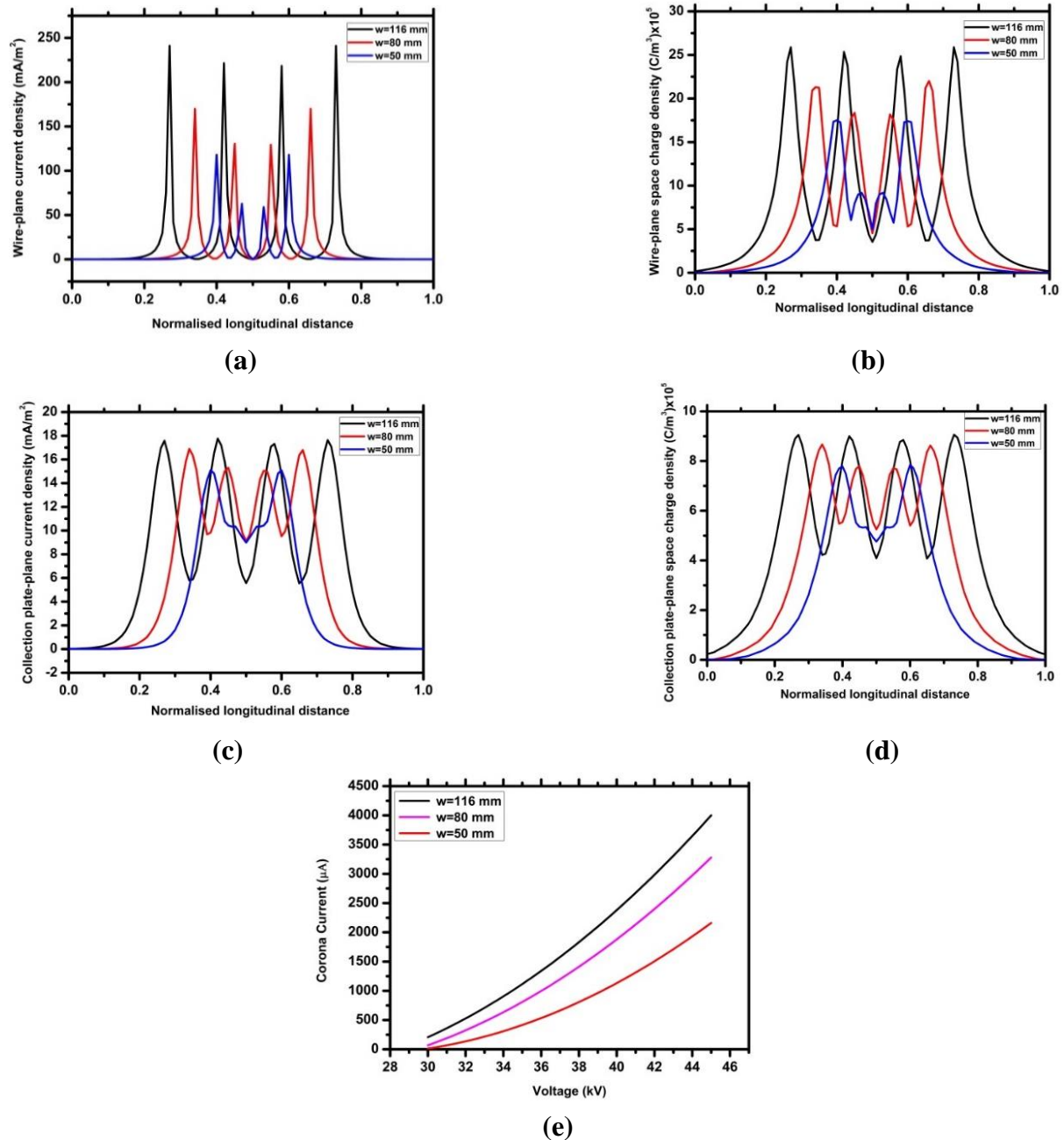


**Fig 4.8:** Current density distribution along the horizontal axis of symmetry (a) and the collecting plate surface (c), and the corresponding space charge density distribution along the horizontal axis of symmetry (b) and the collecting plate surface (d) at wire-to-wire spacings ( $w$ ) of 50, 80, and 116 mm respectively, with a constant discharge electrode voltage of 45 kV. The effect of the wire-to-wire spacing, and therefore the degree of shielding (Table 4.4) on the corona current ( $I$ ) as a function of the applied discharge electrode voltage ( $V$ ) is also shown (e). In all cases the plate-to-plate spacing was 100 mm and four discharge wire-electrodes were modeled.

From the results shown in Fig 4.8 (a) – (d), it is evident that a decrease in the wire-to-wire spacing resulted in an increased degree of shielding (Table 4.4). The result of the increased degree of shielding due to a reduction in the wire-to-wire spacing was a reduction in the total corona current as shown in Fig. 4.8 (e).

**Table 4.4:** The degree of shielding at the wire-plane and the collecting plate-plane with varying wire-to-wire spacing

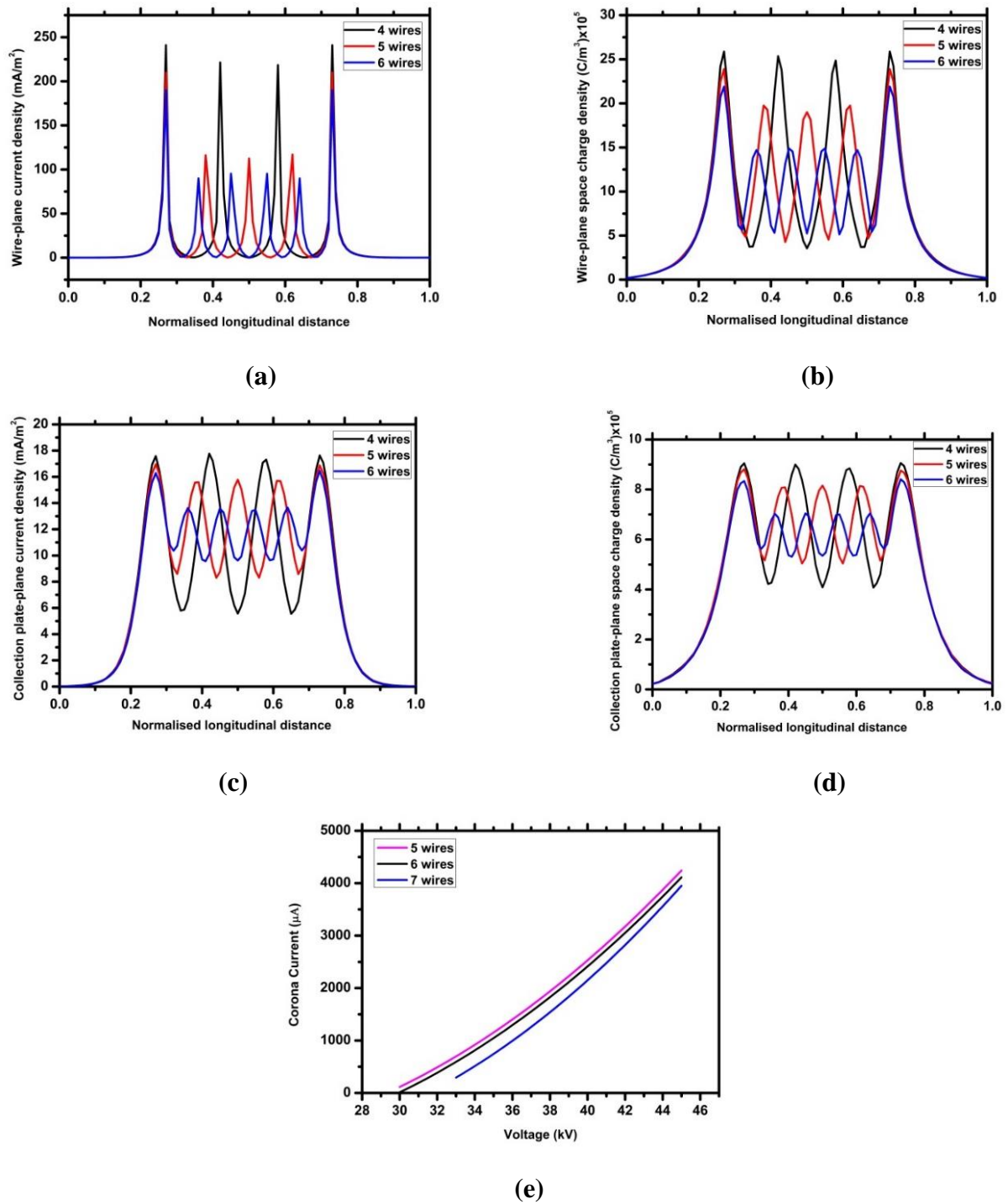
Wire to wire spacing (mm)	Current density ratio		Space charge density ratio	
	Wire-plane	Collecting plate-plane	Wire-plane	Collecting plate-plane
116	1.10	1.02	1.04	1.02
80	1.31	1.12	1.25	1.12
50	2.00	1.46	1.91	1.46

Comparing Fig 4.7 (e) and Fig. 4.8 (e) and Table 4.3 and 4.4 it is evident that the plate-to-plate spacing has a more pronounced effect on the degree of shielding, which in turn negatively affects the discharge characteristics to a greater extent.

#### 4.3.2.3 The influence of the number of discharge wires on the degree of shielding

The effect of the number of discharge wire-electrodes on shielding and the corona discharge characteristics was investigated for plate-to-plate spacings of 100 and 160 mm, at a constant applied discharge electrode voltage of 45 kV, and by varying the number of discharge wires between 4 and 8. In these simulations, the positions of the two outer discharge wires were fixed, and since the ESP (collecting plate) length was also fixed (Table 4.2), the addition of discharge wires to the ESP meant that the wire-to-wire spacing ( $w$ ) was successively reduced.

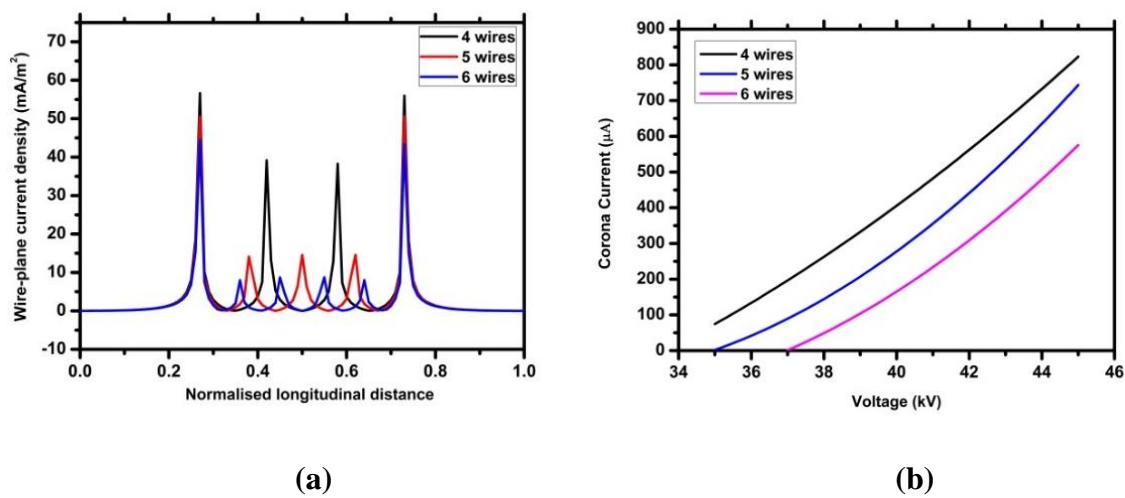
Again, the space charge and current density distribution results as given in Fig. 4.9 for the 100 mm plate-to-plate spacing case shows that shielding significantly influenced the discharge characteristics and that the degree of shielding increased with an increase in the number of discharge wires (Table 4.5). Nonetheless, the degree of shielding and its effect on the discharge characteristics is less severe compared to the previous cases. However, as is evident from Fig. 4.10 (a) and (b), the plate-to-plate spacing again plays an important role, where an increase to  $p = 160$  mm has the effect of significantly amplifying the degree of shielding.



**Fig 4.9:** Current density distribution along the horizontal axis of symmetry (a) and the collecting plate surface (c), and the corresponding space charge density distribution along the horizontal axis of symmetry (b) and the collecting plate surface (d) at a constant plate-to-plate spacing ( $p$ ) of 100 mm, and a constant discharge electrode voltage of 45 kV. The effect of the number of discharge wires, and therefore the degree of shielding (Table 4.5) on the corona current ( $I$ ) as a function of the applied discharge electrode voltage ( $V$ ) is also shown (e).

**Table 4.5:** The degree of shielding at the wire-plane and the collecting plate-plane with a varying number of discharge wires

No. of wires	Current density ratio		Space charge density ratio	
	Wire-plane	Collecting plate-plane	Wire-plane	Collecting plate-plane
4	1.10	1.02	1.04	1.02
5	1.30	1.09	1.21	1.09
6	1.57	1.20	1.49	1.19

**Fig 4.10:** Current density distribution along the horizontal axis of symmetry at a constant discharge electrode voltage of 45 kV (a), and the resulting corona current ( $I$ ) as a function of the applied discharge electrode voltage ( $V$ ) (b) for 4, 5 and 6 discharge wires and a plate-to-plate spacing of 160 mm.

To avoid the negative effects of shielding, it is therefore clear that the wire-to-wire and plate-to-plate spacing together with the electrode type, i.e. the resulting discharge characteristics, need to be carefully considered when increasing the number of discharge electrodes with the aim of increasing the corona current. This is because the suppression of the corona current through shielding caused by ineffective plate-to-plate spacing and a diminishing wire-to-wire spacing when increasing the number of wire-electrodes would lead to a reduction in the particle collection efficiency as shown in Section 4.3.3. Additionally, the electrode design would also have an influence on the inter-electrode spacing below which shielding would become significant relative to a certain plate-to-plate spacing. The best strategy when aiming to increase the discharge current by increasing the number of discharge electrodes is to simultaneously decrease the plate-to-plate spacing, since the preceding results suggest that the plate-to-plate spacing and the interelectrode spacing collectively influence the degree of shielding. This is clear from the results of Fig. 4.9 (e) and Fig. 4.10 (b), where a smaller



plate-to-plate spacing of 100 mm permits the use of more discharge wires to afford a higher discharge current without shielding having a significant negative effect. The current numerical model, with which quantification of this shielding effect is possible, can therefore be used to evaluate or predict whether a certain ESP design might be hampered by shielding.

The current density vector plots as shown in Fig. 4.11 provide a qualitative explanation of how shielding arises, which corresponds with the explanation of Al-Hamouz et al. [24], namely that the electrostatic field lines are “compacted” as the wire-to-wire spacing is decreased, or in other words interference occurs between the electrostatic fields generated by the corona discharge of the individual discharge wires.

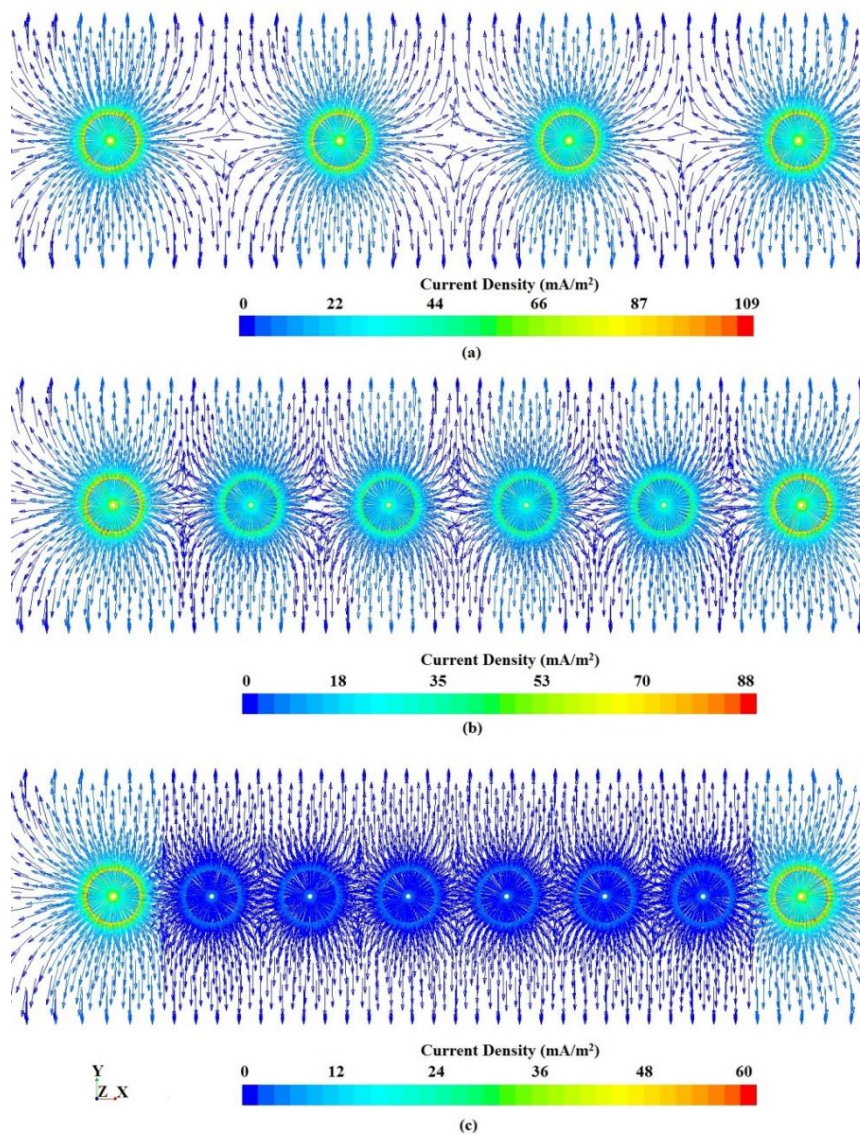


**Fig 4.11:** Current density vector plots of the corona discharge for a plate-to-plate spacing of 100 mm and an applied discharge electrode voltage of 35 kV for 4 wires (a) 6 wires (b), and 8 wires (c).

It is evident from Fig. 4.11 (plate-to-plate spacing of 100 mm) that the degree of interference between the current generated by each individual discharge wire increases as the number of wires are increased, or in other words when the wire-to-wire-spacing is reduced. As mentioned previously, the plate-to-plate spacing also plays a significant role in shielding, and in other words also affects the manner and degree of interference between the electrostatic field produced by each individual discharge wire.

#### 4.3.2.4 The influence of the discharge electrode voltage on the degree of shielding

The effect of the applied discharge electrode voltage on the degree of shielding was analyzed by varying the applied discharge electrode voltage while keeping the plate-to-plate spacing fixed at 100 mm and using five wire electrodes. It was found that the magnitude of the current density increased as the applied discharge electrode voltage was increased, but that the degree of shielding (the ratio of the peak value of current density at the outer wires to that of the peak value of the current density at the inner wires) was not affected significantly with increasing applied discharge electrode voltage (Fig. 4.12).

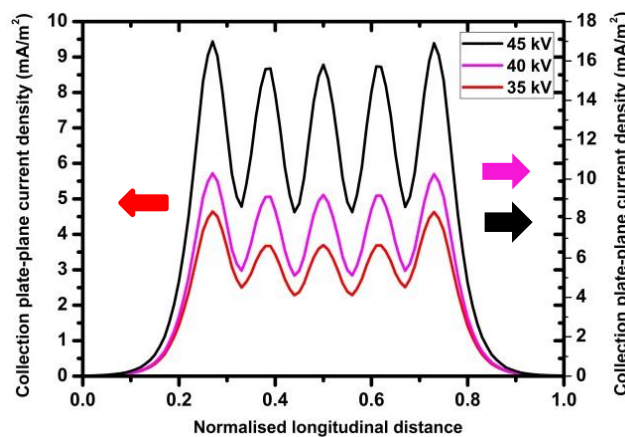


**Fig 4.12:** Current density distribution along the collecting plate surface under varying applied discharge electrode voltage with a constant number of five discharge wires and a constant plate-to-plate spacing of 100 mm.

#### 4.3.3 The influence of shielding on the particle collection efficiency

Simulations were also performed to study the influence of shielding as a result of varying plate-to-plate spacing and a varying number of discharge wires, or in other words a varying wire-to-wire spacing. Particle injection, charging and collection were simulated using the previously published simulation method [16]. The effect of an increased degree of shielding that arose due to an increase in the number of discharge wires from four to eight in an ESP channel with a plate-to-plate spacing of 220 mm is apparent from Fig. 4.13 (a) and (b). In both cases, the discharge electrode voltage was set at 55 kV and particles with a uniform diameter of 5  $\mu\text{m}$  were simulated. It is visually evident (and confirmed in Fig. 4.14) that

lower particle collection efficiency was obtained with eight discharge wires (Fig. 4.13 (b)) compared to four discharge wires (Fig. 4.13 (a)). These results are a good example of the reduction in particle collection due to shielding (Fig. 4.11) that arose because of an increase in the number of discharge wires, i.e. a reduction in the wire-to-wire spacing, and in which the shielding effect is amplified by an inappropriate plate-to-plate spacing.

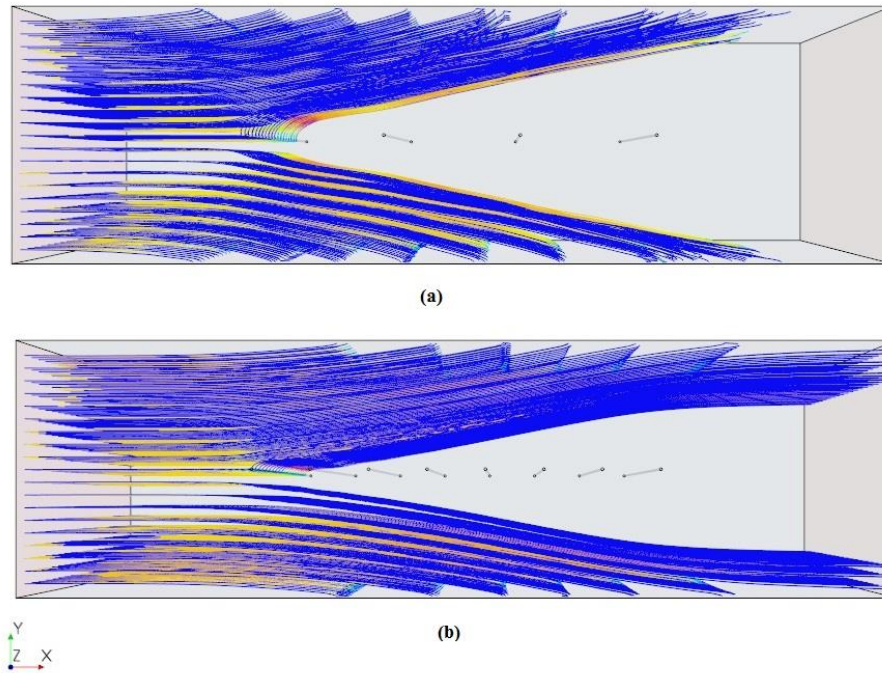


**Fig 4.13:** Particle trajectories for particle collection in a single-channel ESP with a plate-to-plate spacing of 220 mm and an applied discharge electrode voltage of 55 kV with four (a), and eight discharge wires (b) respectively.

The simulated particle collection efficiencies obtained when using plate-to-plate spacing of 100 mm as a function of the number of discharge wires and applied discharge electrode voltage is shown in Fig 4.14 (a-b), from which it is evident that while the particle collection efficiency was increased by increasing the number of discharge wires (Fig. 4.14 (a)), this was only true up to a certain point. After increasing the number of wires further (accompanied by a decrease in the wire-to-wire spacing), a reduction in the particle collection was observed. Following the preceding discussions, this reduction in the particle collection efficiency is attributed to an increased degree of shielding. The same trend of increasing collection efficiency with an increasing number of discharge wires up to a certain threshold, followed by a decrease in collection efficiency with a further increase in the number of wires is evident from Fig. 4.14 (b), which represents the simulation results of two different particle sizes.

From the collection efficiency results of Fig. 4.14 (a) it is evident that a higher applied discharge electrode voltage can partially negate the detrimental effects of shielding on



particle collection when going from 5 to 6 discharge wires. Although shielding would still be present at the higher applied discharge electrode voltage in these two cases, the relative degree of shielding does not vary greatly with increasing applied discharge electrode voltage as was concluded from the results of Fig. 4.12. The applied discharge electrode voltage therefore plays an important role in partially reducing the negative effects of shielding on particle charging and collection.

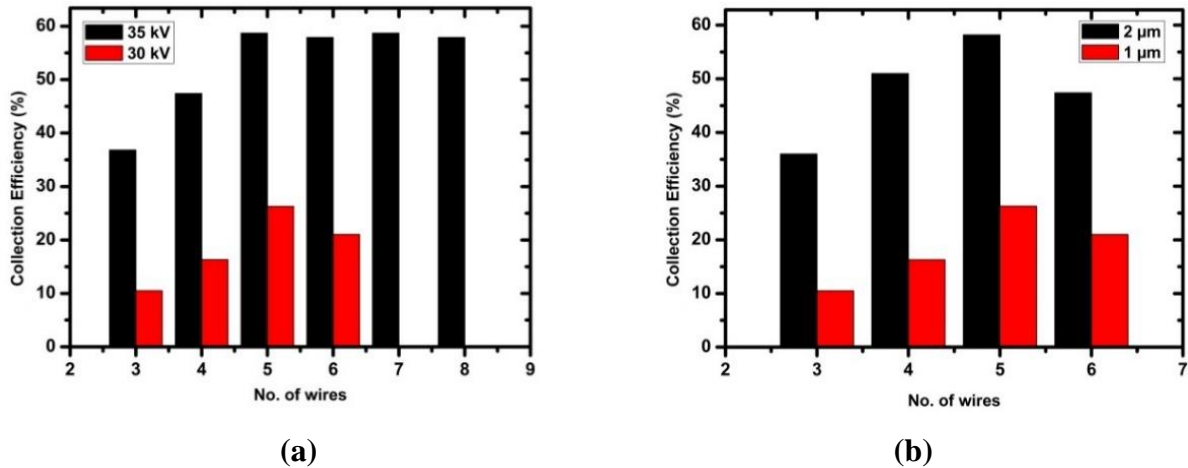


**Fig 4.14:** Particle collection efficiency comparison for 1 μm particles at a plate-to-plate spacing of 100 mm and the applied discharge electrode voltages as shown in the graph (a). Also shown is a comparison between the particle collection efficiency for two different particle diameters using a plate-to-plate spacing of 100 mm and an applied discharge electrode voltage of 30 kV (b).

#### 4.4 Conclusions

It was shown that the current numerical model yielded accurate results that were in good agreement with previously published experimental measurements and numerical modeling results of corona discharge in ESPs. The model was subsequently applied to quantify the influence of various ESP parameters on the degree of shielding, and by analyzing the current density and space charge density distributions it was found that the plate-to-plate spacing had the most significant influence. Nonetheless, the wire-to-wire spacing and number of discharge wires were also found to have a noticeable effect on the degree of shielding. In contrast, the applied discharge electrode voltage was found to have a negligible influence on the degree of shielding.

Due to the incidence of shielding, it was also shown that particle collection is markedly reduced when the number of discharge wire-electrodes are increased beyond a certain threshold. It was therefore shown in this study that the plate-to-plate spacing should be reduced to accommodate a larger number of discharge wires to achieve an increased discharge current and to avoid or reduce the detrimental effects of shielding on corona current and particle collection.

---

In essence, the current model provides a means of quantifying the extent of shielding and its effect on ESP performance, an aspect that has not received much attention to date. Although only simple cylindrical discharge electrodes were analysed in this study, the numerical model may also be extended to analyse shielding effects that arise with more sophisticated discharge electrodes, provided that the discharge current produced by each individual discharge electrode in a multi-electrode assembly is measured.

#### 4.5 References

- [1] K.R. Parker, *Applied Electrostatic Precipitation*, 1997. doi:10.1007/s13398-014-0173-7.2.
- [2] K. Adamiak, Numerical models in simulating wire-plate electrostatic precipitators: A review, *J. Electrostat.* 71 (2013) 673–680. doi:10.1016/j.elstat.2013.03.001.
- [3] J.L. Davis, J.F. Hoburg, Wire-duct precipitator field and charge computation using finite element and characteristics methods, *J. Electrostat.* 14 (1983) 187–199. doi:10.1016/0304-3886(83)90006-2.
- [4] Z.M. Al-Hamouz, A combined algorithm based on finite elements and a modified method of characteristics for the analysis of the corona in wire-duct electrostatic precipitators, *Ind. Appl. IEEE Trans.* 38 (2002) 43–49. <http://ieeexplore.ieee.org/ielx5/28/21119/00980343.pdf?tp=&arnumber=980343&isnumber=21119>.
- [5] Z. Lin, K. Adamiak, Numerical Simulation of the Electrohydrodynamic Flow in a Single Wire-Plate Electrostatic Precipitator, *Ind. Appl. IEEE Trans.* 44 (2008) 683–691. doi:10.1109/TIA.2008.921453.
- [6] A.A. Elmoursi, G.S. Peter Castle, Modeling of corona characteristics in a wire-duct precipitator using the charge simulation technique, *IEEE Trans. Ind. Appl.* IA-23 (1987) 95–102. doi:10.1109/TIA.1987.4504872.
- [7] P.L. Levin, J.F. Hoburg, Donor cell-finite element descriptions of wire-duct precipitator fields, charges, and efficiencies, *Ind. Appl. IEEE Trans.* 26 (1990) 662–670. doi:10.1109/28.55991.
- [8] J. Anagnostopoulos, G. Bergeles, Corona discharge simulation in wire-duct electrostatic precipitator, *J. Electrostat.* 54 (2002) 129–147. doi:10.1016/S0304-3886(01)00172-3.
- [9] S.M.E. Haque, M.G. Rasul, M.M.K. Khan, A. V. Deev, N. Subaschandar, Influence of the inlet velocity profiles on the prediction of velocity distribution inside an electrostatic precipitator, *Exp. Therm. Fluid Sci.* 33 (2009) 322–328. doi:10.1016/j.expthermflusci.2008.09.010.
- [10] S.M.E. Haque, M.G. Rasul, A.V. Deev, M.M.K. Khan, N. Subaschandar, Flow simulation in an electrostatic precipitator of a thermal power plant, *Appl. Therm. Eng.* 29 (2009) 2037–2042. doi:10.1016/j.applthermaleng.2008.10.019.

- 
- 
- [11] N. Farnoosh, K. Adamiak, G.S.P. Castle, 3-D numerical simulation of particle concentration effect on a single-wire ESP performance for collecting poly-dispersed particles, *IEEE Trans. Dielectr. Electr. Insul.* 18 (2011) 211–220. doi:10.1109/TDEI.2011.5704512.
  - [12] N. Farnoosh, K. Adamiak, G.S.P. Castle, 3-D numerical analysis of EHD turbulent flow and mono-disperse charged particle transport and collection in a wire-plate ESP, *J. Electrostat.* 68 (2010) 513–522. doi:10.1016/j.elstat.2010.07.002.
  - [13] Z. Long, Q. Yao, Evaluation of various particle charging models for simulating particle dynamics in electrostatic precipitators, *J. Aerosol Sci.* 41 (2010) 702–718. doi:10.1016/j.jaerosci.2010.04.005.
  - [14] N. Farnoosh, K. Adamiak, G.S.P. Castle, Numerical calculations of submicron particle removal in a spike-plate electrostatic precipitator, in: *IEEE Trans. Dielectr. Electr. Insul.*, 2011: pp. 1439–1452. doi:10.1109/TDEI.2011.6032814.
  - [15] N. Farnoosh, K. Adamiak, G.S.P. Castle, Three-dimensional analysis of electrohydrodynamic flow in a spiked electrode-plate electrostatic precipitator, *J. Electrostat.* 69 (2011) 419–428. doi:10.1016/j.elstat.2011.06.002.
  - [16] S. Arif, D.J. Branken, R.C. Everson, H.W.J.P. Neomagus, L.A. le Grange, A. Arif, CFD modeling of particle charging and collection in electrostatic precipitators, *J. Electrostat.* 84 (2016) 10–22. doi:10.1016/j.elstat.2016.08.008.
  - [17] Z. Al-Hamouz, Numerical and experimental evaluation of fly ash collection efficiency in electrostatic precipitators, *Energy Convers. Manag.* 79 (2014) 487–497. doi:10.1016/j.enconman.2013.11.047.
  - [18] K.D. Kihm, Effects of nonuniformities on particle transport in electrostatic, 1987.
  - [19] S.. Kim, K.. Lee, Experimental study of electrostatic precipitator performance and comparison with existing theoretical prediction models, *J. Electrostat.* 48 (1999) 3–25. doi:10.1016/S0304-3886(99)00044-3.
  - [20] J. Podlinski, A. Niewulis, J. Mizeraczyk, Electrohydrodynamic flow and particle collection efficiency of a spike-plate type electrostatic precipitator, *J. Electrostat.* 67 (2009) 99–104. doi:10.1016/j.elstat.2009.02.009.
  - [21] A. Kasdi, Computation and measurement of corona current density and V<sub>0</sub> characteristics in wires-to-plates electrostatic precipitator, *J. Electrostat.* 81 (2016) 1–8. doi:10.1016/j.elstat.2016.02.005.
  - [22] Z. He, E.T.M. Dass, Correlation of design parameters with performance for electrostatic precipitator. Part II. Design of experiment based on 3D FEM simulation, *Appl. Math. Model.* (2017). doi:https://doi.org/10.1016/j.apm.2017.06.031.
  - [23] Z. He, E.T.M. Dass, Correlation of design parameters with performance for electrostatic Precipitator. Part I. 3D model development and validation, *Appl. Math. Model.* (2017). doi:https://doi.org/10.1016/j.apm.2017.05.042.

- [24] Z. Al-Hamouz, A. El-Hamouz, N. Abuzaid, Simulation and experimental studies of corona power loss in a dust loaded wire-duct electrostatic precipitator, *Adv. Powder Technol.* 22 (2011) 706–714. doi:10.1016/j.apr.2010.10.005.
- [25] M. Abdel-Salam, a. Eid, Finite element simulation of corona in wire-duct precipitators, *Conf. Rec. 2002 IEEE Ind. Appl. Conf. 37th IAS Annu. Meet. (Cat. No.02CH37344)*. 2 (2002) 1383–1389.
- [26] P.A. Lawless, L.E. Sparks, A mathematical model for calculating effects of back corona in wire-duct electrostatic precipitators, *J. Appl. Phys.* 51 (1980) 242–256. doi:10.1063/1.327416.
- [27] OpenFOAM, User Guide (2nd ed.), Open CFD Ltd. (2014).
- [28] CD-ADAPCO, User Guide STAR CCM+ V. 9.02, (2014) 4482–4484.

---

---

## Chapter 5. EXPERIMENTAL VALIDATION OF A COMPUTATIONAL MODEL OF A LABORATORY-SCALE ELECTROSTATIC PRECIPITATOR

This chapter is based on the following submitted manuscript: S. Arif, D.J. Branken, R.C. Everson, H.W.J.P. Neomagus & A. Arif. Experimental validation of a computational model of a laboratory-scale electrostatic precipitator. *To be submitted for review.*

### Abstract

The validation of a computational model for predicting the performance of a laboratory-scale, single channel, multi-electrode electrostatic precipitator (ESP) was undertaken. This consisted of comparison of experimental and modeling results obtained at various geometrical and operating parameters, such as the plate spacing, the inter-electrode spacing, the number of electrodes, the electrode design, the applied discharge electrode voltage, particle size and gas flow rate. Wire discharge electrodes and a spiked, rigid discharge electrode were applied to study the efficiency of fly ash removal from a gas stream. The validation consisted, firstly of comparing applied voltage versus discharge current relationships (V-I), followed by the comparison of the collection efficiencies obtained from experimental measurements and the modelling calculations. The modeling of the V-I results was confined to the electrostatic field only, whereas modeling for the collection efficiencies involved the interaction of the electrostatic field with the fluid and particle dynamics fields. In the case of multi wire-electrode arrangements, the predicted effects of shielding, which is induced at specific plate-to-plate and wire-to-wire spacings, were validated with respect to the influence thereof on the V-I properties and the resulting particle collection efficiencies. Additionally, the computational modeling results obtained with varying gas flow rate, particle sizes and discharge electrode voltages also correlated well with the experimental findings. The computational model also yielded accurate predictions of the fly ash collection efficiency obtained with a single spiked discharge electrode and varying geometric and operating parameters.

**Key words:** *Laboratory-scale ESP, computational modeling, rigid discharge electrode (RDE), particle collection efficiency, electrostatic precipitator (ESP), shielding, OpenFOAM®, Star-CCM+®*

---

## 5.1 Introduction

Since environmental legislation and particulate emission standards are frequently updated with the aim of improving ambient air quality, particulate control technologies need to be regularly improved to yield enhanced particulate collection efficiencies and overall process performance. Electrostatic precipitators (ESPs) are still relevant for particulate matter (PM) control at coal-fired power stations in South Africa [1–3], although ESP units are systematically being replaced with fabric filter units due to the higher collection efficiencies that are routinely achieved with fabric filters. A wide range of experimental studies have been reported in the literature that focused on studying the influence of the electrostatics on the particle collection efficiency in ESPs with the aim of deriving process models that can be used to improve ESP performance [4–6], and in turn reduce PM emissions to acceptable levels. The electrostatic field produced during ESP operation greatly defines the particle charging and resulting collection efficiency, and is in turn influenced by the physical design of the ESP [7,8]. Therefore, the ESP collection efficiency is also dependent on various geometric parameters such as the discharge electrode design, inter-electrode spacing, and the collecting plate spacing, in addition to process parameters such as gas flow velocity and discharge electrode voltage.

Zhongjie He et al. [9] experimented with the design of an ESP for removing suspended particles from the inlet air stream of a gas turbine to determine the optimum combination of the wire-electrode configuration (series and parallel configurations) and applied voltage such that the particle collection efficiency was maximized. In a series configuration the wire-electrodes are arranged in a row, while in a parallel configuration the wire-electrodes are arranged in two or more rows and the electrodes may then be staggered as well. It was concluded that the energy consumption could be minimized while optimum collection efficiency could be achieved when using two wire-electrodes in a parallel arrangement at 15 kV and a 1 m/s gas flow. It was further concluded, however, that the air flow velocity had an insignificant effect on the discharge characteristics, which corroborates the findings of a computational study presented in our previous work [10].

Kim & Lee [11] used a laboratory-scale ESP to derive a set of geometric and operating conditions at which a maximum particle collection efficiency could be achieved with the fly ash samples that they used in the experiments. A series of experiments were conducted by varying the electrode-to-plate spacing, the radii of the electrodes (cylindrical wires), air velocity, turbulence intensity and applied discharge electrode voltage. A set of operating and geometric parameters were subsequently derived from the results obtained from the experiments, with which maximum collection efficiency was obtained for the ESP system used in the study. Kim & Lee [11] also reported that the variation of the turbulence intensity did not affect particle collection efficiency at high discharge electrode voltages, while the collection efficiency could be increased with a decrease in the turbulence intensity at low discharge electrode voltages. By comparing the experimental findings with existing ESP

---

models, it was found that the model of Zhibin & Guoquan [12] gave the best description of the laboratory-scale ESP. Nonetheless, the collection efficiencies were under-predicted for particles diameters ranging between 0.5 and 10  $\mu\text{m}$ , while the collection efficiency was over-predicted for particles with diameters smaller than 0.5  $\mu\text{m}$  and larger than 10  $\mu\text{m}$ .

The velocity with which charged particles migrate to the grounded collecting plates, i.e. the migration velocity, is a key parameter that governs ESP performance and can be used to guide industrial-scale ESP design. The influence of particle diameter and discharge electrode geometry on migration velocity was studied by Jedrusik et al. [13] using barbed plate, barbed tube, wire, and spiked band discharge electrodes respectively. It was found that the migration velocity could be maximized by using the barbed tube discharge electrode. This is due to the migration velocity that is directly related to the rate at which particles are charged by the electrostatic field, which can be manipulated by adjusting the electrode design. Consequently, Jedrusik et al. [14] studied the influence discharge electrode design on the collection efficiency of two different fly ashes, using the spiked band, pipe and double-spike discharge electrodes. It was found that the pipe (a pipe fitted with sharp spikes) and double-spike electrodes had lower corona onset voltages compared to the spiked band electrode. They also found that the V-I curve shape of the pipe and double-spike electrodes could be manipulated, i.e. to afford a higher discharge current at a certain applied voltage, by increasing of the number of double spikes on the pipe of double-spike electrodes. Consequently, the pipe and double-spike electrode also yielded higher collection efficiencies for both ashes used in the study compared to the spiked band electrode. Jedrusik et al. further found that [15] an increase in the uniformity of the measured discharge current distribution, which was reported to also be influenced by the electrode design, yielded increased particle collection efficiency, especially of the fine particles.

Xu et al. [16] studied the effect of the gas temperature and discharge electrode design (rod, saw and screw) on the particle collection efficiency using an experimental-scale ESP. The relative performance of the different electrodes was shown to vary with temperature, with the saw-type electrodes yielding the highest collection efficiency at low temperatures, while wire-electrodes yielded the highest collection efficiency at high temperatures. It was also concluded that the discharge current and ESP collection efficiency was significantly influenced by the inter-electrode spacing, which confirms the computational modelling findings presented in our previous work [17].

One shortcoming of the aforementioned experimental studies, and of the ESP literature in general, is the lack of comprehensive models with which the influence of the various geometric and electrostatic parameters on the particle collection efficiency may be quantified. Computational modelling is advantageous in this regard, since the process can be simulated through an integrated mathematical description of the underlying physical principles. For example, in a computational modelling study done by Kasdi [8], in which the developed computational model was also validated using experimental measurement data, it was found

---

that the current density and space charge density distributions was significantly influenced by the number of discharge wire-electrodes, the wire radii, and the inter-electrode spacing. This was further confirmed in computational modelling study presented in our previous work [17] in which it was shown that the inter-electrode spacing relative to the collecting plate spacing should be carefully selected to avoid the occurrence of shielding. Shielding, in which the current density and space charge density produced during corona discharge of adjacent electrodes are suppressed, leads to a reduction in the discharge current when the number of electrodes is increased beyond a certain threshold. Therefore, a reduction in the collection efficiency is noted under such conditions, despite the addition of discharge electrodes. This aspect has not yet received much attention in the literature, neither as part of experimental or computational modelling studies.

It was also shown in the computational modelling study presented in our previous work [10] that an appreciable increase in the discharge current and space charge density is afforded with the use of spike or saw-type discharge electrodes compared to cylindrical wire-electrodes. Consequently, the validated computational model results predicted that a significant increase in the particle collection efficiency could thus be achieved. These results corroborated the computational simulation results of Farnoosh et al. [18,19], which predicted improved collection efficiencies with spike electrodes, which also correlated well with experimental measurements. With the exception of a limited number of cases as mentioned above [10,18,19], most computational modelling studies on ESP processes [7,20–28] mainly focuses on the modelling of wire-type discharge electrodes since experimentally measured V-I data are required to simulate the corresponding corona discharge produced by such rigid discharge electrodes (RDE's).

Some of the challenges as mentioned in the preceding discussion were addressed in our previous work [10,17], namely illustrating the computational modelling of irregular-shaped discharge electrodes and describing the influence of geometric parameters on the intensity of shielding, and consequently particle collection efficiency. Nonetheless, the computational model used in the two previous studies was validated using literature data, while the modelling predictions related to shielding [17] was done for a laboratory-scale ESP for which experimental data is reported in this paper. The objective of this paper is therefore to establish a rigorous, experimentally validated 3-D computational model that incorporates the effects of shielding and discharge electrode design on the corona discharge characteristics and the resulting influence thereof on the particle collection efficiency. This is done in a staged approach in which the effects of shielding on ESP collection efficiency as predicted in our previous work [17] are first validated for a wire-electrode system. Subsequently, the experimental measurement data and computational modelling predictions of particle collection using wire-electrodes and a commercially available rigid discharge electrode are compared for further validation of the 3-D computational model described in our previous work [10,17]. The locally manufactured commercial discharge electrode, known by its tradename as the G-spike electrode [29], is referred to, here simply as a spiked discharge



electrode. An in-house laboratory-scale ESP unit was used for the experimental measurements, in which the geometric and operating parameters could be varied with respect to the collecting plate spacing, inter-electrode spacing and the number of discharge electrodes, discharge electrode voltage and thus discharge current, air flow rate (superficial gas velocity), dust load, and particle size distribution. Fly ash sampled from the ESP hoppers of one of South African's coal-fired power stations was used in the experiments.

## 5.2 Computational modelling

The open source code, OpenFOAM®, was used to solve the governing Poisson and charge conservation equations to obtain the electrostatic field, current density and space charge density distributions arising due to corona discharge. The results were imported in the form of user-defined field functions into the commercial CFD software package STAR-CCM+® [30] that was used to solve the transport equations for the continuous phase, and dispersed phase. Particle charging was also modelled using user-defined functions in STAR-CCM+. Further details of the modelling method are reported in our previous work [10,17].

### 5.2.1 Modelling parameters

Only the ESP section including the collecting plates and discharge electrodes with the same dimensions as the experimental system described in Section 5.3.1 was simulated using the previously developed computational model [10,17]. A typical ESP arrangement that consists of a single spiked discharge electrode is shown in Fig 5.1, in which the tetrahedral mesh used to discretize the computational domain is also illustrated. The arrangement shown in Fig. 5.1 represents one of the cases modelled in this study, and all other cases were based on the same collecting plate height. The other geometric parameters were varied in accordance with the experiments used for validation as are summarized in Table 5.1.

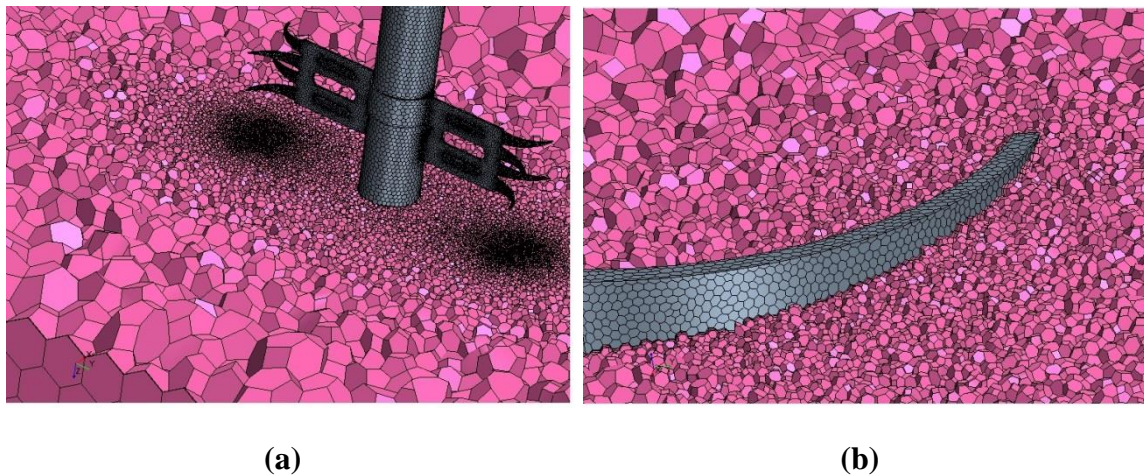


**Fig 5.1:** A discretized 3-D computational model of (a) a single spike in a single-channel ESP system with a spiked discharge electrode (b) close up view of one of the tines of the spiked electrode.

**Table 5.1:** Geometric and operational parameters of the ESP system used in the present computational modelling study

Parameter	Value
Length of collection plate	753 mm
Height of collection plate	376 mm
Spacing between collection & discharge electrode	5, 8, 11 and 20 cm
Number of wire-electrodes	3 - 6
Number of spiked electrodes	1
Diameter of wire-electrodes	1 mm, 2.4 mm
Superficial gas flow velocity	1 - 2 m/s
Discharge electrode voltage	20 - 50 kV
Pressure	101.3 kPa
Temperature of gas	293 K
Ion mobility	$2.6 \times 10^{-4} \text{ m}^2/(\text{V s})$
Particles flow rate	$1.66 \times 10^{-5} \text{ kg/s}$
Relative permittivity of particles	2.5
Particle size distribution	Log-normal distributions

In each of the modelled cases, the computational domain was discretized into tetrahedral cells and a prism layer mesher, surface remesher and extruder mesher was used as meshing models in STAR-CCM+ to reduce the number of computational cells as far as possible. Discretization of the spiked discharge electrode was done such that an extremely fine mesh coincides with the tips of the tines, which were also modelled as the only corona-producing surfaces. Modelling the tips of the tines as the only corona-producing surfaces was in agreement with visual evidence of the corona discharge from these electrodes as provided by the manufacturer (Geecom (Pty) Ltd) [31]. The meshing of the drift zone was also refined near the discharge electrode region so that the gradients of the electrostatic properties could be accurately captured.

The V-I measurement data of the spiked electrodes (Section 5.3.4) was used to solve for the space charge density and electrostatic field distributions, after which particle charging and collection was modelled as described previously [10,17]. In the case of wire-electrodes, Peek's formula was used to predict the V-I characteristics as well as the space charge density and electrostatic field distributions [10,17]. The gas flow was simulated using air as the continuous phase (the gas density and viscosity was set equal to  $1.225 \text{ kg/m}^3$  and  $1.8 \times 10^{-5} \text{ kg/m.s}$  respectively) with a turbulence intensity of 5% at the ESP inlet. The dust particles were introduced into the computational domain at the inlet to the ESP channel and with a particle mass density of  $2000 \text{ kg/m}^3$ , and a relative permittivity of 2.5. The particles were further modelled as having an inlet velocity equal to the operating gas velocity at the inlet, which was assumed to be uniform at ca. 1 m/s and 2 m/s respectively. These flow velocities were also applied in the experiments by setting the blower speed and measuring the flow velocity in a two-dimensional grid at the ESP inlet plane (Section 5.3.2). The measured velocity was used as input to a computational fluid dynamics (CFD) model with which the

velocity distribution was simulated. The blower speed was adjusted until the average flow velocity calculated from the CFD model results correlated with the desired value. This procedure is further detailed in Appendix E. For comparison with the experimental results, the particles were introduced into the computational domain with a log-normal particle size distribution to mimic the measured particle size distribution of the power station fly ash samples.

### 5.3 Experimental method

#### 5.3.1 Laboratory scale ESP

The laboratory-scale ESP unit used in this study, which was largely based on the laboratory-scale ESPs of Kim et al. and Xu et al. [9, 15], was constructed from plexiglass and a high-voltage DC power supply (1) with a maximum output voltage of 50 kV and a maximum output current of 20 mA was used to generate corona discharge. The ESP was designed and commissioned by Geecom (Pty) Ltd, Roodepoort, South Africa, and is illustrated schematically in Figure 5.2.

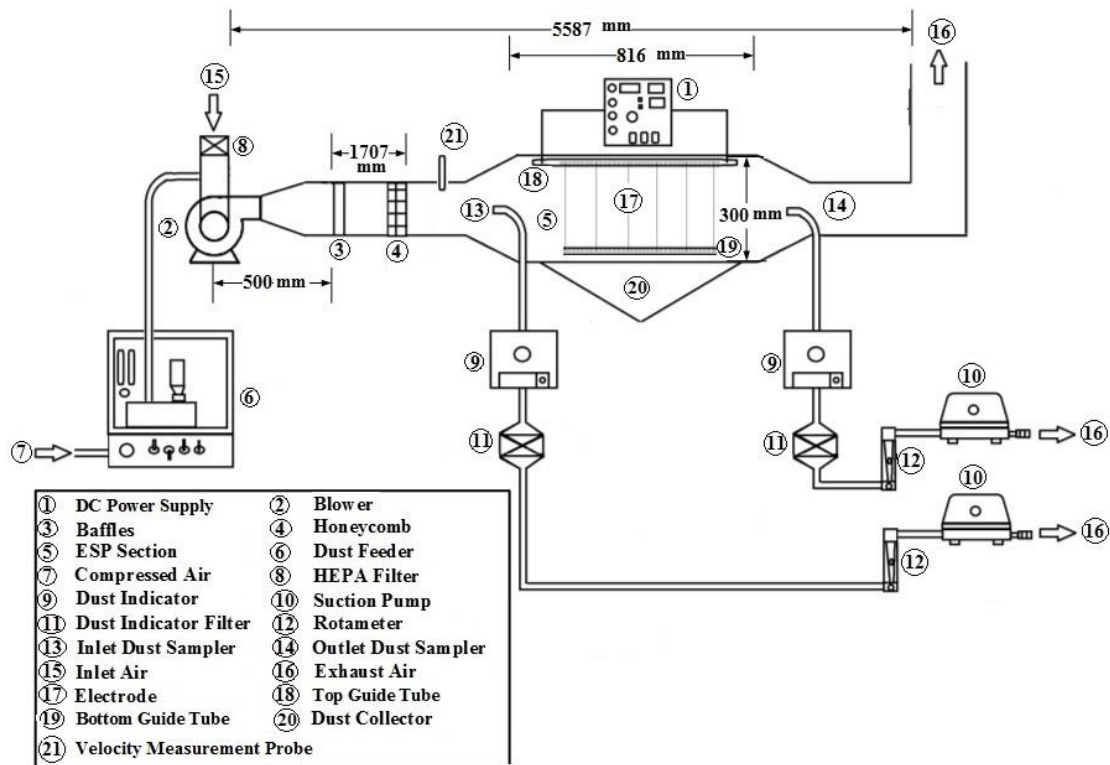


**Fig 5.2:** A schematic diagram of ESP system (not drawn up to the scale)

Ambient air was used as the fluid, of which the flow rate and resulting superficial flow velocity was controlled using a variable speed drive connected to the blower (2). The laboratory-scale unit consisted of three main parts, namely the inlet section that was

connected to the blower, and which was fitted with baffles (3) and a honeycomb structure (4) for homogenizing the air flow, the ESP section (5) for particle collection, and an outlet section. A Sibata Scientific Technology Ltd model DF-3 dust feeder (6), which uses compressed air (7) to transport the particles, was used to introduce fly ash into the ESP system between the blower inlet and the HEPA air filter (8) (protected by a pre-filter) as indicated in Fig. 5.2. Injecting the fly ash upstream of the blower, assisted in producing a uniform fly ash distribution at the ESP inlet plane. By adjusting the dust feeder's feed rate, which is controlled through a variable speed turntable, and the blower speed, fly ash concentrations of between 30 g/hr and 60 g/hr could be achieved.

The ESP section could be equipped with up to 6 cylindrical wire-type discharge electrodes that each had a radius of 1.2 mm. This was achieved using a steel discharge electrode assembly as illustrated in Fig. 5.3 (a). A maximum of two commercial spiked electrodes [29] could be accommodated in the ESP section which consisted of the collecting plates that were 753 mm in length and 370 mm in height, and which could be positioned at inter-plate spacings varying between 100 mm and 400 mm. The design of the spiked discharge electrodes used in this study is depicted in Fig 5.3 (b) and consisted of a stainless-steel pipe to which two stainless-steel spikes were fastened at 120 mm apart from each other. Each spiked electrode has four tines on each side that are curved in alternating directions to enhance corona discharge in both directions. A detailed description of the dimensions and other geometric parameters of the spiked discharge electrodes used in this study is given elsewhere [29], and additional descriptive illustrations of the ESP used in this study are shown in Appendix F.

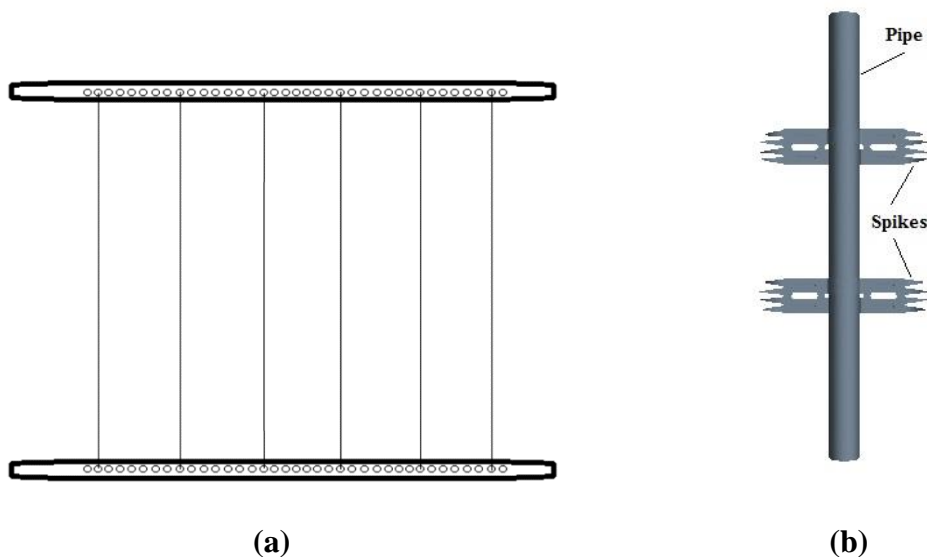


**Fig 5.3:** (a) Wire discharge electrode assembly, and (b) spiked discharge electrode.

---

### 5.3.2 Fly ash concentration and air flow velocity measurements

The inlet dust concentration as well as the dust concentration in the air stream leaving the ESP (Fig. 5.2) was measured using digital dust indicators (9) from Sibata Scientific Technology Ltd. An AP-632 TM model (measuring range of 0.1 to 100 mg/m<sup>3</sup>) was used for measuring the inlet particulate concentration, while an AP-632 TH model (measuring range: 0.01 to 10 mg/m<sup>3</sup>) was used to measure the particulate concentration at the outlet of the ESP section. These digital dust indicators measure the relative particulate concentration based on dispersion/scattering of light by the dust particles present in the sampled air stream. The samples were withdrawn with Sibata Scientific Technology Ltd model SIP-32L suction pumps (10) that were equipped with in-line filters (11) located downstream from the dust indicators. The in-line rotameters (12) were used to set the appropriate flow rate at which the particle laden air samples were withdrawn.

An FMA 100XR thermal anemometer (Omega, FMA 1000 series with remote sensor probe), with a measuring range of 0 to 50 m/s and a rated accuracy of 1.5% (full scale) for air flow was used to measure the air flow velocity profile just before the ESP section at discrete points in a 5 x 11 array. Each measurement was repeated three times and the average was used as input to a CFD model consisting of the ESP section, with which the flow distribution through the ESP section could be modelled. The CFD modelling was performed in Star-CCM+ and only the continuous phase (air) was simulated to predict the air flow pattern through the ESP section (Appendix E). The average velocity in the ESP section was calculated from the velocity distribution results and was subsequently used as a uniform velocity in the computational modelling of the combined electrostatics, particle dynamics and collection (Section 1.2).

### 5.3.3 Fly ash preparation and characterization

Fly ash was sampled from the ESP hoppers of one of South African's coal-fired power stations, and the bulk sample was subsequently split into representative samples by following a cone and quartering procedure, and thereafter riffing out smaller samples using a rotary sample splitter. One of the riffled samples were then sieved using a 300 µm sieve to remove any coarse particles. The sieved sample was consecutively sieved using a 150 µm, and finally a 75 µm sieve to obtain two size fractions, namely the -75 µm fraction (1800 g) and the -150 µm fraction (1300 g) that were used in the ESP experiments. The particle size distributions of the two samples were analyzed with a Malvern master sizer 2000 using distilled water as dispersant fluid and the results are given in Appendix E. The particle laden air was exhausted through the outlet duct and released into atmosphere. The outlet PM concentration was less than 10 mg/Nm<sup>3</sup>, which is well below the minimum emissions standard of 100 mg/Nm<sup>3</sup> that is applicable to industrial installations. Therefore, the release of the PM to the local atmosphere did not pose any health risk to persons in the immediate vicinity of the ESP.

For comparison of the experimental and computational modelling results, the fly ash relative permittivity, which is used as input to model particle charging [10], was required. Relative permittivity measurements were provided by Prof. Maciej Noras of the University of North Carolina, USA. The fly ash permittivity was measured relative to that of air with varying temperature (20 to 40°C) and relative humidity (20 to 80%) using a dielectric cell and an LCR meter (an LCR meter is used to measure inductance (L), capacitance (C) and resistance (R) of components). The results of these measurements are given in Table E-1 in Appendix E. Accordingly, the relative permittivity value (2.5) that was measured at a temperature and relative humidity of 30 °C and 60% respectively (the nominal environmental conditions at the time of the experiments) and a frequency of 1MHz (as permittivity values are more stable at higher frequencies) was used in the computational modelling.

#### **5.3.4 Experiment program**

Using the ESP apparatus as described in the preceding paragraphs, the effect of varying geometric and operating parameters such as the plate-to-plate spacing, the inter-electrode spacing, the number of electrodes, the electrode design (wires and spiked electrodes), the applied voltage, the particle size distribution, and the superficial air velocity on the fly ash collection efficiency could be determined. The parameters used for the various experiments are summarized in Table 5.2 for wire-electrodes and Table 5.3 for the spiked discharge electrodes.

The results of these experiments are subsequently discussed and compared to the computational model predictions for validation purposes. The experimentally measured V-I data of the spiked electrodes were used as input to the computational model to accurately simulate the corona discharge produced by the spiked electrodes. The V-I curves were measured using the DC power supply's built-in digital ammeter, which was accurate to 0.1 mA. The voltage was incrementally increased, and the corresponding current was recorded up until the point where arching occurred.

The experimental results that were obtained for ESP operation with the wire-electrodes (Table 5.2) and a single spiked discharge electrode (Table 5.3) were used for validation of the corresponding computational modelling results as discussed in Section 5.4.2 and Section 5.4.3 respectively.

**Table 5.2:** Summary of experiments performed with the wire discharge electrode assembly. #E is the number of electrodes, w is the wire-to-wire spacing, P is the plate-to-plate spacing.

Exp	Voltage (kV)	#E	w (mm)	P (mm)	Velocity (m/s)	Particle size ( $\mu\text{m}$ )
1	25-35	4	116	100	1	<75 >75
2	30-45	4	116	160	1	<75
3	35-50	4	116	220	1	<75 >75
4	25-35	4	80	100	1	<75
5	25-35	4	50	100	1	<75
6	25-35	3	116	100	1	<75 >75
7	35-50	3	116	220	1	<75 >75
8	35-50	3	175	220	1, 2	<75 >75
9	25-50	1	middle	220	1	<75

**Table 5.3:** Summary of experiments performed with the spiked discharge electrode assembly, P is the plate-to-plate spacing.

Exp	Voltage (kV)	# Spiked electrodes	P (mm)	Velocity (m/s)	Particle size ( $\mu\text{m}$ )
1	25-50	1	220	1,2	<75 >75
2	20-35	1	160	1	<75
3	25-50	1	400	1	<75

## 5.4 Results and discussion

The experimental findings are discussed and compared to the computational model predictions in the following sub-sections with respect to the different operating and geometric parameters that were used. These variables were namely: the plate-to-plate spacing (P), wire-to-wire spacing (w) when using wire-electrodes, discharge electrode voltage, gas flow velocity and particle size. The effects of shielding on the electrostatic properties are first discussed for the wire-electrode configurations, where after ESP performance with respect to the particle collection efficiency is analyzed. Additionally, ESP performance with a single spiked electrode was also studied, and again, the experimental and computational modelling results are compared.



### 5.4.1 Validation of the shielding effects predicted by the computational model

#### *Non-shielding conditions*

It was shown in our previous work [17] that the plate-to-plate spacing and wire-to-wire spacing of wire-plate ESPs are critical parameters which govern the onset of shielding, i.e. when the current density produced by the central discharge electrodes are suppressed relative to that of the outer electrodes. As also shown previously [17], shielding was predicted to occur for the present ESP geometry (Table 5.1) at plate-to-plate spacings larger than 100 mm for a wire-to-wire spacing of 175 mm. To validate the computational modelling predictions with respect to the simulated electrostatic field properties under non-shielding conditions, the discharge voltage vs. corona current curve as calculated from the modelling results was compared to the experimental measurements. In this specific case, three discharge wire-electrodes were used for the experiment and the corresponding modelling and were spaced 175 mm apart (w) while the plate-to-plate spacing (P) was 100 mm and 160 mm. The results are shown in Fig. 5.4, where close agreement between the modelled and measured data is observed. In this and each of the subsequent cases, the experimental measurements were repeated at least twice, and repeatable measurements were obtained within the measuring accuracy of the ammeter (calibrated in milliamps) of the DC power supply, i.e. less than 0.1 mA variation.

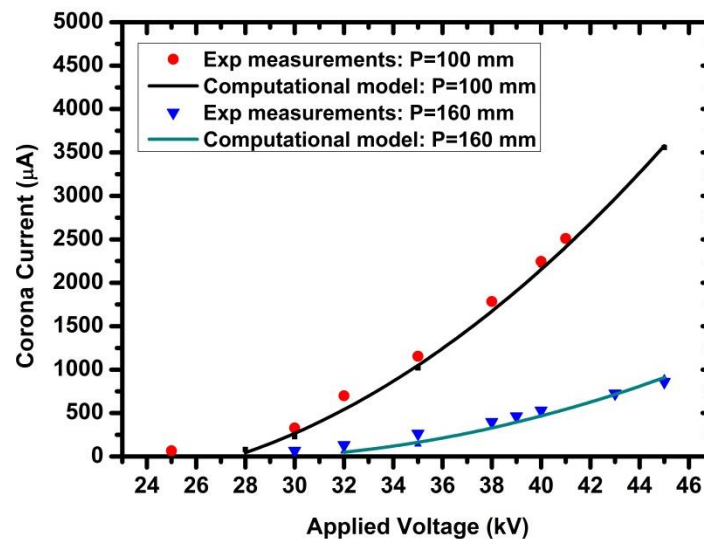


**Fig 5.4:** Comparison of the experimentally measured V-I relationship and that calculated from the computational modelling results for three discharge wire-electrodes spaced 175 mm apart and with a plate-to-plate spacing of 100 mm and 160 mm.

The good agreement between the modelled and measured data indicated that the model accurately predicted the discharge characteristics of the laboratory-scale ESP when equipped with wire-electrodes, i.e. when Peek's law can be used to calculate the electrostatic field strength [10,17], and when no shielding effects were present.



*Shielding conditions*

The parameters that were previously predicted [17] to lead to the incidence of shielding to varying degrees were subsequently tested experimentally, i.e. when four discharge wire-electrodes were used while the plate-to-plate spacing was varied between 100 and 220 mm and when the plate-to-plate spacing was fixed at 100 mm while the inter-electrode spacing was varied between 50 and 116 mm. The V-I results are shown in Fig 5.5 along with the computational model predictions [17]. Good agreement was again found between the experimentally measured V-I data and the model predictions, especially in the case of varying plate-to-plate spacing while the inter-electrode spacing was kept fixed (Fig. 5.5 (a)).

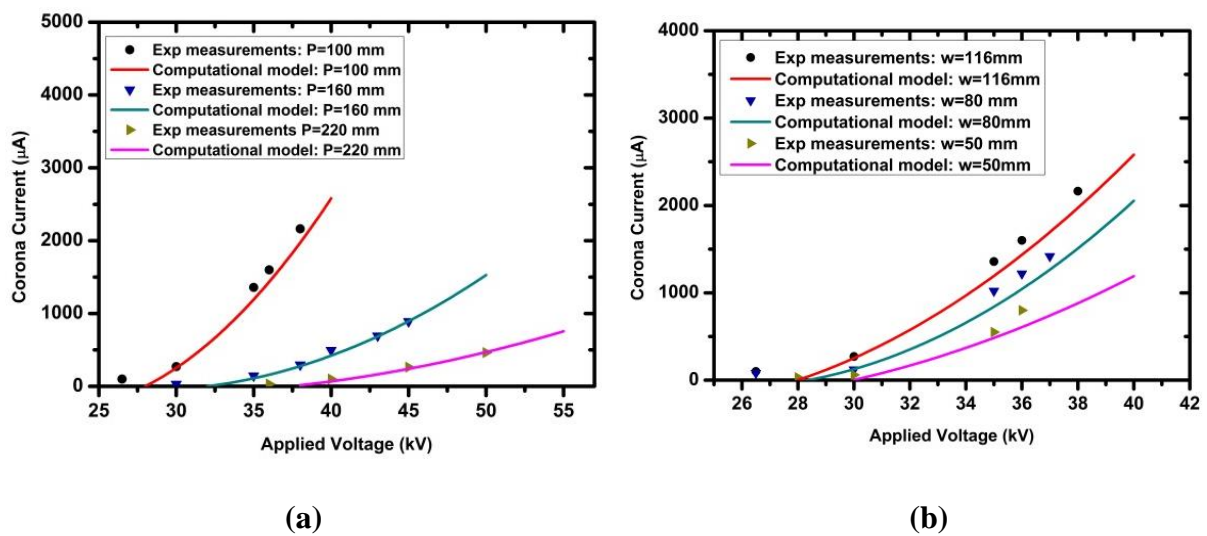


**Fig 5.5:** Comparison of the experimentally measured and modelled V-I curves for a single-channel wire-plate ESP equipped with four wire-electrodes. The effect of varying (a) plate-to-plate spacing while the wires were spaced 116 mm apart, and the effect of (b) the wire-to-wire spacing while the plate-to-plate spacing was kept fixed at 100 mm are shown.

In the case of a fixed plate-to-plate spacing and varying inter-electrode spacing, a larger deviation was observed between the measured and the modelled V-I values at a discharge voltage higher than 35 kV for  $w = 50$  mm (Fig. 5.5 (b)). Nonetheless, in both cases the model results were validated with respect to the reduction in the corona current that is partly due to shielding, which increases in intensity as the plate-to-plate spacing is increased, or as the wire-to-wire spacing is reduced [8,17].

#### 5.4.2 ESP performance with wire-electrodes

Experiments were subsequently performed with wire-electrodes according to the experimental program as summarized in Table 5.2. The full range of experimental results is shown in Fig. 5.6 (a – d), of which experimental data sets were used for validation of the computational modelling results. These collection efficiency experiments were repeated twice and in some cases three times and in all cases the measurements were repeatable to within the

measuring accuracy of the digital dust indicators. The simulations were performed by applying the same parameters to the 3-D computational model as was used in each experimental set. The computational modelling results are shown in Fig. 5.6 (a – d) along with the comparison to the corresponding experimental measurements. The parameters that were kept constant in each case are indicated on each figure.

The effect of varying plate-to-plate spacing is analyzed in Fig. 5.6 (a), from which it is concluded that an increase in the plate-to-plate spacing ( $P$ ) resulted in a decrease in the particle collection efficiency. This reduction in the particle collection efficiency is caused by a reduced space charge density at increased distances from the wire surface as the value of  $P$  is increased.

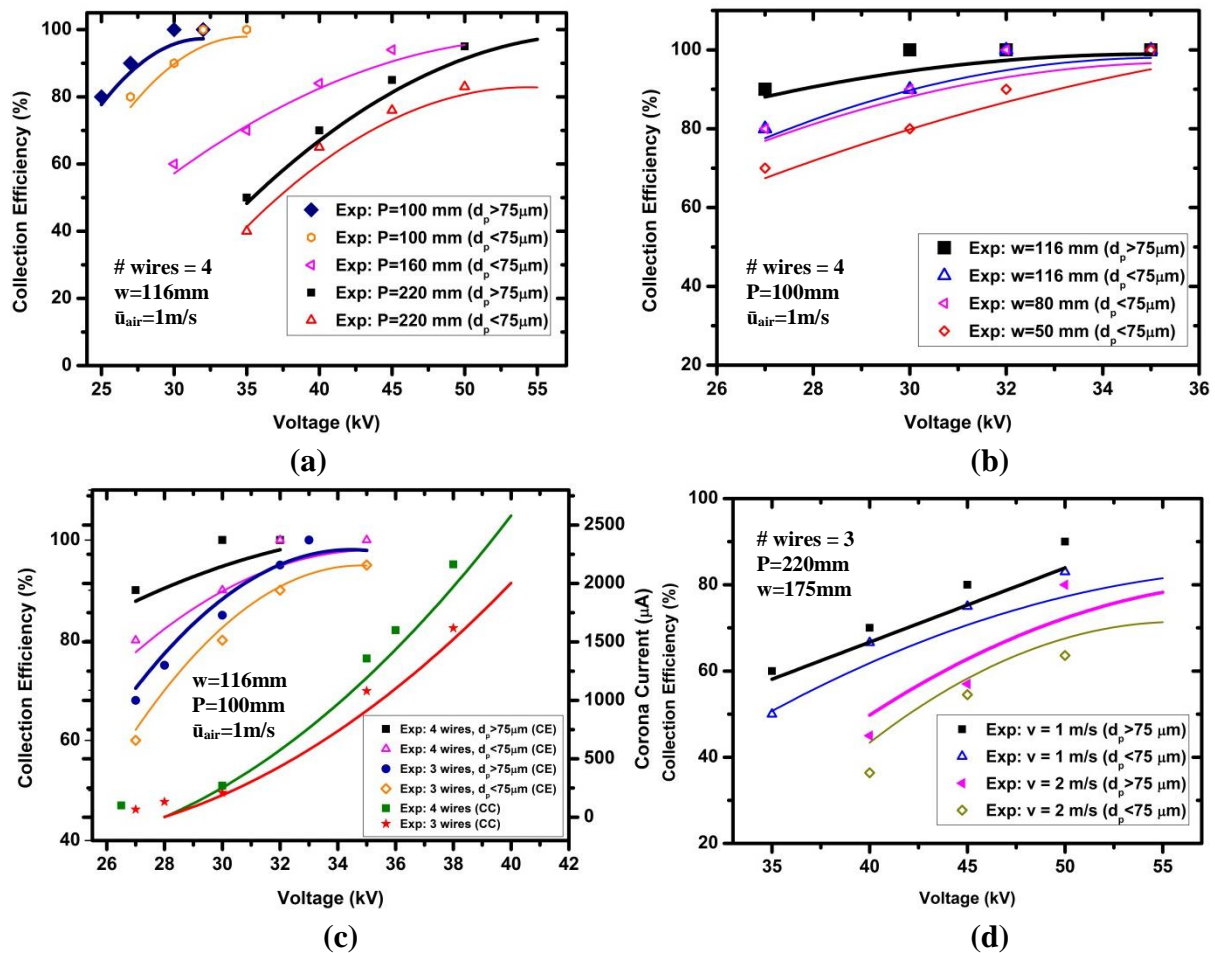


**Fig 5.6:** Comparison of the computational modelling results with the experimental measurements obtained under varying (a) plate-to-plate spacing ( $P$ ), (b) wire-to-wire spacing ( $w$ ), (c) number of wires, and (d) air flow velocity. The solid curves represent the computational modelling predictions (thick lines for  $d_p > 75 \mu\text{m}$ , and thin lines for  $d_p < 75 \mu\text{m}$ ). CE means collection efficiency and CC means corona current.

---

However, as shown previously [17], the shielding intensity also increases with increasing  $P$  that correlates with the geometric parameters for the cases represented in Fig. 5.6 (a). This increase in the shielding intensity is characterized by an increased suppression of the current density around the inner wire-electrodes compared to that of the outer electrodes [7,8,20,32] that in turn results in a further decreased current as validated by the results shown in Fig. 5.5 (a). It may therefore be concluded that the increasing shielding intensity also negatively impacted the collection efficiency when the plate-to-plate spacing was increased from 100 to 220 mm (Fig. 5.6 (a)). The root-mean-square deviation (RMSD) of the computational modelling predictions relative to the experimental measurements were found to range between 2.4 and 3.4 % for the results depicted in Fig. 5.6.

While keeping the plate-to-plate spacing ( $P$ ) fixed at 100 mm, and again using a constant number of four wire-electrodes, the effect of wire-to-wire spacing ( $w$ ) on particle collection efficiency was studied at  $w = 116, 80$ , and 50 mm. The results of this experimental set together with the comparison to the corresponding computational modelling results are shown in Fig. 5.6 (b). It is evident (Fig. 5.6 (b)) that the collection efficiency was reduced upon decreasing the wire-to-wire spacing from 116 to 50 mm. This decreased collection efficiency also correlates with an increase in the shielding intensity as the wire-to-wire spacing is reduced [17], which leads to a notable decrease in the corona current as validated by the results shown in Fig. 5.5 (b). The computational model slightly overestimated the amount by which the current is reduced when the wire-to-wire spacing was decreased from 116 to 80 mm (Fig. (5.6 (b))), which also led to the reduction in the collection efficiency being slightly overestimated by the computational model (Fig. 5.6 (b)). However, the computational model more accurately predicted the decrease in the collection efficiency at relatively low discharge electrode voltages up to 32 kV, when the wire-to-wire spacing was further reduced to 50 mm.

When the number of wire-electrodes were reduced from four to three, while a constant plate-to-plate spacing of 100 mm and a constant wire-to-wire spacing of 116 mm was used, a decrease in the collection efficiency was also noted as shown in Fig 5.6 (c). The decrease in the collection efficiency was comparatively more pronounced at lower discharge electrode voltages due to significantly reduced corona current as shown by the V-I results that are superimposed in Fig. 5.6 (c). It is also evident that the computational modelling predictions correlated well with the measured collection efficiencies over the range of discharge electrode voltages investigated.

Additional experiments were also performed using the same parameters as in the cases presented in Fig. 5.6 (c), except that the plate-to-plate spacing was increased to 220 mm. The results are shown in Fig. 5.7 in which there was no significant increase in the particle collection efficiency when replacing three wires with four wires for both particle size ranges. Such an insignificant change in the collection efficiency with an increase in the number of discharge electrodes can be ascribed to an increased degree of shielding as a result of a larger

plate-to-plate spacing [17]. In the case of Fig. 5.6 (c), the plate-to plate spacing was set at 100 mm, and as shown in Chapter 4 (Section 4.3.2.1), a smaller plate-to plate spacing is associated with decreased shielding intensity. In other words, the expected increase in the discharge current when adding an additional discharge electrode was offset by an increased degree of shielding, resulting in little to no change in the collection efficiency.

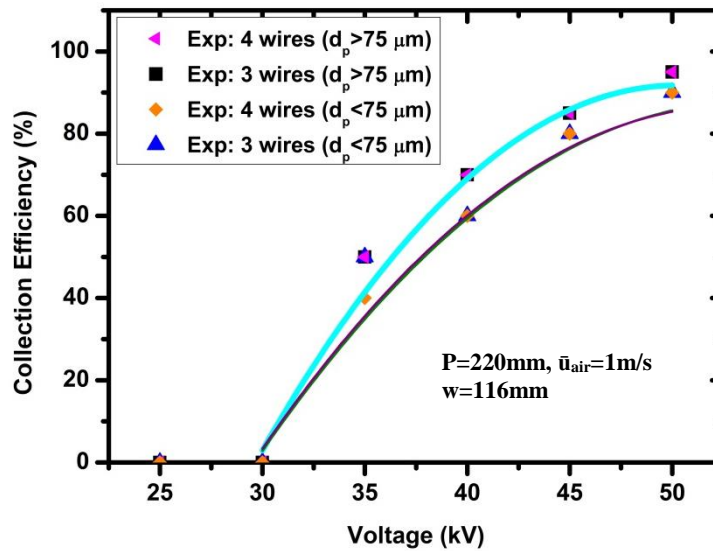


**Fig 5.7:** Comparison of the computational modelling results with the experimental measurements obtained under varying number of wires for both particle size ranges of fly ash and plate to plate spacing of 220 mm. The solid curves represent the computational modelling predictions (thick lines for  $d_p > 75 \mu\text{m}$ , and thin lines for  $d_p < 75 \mu\text{m}$ ).

The effect of superficial air flow velocity was also evaluated by adjusting the blower speed to achieve velocities of 1 and 2 m/s respectively as explained in Section 5.3.2 and in Appendix E in Section E.3.2. A plate-to-plate spacing of 220 mm with three wire-electrodes spaced 175 mm apart was used in both cases. The results are shown in Fig. 5.6 (d) from which it is clear that the collection efficiency was negatively influenced by doubling the air flow velocity. This is to be expected, since a higher flow velocity reduces the particle residence time in the ESP channel, which at a constant particle charging rate means the particles are charged to a lesser extent at higher velocities. Although the absolute values of the particle collection efficiency calculated with the computational model differed somewhat from the experimental values, the trend was accurately predicted. The slight deviation of the calculated values from the measured values indicates that further refinement of the fluid dynamics component of the computational model is required to improve the accuracy.

Furthermore, it is observed that the results presented in the different cases of Fig. 5.6 that the particle collection efficiencies increased with the reduction of the plate-to-plate spacing ( $P$ ) while increasing the wire-to-wire spacing ( $w$ ). This general trend corresponds with recently reported findings of other experimental and computational modelling studies [16,33]. It is therefore concluded that the current computational model accurately accounted for the

influence of the various geometric and operating parameters on the ESP collection efficiency, although the effect of the wire-to-wire spacing at high discharge electrode voltages, as well as the influence of air flow velocity were not as accurately predicted. Nonetheless, it is evident that the model also captures the influence of shielding, as described in our previous work [17], on the particle collection efficiency in wire-plate electrodes [8,10,17,27,34].

The experimental results, however, indicated that higher particle collection efficiencies were achieved for particles larger than 75  $\mu\text{m}$  compared to the collection efficiency achieved with particles smaller than 75  $\mu\text{m}$  as shown in Fig. E.1 in Appendix E.

### 5.4.3 ESP performance with a commercial spiked electrode

To further validate the suitability of the computational model to describe ESP performance when using irregularly shaped electrodes, ESP experiments were also conducted with the commercial spiked electrode [29,31] and the measurement results were compared with the computational modelling results. Only one electrode was used, and therefore no shielding effects

#### 5.4.3.1 Electrostatic properties of the spiked electrode

The relationship between the applied discharge electrode voltage and the corona current achieved with the spiked electrode was determined experimentally for all the geometries investigated. Representative results are shown in Fig. 5.8 in which the V-I profile of the spiked electrode is compared with respectively one and three wire-electrodes. The wire-electrodes were configured with a wire-to-wire spacing of 175 mm and the plate-to-plate spacing was fixed at 220 mm.

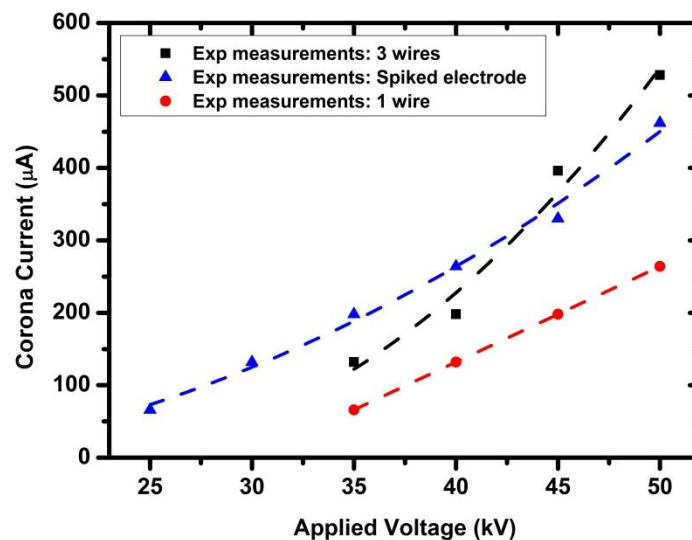


**Fig 5.8:** Comparison of the experimentally measured V-I relationship of the commercial spiked electrode to that of respectively one and three discharge wire-electrodes. The wire-to-

wire spacing for the three wire electrodes was 175 mm, and a plate-to-plate spacing of 220 mm was used in all cases. The broken lines are drawn to serve as a visual aid.

At a plate-to-plate spacing of 220 mm, it is clear from Fig. 5.8 that the single spiked electrode produced a corona current that was 2- to 4-fold higher than a single wire-electrode. A higher discharge current was also measured for the spiked electrode compared to that achieved with three wire-electrodes at discharge electrode voltages up to ca. 40 kV.

Representative results that illustrate the effect of the plate-to-plate spacing on the V-I relationship for a single spiked electrode is shown in Fig. 5.9. It is evident from that the corona onset voltage was lowered as the plate-to-plate spacing was reduced. Simultaneously, a steeper increase in the corona current is noted at a plate-to-plate spacing of 160 mm compared to that at 400 mm.

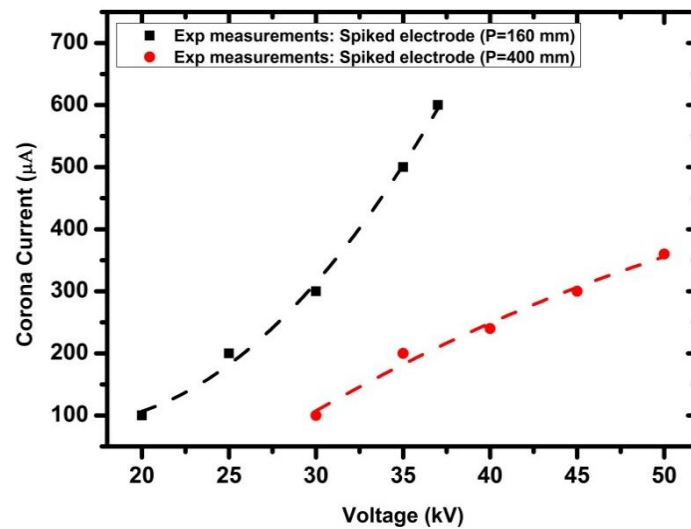


**Fig 5.9:** Experimentally measured V-I relationships of a single spiked electrode at plate-to-plate spacings of 160 and 400 mm respectively. The broken lines are drawn to serve as a visual aid.

These results as well as the V-I measurement results of all other geometries for which results are subsequently reported were used as input to the computational model. This was done to solve for the space charge density and current density distribution produced by the corona discharge from the spiked electrode for each of the cases that were investigated as Peek's law is not applicable to irregularly shaped electrodes. As previously noted, the electric discharge was assumed to occur only from the spike tips. Consequently, a guessed value for the space charge density at the spike tips was used to compute the current density at the spike tips, from which the total corona current was calculated and compared to the measured current at each discharge electrode voltage. The space charge density was subsequently rescaled and the



corona current recalculated, and this procedure was repeated until the calculated and measured currents differed by less than 0.5 – 1.5%.

Representative result of the modelled space charge density distribution achieved with a single spiked-electrode at a plate-to-plate spacing of 400 mm is shown in Fig 5.10 (a). The space charge density distribution is represented in Fig. 5.10 (a) as a scalar plot of the  $z$ - $x$  plane that intersects with the spike tips. The spikes are alternatingly curved towards opposite  $y$ -directions to enhance the distribution of the corona current and space charge density distribution. It is evident from comparison of Fig. 5.10 (a) and (b) that the space charge density achieved with the spiked electrode is almost one order of magnitude larger than that achieved with the wire-electrode. This is the case both at the discharge surface and upstream and downstream of the electrodes.

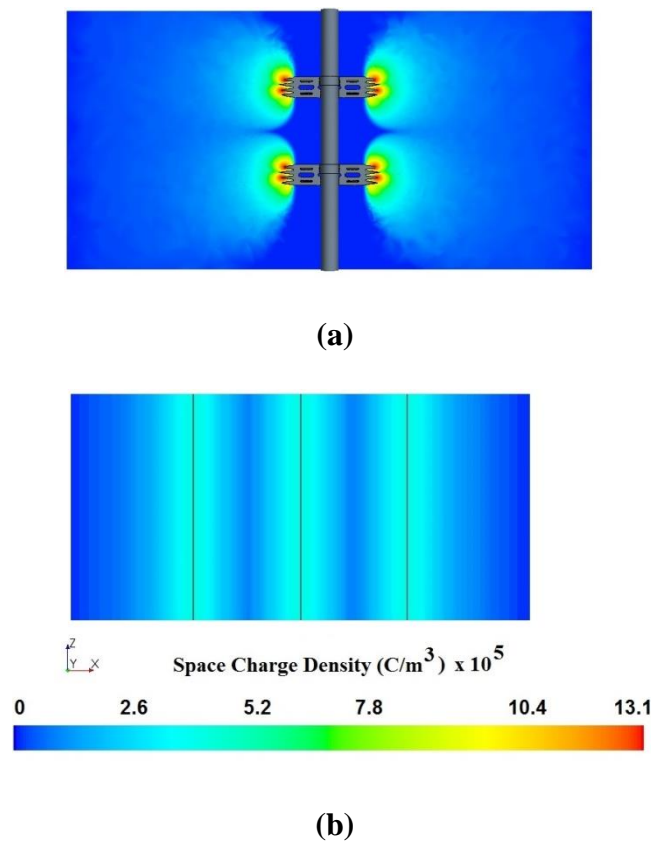


**Fig 5.10:** Two-dimensional space charge density distributions for (a) the commercial spiked discharge electrode, and (b) a wire-electrode. In both cases the plate-to-plate spacing was 400 mm and the model calculations were done at a discharge electrode voltage of 40 kV.

The higher space charge density generated with the spiked electrode, which in turn leads to a higher corona current compared to a simple wire-electrode (Fig. 5.8 and Fig. 5.9), facilitates more efficient charging of the dust particles as they are transported through the ESP channel. It is therefore expected that enhanced particle collection efficiency should be achieved with the spiked discharge electrode, which is illustrated in the following section.

### 5.4.3.2 Particle collection efficiency

The computational modelling and experimental results of collection efficiency achieved with one and three wire-electrodes ( $w = 175$  mm) and one spiked discharge electrode respectively are shown in Fig 5.11. Good correlation between the experimental measurements and the modelling predictions is evident. The spiked electrode clearly outperformed a single wire-electrode, which corresponds with findings reported in the literature [33]. However, the collection efficiency obtained with three wire-electrodes was higher than that obtained with a single spike electrode (Fig. 5.11).

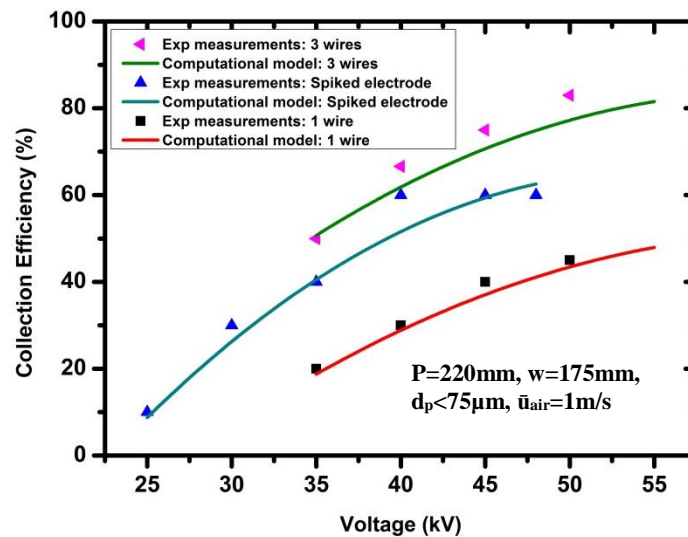


**Fig 5.11:** Comparison of experimental and computational modelling results of ESP collection efficiency obtained when using one and three wire-electrodes and a single spiked electrode respectively. The parameters that were kept constant in each case are summarized on the figure as well.

The effect of plate-to-plate spacing on the collection efficiency obtained with a single spiked electrode is shown in Fig. 5.12 in which the computational modelling predictions are again compared to the experimental measurements. Again, the computational modelling results corresponded well with the experimental measurements as shown in Fig. 5.12. The computational model therefore correctly predicted the general trend of reduced particle collection efficiency at a larger plate-to-plate spacing.



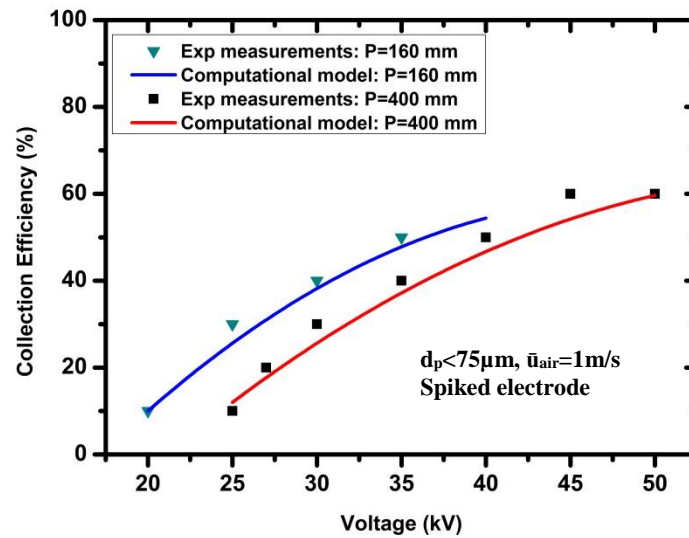


**Fig 5.12:** Particle collection efficiency obtained from computational modelling calculations and experimental measurements for plate-to-plate spacings of 160 and 400 mm respectively while using a spiked electrode and fly ash particles with diameters smaller than 75  $\mu\text{m}$ .

The validity of the computational model to describe the particle collection efficiency obtained for particles with diameters larger than 75  $\mu\text{m}$  when using the spiked electrode was also tested against experimental measurements as shown in Fig. 5.13.

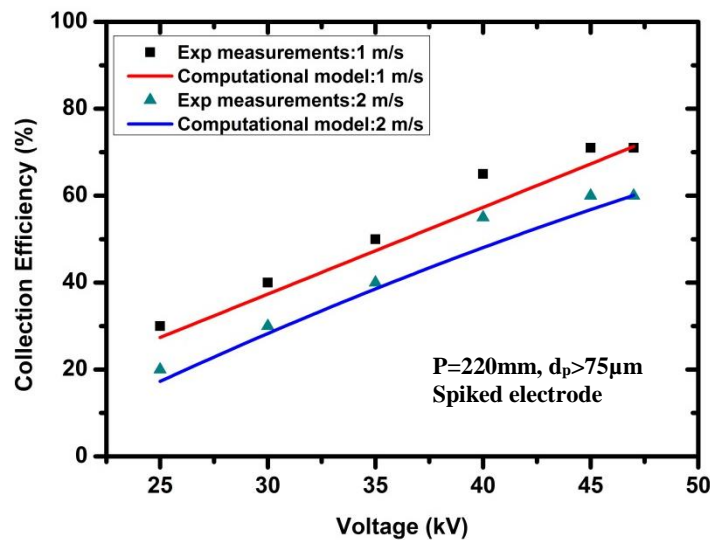


**Fig 5.13:** Particle collection efficiency obtained from computational modelling calculations and experimental measurements for two different air flow velocities while using a single spiked electrode and fly ash particles with diameters larger than 75  $\mu\text{m}$ .

A plate-to-plate spacing of 220 mm was again used in all cases illustrated in Fig. 5.13, while the superficial air flow velocity was set to 1 and 2 m/s respectively. The computational

modelling results once again corresponded closely with the experimental measurements, and in both cases the collection efficiency was reduced when the air flow velocity was doubled from 1 to 2 m/s. Although this result is to be expected, it is interesting to note that the reduction in the collection efficiency is less when compared to the reduction that was observed when using three wire-electrodes (Fig. 5.6 (d)). This is partly due to fly ash with a larger particle diameter having been used with the spiked electrode, which is generally more efficiently collected than smaller particles [27,28,35].

The validity of the computational model to describe the relationship between particle size and collection efficiency for an irregularly shaped electrode was subsequently also investigated, of which the results are shown in Fig. 5.14. A constant plate-to-plate spacing of 220 mm was used with the spiked electrode, and as expected, slightly higher collection efficiency was obtained experimentally. Furthermore, satisfactory agreement between the experimental results and the computational modelling calculations were again obtained.

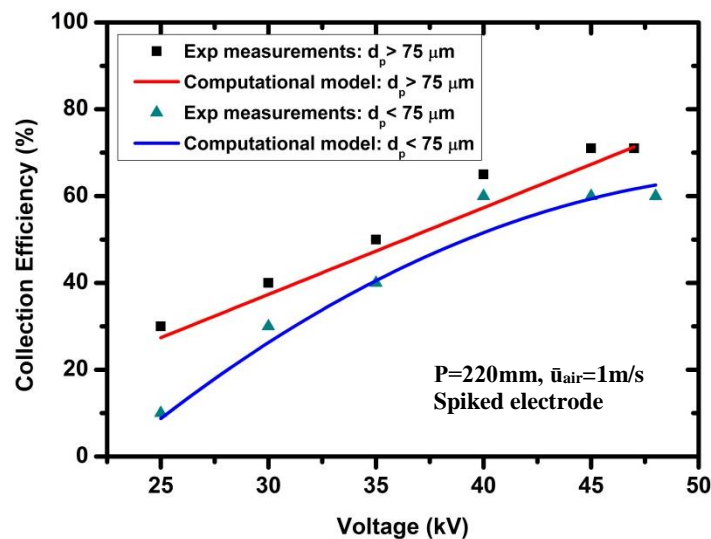


**Fig 5.14:** Particle collection efficiency obtained from computational modelling calculations and experimental measurements for two different fly ash particle size ranges while using a single spiked electrode and a plate-to-plate spacing of 220 mm.

The results of the comparisons between the computational modelling predictions and the experimental particle collection efficiency measurements as presented in this section shows that the current computational model can describe the influence of all the parameters investigated on ESP performance with good accuracy. The applicability of the computational model to predict particle collection efficiency of a single-channel ESP with multiple wire-electrodes, or a single rigid discharge electrode is therefore validated.

---

## 5.5 Conclusions

A laboratory scale ESP was constructed for the generation of results suitable for comparison to and validation of computational modeling results. The model consisted essentially of two parts with the first confined to the electrostatic field and the second part describing the fluid and particle dynamics, which included particle charging, to calculate particle collection efficiency as a function of various ESP parameters.

The comparison of the experimental and modelling results consisted of the V-I relationships and the collection efficiencies for various ESP geometries and operational parameters, and for two different discharge electrode types. Good comparison was found for the experimental and modeling results obtained for the wire-electrodes with respect to the V-I relationships under shielding and non-shielding conditions. Consequently, the effect of shielding on the particle collection efficiency as predicted by the computational model was also validated with the experimental results obtained with varying plate-to-plate and wire-to-wire spacing. Moreover, the computational model was shown to account for the influence of the number of electrodes, the applied discharge electrode voltage, gas flow rate, and particle sizes on the particle collection efficiency with good accuracy.

In the case of wire-electrodes, Peek's law could be used to simulate the corona discharge by modeling each individual wire-electrode to account for the interaction of the electrostatic field produced by each electrode. However, in the case of the spiked discharge electrode, the space charge density current density distributions were calculated using the experimentally measure V-I relationship as input to the computational model. While assuming that the spike-tips were the only corona-producing surfaces, it was found that the modelling predictions correlated well with the experimental measurements in terms of collection efficiency when using a single spiked electrode. The collection efficiencies achieved with the spiked electrode were also considerably higher than those obtained when using a single wire-electrode, which is ascribed to the higher space charge densities generated with the spiked electrode.

## 5.6 References

- [1] E.W. Stenby, R.W. Scheck, S.D. Severson, F.A. Horney, D.P. Teixeira, Fabric filters versus electrostatic precipitators, *Environ. Int.* 6 (1981) 103–114. doi:10.1016/0160-4120(81)90016-7.
- [2] Norton Engineering LLC, Environmental Balance: Baghouses vs Precipitators, <http://www.environmentalengineering.net/environmental/baghouses.php>.
- [3] Van Wyk, Marabwa, ESKOM Holdings SOC Ltd, (2015).
- [4] B. Guo, D. Yang, Y. Su, A.B. Yu, Process modelling of low temperature electrostatic precipitators, *Powder Technol.* 314 (2016) 567–576. doi:10.1016/j.powtec.2016.09.071.
- [5] A.Z. El Dein, K. Usama, Experimental and Simulation Study of V-I Characteristics of Wire-Plate Electrostatic Precipitators Under Clean Air Conditions, *Arab. J. Sci. Eng.* 39 (2014) 4037–4045. doi:10.1007/s13369-014-1046-2.

- 
- [6] D.U. Kogelschatz, E.A. Gerteisen, Advanced computer modelling of electrostatic precipitators, *Filtr. Sep.* 38 (2001) 32–37. doi:10.1016/S0015-1882(01)80538-3.
- [7] Z. Al-Hamouz, A. El-Hamouz, N. Abuzaid, Simulation and experimental studies of corona power loss in a dust loaded wire-duct electrostatic precipitator, *Adv. Powder Technol.* 22 (2011) 706–714. doi:10.1016/j.appt.2010.10.005.
- [8] A. Kasdi, Computation and measurement of corona current density and V-I characteristics in wires-to-plates electrostatic precipitator, *J. Electrostat.* 81 (2016) 1–8. doi:10.1016/j.elstat.2016.02.005.
- [9] Z. He, E.T.M. Dass, G. Karthik, Design of electrostatic precipitator to remove suspended micro particulate matter from gas turbine inlet airflow: Part I. Experimental study, *J. Aerosol Sci.* 108 (2017) 14–28. doi:https://doi.org/10.1016/j.jaerosci.2017.03.003.
- [10] S. Arif, D.J. Branken, R.C. Everson, H.W.J.P. Neomagus, L.A. le Grange, A. Arif, CFD modeling of particle charging and collection in electrostatic precipitators, *J. Electrostat.* 84 (2016). doi:10.1016/j.elstat.2016.08.008.
- [11] S. Kim, K. Lee, Experimental study of electrostatic precipitator performance and comparison with existing theoretical prediction models, *J. Electrostat.* 48 (1999) 3–25. doi:10.1016/S0304-3886(99)00044-3.
- [12] Z. Zhibin, Z. Guoquan, Investigations of the collection efficiency of an electrostatic precipitator with turbulent effects, *Aerosol Sci. Technol.* 20 (1994) 169–176. doi:10.1080/02786829408959674.
- [13] M. Jdrusik, J.B. Gajewski, A.J. Wierczok, Effect of the particle diameter and corona electrode geometry on the particle migration velocity in electrostatic precipitators, *J. Electrostat.* 51-52 (2001) 245–251. doi:10.1016/S0304-3886(01)00047-X.
- [14] M. Jedrusik, A. Swierczok, R. Teisseyre, Experimental study of fly ash precipitation in a model electrostatic precipitator with discharge electrodes of different design, *Powder Technol.* 135-136 (2003) 295–301. doi:10.1016/j.powtec.2003.08.021.
- [15] M. Jedrusik, A. Świerczok, The correlation between corona current distribution and collection of fine particles in a laboratory-scale electrostatic precipitator, *J. Electrostat.* 71 (2013) 199–203. doi:10.1016/j.elstat.2013.01.002.
- [16] X. Xu, C. Zheng, P. Yan, W. Zhu, Y. Wang, X. Gao, et al., Effect of electrode configuration on particle collection in a high-temperature electrostatic precipitator, *Sep. Purif. Technol.* 166 (2016) 157–163. doi:10.1016/j.seppur.2016.04.039.
- [17] S. Arif, D.J. Branken, R.C. Everson, H.W.J.P. Neomagus, A. Arif, The influence of design parameters on the occurrence of shielding in multi-electrode ESPs and its effect on performance, *J. Electrostat.* 93 (2018). doi:10.1016/j.elstat.2018.03.001.
- [18] N. Farnoosh, K. Adamiak, G.S.P. Castle, Three-dimensional analysis of electrohydrodynamic flow in a spiked electrode-plate electrostatic precipitator, *J. Electrostat.* 69 (2011) 419–428. doi:10.1016/j.elstat.2011.06.002.
- [19] N. Farnoosh, K. Adamiak, G.S.P. Castle, Numerical calculations of submicron particle removal in a spike-plate electrostatic precipitator, in: *IEEE Trans. Dielectr. Electr. Insul.*, 2011: pp. 1439–1452. doi:10.1109/TDEL.2011.6032814.

- 
- [20] Z. He, E.T.M. Dass, Correlation of design parameters with performance for electrostatic Precipitator. Part I. 3D model development and validation, *Appl. Math. Model.* (2017). doi:<https://doi.org/10.1016/j.apm.2017.05.042>.
- [21] Z. He, E.T.M. Dass, Correlation of design parameters with performance for electrostatic precipitator. Part II. Design of experiment based on 3D FEM simulation, *Appl. Math. Model.* (2017). doi:<https://doi.org/10.1016/j.apm.2017.06.031>.
- [22] H. Nouri, N. Zouzou, L. Dascalescu, Y. Zebboudj, Investigation of relative humidity effect on the particles velocity and collection efficiency of laboratory scale electrostatic precipitator, *Process Saf. Environ. Prot.* 104 (2016) 225–232. doi:[10.1016/j.psep.2016.09.001](https://doi.org/10.1016/j.psep.2016.09.001).
- [23] K. Luo, Y. Li, C. Zheng, X. Gao, J. Fan, Numerical simulation of temperature effect on particles behavior via electrostatic precipitators, *Appl. Therm. Eng.* 88 (2014) 127–139. doi:[10.1016/j.applthermaleng.2014.11.078](https://doi.org/10.1016/j.applthermaleng.2014.11.078).
- [24] N. Farnoosh, K. Adamiak, G.S.P. Castle, 3-D numerical simulation of particle concentration effect on a single-wire ESP performance for collecting poly-dispersed particles, *IEEE Trans. Dielectr. Electr. Insul.* 18 (2011) 211–220. doi:[10.1109/TDEI.2011.5704512](https://doi.org/10.1109/TDEI.2011.5704512).
- [25] Z. Long, Q. Yao, Evaluation of various particle charging models for simulating particle dynamics in electrostatic precipitators, *J. Aerosol Sci.* 41 (2010) 702–718. doi:[10.1016/j.jaerosci.2010.04.005](https://doi.org/10.1016/j.jaerosci.2010.04.005).
- [26] T. Iváncsy, J.M. Suda, Behavior of polydisperse dust in electrostatic precipitators, *J. Electrostat.* 63 (2005) 923–927. doi:[10.1016/j.elstat.2005.03.062](https://doi.org/10.1016/j.elstat.2005.03.062).
- [27] N. Farnoosh, K. Adamiak, G.S.P. Castle, 3-D numerical analysis of EHD turbulent flow and mono-disperse charged particle transport and collection in a wire-plate ESP, *J. Electrostat.* 68 (2010) 513–522. doi:[10.1016/j.elstat.2010.07.002](https://doi.org/10.1016/j.elstat.2010.07.002).
- [28] G. Skodras, S.P. Kaldis, D. Sofialidis, O. Faltsi, P. Grammelis, G.P. Sakellariopoulos, Particulate removal via electrostatic precipitators - CFD simulation, *Fuel Process. Technol.* 87 (2006) 623–631. doi:[10.1016/j.fuproc.2006.01.012](https://doi.org/10.1016/j.fuproc.2006.01.012).
- [29] F. August Mischkulnig, Discharge electrode, US Patent 7,160,364B2 (2007).
- [30] CD-ADAPCO, User Guide STAR CCM+ V. 9.02, (2014) 4482–4484.
- [31] G. Mischkulnig, P. Bento, Enhanced corona discharge using innovative rigid discharge electrodes (RDE), in: 9th Int. Conf. Electrostat. Precip.: pp. 1–12.
- [32] M. Abdel-Salam, A. Eid, Finite element simulation of corona in wire-duct precipitators, *Conf. Rec. 2002 IEEE Ind. Appl. Conf. 37th IAS Annu. Meet. (Cat. No.02CH37344)*. 2 (2002) 1383–1389.
- [33] S. Sander, S. Gawor, U. Fritsching, Separating polydisperse particles using electrostatic precipitators with wire and spiked-wire discharge electrode design, *Particuology*. (2017). doi:[10.1016/j.partic.2017.05.014](https://doi.org/10.1016/j.partic.2017.05.014).
- [34] Z. Al-Hamouz, Numerical and experimental evaluation of fly ash collection efficiency in electrostatic precipitators, *Energy Convers. Manag.* 79 (2014) 487–497. doi:[10.1016/j.enconman.2013.11.047](https://doi.org/10.1016/j.enconman.2013.11.047).
- [35] Q. Liu, S. S. Zhang, J. P. Chen, Numerical analysis of charged particle collection in wire-plate

ESP, J. Electrostat. 74 (2015) 56–65. doi:10.1016/j.elstat.2014.11.007.

---

## Chapter 6. CONCLUSIONS AND RECOMMENDATIONS

A summary of the main findings and outcomes of the work presented in this thesis according to the defined aim and objectives is presented in this chapter. The contributions made in the thesis to the field of computational modelling of electrostatic precipitation are also listed. Finally, recommendations with respect to refinements that can be made to the experimental system for future studies and aspects that may be considered for further work are also briefly discussed.

### 6.1 Summary and conclusions

The following conclusions can be drawn from the findings of the present research work:

1. A composite computational model that can account for the interacting fields of fluid dynamics, particle dynamics and electrostatics was developed using the commercial CFD software package STAR-CCM+® and the open source software code OpenFOAM®. The electrostatic field could be successfully solved using OpenFOAM and was introduced into STAR-CCM+ as user-defined field functions. The STAR-CCM+ software was subsequently used to model the coupling between the particle and fluid dynamics.
2. Particle charging was modeled using two charging equations, i.e. that of Lawless and the charging model developed by Pauthenier Moreau-Hanot and White (PMHW), and the latter was found to yield the most accurate results when compared with experimental results taken from the literature.
3. The relative permittivity of the coal ash showed to have a significant influence on particle collection efficiency, which increases with the relative permittivity of the ash. A sensitivity analysis using the computational model as validated using bench-scale ESP data available in the literature further revealed that geometric and operating parameters as listed below also significantly influences the particle collection efficiency. These are namely:
  - I. Wire-to-wire spacing,
  - II. Wire-to-plate spacing,
  - III. Radius of the wire-electrodes,
  - IV. Discharge electrode design,
  - V. Applied discharge electrode voltage,
  - VI. Air velocity, and
  - VII. Particle diameter.
4. The developed model was also shown to be capable of modelling the corona discharge for more sophisticated discharge electrodes such as simple spike electrodes. In agreement with literature information, improved particle collection efficiencies were predicted for a single-channel, single electrode ESP equipped with a spike discharge

---

electrode compared to a wire-electrode. This improvement in the collection efficiency also correlated with an increased corona current and space charge density.

5. It was subsequently shown that the developed computational model could be further adapted to quantify the shielding effect that can arise between adjacent discharge electrodes in multi-electrode ESP systems by applying the boundary conditions for solving the governing equations separately for each electrode. The effect of various geometric parameters such as the inter-electrode spacing for wire electrodes, the inter-plate spacing and the number of discharge electrodes on the extent of shielding could be analyzed by studying the space charge density and current density distribution. It was found that all these parameters had a significant influence on the degree of shielding, but that the plate-to-plate spacing is a critical factor in this regard.
6. The negative effect of shielding on the discharge current that was predicted by the computational modelling results was subsequently confirmed, and an increased shielding intensity was also shown to correlate with a reduced particle collection efficiency. Although shielding was only studied in the case of wire electrodes, since the corona discharge characteristics can be modeled by applying Peek's law, the modelling method can be easily extended to other electrode designs. However, experimental measurement of the discharge current produced by each individual electrode in a multi-electrode arrangement is required to model the corona discharge from each electrode.
7. Subsequent comparison of the computational modelling predictions with experimental measurements on ESP collection efficiency as a function of geometric and operating parameters using a custom designed and built laboratory-scale ESP were performed. The results showed that the computational model developed in this study yielded predicted collection efficiencies that agreed well with experimental results, as RMSD values of typically 3% were found. In addition to being capable of describing the effect of various operating and ESP design parameters on particle collection efficiency, the additional effects of shielding on the electrostatic field and consequently the particle collection efficiency are also incorporated in the developed model. To date, no other integrated ESP model has been reported in the literature that incorporates the effects of shielding.
8. The developed model was further applied to model the effects of discharge electrode design on particle collection efficiency, of which the results were compared with experimental measurements. A spiked ridged discharge electrode served as model electrode in this regard, of which the measured V-I characteristics was used as input to the computational model. Hereby, the space charge density and current density distribution resulting from corona discharge from this spiked electrode could be characterized. Because of a high discharge current and space charge density, a significantly increased collection efficiency was afforded with the use of a single spiked electrode compared to a single wire-electrode. Again, the experimental and computational modelling results agreed reasonably well.



9. It is envisaged that the developed model be subsequently applied to provide a framework for evaluating options for operating and design modification that can be implemented on plant-scale ESPs such that adherence to the minimum emissions standards as stipulated in the NEM: AQA may be achieved.

## **6.2 Contribution to the current knowledge**

The following achievements can be considered as valuable contributions to the field of computational modelling of electrostatic precipitators:

1. It was shown that the open source software OpenFOAM provides a convenient platform to solve the governing equations related to the electrostatic field without the need for any specialized computational modeling techniques or algorithms. Moreover, the results can be conveniently coupled with a detailed CFD model of the ESP system being studied, whereby the coupled effect of the electrostatic field, the particle dynamics field, and the fluid dynamics field on particle collection efficiency may be evaluated as a function of ESP design and operating parameters.
2. The developed model was shown to allow the quantification of the extent of shielding. Thus, in addition to the model's capability of accounting for the effect of ESP design and operational parameters on particle collection efficiency, the model also allows the inclusion of the effect of shielding on the corona discharge characteristics and subsequently on the ESP performance. Alternatively, the model may be used to identify the conditions under which shielding would occur, and which should thus be avoided on full-scale ESPs. In other words, the model may also be used to evaluate the optimum ESP design parameters where the discharge current is maximized, while avoiding or minimizing the incidence of shielding.
3. It was shown that the current computational model could also be applied to model and evaluate the performance of discharge electrodes as a function of their geometric design. Furthermore, the spiked electrode that was used as a model electrode in this respect was found to afford greater discharge currents and consequently increased particle collection efficiencies compared to wire-type discharge electrodes.

## **6.3 Recommendations**

Based on the findings presented in this thesis, it is recommended that the following aspects be considered to further expand the computational model and the laboratory-scale ESP unit:

1. Using the developed computational model, the coal ash relative permittivity was shown to significantly influence particle charging and collection. However, resistivity is predominantly used as an important parameter in industry and in the literature to estimate ESP collection efficiency, and therefore the correlation between fly ash resistivity and relative permittivity, should be investigated. Furthermore, the relation between the two parameters as a function of ambient conditions such as temperature, relative humidity, and the concentration of conditioning agents, should be studied to allow further refinement of the current model.

2. The inclusion of particle space charge effects can be incorporated in the present model to allow accurate modelling of cases in which the particle concentrations are high enough such that their effect on the electrostatic field cannot be neglected.
3. The laboratory-scale ESP may be modified to allow measurement of the discharge current produced by each individual electrode in a multi-electrode assembly to allow the shielding effects that can arise when using sophisticated electrodes such as the spiked electrode to be evaluated both experimentally and computationally. This would assist in finding the optimum geometrical parameters under which a multi-electrode assembly would provide maximum performance. More specifically, the efficiency of various electrode designs can be evaluated and the optimum inter-electrode and plate-to-plate spacing at which the corona discharge current is maximized can be determined. Such information would be valuable for improving the efficiency of industrial ESPs where emissions limits are not being met.
4. The experimental ESP unit can also be modified to allow control of the air temperature and composition in terms of moisture content and possibly other conditioning agents. Thereby, the model can be further refined, as mentioned in point (1), and may be validated using experimental data generated with the modified ESP unit.
5. The accuracy of the model can also be improved by expanding the electrostatic sub-model to include back-corona effects.

## Appendix A. SUPPLEMENTARY INFORMATION FOR CHAPTER 3

Supplementary information regarding the influence of fluid velocity on the electrostatic field properties accompanies the publication that was based on Chapter 3 and is available for download from the <https://doi.org/10.1016/j.elstat.2016.08.008>. For convenience, the supplementary information is also presented in this appendix.

### A.1 Introduction

The effect of air flow velocity on the electrostatic field, or more specifically the space charge density was investigated to evaluate the significance thereof w.r.t. the numerical simulations. In other words, to determine whether coupling between the electrostatic field and the fluid dynamic field should be considered in the numerical modelling of practical ESP processes.

### A.2 Method

The open source software OpenFOAM was used for the simulations. The fluid dynamic and electrostatic fields were coupled by in the OpenFOAM simulations by combining the numerical solution method (solver) of each, instead of exporting the electrostatic field results from OpenFOAM into STAR-CCM+ and subsequently solving the governing equations for fluid dynamics as was done in the simulations described in the chapter 3. Consequently, the influence of the fluid dynamics on the electrostatic properties, particularly the space charge density, could be evaluated as a function of gas flow velocity. The flow velocity was therefore varied between 1 and 200 m/s. The detailed ESP geometry as well as the simulation method used for this investigation is described in the following sections.

#### A.2.1 ESP geometry

The simulated ESP geometry consisted of a single channel system with eight wire-type discharge electrodes and two collecting plates as shown in Fig 3.1 of the chapter 3. The wire-type discharge electrodes were mounted in the middle of the two collecting plates in the  $z$ -direction. The gas flow was considered to be in the positive  $x$ -direction. The total length of the ESP channel was 0.75 m, with a side length of 0.05m and the discharge wires had a diameter of 0.1 mm. More detailed information relating to geometric and simulation parameters are given in Table 3.3 of chapter 3.

#### A.2.2 Simulation method

As for the simulations described in chapter 3, the Poisson equation as defined in Eq. (A.1) was used to describe the electrostatic field inside the ESP:

$$\nabla^2 V = -\frac{\rho_w}{\epsilon_0} \quad (\text{A.1})$$

where

$$\vec{E} = -\nabla V \quad (\text{A.2})$$

The resulting gas ions are attracted to the collection electrodes under the influence of Coulomb body forces that result in an electric current with a density defined by Eq. (A.3):

$$\vec{J} = \rho_w (b\vec{E} + \vec{u}_{gas}) - D_i \nabla \rho_w \quad (\text{A.3})$$

Under steady state conditions, charge conservation must be satisfied, and therefore:

$$\begin{aligned} \nabla \cdot \vec{J} &= 0 \\ \nabla \cdot (b\rho_w \vec{E} + \rho_w \vec{u}_{gas} - D_i \nabla \rho_w) &= 0 \end{aligned} \quad (\text{A.4})$$

The diffusion term ( $D_i \nabla \rho_w$ ) is negligible compared to the convective and drift terms, and unlike the simulations described in chapter 3 the influence of convective gas flow ( $\rho_w \vec{u}_{gas}$ ) on the electrostatic field was also considered for the simulation reported herein. Therefore, Eq. (A.5) was used:

$$\nabla \cdot (b\rho_w \vec{E} + \rho_w \vec{u}_{gas}) = 0 \quad (\text{A.5})$$

The above Eq. (A.1), (A.2) and (A.5) were solved simultaneously in OpenFOAM, together with the continuity equation for gas flow (Eq. (3.8) in the chapter 3), thereby achieving two-way coupling between the electric and fluid dynamic field. The corresponding OpenFOAM code is shown in the Appendix B. The simulations were performed only to evaluate the effect of convection on the electrostatic field, and therefore particles were not included in these simulations. The boundary conditions used for the simulations are the same as those given in Table 3.1 of chapter 3.

### A.3 Results and discussion

The simulation results are shown in Fig. A-1 (a) – (g), from which it is apparent that gas flow has a significant effect on the space charge density when the flow velocity is very high, i.e. in the order of 100 m/s. However, in practical ESP processes the typical air flow velocity is two orders of magnitude smaller, i.e. in the order of 1 m/s to 2 m/s, and it is apparent from the results that the electrostatic field is unaffected at such low gas flow velocities.

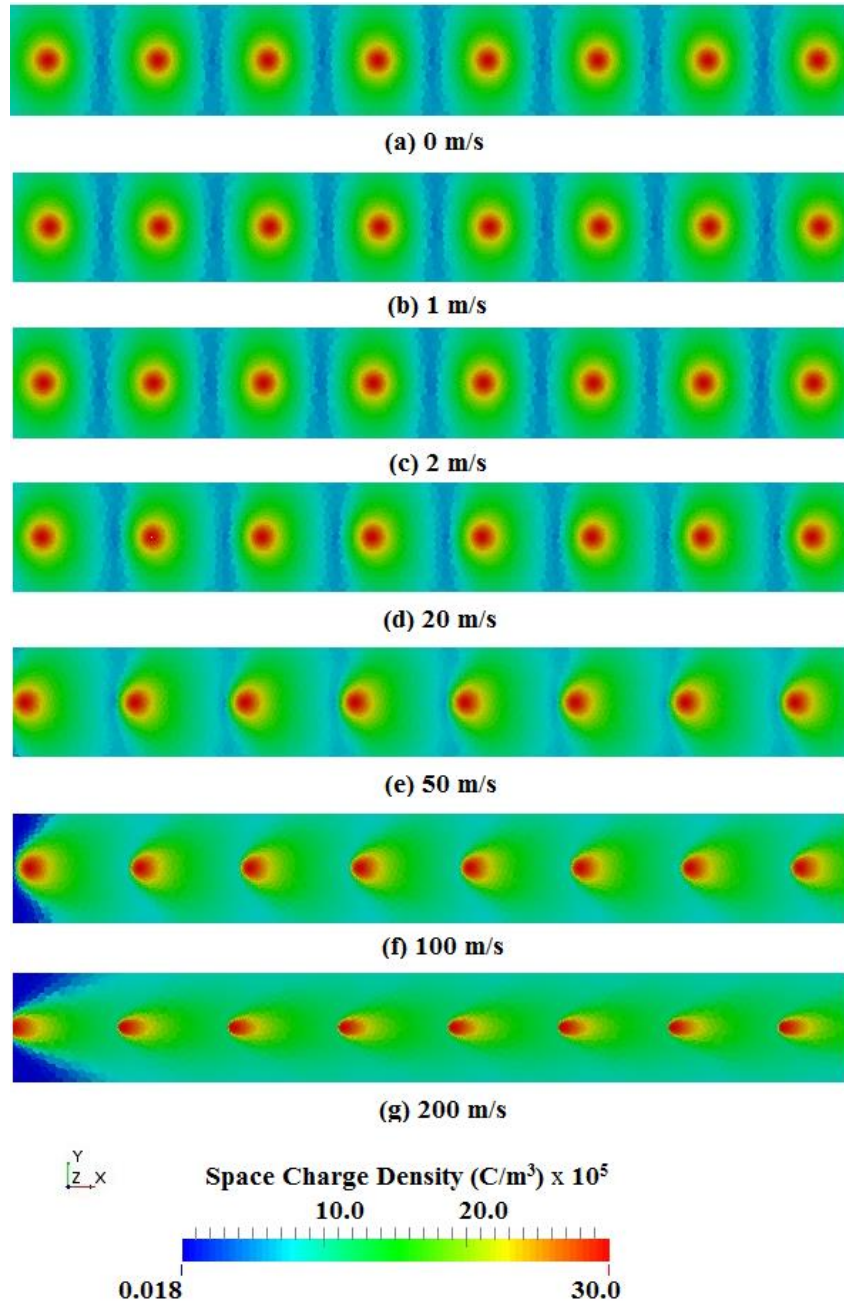


**Fig A-1:** Space Charge Density distributions for different flow velocities ranging from 0 m/s to 200 m/s

At such low air flow velocities the fluid dynamic field therefore has an insignificant influence on the space charge density, and therefore also the electrostatic field and current density distributions. This conclusion is further corroborated by the results as shown in Fig. A-2, in which the space charge density variation in the  $x$ -direction at the  $y$ -position of the two discharge electrodes (wire 2 & wire 3) is shown for the plane  $z = 0.05$  m.

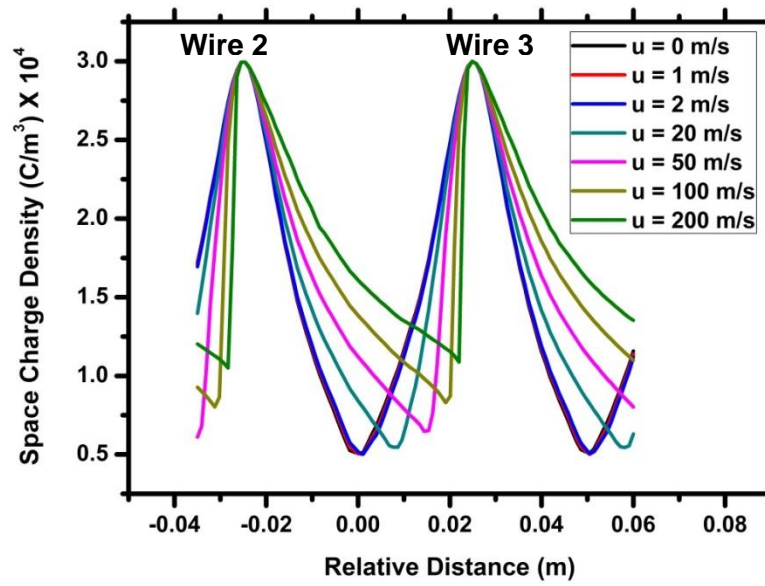


**Fig A-2:** Variation of space charge density with gas flow velocity between two successive wire discharge electrodes.

From the results shown in Fig. A-2, a small effect on the space charge density can be noted at a gas flow velocity of 20 m/s, which intensifies as the flow velocity is increased to 200 m/s. In contrast, the effect on the space charge density diminishes as the flow velocity is decreased from 20 m/s to 1 m/s. It is also clear from the Fig. A-2 that at flow velocities of more than 20 m/s, the space charge density between the successive discharge wires are noticeably increased, which would benefit particle charging and therefore collection efficiency. However, such high velocities are not found in either industrial ESPs or laboratory-scale systems.

#### A.4 Conclusions

It is therefore clear that the fluid dynamic field does not influence the electrostatic field at the relatively low flow velocities that are used in practical ESP processes. Therefore, the current density equation, Eq. (A.4), as used in the simulations described in chapter 3 represents a valid simplification when gas flow velocities are lower than 10 m/s. It is therefore further concluded that the method used in chapter 3, in which the space charge density simulation results obtained from the OpenFOAM simulations are imported into the STAR-CCM+ models, is sound and justified. The reason being that coupling between the fluid dynamic field and the electrostatic field can be ignored under the conditions investigated in chapter 3.

## Appendix B. COMPUTATIONAL MODELLING SUMMARY

**Table B-1:** Description of governing equations for CFD modelling

Parameters	Governing equations
<b>Electrostatics</b>	
Poisson equation	$\nabla^2 V = -\frac{\rho_w}{\epsilon_0}$
Electric current density	$\vec{J} = \rho_w \left( b\vec{E} + \vec{u}_{gas} \right) - D_i \nabla \rho_w$
Charge conservation equation	$\nabla \cdot \vec{J} = 0$ $\nabla \cdot (b\rho_w \vec{E}) = 0$
Peek's law formula	$\vec{E}_p = 3.1 \times 10^6 \left( 1 + \frac{0.308}{\sqrt{r_c}} \right)$
<b>Continuous phase fluid dynamics</b>	
Navier Stokes equation (EHD flow included)	$\rho_f \left[ \frac{\partial \vec{u}_{gas}}{\partial t} + \vec{u}_{gas} \cdot \nabla \vec{u}_{gas} \right] = -\nabla P + \mu_{eff} \nabla^2 \vec{u}_{gas} + \rho_w \vec{E}$
Continuity equation	$\nabla \cdot \vec{u}_{gas} = 0$
<b>Particle dynamics</b>	
Force balance (particle charging included)	$m_p \frac{dv_p}{dt} = \frac{1}{2} C_d \rho_f A_p  v_s  v_s + m_p g \left( \frac{\rho_p - \rho_f}{\rho_f} \right) + Q_p \vec{E}$
<b>Particle Charging</b>	
Saturation charge	$Q_{sat} = \frac{3\epsilon_r}{\epsilon_r + 2} \pi \epsilon_0 d_p^2  \vec{E} $
Particle charge	$Q_p(t) = Q_{sat} \left( \frac{t}{t + \tau_c} \right) + \frac{2\pi \epsilon_0 d_p K_B T}{e} \ln \left( 1 + \frac{t}{\tau_l} \right)$
Charging time constant	$\tau_c = \frac{4\epsilon_o}{b\rho_w}$
Model constant	$\tau_l = \frac{8\epsilon_o K_B T}{d_p e u \rho_w}$

**Table B-2:** Summary of boundary conditions

<b>Geometric surface</b>	<b>Gas flow</b>	<b>Electric potential</b>	<b>Space charge density</b>	<b>Particle</b>
Inlet	Velocity inlet	$\frac{\partial V}{\partial n} = 0$	$\frac{\partial \rho_w}{\partial n} = 0$	Enter
Outlet	Pressure outlet	$\frac{\partial V}{\partial n} = 0$	$\frac{\partial \rho_w}{\partial n} = 0$	Escape
Collection plates	Stationary walls	$V=0$	$\frac{\partial \rho_w}{\partial n} = 0$	Trap
Side walls	Stationary walls	$\frac{\partial V}{\partial n} = 0$	$\frac{\partial \rho_w}{\partial n} = 0$	Reflect
Wires	Stationary walls	$V = 6 - 60 \text{ kV}$	Iteratively adjusted (each individual wire)	Reflect



***OpenFOAM Code used for simulations***

The following OpenFOAM code was used for the simulations:

```
#include "fvCFD.H"
// ****

int main(int argc, char *argv[])
{
    #include "setRootCase.H"
    #include "createTime.H"
    #include "createMesh.H"
    #include "createFields.H"
    #include "initContinuityErrs.H"

    // ****

    Info<< "\nStarting time loop\n" << endl;

    while (runTime.loop())
    {
        Info<< "Time = " << runTime.timeName() << nl << endl;
        ///////////////////////////////////

        tmp<fvScalarMatrix> phiEqn
        (
            fvm::laplacian(phi)
        );

        phiEqn().relax();

        solve( phiEqn() == -rho/epsilon0 );

        E = -fvc::grad(phi);

        rhoFlux = -K*mesh.magSf()*fvc::snGrad(phi) + mesh.magSf()*U;

        tmp<fvScalarMatrix> rhoEqn
        (
            fvm::ddt(rho) +
                fvm::div(rhoFlux+phi, rho)
            - fvm::laplacian(D,rho)
        );

        solve( rhoEqn() );
        ///////////////////////////////////
        #include "readPISOControls.H"
        #include "CourantNo.H"

        fvVectorMatrix UEqn
        (
            fvm::ddt(U)
            + fvm::div(phi, U)
            - fvm::laplacian(nu, U)
        );

        solve(UEqn == -fvc::grad(p));
```

---

```

// --- PISO loop

for (int corr=0; corr<nCorr; corr++)
{
    volScalarField rAU(1.0/UEqn.A());

    volVectorField HbyA("HbyA", U);
    HbyA = rAU*UEqn.H();
    surfaceScalarField phiHbyA
    (
        "phiHbyA",
        (fvc::interpolate(HbyA) & mesh.Sf())
        + fvc::interpolate(rAU)*fvc::ddtCorr(U, phi)
    );

    adjustPhi(phiHbyA, U, p);

    for (int nonOrth=0; nonOrth<=nNonOrthCorr; nonOrth++)
    {
        fvScalarMatrix pEqn
        (
            fvm::laplacian(rAU, p) == fvc::div(phiHbyA)
        );

        pEqn.setReference(pRefCell, pRefValue);
        pEqn.solve();

        if (nonOrth == nNonOrthCorr)
        {
            phi = phiHbyA - pEqn.flux();
        }
    }

    #include "continuityErrs.H"

    U = HbyA - rAU*fvc::grad(p);
    U.correctBoundaryConditions();
}

runTime.write();

Info<< "ExecutionTime = " << runTime.elapsedCpuTime() << " s"
    << " ClockTime = " << runTime.elapsedClockTime() << " s"
    << nl << endl;
}

Info<< "End\n" << endl;

return 0;
}

```

The main steps in the computational modelling procedure as developed in this study are summarised in the flow charts shown in Fig G-1 and Fig G-2.

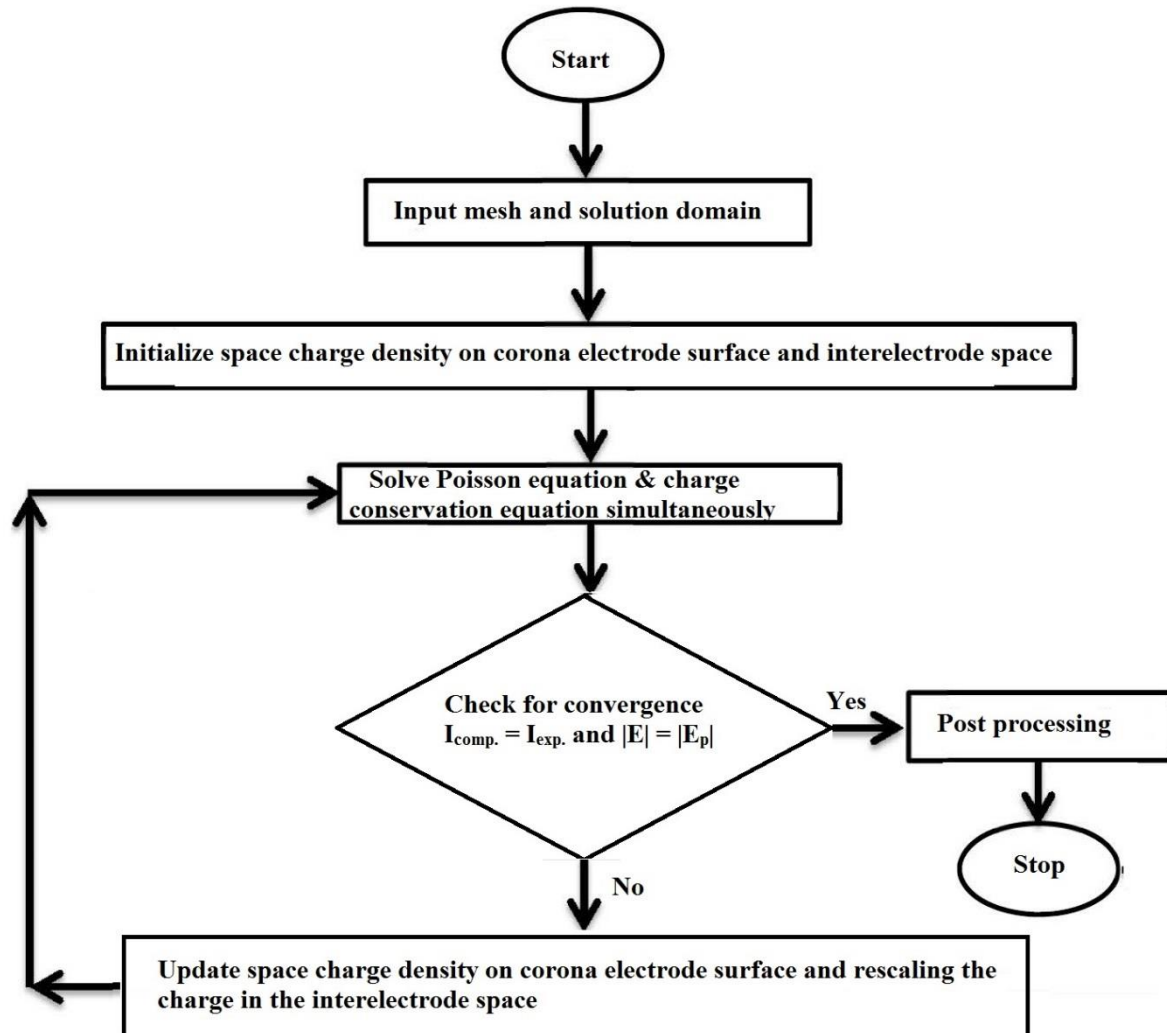


**Fig. B-1:** Main steps in the OpenFOAM modeling of the electrostatic field.

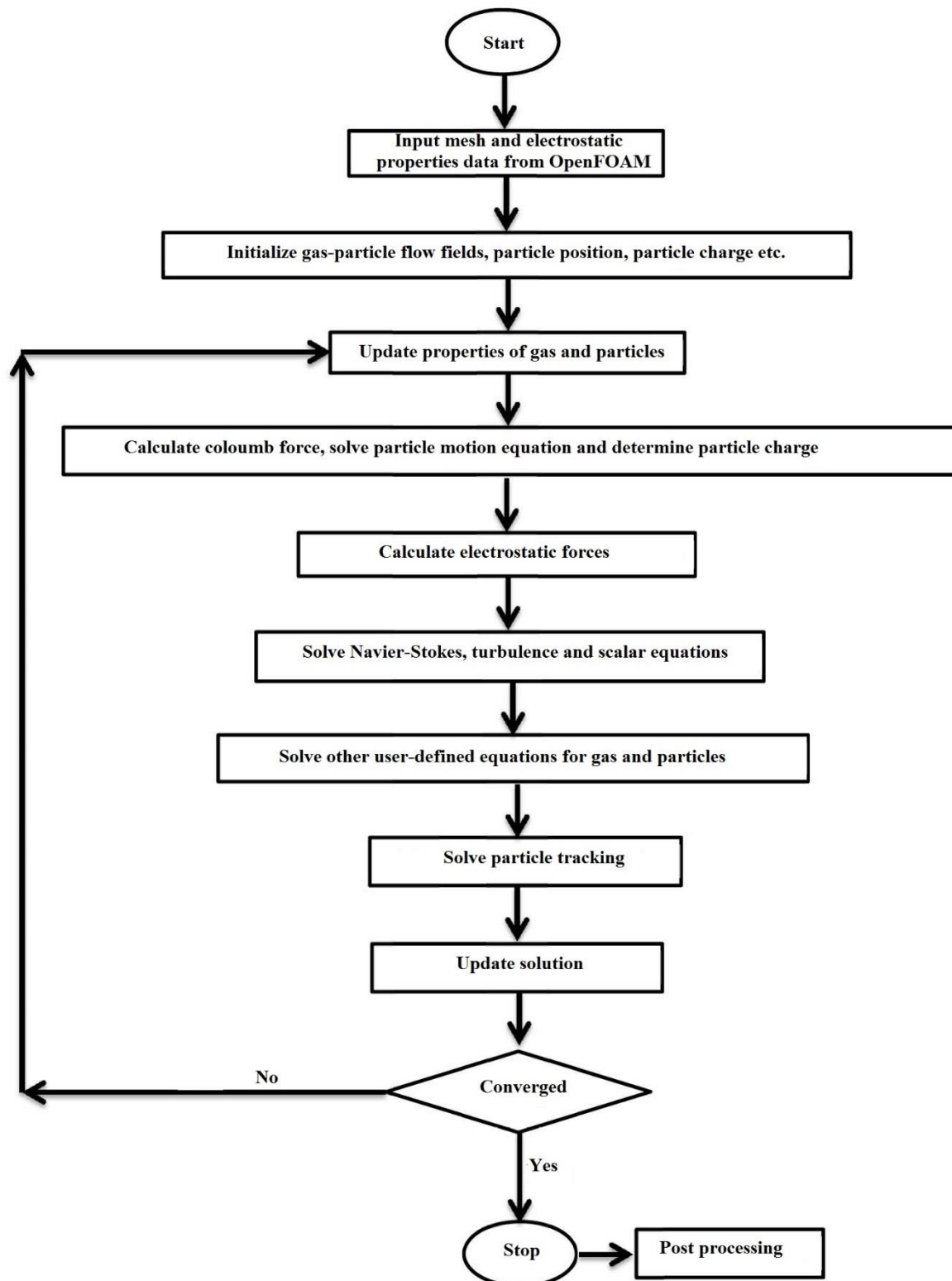


**Fig. B-2:** Main steps in the STAR CCM+ modeling of the fluid and particle dynamic fields.

## Appendix C. SUPPLEMENTARY INFORMATION ON THE COMPUTATIONAL MODELLING PROCEDURE

Supplementary detail of the computational modelling method used in this study that is not explicitly stated in the individual chapters is presented in this appendix.

### C.1 Computational modelling approach and solution procedure

The basic computational model was initially developed using a simplified single-channel ESP geometry [1] consisting of a single wire-electrode. The set of governing equations (Equations (3.1) to (3.19)) that need to be solved simultaneously are explained in Chapter 3 of the thesis. Equations (3.3) to (3.5), which relate to the electrostatic field and the charge conservation condition, could not be solved using STAR-CCM+ since the commercial software does not allow user defined transport equations to be added and solved. To circumvent this, the electrostatic field equations (Equation (3.1) to (3.5)) were solved using the open source software package OpenFOAM together with the computational solver algorithms that accompany the software. The finite volume method is implemented in both STAR-CCM+ and OpenFOAM and therefore meshing data and simulation results could be transferred between the two platforms. Thus, Equations (3.1) to (3.5) were solved in OpenFOAM while the fluid dynamics, particle dynamics, and particle charging equations (Equation (3.7) to Equation (3.19)) were solved in STAR-CCM+.

The discretized mesh of each ESP geometry that was modelled in this study was generated using STAR-CCM+ and subsequently exported to OpenFOAM where the electrostatic field was modelled using the electrostaticFoam solver [2] to solve the governing equations for the corona discharge (Equations (3.1) to (3.5)). The effect of fluid flow (velocity) on the electrostatic properties i.e. space charge density, discharge electrode voltage, current density was incorporated by combining the electrostaticFoam solver [2] with the icoFoam solver [2], yielding the code as shown in Appendix B. The electrostaticFoam solver solves equations for electrostatics (Equations 3.1 to 3.5) while icoFoam solver solves for continuous phase fluid flow and combining and coupling the two solvers yield solution showing effect of fluid flow (velocity) on the electrostatics. The OpenFOAM simulation results were exported in the form of data tables corresponding to values of electric potential, space charge density and electrostatic field for each individual discretized cell. Since the same discretized model was used in both the OpenFOAM and STAR-CCM+ modelling environments, the solved OpenFOAM data was subsequently imported to the corresponding discretized cells in STAR-CCM+ as user defined field functions and passive scalars.

Dynamic two-way coupling between the fluid field and the electrostatic field could not be modelled as a result of this modelling method. Therefore, as mentioned in Section A.3 (Appendix A), the extent of potential coupling between these two fields was investigated by using OpenFOAM to simulate the corona discharge and analysing the resulting space charge density under varying air flow velocities. Since it was found that the electrostatic field properties were only influenced by the fluid flow when the flow velocity was larger than 50

m/s, dynamic coupling between the fluid and electrostatic fields was neglected, i.e. the fluid field does not significantly influence the electrostatic field. As also shown in Chapter 3, the effect of EHD on fluid flow could also be neglected. In other words, the fluid flow velocity could be fixed, or fluid flow could even be neglected during the OpenFOAM modelling stage while the electrostatic field did not need to be solved again in OpenFOAM before simulating varying fluid flow velocities during the STAR-CCM+ modelling stage, provided that the fluid flow velocity was one order of magnitude smaller than the 50 m/s threshold.

After importing the OpenFOAM results into STAR-CCM+, the fluid and particle dynamics were then modelled using a computational fluid dynamics approach using the basic parameters as summarized in Table C-1. As is apparent from Chapter 3 and 4, the validated single-channel, single electrode ESP model was subsequently expanded and included in the description of a multi-electrode ESP while also taking shielding with respect to the corona discharge from adjacent discharge electrodes into account.

**Table C-1:** The basic characteristics of the computational model

Parameters	Modelling Method
Modelling packages	STAR-CCM+ (CD-Adapco) & OpenFOAM
Modelling approach	Euler-Lagrange
Flow field	Steady, incompressible and turbulent
Phase interaction	One way coupling
Turbulence model	Standard $k$ - $\epsilon$ turbulence model
Drag force	User defined field function
Particle wall interaction	Escape, rebound and trap
Particle size distribution	1-10 $\mu\text{m}$ , log normal distribution
Domain discretization	Tetrahedral/polyhedral and prism layer cells with surface remesher
Body force	User defined field function (Coulomb's force)
Passive scalar source	User defined field function (Individual particle charge)
Momentum source term	User defined field function (Induced EHD flow)
Passive scalars	Space charge density and voltage distribution (OpenFOAM)

The basic iterative procedure for solving the governing equations for the electrostatic field has the following main steps:

1. An initial guess value for the space charge density was set everywhere within the computational domain,
2. An initial guess value for the space charge density was also specified on the discharge wire-electrode surface, or on the spike tips in the case of spiked electrodes,
3. The Poisson equation (equation 3.1) was then solved for electric potential while the charge conservation equation (equation 3.5) was solved simultaneously using the initial space charge density values as input,
4. The two equations were solved computationally until the solution converged, and as explained in Chapter 3 and 4, the simulated electrostatic field magnitude (Equations

- (3.1) and (3.2)) was compared with the value obtained using Peek's formula (Equation (3.6)) in the case of cylindrical wire-electrodes. In the case of spiked discharge electrodes, the modelled discharge current was compared with the experimentally measured value.
5. The solver routine, i.e. Step 3, was repeated iteratively after adjusting the space charge density on the surface of the wire-electrodes, which was assumed to be constant over the surface of each wire. The space charge density in the computational domain was subsequently rescaled based on the new value at the surface of each electrode until, in the case of cylindrical wire-electrodes, the modelled electrostatic field magnitude and the value calculated with Peek's law converged to within a tolerance of 0.5%. In the case of spiked electrodes, the space charge density was rescaled until the modelled discharge current, which was calculated through the surface integral of the current density (the product of the ion mobility, the electrostatic field magnitude and the space charge density) at the spike tips of the spiked electrode, converged with the experimentally determined value to within a tolerance of 0.5% to 1%.

After obtaining a converged solution for the electrostatic field using OpenFOAM and introducing the results into STAR-CCM+, the next step was to solve the time averaged Navier-Stokes equation for the continuous phase (airflow), which was done using the Eulerian approach. The airflow was assumed to be incompressible and turbulent. and STAR-CCM+ was thus used for the solution of the momentum and continuity equations using the Finite Volume Method. The static electrostatic field, i.e. as solved using OpenFOAM, and the resulting space charge density distributions that were imported from OpenFOAM, were used for modelling particle charging and to also incorporate the effect of the electro-hydrodynamics on the fluid flow to model the particle trajectories as accurate as possible. This was done in STAR-CCM+ by determining the electric body-force at each volume element through a user defined function and then introducing the value into the momentum equation (Equation (3.7)) as a source term ( $\rho_w \vec{E}$ ).

Once the governing equations for the continuous phase were solved, particles were introduced into the system at the inlet using a part injector. The particles were introduced into the computational domain with a constant diameter of 4  $\mu\text{m}$  using one parcel stream (361 parcels) for simulations of Chapter 3, while the particle diameters were varied between 1 and 5  $\mu\text{m}$  for the simulations of Chapter 4. For these simulations (Chapter 3 and 4), a particle flow rate of  $7.49 \times 10^{-10} \text{ kg/s}$  was used, which relative to the air flow rate of between  $2.5 \times 10^{-3} \text{ m}^3/\text{s}$  and  $0.0814 \text{ m}^3/\text{s}$  yielded a particle concentration of  $3.0 \times 10^{-7} \text{ kg/m}^3$  to  $9.2 \times 10^{-9} \text{ kg/m}^3$ . For the simulations of Chapter 5, a log-normal distribution of particle sizes ranging from 1 to 100  $\mu\text{m}$  were used to more accurately reflect the particle size distribution of the fly ash samples used in the experiments, which is reported in Appendix E. The particles were introduced into the computational domain at the ESP inlet-plane using 40 parcel streams (361 x 40 parcels) to represent various particle diameters with a particle flow rate of  $1.66 \times 10^{-5} \text{ kg/s}$ , which relative to the inlet flow rate that varied between  $0.037 \text{ m}^3/\text{s}$  and  $0.1628 \text{ m}^3/\text{s}$  yielded a particle concentration ranging between  $4.48 \times 10^{-4} \text{ kg/m}^3$  and  $1.01 \times 10^{-4} \text{ kg/m}^3$ .

The Lagrangian model was used to model the particle transport and trajectories as well as particle charging. The latter is achieved by solving the Lagrangian equation of motion and performing a force balance on the particles in the dispersed phase while using the solved Eulerian equations for the continuous phase. Particle charging was modelled by defining passive scalar source terms and user defined functions for the Lagrangian phase which calculates the individual particle charge after each time step and then adds the value to the particle charge calculated during the previous timestep. Thus, as a particle passes through the computational domain it accumulates an electric charge that is defined by the charging model (Equation (3.14) to Equation (3.19)), which is incorporated as a user-defined function. Charge can accumulate on each particle up to the maximum saturation charge that is defined by Equation (3.13).

## **C.2 Mesh independence studies**

Mesh independence studies were conducted for the various ESP geometries that were modelled as part of this thesis (Chapter 3 to 5) to ensure that reliable results were obtained. A representative case of single-channel ESP with four wire-electrodes is used here to explain the procedure that was followed to test for mesh independence. The length, width and height of the ESP system in this representative case were 753, 100 and 370 mm respectively. The wire radius was equal to 1.2 mm and the four electrodes were spaced 80 mm apart from each other. The electrostatics and particle collection simulations were done as described in the preceding section using four different mesh sizes that resulted in the number of discretized cells ranging between 55 357 and 121 178. The prism layer mesher, surface remesher and extruder mesher models of STAR-CCM+ were used for generating tetrahedral and polyhedral meshes. Two of the mesh sizes are illustrated in Fig C-1, namely a coarse mesh with 70120 cells in Fig. C-1 (a), and the fine mesh with 121 178 cells in Fig. C-1 (b) The results of the respective electrostatic and particle collection simulations using are presented in Fig C-2 from which it is clear that the calculated particle collection efficiency and corona current did not vary significantly when 95 040 or more number of discretized cells were used. So for the rest of computational modelling studies for this particular geometry 95 040 cells were used. The meshing conditions used for the wires were different to that used for the rest of the geometric model due to the small diameter of the wires, and to ensure that the wire surface is sufficiently circular. The mesh was more refined near the wire surface with gradual coarsening in the radial direction as shown in Fig C-1.



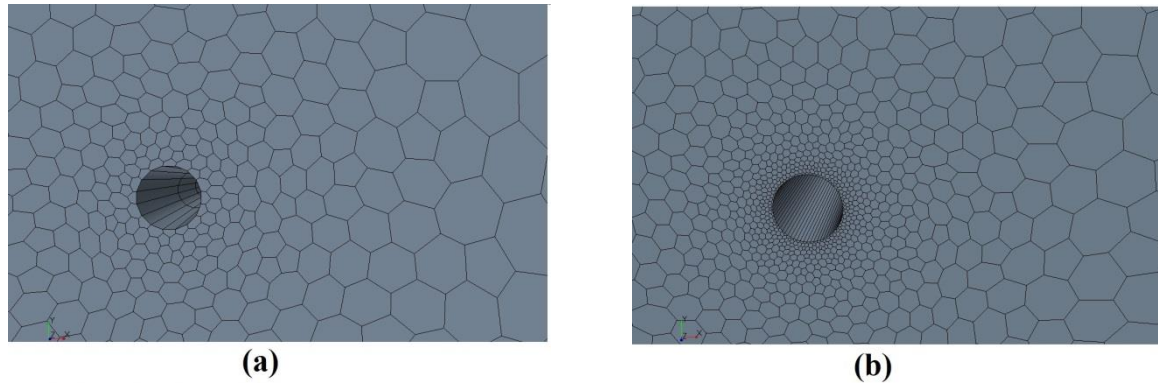


**Fig C-1:** Close-up view of a cylindrical wire-electrode and surrounding computational zone that was discretized using (a) a coarse mesh with 70 120 cells, and (b) a fine mesh with 121 780 cells.

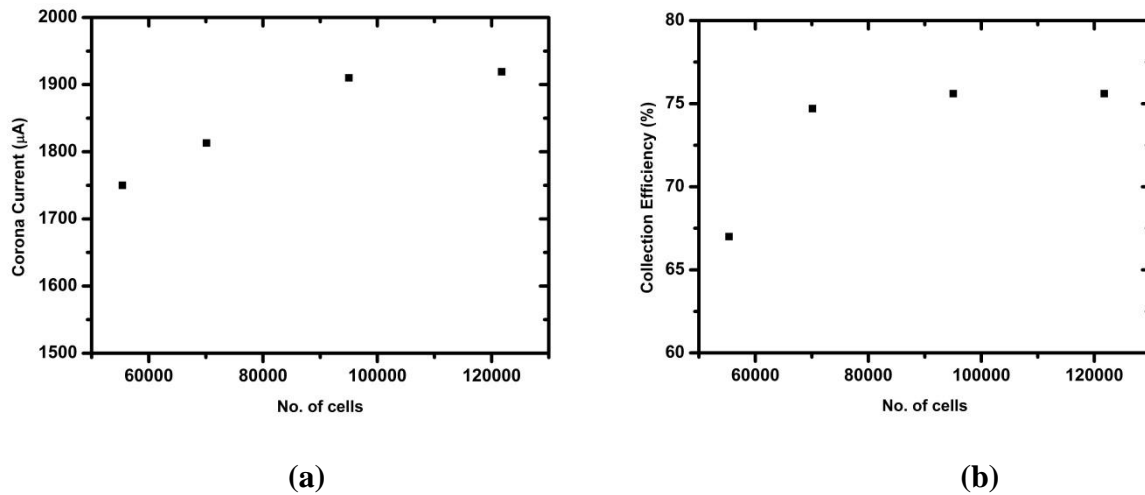


**Fig C-2:** The results of mesh independence studies to characterise the influence of the number of discretized cells on (a) the corona current, and (b) the collection efficiency for the ESP geometry as described above.

It was found that the corona current and the electrostatic field properties were more strongly dependent on the mesh size as compared to the particle collection efficiencies. Each simulated geometry was subjected to similar mesh independence tests to determine the minimum number of cells required to yield consistent results. The initial meshing conditions in each case were similar to that of the abovementioned case and were then modified accordingly i.e. increased or decreased from the base size.

### C.3 Solution times, convergence and accuracy of simulations

The degree of convergence of the computational modelling solutions were judged by monitoring the residuals with respect to the continuity, momentum and turbulence equations, together with other critical parameters such as the space charge density, velocity, and current density as a function of the number of iterations or the time steps. Convergence [3] was deemed to have occurred when the change in the solution (residuals) with an increasing

number of iterations or time steps occurred according to the defined tolerances ( $1 \times 10^{-6}$ ). Furthermore, the convergence criteria had to be satisfied in all cells according to the defined tolerances. It was found that the computational modelling solutions started to converge in most of the simulations after 2 seconds simulation time with a time step of 0.001 s. The reproducibility of the computational modelling results was reasonable with deviation of 0.5-1% after steady state is achieved (after simulation time of 2 sec).

#### **C.4 References**

- [1] N. Farnoosh, K. Adamiak, G.S.P. Castle, 3-D numerical analysis of EHD turbulent flow and mono-disperse charged particle transport and collection in a wire-plate ESP, *J. Electrostat.* 68 (2010) 513–522. doi:10.1016/j.elstat.2010.07.002.
- [2] OpenFOAM. (2014). User Guide (2<sup>nd</sup> ed.). OpenCFD Ltd.
- [3] CD-ADAPCO, User Guide STAR CCM+ V. 11.02.009, (2017).

## Appendix D. ADDITIONAL COMPUTATIONAL MODELLING RESULTS FOR SPIKE DISCHARGE ELECTRODE

The computational modelling results for a spike discharge electrode that includes a sensitivity analysis by varying geometric and operating parameters for the ESP design as indicated in Fig. D-1 is presented in this appendix. Additionally, the effect of air flow velocity on space charge density distributions is analyzed for a simple spiked discharge electrode.

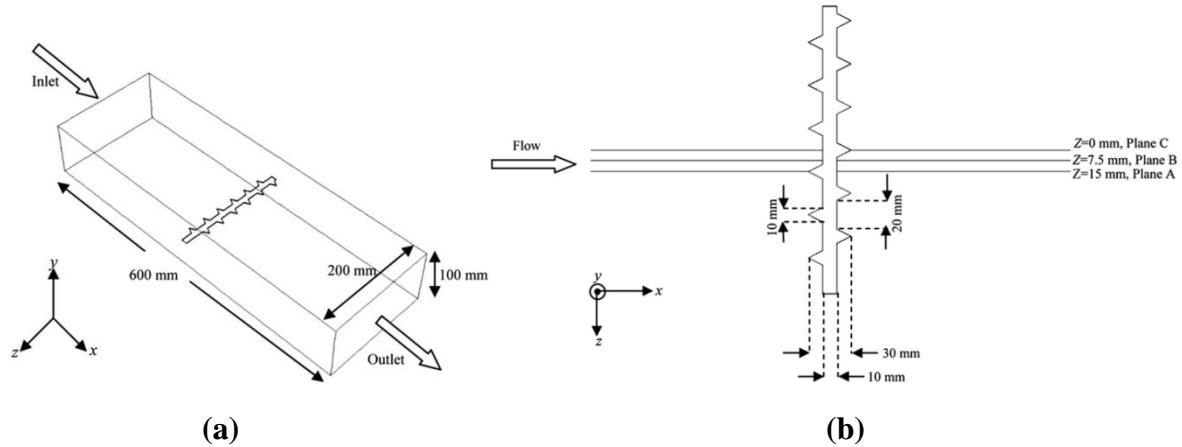


**Fig. D-1:** (a) 3-D geometry of a single-electrode ESP channel, and (b) dimensions of the spiked discharge electrode.

The comparison of computationally modelled discharge current for a spiked and a wire-type discharge electrode with the geometry as given in Fig D-1 are shown in Fig D-2. It is clear from the figure that the spike discharge electrode produces a larger discharge current compared to that of the wire-electrode for the same ESP dimensions. The improvement of discharge current leads to a significant increase in the collection efficiency when using a spiked electrode as opposed to a wire-electrode as is discussed in Chapter 3 and Chapter 5.

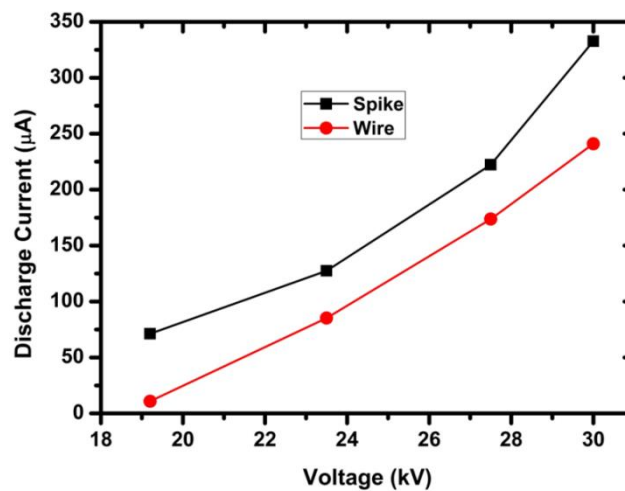


**Fig. D-2:** Comparison of the computational modelling results of discharge current produced by a spike and wire discharge electrode respectively for the same ESP geometry.

The computational modelling results for the effect of linear air flow velocity on the collection efficiency under varying applied discharge electrode voltage was also analyzed for the spiked discharge electrode setup as shown in Fig. D-1 of which the results are shown in Fig D-3. As was the case with wire-electrodes (Chapter 3) the collection efficiency was found to also decrease with an increase in the air flow velocity with the spiked discharge electrode.

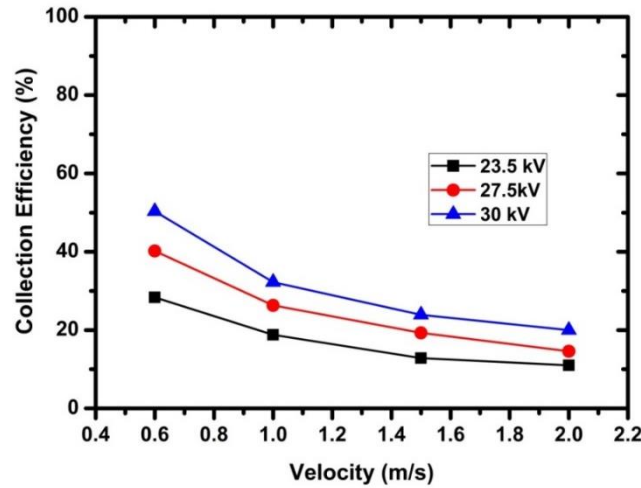


**Fig. D-3:** Computational modelling results for the effect of the air flow velocity on collection efficiency for the single-channel ESP depicted in Fig. D-1.

Using the computational model as described in Section 3.2, the collection efficiency was predicted to increase with an increase in the particle diameter (Fig. D-4) for the spiked discharge electrode ESP depicted in Fig. D-1. These results are also in line with the findings reported in Chapter 3 for the wire-electrode ESP cases.

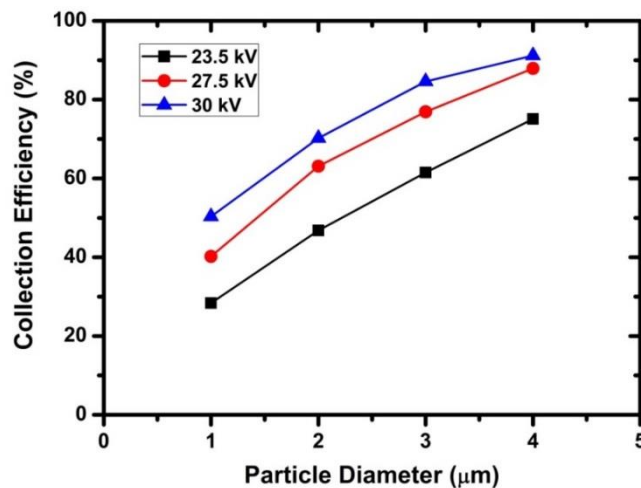


**Fig. D-4:** Computational modelling results for the effect of particle diameter on collection efficiency for a single-channel ESP equipped with a spiked discharge electrode (Fig. D-1).

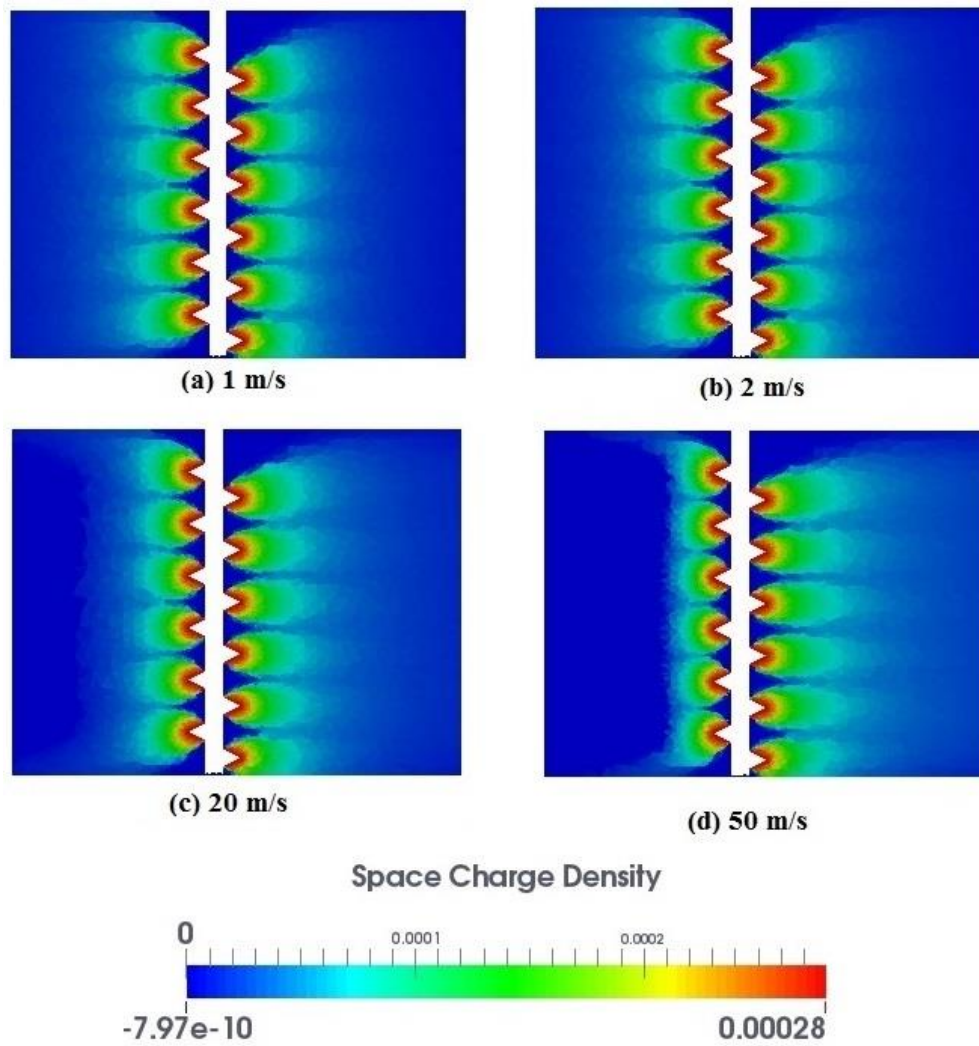


**Fig. D-5:** The effect of air flow velocity on the space charge density distribution of a simple spiked discharge electrode.

The effect of air flow on the space charge density distribution resulting from the corona discharge of the spike discharge electrode ESP assembly (Fig. D-1) is presented in Fig. D-5. As was the case with the wire-electrodes, the space charge density distribution is significantly affected when the linear air flow velocity is 50 m/s. The space charge density distributions are more prominently disturbed with a further increase in the air flow velocity.

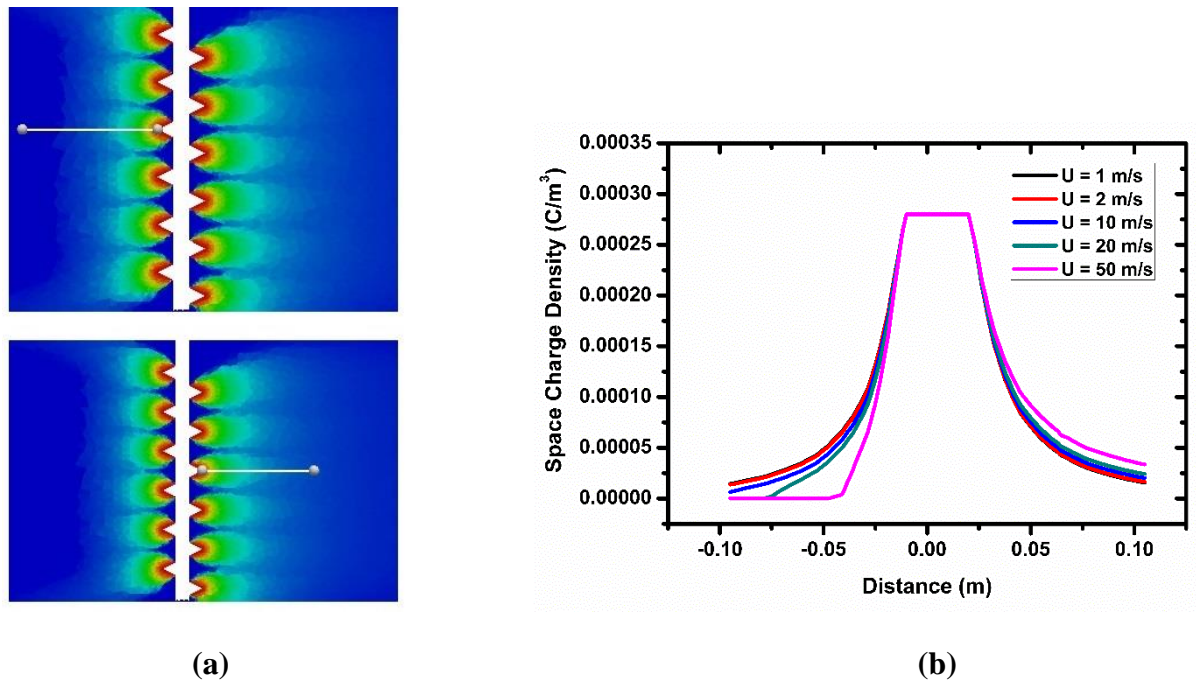


**Fig. D-6:** Graphical representation of the effect of air flow velocity on the space charge density distributions for a spike discharge electrode. The planes along which data was extracted for the plot (b) is shown in the figure on the left (a).

A two-dimensional plot of the space charge density distribution along the positions as shown in Fig. D-6 (a) is presented in Fig. D-6 (b), from which it is clear that the space charge density produced by the corona discharge on the spikes facing the air flow is compressed towards the spike tips. In contrast, the space charge density resulting from the corona discharge from the spikes on the opposite side are elongated slightly at high air flow velocities in order of 50 m/s. However, as mentioned in Section A.3, such high velocities are not found in either industrial ESPs or laboratory-scale systems, where typical velocities range between 0.5 to 2 m/s. At these velocities the electrostatic field is not affected (Figs. D-5 and D-6), and the coupling between the fluid dynamic and electrostatic field need not be considered in such practical situations.

## **Appendix E.        EXPERIMENTAL METHOD – SUPPLEMENTARY INFORMATION**

A detailed description of the in-house laboratory-scale ESP that was used to gather experimental data, which was compared to the results obtained from computational modelling of the unit, is presented in this appendix. Supplementary detail is also provided with regards to the measuring instruments and methods used to conduct the experiments, in addition to results obtained from reproducibility tests and fly ash sample characterisation.

### **E.1    Fly ash preparation and characterisation**

Fly ash was sampled from one of South Africa's coal-fired power stations from the ESP hoppers and was subsequently split into smaller samples by cone and quartering the bulk sample. Subsequently, one of the quartered samples were further processed using a rotary sample splitter to riffle out smaller samples, of which a single sample was taken and sieved using a 300  $\mu\text{m}$  sieve to remove coarse material present in the sample. The resulting sample was then subsequently processed using a 150  $\mu\text{m}$  sieve, followed by a 75  $\mu\text{m}$  sieve to obtain two sample fractions, i.e. one that passed through the 150  $\mu\text{m}$  sieve but which was retained by the 75  $\mu\text{m}$  sieve, and the other that passed through the 75  $\mu\text{m}$  sieve.

Particle size distribution (PSD) analysis was done on the two sample fractions obtained from the procedure outlined above. This was done using a Malvern Master Sizer 2000 with distilled water as dispersant. The sample (ash sample in distilled water) is passed through the laser beam as a result of which light is scattered at different angles depending upon the particle diameters. The detectors present inside the instrument measured the intensity of light corresponding to different positions/angles and a particle size distribution is generated using a mathematical model. The results of the PSD analysis of the two sample fractions are shown in Fig. E-1 from which it is clear that the sample fraction which passed through the 75  $\mu\text{m}$  sieve (Fig. E-1 (a)) consisted mostly of particles that were smaller than 75  $\mu\text{m}$ , although a relatively small fraction of particles that were larger than 75  $\mu\text{m}$  was also present.



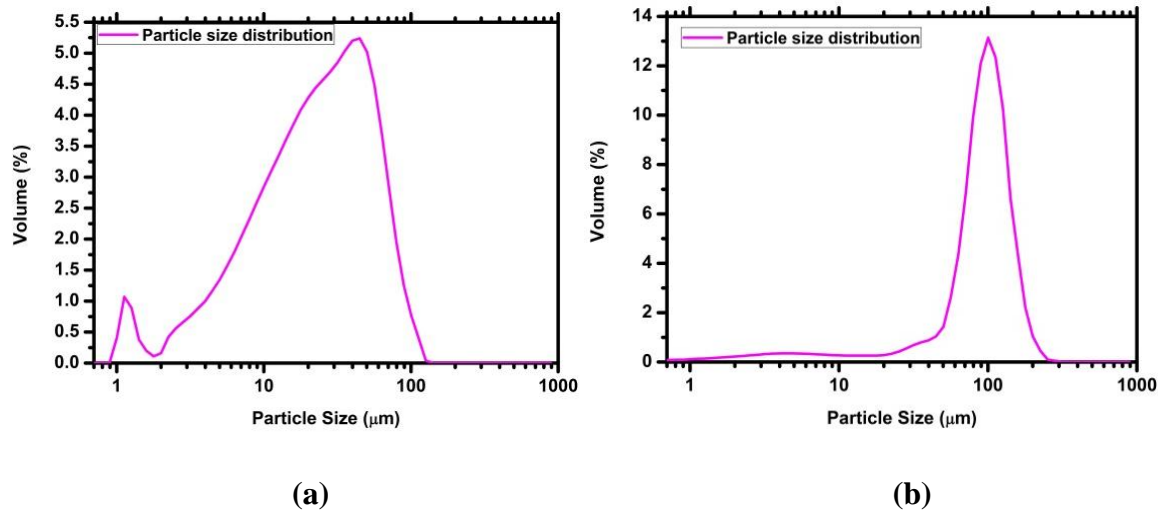


**Fig E-1:** Particle size distribution of the power plant fly ash used in this study for (a) the sample fraction that passed through the 75  $\mu\text{m}$  sieve, and (b) the sample fraction that passed through the 150  $\mu\text{m}$  sieve while being retained by the 75  $\mu\text{m}$  sieve.

The other sample fraction that passed through the 150  $\mu\text{m}$  sieve, and which was retained by the 75  $\mu\text{m}$  sieve (Fig. E-1 (b)) comprised of particles with an average diameter of 100  $\mu\text{m}$ , although a significant fraction of smaller particles was also still present. The particle size distribution results of the fly ash samples were modelled according to a log-normal distribution described by equation E.1 from which particles of varying size were generated within the computational model and their injection into the computational domain was subsequently simulated to allow accurate comparison of the experimental and modelling results.

$$F(D) = \frac{1}{2} \left[ 1 + \operatorname{erf} \left( \frac{\ln D - \ln D_{\text{mean}}}{\sigma \sqrt{2}} \right) \right] \quad (\text{E.1})$$

where  $\sigma$  is the standard deviation,  $D_{\text{mean}}$  is the mean particle diameter and  $D$  is the particle diameter.  $\sigma$  is 1.73 whereas  $D_{\text{mean}}$  (surface weighted mean) is 11.602  $\mu\text{m}$  and 30.848  $\mu\text{m}$  respectively for both particle size ranges.

In addition to the particle size distribution, the relative permittivity is another input parameter in the computational model, which used to model particle charging through the charging equations as explained in Section 3.2.2.3. Therefore, to further facilitate the reliable validation of the computational modelling results with the experimental results in terms of the collection efficiency obtained under varying experimental conditions, the relative permittivity of the fly ash samples needed to be determined. This was done on representative fly ash samples taken from the first sieved batch (particle size range of less than 75  $\mu\text{m}$  and less than 150  $\mu\text{m}$ ), which was analyzed by Dr. Maciej Noras at the University of North Carolina at Charlotte, Department of Engineering Technology, Charlotte, USA at varying temperatures and relative humidity. A dielectric cell, i.e. a MC-100 powder and paste dielectric cell (IET Labs Inc., USA) [1] and a precision 7600 Plus LCR meter (to measure inductance (L),



capacitance (C) and resistance (R)) (IET Labs Inc., USA) [2] was used for these purposes. The cell is equipped with three electrodes, of which one is a guard electrode. Fly ash samples were conditioned for at least 24 hours at the specified relative humidity and temperature in an environmental chamber before the relative permittivity measurements were done. The respective environmental conditions were also subsequently maintained while measurements were taken.

To achieve accurate relative permittivity measurements, the system's impedance needed to be compensated for, which was done by characterising the capacitance of the empty cell under the same environmental conditions at which each measurement was performed for each measurement frequency. The capacitance of the cell was then measured with the ash sample and the relative permittivity was then computed as the ratio of the capacitance of the cell loaded with the ash sample relative to that without the ash sample for each measurement frequency. All measurements were done with 5 V AC sine wave voltage signals. The results of the relative permittivity measurements are shown in Table E-1 as a function of temperature and relative humidity. Corresponding to relative humidity of 60%, temperature of 30°C (conditions at the time of experiments) and frequency of  $10^6$  Hz a value of 2.5 is taken from Table E-1 to be used for computational modelling studies of chapter 5. Table E-1 shows that relative permittivity values first increases and then decreases with increase of frequencies and are more stable at higher frequencies (greater than 500 Hz) as compared to lower frequencies [3,4]. Each data point represents the average of at least ten measurements.

**Table E-1:** Measured relative permittivity of a South African CFPP fly ash at varying temperature and humidity

Relative Humidity (%)	20	30	30	30	40	40	40	50	50	50	60	60	60	60	70	70	70	70	80	80	80	80
Temperature (°C)	40	30	40	50	20	30	40	20	30	40	20	25	30	35	20	25	30	35	20	25	30	35
Frequency (Hz)	Relative permittivity																					
10	0.9	1.0	0.7	1.3	0.9	1.4	0.9	1.6	1.8	1.4	1.8	1.0	1.9	1.9	1.9	1.8	1.5	2.0	2.9	3.0	2.0	2.1
20	2.2	2.3	2.7	2.6	2.5	2.9	2.4	3.4	3.8	3.0	4.9	2.7	3.3	3.6	5.4	4.0	3.8	3.0	7.7	3.9	5.0	5.3
50	2.8	2.8	3.2	2.5	3.3	4.2	3.0	3.2	5.1	4.0	5.3	3.4	2.9	3.0	5.7	4.2	5.3	4.0	9.6	4.6	5.2	7.2
100	2.9	2.9	3.2	2.7	3.0	3.5	2.8	3.1	4.7	3.8	4.7	3.1	2.6	2.9	5.2	4.4	3.9	4.0	7.8	3.4	4.6	4.8
200	2.8	3.0	2.7	2.8	2.9	3.0	2.9	3.1	3.9	3.6	4.4	3.0	2.4	3.3	4.9	4.2	3.8	4.0	6.5	3.2	4.6	3.8
500	2.8	2.9	2.8	2.6	2.9	2.8	3.0	3.1	3.5	3.9	3.8	3.0	2.6	3.4	4.3	2.8	3.6	4.0	5.5	3.1	4.2	3.7
1000	2.8	3.0	3.0	2.7	2.9	2.8	3.0	3.1	3.2	3.4	3.6	3.0	2.6	3.4	4.0	3.0	3.5	4.0	5.0	3.1	4.0	3.6
2000	2.8	2.9	2.9	2.7	2.9	2.8	3.0	3.0	3.0	3.2	3.5	3.0	2.6	3.3	3.8	3.0	3.4	4.0	4.6	3.0	3.8	3.5
5000	2.7	2.9	2.9	2.6	2.9	2.8	3.0	3.0	2.9	3.0	3.3	2.9	2.6	3.2	3.6	2.9	3.3	3.0	4.2	3.0	3.7	3.4
10000	2.8	2.9	2.9	2.6	2.9	2.8	3.0	3.0	2.9	2.9	3.2	2.9	2.6	3.2	3.5	2.9	3.2	3.0	4.0	2.8	3.6	3.4
20000	2.8	2.9	2.8	2.6	2.9	2.7	3.0	3.0	2.8	2.8	3.2	2.9	2.6	3.0	3.3	2.8	3.1	3.0	3.9	3.0	3.5	3.3
50000	2.8	2.9	2.9	2.6	2.9	2.8	3.0	3.0	2.8	2.8	3.1	2.9	2.6	3.0	3.2	2.9	3.0	3.0	3.7	2.9	3.4	3.1
100000	2.7	2.9	2.9	2.6	2.9	2.8	3.0	3.0	2.8	2.8	3.0	2.9	2.6	3.0	3.0	2.8	3.0	3.0	3.5	2.9	3.3	3.0
200000	2.7	2.9	2.8	2.6	2.9	2.7	3.0	3.0	2.8	2.7	3.0	2.9	2.6	2.9	3.1	2.8	2.9	3.0	3.4	2.9	3.2	2.9
500000	2.7	2.9	2.8	2.6	2.9	2.7	3.0	3.0	2.8	2.7	3.0	2.9	2.5	2.9	3.0	2.8	2.9	3.0	3.3	2.9	3.2	2.9
1000000	2.8	2.9	2.9	2.6	2.9	2.7	3.0	3.0	2.8	2.7	3.0	2.9	2.5	2.9	3.0	2.8	2.9	3.0	3.3	2.9	3.1	2.9

## E.2 Laboratory-scale ESP design

To assist in designing a suitable laboratory-scale ESP unit, a literature survey was conducted to get a sense of the dimensions of ESP units that have been used in other published experimental studies. A summary of the results of the literature survey with respect to the ESP dimensions and other operating parameters that were used in the respective studies are given in Table E-2.

**Table E-2:** ESP parameters that have been used in previous experimental studies

Parameter	Kim & Lee [5]	H. Nouri et al. [6]	Xi Xu et al [7]	M. Jedrusik et al. [8,9]	Z. Al-Hamouz [10,11]
Collection plate length (mm).	750	200	840	2000	2000
Collecting plate height (mm)	300	100	240	450	1000
Plate-to-plate spacing (mm)	100 - 400	100	120	400	300, 400
Wire-electrode spacing (mm)	12.5 - 50	40	55, 110, 165	170	160, 210
Wire diameter (mm)	1,2,3,4	0.2	3,5,8	-	0.7, 1, 1.7
Discharge electrode voltage (kV)	10 - 70	10 - 40	25 - 55	0 - 100	0 - 100

Based on the dimensions used in the studies cited in Table E-2, a collecting plate length of 750 mm and height of 370 mm was selected, since in most of the literature studies a collecting plate length-to-height ratio of 2 was used. A discharge electrode with wire diameter of 2.4 mm was used for the wire-type discharge electrodes. The ESP set up was subsequently designed such that the wire-to-wire spacing and plate-to-plate spacing could be varied to study the effects of these parameters on ESP performance while keeping the length and height of the collecting plates, as well as the wire-electrode diameter fixed.

Having identified suitable dimensions, the detailed design of the ESP and accompanying ducts were further based on the unit used in the study of Kim and Lee [5]. Geecom (Pty) Ltd was contracted to design and commission the electrical supply and control systems, and a 3-D representation of the final design of the laboratory-scale ESP used in the present study is shown in Fig. E-2 in which the blower, inlet and outlet ducts, and the ESP section are illustrated.

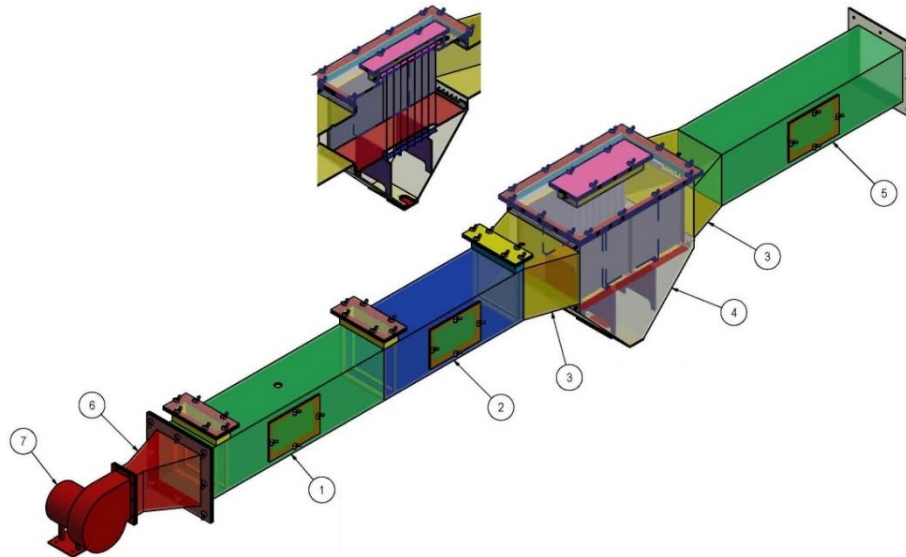


**Fig. E-2:** 3-D Representation of the laboratory-scale ESP system used for fly ash collection experiments in the present study. The following components are shown, namely: (1) the inlet duct, (2) removeable window to assist with cleaning between experiments, (3) the diverging and converging sections before and after the ESP section, (4) collection hopper, (5) outlet duct, (6) diverging section after blower, and (7) blower inlet. (taken from Geecom design drawings for ESP unit)

The experimental set up consisted mainly of the following parts as shown in Fig. E-2, namely a blower that drew ambient air through a HEPA filter (protected with a prefilter), a diverging section connecting the blower and the inlet duct, a series of baffles and a honeycomb structure to homogenise the air flow and to attain to a homogeneous fly ash distribution. The air flow rate, and thus the superficial flow velocity (Section E.3.2) were controlled by adjusting the blower speed through a variable speed drive. A 3-D representation of the inlet duct with the baffles and honeycomb structure is shown in Fig. E-3.

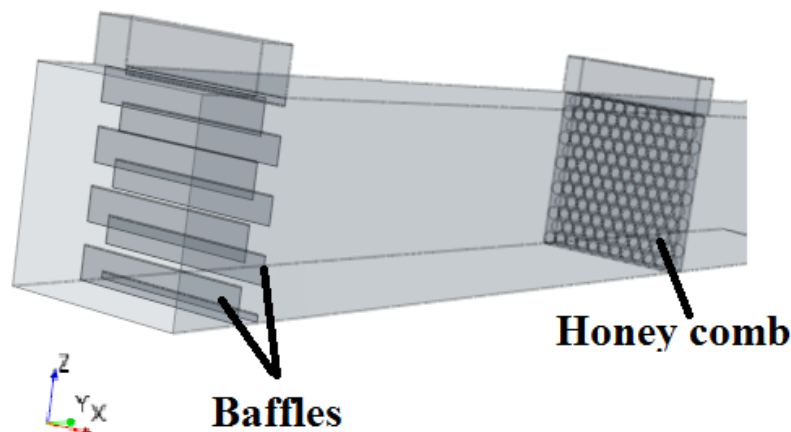


**Fig E-3:** 3-D representation of the inlet duct to the ESP with the baffles and honeycomb structure that was used to homogenize the air flow.

The inlet duct was connected to the ESP section that housed the collecting plates and discharge electrodes through a diverging section. The ESP section was equipped with a hopper to help extract collected ash after each experiment but was sealed off during experiments. The outlet duct was connected to the ESP section through another diverging section. The ESP section and ducting were constructed from plexiglass as pictured in Fig E-4.



**Fig E-4:** Close-up view of the inlet duct and ESP section.

The total length of the inlet duct, ESP and outlet duct assembly was 5 m, while the inlet and outlet duct were 2.6 m and 1.6 m in length respectively, and the ESP section was 0.8 m in length. The collecting plates were secured to a series of plate guide bars as shown in Fig. E-5 with which the plate-to-plate spacing could be varied between 100 and 400 mm in 60 mm intervals.

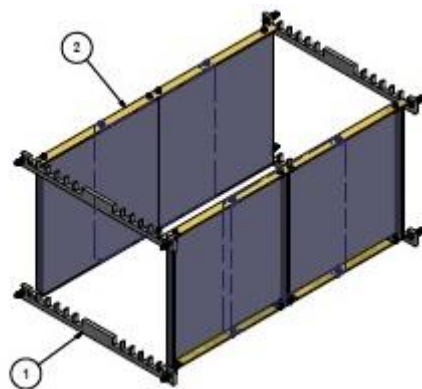


**Fig. E-5:** Collecting plate assembly with (1) collecting plate guide bars, and (2) collecting plates.

To vary the electrode spacing when using cylindrical wires as the discharge electrodes, two guide tubes, which were each 0.35 m in length with holes drilled 7 mm apart from each other, were used to secure the wire-electrodes. The discharge electrode assembly with the guide

tubes and discharge electrodes are illustrated in Fig E-6(a), and the spiked rigid discharge electrode (RDE) that is manufactured by Geecom (Pty) Ltd., i.e. the G-Spike electrode that was also used in this study, is shown in Fig E-6(b). The spiked RDE as shown in Fig E-6(b) was secured to the top guide tube using leads. Additional illustrations of the various components of the ESP unit used in this study, along with the dimensions of each, are shown in Appendix F.

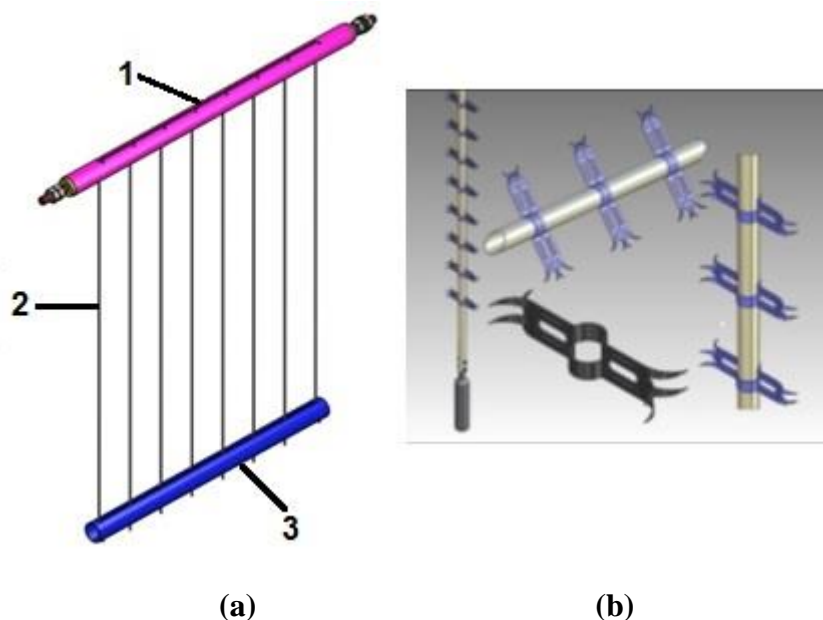


**Fig. E-6:** (a) Discharge electrode assembly with (1) top guide tube that was also connected to the electrical supply, (2) wire-electrodes, (3) bottom guide tube, and (b) the spiked RDE (G-Spike electrode) as used in this study.

The top discharge electrode guide tube was connected to the 50 kV high voltage DC power supply unit manufactured by Jeenel Technology Services (Pty) Ltd, which had a maximum output current of 20 mA, through which the applied discharge electrode voltage was controlled, and the resulting discharge current measured.

The operation of the lab-scale ESP rig involved adjustment of the discharge electrodes and collecting plates of the ESP section according to the specific requirements with respect to the inter-electrode and plate-to-plate spacing for a particular experiment. The blower was then switched on and after some time was allowed for the flow to stabilise, velocity measurements were recorded at the inlet and outlet planes of the ESP section using a thermal anemometer (Omega Engineering) (further described in Section E.3.2). The anemometer measurements were logged on a computer from which an average velocity was calculated from multiple measurements at each blower fan speed setting. A compressed air line was connected to the dust feeder inlet, where the inlet pressure was regulated with an in-line forward pressure regulator to provide air for generating the aerosol and for feeding it to the inlet of the wind tunnel. The dust indicator units were connected to the sampling points and after the velocity measurements were completed, compressed air was supplied to the dust feeder after switching on the unit. Fly ash was loaded into the hopper of the dust feeder, which generates

the fly ash aerosol with the rotation of the turn table. Through adjusting the rotation rate of the turntable, the rate at which fly ash was fed to the wind tunnel (as measured at the ESP inlet) could be controlled.

The dust indicator units were then switched on together with the suction pumps and time was allowed (2 – 3 hours) for the system to reach steady state before measurements were recorded. Thereafter, the electrical section of the ESP was switched on and set to the required input voltage. The applied voltage was increased in increments of 5 kV, and dust concentration measurements were recorded at the inlet and outlet for each incremental voltage. The experiments were performed with different discharge electrodes and electrode configurations (a varying number of wire-electrodes and G-Spikes) and varying plate-to-plate spacing. At each voltage set point dust concentration measurements were only taken after the readings stabilised.

The process involved in the aforementioned steps are described in further detail in the subsequent sections.

### **E.3 Fly ash injection, measurements, and air flow modelling**

The equipment and methods used to inject fly ash into the ESP assembly, and to measure the resulting inlet and outlet fly ash concentration, as well as the air flow velocity, are described in this section.

#### **E.3.1 Fly ash injection and concentration measurement**

Fly ash was injected between the HEPA filter and the blower inlet using a DF-3 type dust feeder obtained from Sibata Scientific Technology Ltd, Japan [8, 9]. The dust feeder features a turn table to control the rate at which the fly ash is fed to the system by adjusting the rotation speed vibrations. An air ejector, fed with filtered pressurized air at 2 bar from a compressor, was used to disperse the fly ash by aspirating it through the grooves built into the turn table ring. The dispersed fly ash was subsequently transported to the injection point via the supplied tubing.

The fly ash concentration in the air stream was measured at the ESP inlet and outlet planes using two digital dust indicators [13] from Sibata Scientific Technology Ltd, Japan [8, 9]. A dedicated dust indicator was used for each measuring point, i.e. for measuring the inlet fly ash concentration (model AP-632 TM with a measuring range of 0.1 to 100 mg/m<sup>3</sup>) and the outlet fly ash concentration (model AP-632 TH with a measuring range of 0.01 to 10 mg/m<sup>3</sup>). These dust indicators quantify the particle concentration by measuring the intensity of dispersed light and reports the particle concentration in ppm units. Samples were withdrawn from the ESP inlet and outlet planes respectively using the supplied suction pumps, which themselves are protected by in-line filters. The suction pumps were equipped with rotameters for controlling the flow rate of the sampled air at a constant rate of 30 L/min.

### **E.3.2 Air velocity measurements and CFD modelling of air flow**

The air velocity was measured using an FMA-1000 series air velocity and temperature indicator and transmitter (Omega Engineering) [14] with a rated measuring range of 0 to 25 m/s and a certified accuracy of 1.5% (full scale). The sensor is equipped with three RTD elements of which one measure the air temperature and the other two sensors are used to measure the air velocity. The sensor probe is 30.5 cm long and velocity measurements were done in the inlet duct after the honey comb and at the ESP inlet-plane in a two-dimensional grid of discrete measuring points. The measuring grid consisted of 5 measuring ports spaced 70 mm from each other, and the probe was inserted into each port to varying depths at 25 mm intervals, yielding 11 point-measurements at each measuring port and a total of 55 data points.

The measurements at the ESP inlet plane were used to assess whether the air flow was sufficiently homogenous at the ESP inlet plane after passing the baffles and the honeycomb structure. To study the air flow velocity distribution throughout the ESP section, the velocity measurements at the ESP inlet plane was used as input to a CFD model in STAR-CCM+ to visualise the flow distribution throughout the ESP section. The CFD model consisted of only the air flow simulations through the ESP section without considering particle dynamics and electrostatics. The meshing conditions used were relatively coarse as compared to those used for electrostatics, fluid, and particle dynamics modelling in the detailed simulations.

The velocity measurement results at the ESP inlet plane are visualized in Figure E-7(a) according to the measuring grid that was used. The subsequent CFD modelling results of the air flow velocity distribution inside ESP section of one representative case are illustrated in Fig. E-7(b). The air flow velocity was subsequently predicted by the model to be more uniformly distributed throughout the ESP section (Fig. E-7 (b)) compared to the measured distribution at the inlet, and that an average velocity of 2.7 m/s was calculated in this case. The air flow velocity was thus adjusted to meet experimental requirements by changing the blower speed and measuring the resulting flow velocity distribution at the ESP inlet-plane, which was then used as input velocity to the CFD model from which the flow velocity distribution was calculated throughout the ESP section. The resulting average flow velocity was subsequently used as uniform input velocity to the detailed model with which the ESP operation was simulated and the resulting collection efficiency evaluated for each specific case.



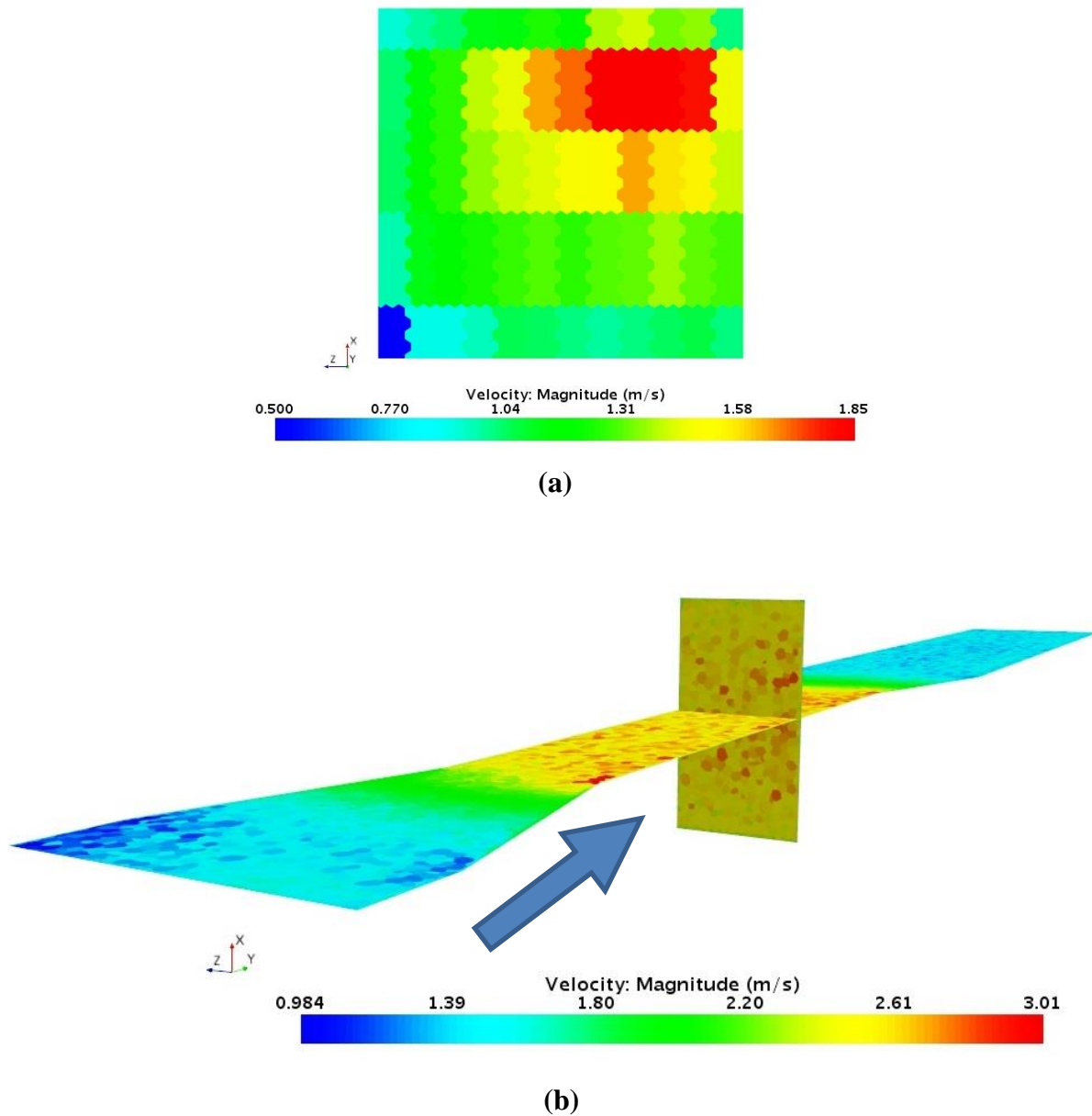


**Fig E-7:** (a) Experimentally measured air flow velocity distributions at the ESP inlet-plane, and (b) air flow distribution through the ESP section along the vertical and the horizontal centre-line plane as predicted by the CFD model. The arrow indicates the direction of flow.

#### E.4 References

- [1] IET Labs, Inc., <http://www.ietlabs.com/dielectric-cells/mc-100.html>.
- [2] IET Labs, Inc., <http://www.ietlabs.com/lcr-meter/7600-lcr-meter.html>.
- [3] M. Hotta, M. Hayashi, M.T. Lanagan, D.K. Agrawal, K. Nagata, Complex Permittivity of Graphite, Carbon Black and Coal Powders in the Ranges of X-band Frequencies (8.2 to 12.4 GHz) and between 1 and 10 GHz, *ISIJ Int.* 51 (2011) 1766–1772.

- doi:10.2355/isijinternational.51.1766.
- [4] L. Han, E. Li, G. Guo, H. Zheng, Application of Transmission/Reflection method for Permittivity Measurement in Coal Desulfurization, *Prog. Electromagn. Research Lett.* 37 (2013) 177–187. doi:10.2528/PIERL12123002.
  - [5] S. Kim, K. Lee, Experimental study of electrostatic precipitator performance and comparison with existing theoretical prediction models, *J. Electrostat.* 48 (1999) 3–25. doi:10.1016/S0304-3886(99)00044-3.
  - [6] H. Nouri, N. Zouzou, L. Dascalescu, Y. Zebboudj, Investigation of relative humidity effect on the particles velocity and collection efficiency of laboratory scale electrostatic precipitator, *Process Saf. Environ. Prot.* 104 (2016) 225–232. doi:10.1016/j.psep.2016.09.001.
  - [7] X. Xu, C. Zheng, P. Yan, W. Zhu, Y. Wang, X. Gao, et al., Effect of electrode configuration on particle collection in a high-temperature electrostatic precipitator, *Sep. Purif. Technol.* 166 (2016) 157–163. doi:10.1016/j.seppur.2016.04.039.
  - [8] M. Jedrusik, A. Świerczok, The correlation between corona current distribution and collection of fine particles in a laboratory-scale electrostatic precipitator, *J. Electrostat.* 71 (2013) 199–203. doi:10.1016/j.elstat.2013.01.002.
  - [9] M. Jedrusik, A. Swierczok, R. Teisseyre, Experimental study of fly ash precipitation in a model electrostatic precipitator with discharge electrodes of different design, *Powder Technol.* 135-136 (2003) 295–301. doi:10.1016/j.powtec.2003.08.021.
  - [10] Z. Al-Hamouz, A. El-Hamouz, N. Abuzaid, Simulation and experimental studies of corona power loss in a dust loaded wire-duct electrostatic precipitator, *Adv. Powder Technol.* 22 (2011) 706–714. doi:10.1016/j.apr.2010.10.005.
  - [11] Z. Al-Hamouz, Numerical and experimental evaluation of fly ash collection efficiency in electrostatic precipitators, *Energy Convers. Manag.* 79 (2014) 487–497. doi:10.1016/j.enconman.2013.11.047.
  - [12] S.S.T. LTD, Operating manual dust indicator, dust feeder and pumps, <https://www.sibata.co.jp>
  - [13] S.S.T. LTD, Introduction of the environmental dust test device, [https://www.sibata.co.jp/wpcms/wp-content/themes/sibata/en/pdf/DTS\\_presentation.pdf](https://www.sibata.co.jp/wpcms/wp-content/themes/sibata/en/pdf/DTS_presentation.pdf).
  - [14] F. 1000 Series, Omega user's guide, Air Veloc. Transm. Indic. <https://www.omega.com/manuals/manualpdf/M4791.pdf>.

## Appendix F. NORTH-WEST UNIVERSITY EXPERIMENTAL SET UP DRAWINGS AND GEECOM G-SPIKE DISCHARGE ELECTRODE DATA

Design drawings of the experimental ESP unit prepared by Geecom, South Africa for the experimental ESP unit that was used for measurement of fly ash collection efficiency as a function of various parameters are given in this appendix. The top, front and side view of the ESP unit is illustrated in Fig. F-1.

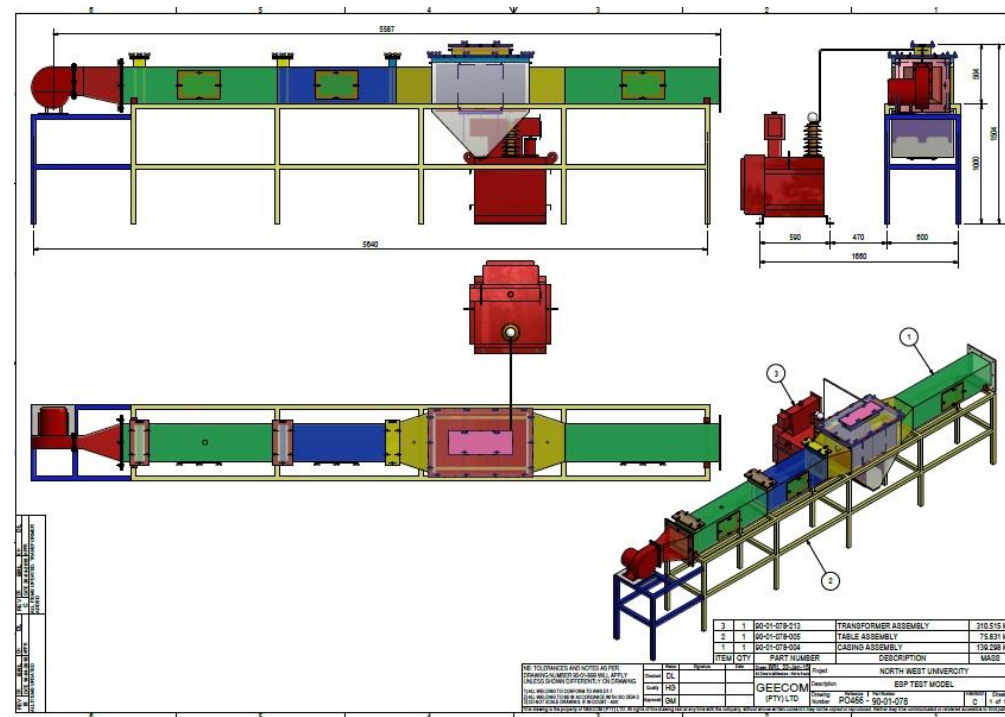


**Fig. F-1:** Top, front and side view of the laboratory-scale ESP unit.

[illegible]

140

A close-up view of the ESP section along with its internal and external parts and their dimensions are shown schematically in Fig F-3.

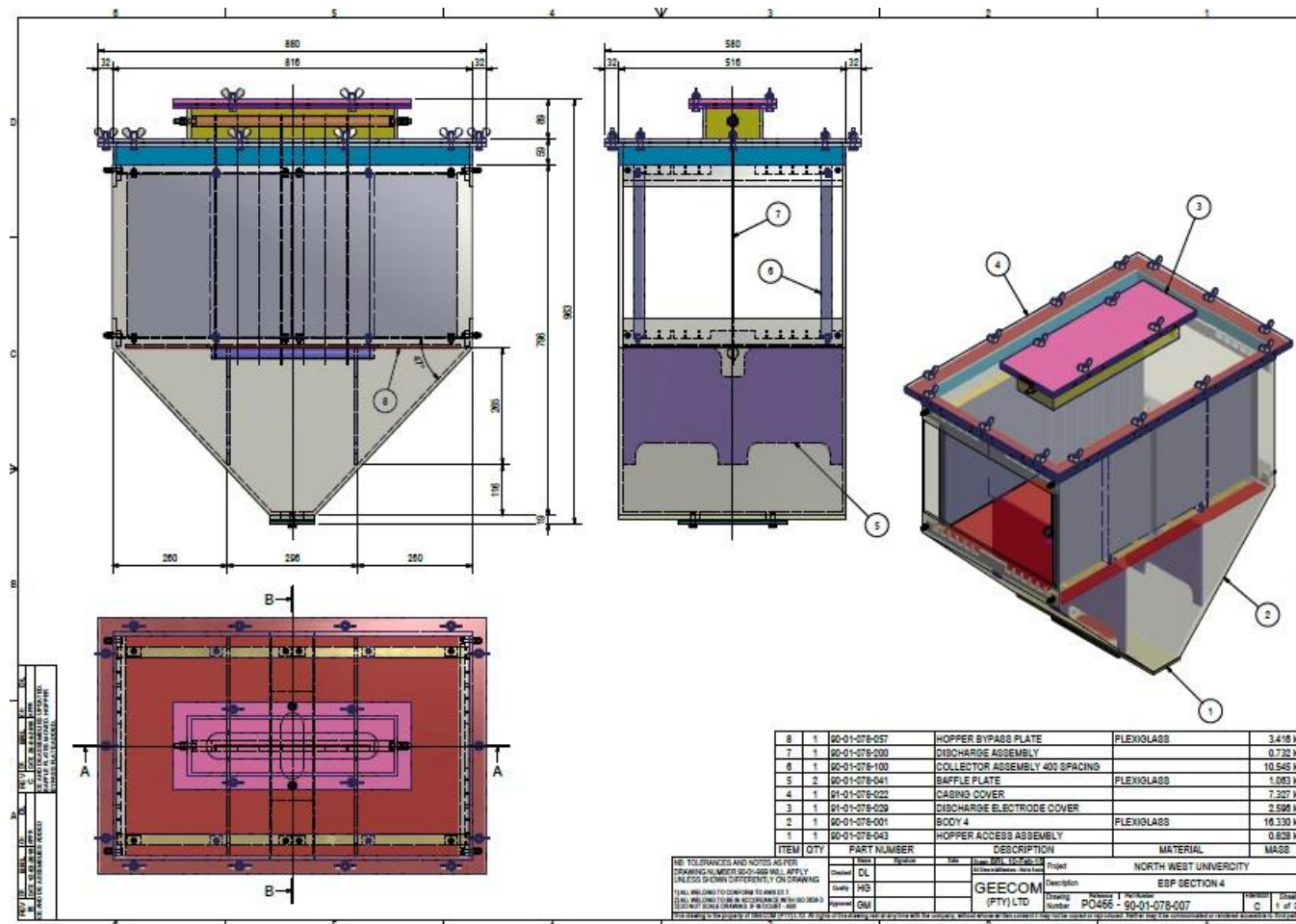
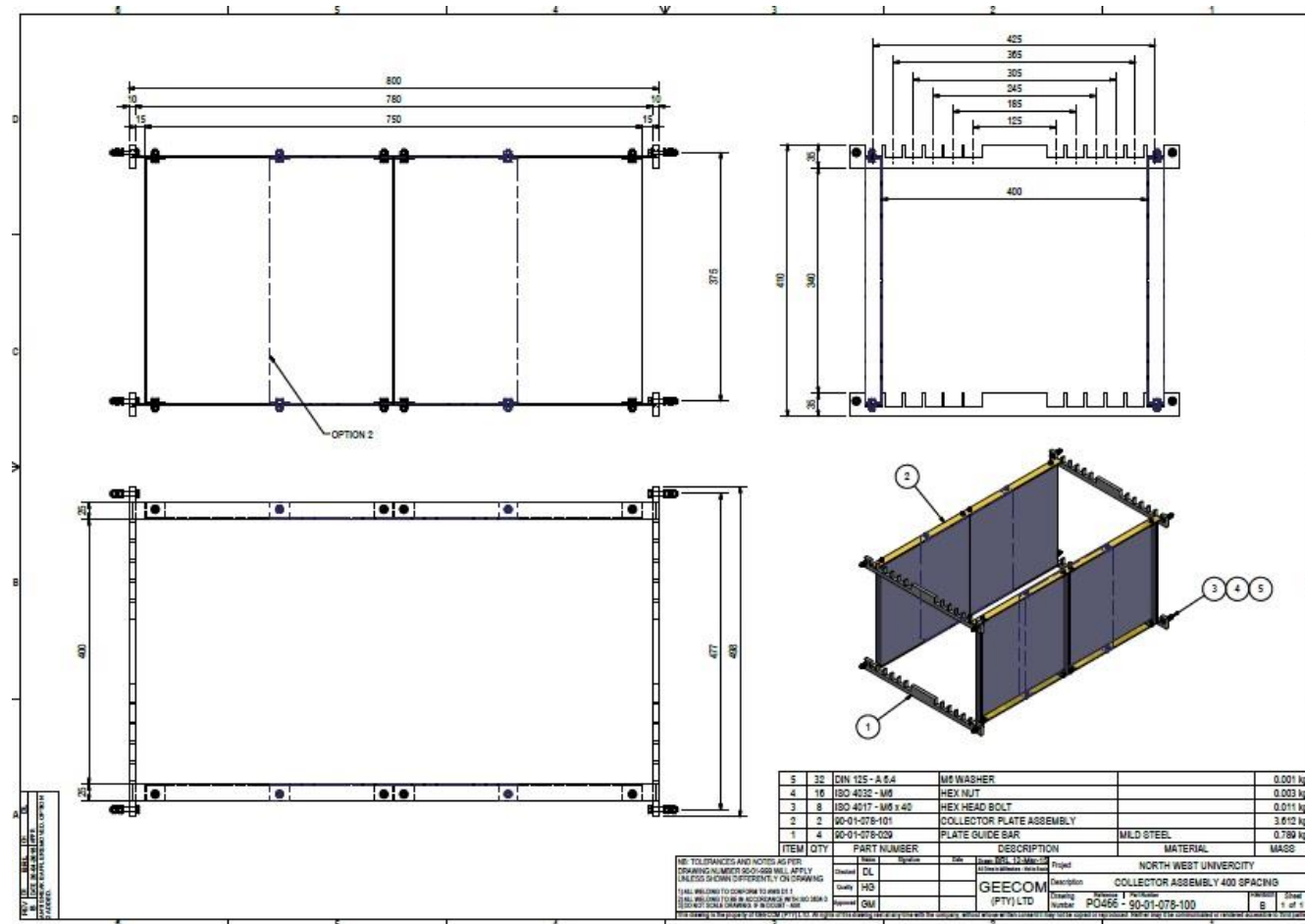


Fig. F-3: Close-up view of the ESP section.

The collection plate assembly is shown in Fig F-4 in which the length and height of the collection plates are also shown. The collection plate guide bar with the slots to hold the collection plates at various plate-to-plate spacings of 100 mm to 400 mm in increments of 60 mm are also visible.



**Fig. F-4:** Collecting plates assembly.



The discharge electrode assembly including the top and bottom guide tubes to hold the discharge wires in place during ESP operation is shown in Fig F-5. The guide tubes have holes drilled through them to change the spacings between the wires during ESP operation.

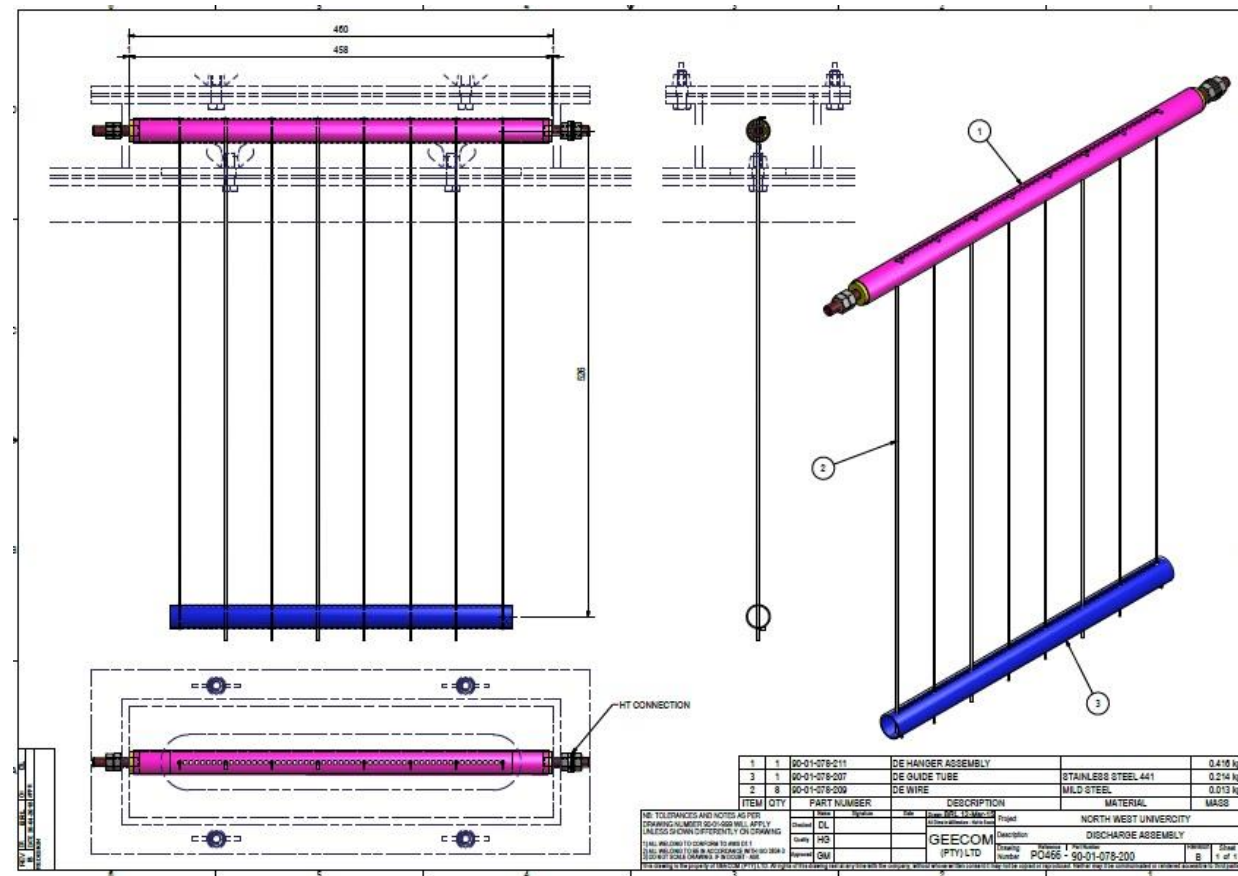


**Fig. F-5:** Discharge electrode assembly with wire electrodes.

The G-Spike discharge electrode design data obtained from Geecom (Pty) Ltd [1, 2], which were used to construct the 3-D models required for the simulations of spiked electrode, are given in Fig. F-6 and Fig. F-7. The dimensions of the spike of a spiked electrode designed by Geecom (Pty) Ltd. is illustrated in Fig F-6.

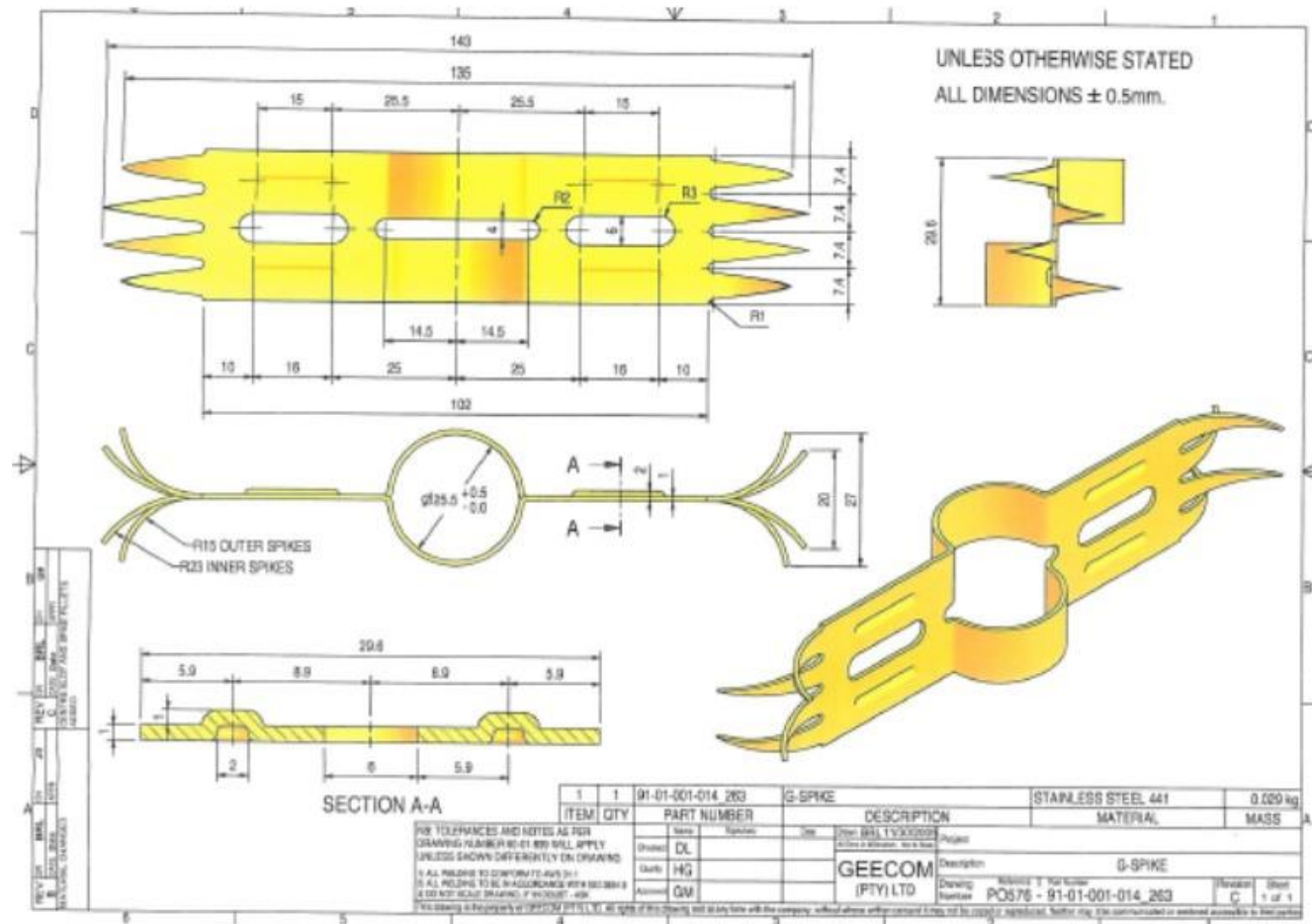
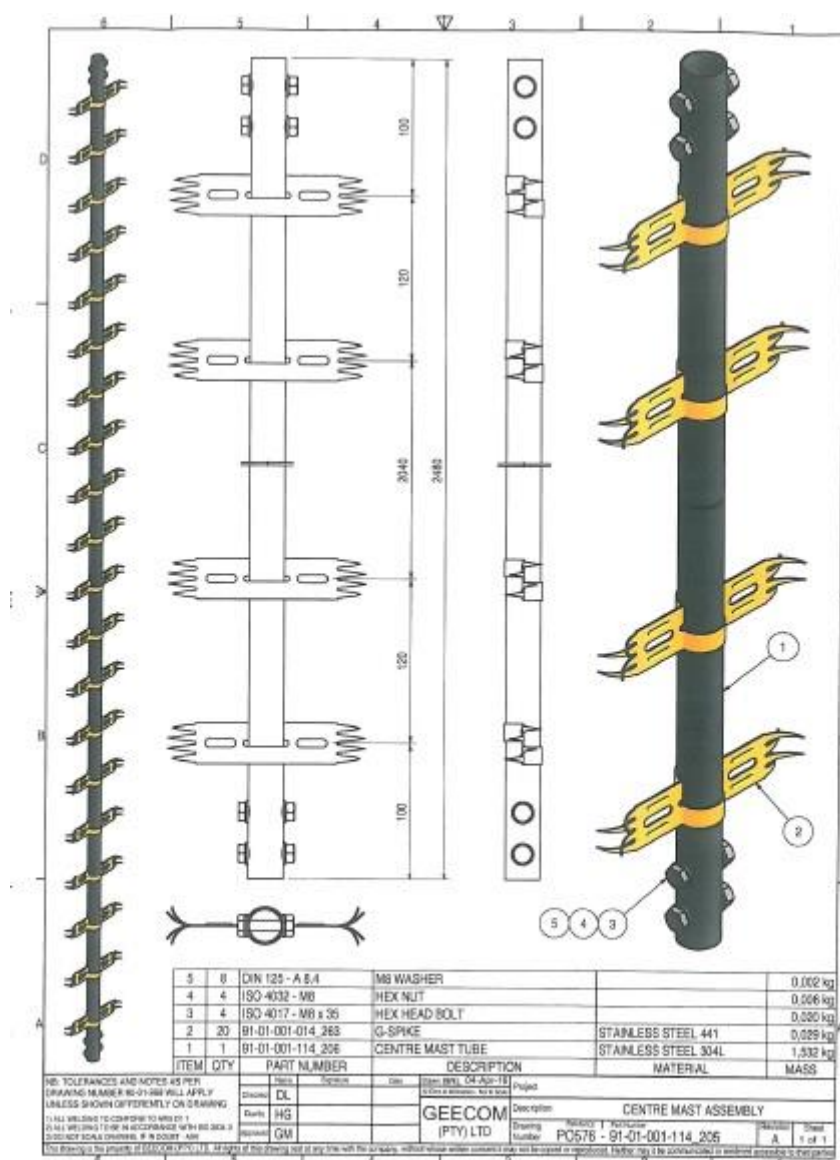


Fig. F-6: Dimensions of the Geecom G-Spike electrode.

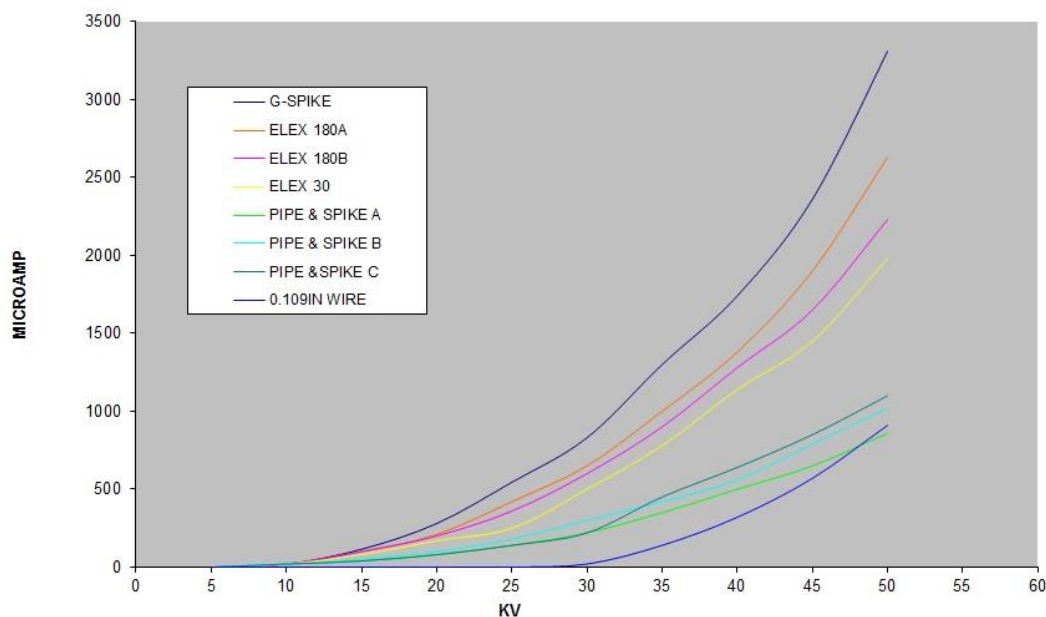


The spiked discharge electrode assembly with the spike arrangement are shown in Fig F-7.



**Fig. F-7:** Geecom G-Spike electrode assembly.

The V-I curves as reported by Geecom (Pty) Ltd. for different discharge electrodes are compared with that obtained with a spiked discharge electrode in Fig F-8. It is concluded from Fig F-8 that the G-Spike (spiked electrode) produced the highest corona current compared to the other electrodes when measured under the same conditions. The numerical data corresponding to the curves shown in Fig. F-8 are summarized in Table F-1.

**VI CURVES - G SPIKE vs OTHER TYPES**


**Fig. F-8:** V-I curves for different discharge electrodes including the G-Spike electrode. Data was provided by Geecom.

**Table. F-1:** V-I Data for different discharge electrodes including the G-Spike electrode.

V/I CURVES - GEECOM G-SPIKE ELECTRODE vs OTHER TYPE DEs															
GEECOM SPIKE		ELEX 180A		ELEX 180B		ELEX 30		PIPE & SPIKE A		PIPE & SPIKE B		PIPE & SPIKE C		0.109 in WIRE	
KV	Micro Amp	KV	Micro Amp	KV	Micro Amp	KV	Micro Amp	KV	Micro Amp	KV	Micro Amp	KV	Micro Amp	KV	Micro Amp
5	0	5	0	5	0	5	0	5	0	5	0	5	0	5	0
10	20	10	20	10	20	10	20	10	20	10	20	10	20	10	0
15	115	15	100	15	100	15	80	15	40	15	50	15	40	15	0
20	280	20	210	20	200	20	170	20	80	20	100	20	80	20	0
25	545	25	420	25	360	25	250	25	140	25	180	25	140	25	0
30	830	30	650	30	600	30	500	30	220	30	300	30	220	30	20
35	1300	35	1000	35	900	35	780	35	350	35	420	35	450	35	140
40	1740	40	1380	40	1280	40	1140	40	500	40	560	40	640	40	320
45	2360	45	1900	45	1650	45	1450	45	650	45	790	45	850	45	570
50	3310	50	2630	50	2230	50	1980	50	860	50	1020	50	1100	50	910

## F.1 References

- [1] F. August Mischkulnig, Discharge electrode, US Patent 7, 160, 364B2 (2007).
- [2] G. Mischkulnig, P. Bento, Enhanced corona discharge using innovative rigid discharge electrodes (RDE), in: 9th Int. Conf. Electrostatic Precip.: pp. 1–12.